THE EFFECT OF GRAIN BOUNDARY ENGINEERING ON THE PROPERTIES OF INCOLOY 800H/HT

A thesis

submitted in partial fulfilment

of the requirements for the Degree of

DOCTOR OF PHILOSOPHY IN MECHANICAL ENGINEERING

IN THE

UNIVERSITY OF CANTERBURY

by

DANIEL DRABBLE

University of Canterbury

2010

Preface

This thesis is submitted as a partial requirement for the degree of Doctor of Philosophy in Mechanical Engineering in the University of Canterbury. This research was conducted under the supervision of Senior Supervisor Associate Professor Milo V. Kral in the Mechanical Engineering Department, University of Canterbury, between July 2006 and September 2010.

Acknowledgements

I would like to acknowledge the following people and organisations that have contributed to this research:

- Associate Professor Milo V. Kral and Dr. Catherine Bishop for their supervision, help, advice and support.
- Methanex (NZ) Ltd., Schmidt-Clemens Spain S.A., and Tubacex (S.A.) for their financial contributions to this project, and specifically Peter Tait (Methanex), Pedro Imizcoz (Schmidt-Clemens) and Echevarria Gorka (Tubacex) for their assistance and technical advice.
- The New Zealand Tertiary Education Commission (TEC) for the provision of a Top Achiever's Scholarship.
- The members of the University of Canterbury Materials Engineering Group, including Dr. Mark Staiger, Emeritus Professor John Smaill, Emeritus Professor Les Erasmus, Emeritus Professor Frank Fahy, Mike Flaws and Kevin Stobbs, as well as fellow MEG students for all their help, comments and critique.
- The administrative and technical staff of the Mechanical Engineering Department; in particular, Scott Amies and Ken Brown (workshop), and Julian Philips (electronics workshop) for their time and expertise.

I would also like to thank my partner, Gina, and my family, Wyn, Judith, Thomas and Christopher, for their unwavering belief and unconditional support.

Abstract

The following document details an investigation into grain boundary engineering (GBE) and its applicability to a high nickel stainless steel known as alloy 800H, which is used for high-temperature piping in industrial applications such as methanol reformers. The grain boundary engineering process comprises several repeated cycles of deformation and intermediate annealing, with the aim of increasing the relative fraction of "special" grain boundaries described generally by their lattice misorientation. In the current work, the $\Sigma 3^n$ ($n<4$) boundary fraction of plate samples has been optimised by the adjustment of parameters such as deformation per cycle, annealing temperature, annealing time and number of cycles. The measurement of grain size in GBE materials has been investigated and performed for all GBE samples.

Several GBE conditions were subsequently examined in terms of their grain boundary spatial distribution, using a model of two-dimensional transport which was derived as part of this work. GBE materials were also tested for their room-temperature mechanical properties (yield strength, ultimate tensile strength, elongation at failure) and their creep rates at high temperature, low stress conditions. It was also showed that a GBE state could be replicated in tube by employing a swaging operation in place of the plate rolling process.

Table of Contents

List of Figures

List of Tables

CHAPTER 1: INTRODUCTION

1.1 Introduction

Methanex Ltd is the world's largest producer of methanol, a common solvent which also forms the basis for many other products such as recyclable plastics. The production process involves a series of chemical reactions beginning with natural gas, which is converted into 'syngas', a mixture of carbon monoxide, hydrogen and carbon dioxide. This conversion occurs at temperatures in excess of 850°C, and therefore containing the gas requires materials which can withstand the combination of high temperature and stress caused by the pressure of the gas. The deformation of materials associated with stress and high temperature is called creep, and is of high significance for Methanex Ltd. and the petrochemical industry in general. Reducing creep damage through materials engineering has potential to improve the service life of high-temperature piping within Methanex plants, potentially saving millions of dollars of replacement, maintenance and lost production costs. This is the industrial focus of this research. The scientific focus of the work is to propose and investigate a method of materials engineering which has a likelihood of mitigating creep damage in relevant materials, and to better understand the behaviour of such materials based on extensive microstructural analysis.

Grain boundary engineering (GBE) has recently emerged as a method for the improvement of material properties in face-centred-cubic (f.c.c.) materials such as austenitic stainless steels. Specifically, GBE materials have shown improvements in creep resistance [1-3], which is directly relevant to the industrial application. Therefore, Methanex NZ Ltd. agreed to sponsor this research project, with the aim of investigating the effect of GBE on alloy 800H,

a high nickel stainless steel used extensively in high-temperature tubing in Methanex plants. This thesis describes the background, methodology and results of the research, which was carried out between July 2006 and September 2010.

1.2 Current Issues in Existing Literature

Although grain boundary engineering has shown improvements in many different materials and material properties, there are still some areas of research which are not well documented or understood. Some of these issues are briefly highlighted in the following paragraphs.

The evolution of the microstructure throughout GBE processing has been reported only on a few occasions in the literature [4-7], and is not well understood. As such, studies that add weight to the previous results (or vice versa) are valuable for the academic community. Such studies are required in order to confirm or disprove trends which have been reported, and increase understanding of the microstructural process of GBE. Greater understanding of the process will inevitably lead to greater success in the production and industrial application of GBE materials.

There have also been recent endeavours in the GBE field to quantify the effect of grain boundary connectivity. Typically, property correlations have been reported as a function of the special grain boundary fraction (e.g.[1-3]), however this factor does not take into account the geometrical arrangement of such boundaries, which is also important. Models have been proposed which offer quantification of grain boundary connectivity, however all existing models have limitations which may affect their accuracy or usefulness. Hence, there is room in the literature for a new model of grain boundary connectivity, which more accurately predicts the correlations between boundary connectivity and material properties.

Finally, although improvements in creep properties due to GBE have been reported previously [1-3], the creep tests have been accelerated via large increases in stress. The applicability of previous creep results to industrial service (in particular, Methanex tubing) is in doubt due to the large discrepancy between the testing conditions and typical service conditions. As yet, there have been no reported studies of GBE microstructures at creep conditions which approach the high temperature, low stress conditions typical of industrial applications, and therefore this an important direction of research.

1.3 Project Scope

The scope of this project was defined to include the following avenues of research:

- The review of existing studies in the grain boundary engineering field, with particular emphasis on those involving creep behaviour, and high-nickel stainless steels.
- The determination of the optimum conditions for creating a grain boundary engineered condition in Incoloy 800H, including an investigation into the evolution of the microstructure as a function of processing cycle, and the effects of deformation level, annealing temperature and annealing time.
- The development of appropriate techniques with which to evaluate GBE microstructures, including a particular emphasis on the measurement of grain size.
- The evaluation of current grain boundary connectivity analysis methods and the analysis of grain boundary connectivity in GBE 800H.
- The determination of the mechanical properties of 800H, both in the as-received condition and the GBE condition, and the subsequent correlation with microstructural properties.

- The design and build of a creep test machine capable of the measurement of low strain rates under similar conditions to pigtail service conditions.
- The evaluation of creep properties of GBE 800H in comparison with the as-received condition, and the correlation between creep properties and microstructure.
- The development of GBE pipe and the subsequent microstructural analysis in order to determine the feasibility of GBE as an industrial process.

1.4 Research Achievements

This study has resulted in several academic contributions, as listed below. One further journal article is a direct result of this research, but is in progress at the time of writing this thesis, and is expected to be published as a follow-up to the microstructural analysis article at a later date.

- **Milo V. Kral, Daniel J.F. Drabble, Benjamin R. Gardiner and Peter C. Tait**, "*Implications of EBSD-based Grain Size Measurement on Structure-Property Correlations*", Praktische Metallographie (2009), 46, 9, 469-482
- **Daniel J.F. Drabble and Milo V. Kral**, "*Grain Boundary Engineering Alloy 800H/HT*", presented at TMS Annual Meeting, 9-12 March 2008, New Orleans, LA, USA
- **Daniel J.F. Drabble, Catherine M. Bishop and Milo V. Kral**, "*A Microstructural Study of Grain Boundary Engineered Alloy 800H*", Metallurgical and Materials Transactions A (in press)

1.5 Layout of this Thesis

This thesis is divided into eleven chapters, each detailing a separate section of the research. Each chapter is briefly summarised below.

Chapter 2 provides the reader with some background information regarding the production of methanol, and the purpose and service conditions of Methanex 'pigtail' tubes. The pigtail tube material, alloy 800H/HT is introduced and information regarding its composition and microstructure is provided. The stress state of the pigtail tubes is then calculated, including a finite element analysis of a stress concentration within the bent sections of the tube. Finally, the mechanisms responsible for material damage are overviewed, including a description of the creep mechanism which is thought to be significant in this application.

Chapter 3 provides a comprehensive literature review on the topic of grain boundary engineering (GBE), beginning with a description of the structure of a grain boundary, including the coincident site lattice (CSL) model, and its relation to special properties of grain boundaries. The aim and method of typical GBE processes are then outlined, and many successful applications of GBE are presented, including effects on mechanical properties, segregation and precipitation, creep and corrosion.

Chapter 4 initially details the specific method of GBE processing used in this work, including both the thermomechanical processing and the methods of microstructural analysis. In particular, the measurement of grain size in GBE materials is of high importance with respect to material properties, and is therefore presented in significant detail. Finally, the results of various combinations of GBE parameters (number of cycles, deformation per cycle, annealing temperature/time) are evaluated in terms of $\Sigma 3^n$ boundary length fraction and average grain size.

Chapter 5 describes the importance of a measure of grain boundary connectivity in a GBE analysis, before discussing existing models presented in the literature. A new model for evaluating grain boundary connectivity is subsequently presented, and its advantages and limitations are determined. The microstructures from the previous chapter are then evaluated in terms of this new model.

Chapter 6 provides a study on the evolution of the microstructure throughout the GBE process. The chapter begins by introducing the deviation from ideal parameter (v/v_m), and explaining its calculation. The microstructural parameters ($\Sigma 3^n$ boundary length fraction and grain size) are then presented as a function of the processing cycle. The results are also compared to the results of similar analyses available in the literature.

Chapter 7 describes the mechanical properties of two different GBE conditions, in comparison with the as-received structure. Both hardness tests and tensile tests are presented, including the methods and results of each. Tensile test results are also compared after an aging treatment, which was designed to simulate some microstructural evolution.

Chapter 8 is focused on the creep properties of the GBE materials. The method of testing is explained, including emphasis on the selection of the test conditions. The minimum creep rates of all samples are presented and evaluated in terms of grain size and the grain boundary connectivity model introduced in Chapter 5.

Chapter 9 presents a preliminary analysis into the application of a GBE process to short sections of pipe. The processing is described, and the results of microstructural analysis are presented and discussed.

Chapter 10 provides a summary of the major achievements of this work in list form, and leaves the reader with some concluding remarks regarding the outcomes of the project in relation to the initial objectives.

Chapter 11 explains possible further research which stems from this project, namely the identification and analysis of coherent twin boundaries and their effect on material properties, the effect of reduced creep rate on creep rupture life of pigtail tubes, and the effects of the current GBE processes on other material properties, such as its corrosion resistance.

Appendix A describes the methodology used for the EBSD analysis, including the microscope settings, calibration and post processing algorithms. These are included as a guide to potential further work in this field.

Appendix B summarises the design and build of a creep testing rig for the determination of minimum creep rate at low strain rates. Information regarding the design, calibration and evaluation is provided in this section.

Appendix C contains a text copy of the MATLAB code, used to determine Σ3 deviation from ideal from the original EBSD data set.

Appendix D contains a copy of the major journal article, "A Microstructural Study of Grain Boundary Engineered 800H", which is currently in press and due to be published in Metallurgical and Materials Transactions A.

1.6 References

[1] Lehockey, E. M., Palumbo, G., *On the creep behaviour of grain boundary engineered nickel*, Mat. Sci. & Eng. A 237 (1997) 168-172.

[2] Thaveeprungsriporn, V., Was, G.S., *The role of coincidence-site-lattice boundaries in creep of Ni-16Cr-9Fe at 360C*, Metall. and Mat. Trans. A 28A (1997) 2101-2112.

[3] Was, G. S., Thaveeprungsriporn, V., Crawford, D.C., *Grain boundary misorientation effects on creep and cracking in Ni-based alloys*, J. of Mat. 50 (1998) 44-49.

[4] Engelberg, D. L., Humphreys, F. J., Marrow, T. J., *The influence of low-strain thermo-mechanical processing on grain boundary network characteristics in type 304 austenitic stainless steel*, J. of Microscopy (2008) 435-444.

[5] Randle, V., Davies, H., *Evolution of microstructure and properties in alpha-brass after iterative processing*, Metall. & Mater. Trans. A 33 (2002) 1853-1857.

[6] Owen, G., Randle, V., *On the role of iterative processing in grain boundary engineering*, Scripta Mat. 55 (2006) 959-962.

[7] Schuh, C. A., Kumar, M., King, W. E., *Analysis of grain boundary networks and their evolution during grain boundary engineering*, Acta Mater. 51 (2003) 687-700.

CHAPTER 2: BACKGROUND INFORMATION

2.1 Introduction

The aim of this chapter is to provide the reader with some broad background information pertinent to the purpose of this work. The process of methanol production is briefly outlined, and the specific application of pigtail tubes is explained. An overview of the stress state and major damage mechanisms for these pigtail tubes is then presented, along with a detailed overview of the material currently utilised, alloy 800H/HT. Finally, the damage mechanisms including creep, oxidation and nitridation are overviewed.

2.2 Methanol Production

Methanol has the chemical formula CH_3OH and is commonly used as an antifreeze, a solvent or a fuel. It also forms the basis for many other products such as recyclable plastics, plywood, paints and explosives. Methanol is mainly produced from natural gas (CH_4), through a process called steam-methane reforming (SMR), although other sources such as coal or biomass may also be used as a feedstock.

Methanex Ltd. is the world's largest supplier of methanol to major international markets including North America, Asia and Europe, and exclusively uses natural gas as a feedstock. The methanol production process in this case consists of four stages:

- Desulphurisation of natural gas
- Reforming
- Compression and synthesis
- Distillation

The desulphurisation and reforming processes are shown schematically in Figure 2.1.

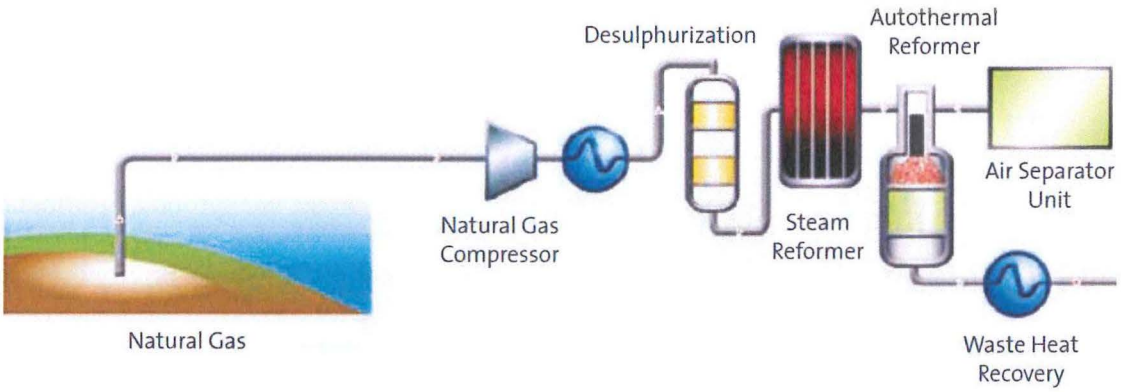

Figure 2.1 Methanol manufacturing process – desulphurisation and reforming [1]

Natural gas is first preheated and a cobalt-molybdenum or nickel-molybdenum catalyst is used to convert any contained sulphur into hydrogen sulphide (H_2S), according to the reaction:

$$CH_3HS + H_2 \rightarrow H_2S + CH_4$$

The gas is then passed through a bed of zinc oxide (ZnO) to remove the hydrogen sulphide, according to the reaction:

$$H_2S + ZnO \rightarrow ZnS + H_2O$$

The desulphurised natural gas stream is then mixed with steam and preheated further before entering the reforming section of the process. The reforming section of the plant consists of many vertical tubes known as reformer tubes, which are contained in a furnace and operate in excess of 900°C. The steam/natural gas mixture is flowed through the reformer tubes and across a nickel catalyst at high temperature producing the steam reforming reactions:

$$CH_4 + H_2O \rightarrow CO + 3H_2$$

$$CO + H_2O \rightarrow CO_2 + H_2$$

The mixture of carbon monoxide (CO), hydrogen (H_2) and carbon dioxide (CO_2) is referred to as synthesis gas, or syngas for short. The syngas leaves the reformer tubes through welded exhaust tubes called 'pigtails' and is then cooled from 850°C to ambient temperature before entering the next stage of production.

The remaining two steps (compression/synthesis and distillation) are shown in Figure 2.2.

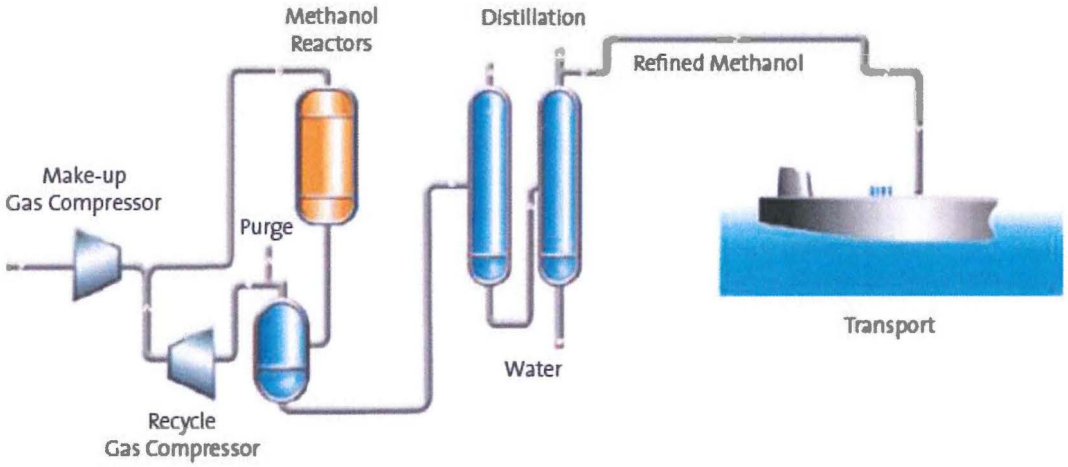

Figure 2.2 Methanol manufacturing process – synthesis and distillation [1]

The syngas first passes through a compressor which raises its pressure from approximately 1.5MPa to 8.6MPa. The compressed gas is then sent to the methanol reactor, where "crude methanol" (a mixture of 80% methanol, 18% water and 2% impurities) is formed according to the reactions:

$$CO + 2H_2 \rightarrow CH_3OH$$

$$CO_2 + 3H_2 \rightarrow CH_3OH + H_2O$$

Any unreacted syngas is then separated from the crude methanol in a separator vessel, which is then either purged to remove unreactive compounds or recirculated back into the incoming syngas stream to produce additional crude methanol. Finally, the crude methanol must be

distilled to form the high-purity final product. In the distillation towers, the dissolved unreacted gases (light ends) are removed, followed by the water, and then the heavy alcohols, ketones and aldehydes (these are often returned to the fuel system for combustion). The high-purity methanol (99.85%) then undergoes compositional analysis and quality control before being transferred to storage tanks and transportation.

2.3 Pigtail Tubes

The greatest challenges in terms of materials performance and design occur within the reforming section of the production process. In the Methanex facilities, the syngas is passed through the vertically-hanging reformer tubes at temperatures in excess of 900°C. The exhaust is then ejected through the 'pigtail' tube and collected into a single outlet. An example of a typical pigtail setup is shown in Figure 2.3.

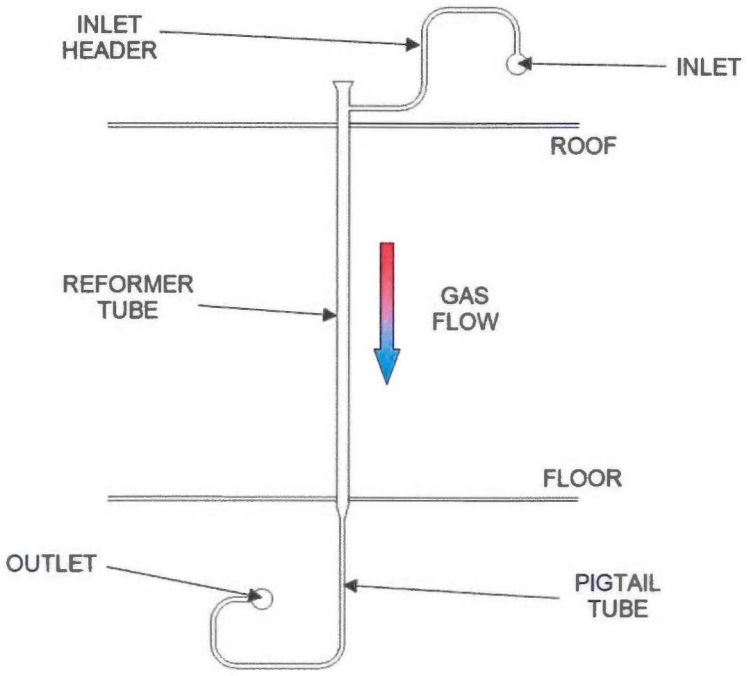

Figure 2.3 Reformer tube and pigtail setup

Significant scientific work has recently been put in to improving the operating life of the reformer tubes. Much of this work has been successful, and in service, the effective life of the reformer tubes has recently seen an increase from 10-12 years to approximately 15 years. Although this is a definite improvement, the life of the reformer tubes now exceeds the operating life of the pigtail tubes, which generally exhibit a useful life of 10-12 years (approximately 100,000 hours). The cost of replacement for either the reformer tubes or the pigtails is significantly greater than simply the new material cost, because the replacement cannot be performed *in situ*. This means that the entire plant must be shut down, and significant lost production costs are incurred. The ideal solution to this problem is to increase the operating life of the pigtail tubes to match that of the reformer tubes (i.e. approximately 15 years). This would allow both the reformer tubes and the pigtails to be replaced in a single maintenance session, and remove the current need for two separate plant shutdown procedures.

The Methanex pigtail tubes measure approximately 42mm outer diameter with a wall thickness between 4.75mm and 6.5mm. The shape of the pigtail tube is shown in Figure 2.4.

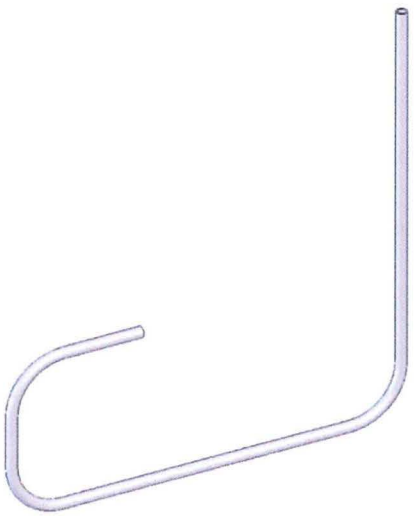

Figure 2.4 General shape of a pigtail tube

The pigtails are produced by either extrusion or cold pilgering, a longitudinal cold-rolling process which reduces the diameter and wall thickness of large tube to the final dimensions. This is normally done in a single working cycle, resulting in cross-sectional reductions of up to 90%. The working cycle is then followed by annealing at high temperature (1150°C) for 30-60 minutes, required to meet the grain size specifications of the particular alloy. Three 90° bends are subsequently performed by cold bending to obtain the desired configuration. This bending operation introduces a level of deformation into the tube walls, which can be calculated according to the ASME Boiler and Pressure Vessel Code [2] using the parameters r (the radius of the cross section) and R (the radius of the bend):

$$\%\, work = \frac{100r}{R} = \frac{100 \times 21.2mm}{200mm} \approx 10\% \tag{2.1}$$

This level of 10% cold work is found only at the intrados and extrados of the bend, where these terms are used to describe the points furthest from the neutral axis. At the neutral axis of the bend, there is theoretically no cold work, and therefore the level of work must increase towards the intrados or extrados. Because of this extra cold work, the entire tube then requires a second anneal (at the same temperature), in order to remove the microstructural deformation and restore the required grain size in the bend sections.

The material selected for the pigtail application is a nickel-iron-based stainless steel called INCOLOY 800H. The characteristics and properties of this material are detailed in the following section.

2.4 Material Overview

2.4.1 Alloy Background

INCOLOY alloy 800 was invented by the Special Metals Corporation Group of Companies, and was first introduced to the market in the 1950's [3]. Since then, it has been widely used for its high temperature strength and oxidation resistance.

The alloy was approved by the ASME Boiler and Pressure Vessel Committee in 1963, for the first time listing aluminium and titanium as purposeful additions and differentiating between annealed material and solution-annealed material.

The solution-annealed material (previously called Grade 2 alloy 800) was renamed alloy 800H after Special Metals tightened the carbon level to the upper half of alloy 800, and presented data to the ASME Code. With the tighter carbon range, 800H also required an average grain size of ASTM 5 or coarser. Grade 1 alloy 800 (annealed at 980°C) became alloy 800. The company later introduced a variation of 800H which was named 800HT. INCOLOY 800HT has a further restricted chemistry but remains within the limits of alloy 800H, and also requires a grain size of ASTM 5 or coarser. The compositional differences are detailed in the following section.

2.4.2 800H/HT Composition

The composition of alloy 800 and its two variants are detailed in Table 2.1 overleaf.

Table 2.1 Composition of alloys 800, 800H & 800HT [3]

Element	Alloy 800	Alloy 800H	Alloy 800HT
Nickel (Ni)	30 – 35%	30 – 35%	30 – 35%
Chromium (Cr)	19 – 23%	19 – 23%	19 – 23%
Iron (Fe)	39.5% min	39.5% min	39.5% min
Carbon (C)	0.10% max	0.05 – 0.10%	0.06 – 0.10%
Aluminium (Al)	0.15 – 0.60%	0.15 – 0.60%	0.25 – 0.60%
Titanium (Ti)	0.15 – 0.60%	0.15 – 0.60%	0.25 – 0.60%
Aluminium + Titanium	0.30 – 1.20%	0.30 – 1.20%	0.85 – 1.20%
ASTM Grain Size	No requirement	5 or coarser	5 or coarser

The differences between the three alloy variants are limited to the carbon content, the aluminium and titanium levels, and the required grain size. Alloy 800HT is the most recent of the three, and is claimed to exhibit the highest creep strength. This is reportedly due to its increased carbon content combined with the increased Al and Ti for precipitation in the relevant temperature range.

2.4.3 Alloy Microstructure

Alloy 800H and its variants are austenitic iron-nickel-chromium alloys with controlled levels of carbon, aluminium, titanium, silicon and manganese. The alloys are used in the as-annealed condition, which have been solution treated at a temperature of approximately 1150°C to promote grain growth and dissolution of carbides. This leaves some of the carbon available for precipitation during service. A typical as-annealed (also referred to as as-received throughout this document) microstructure for 800H is shown in Figure 2.5.

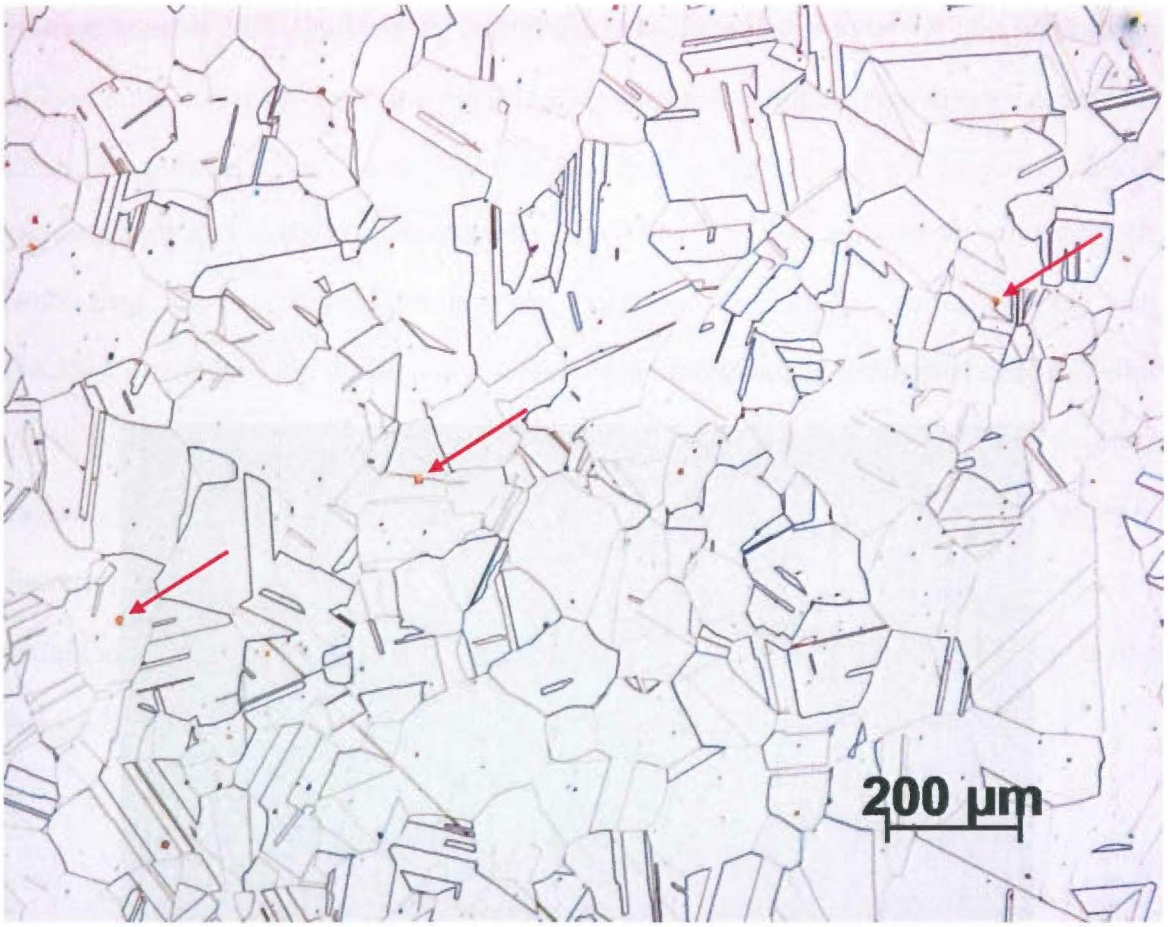

Figure 2.5 Typical microstructure of as-received 800H. Etched with glyceregia.

The as-received microstructure reveals a heavily twinned austenitic grain structure with small amounts of intragranular titanium carbonitrides (Ti(C,N)), some of which are indicated by arrows in the preceding figure. The grain size is often in the range 100-150µ, representing an ASTM grain size of ~3.5 to ~2.5, well within the requirements of ASTM 5 or coarser. In fact, Methanex imposes an additional constraint on the pigtail grain size, specifying that it must be in the range ASTM 3-4 after processing.

This alloy is strengthened by the γ' phase, $Ni_3(Al,Ti)$. At temperatures higher than approximately 760°C, and therefore at the design service temperature of the pigtails (870°C), the γ' phase is unstable. This is intended, as the γ' phase, despite strengthening the matrix

against creep, is very brittle and reduces the ductility of the material. This reduced ductility is particularly undesirable during plant start-ups and shutdowns.

At the service temperature of 870°C and above, strengthening mainly comes from carbides that develop during service. A secondary electron image (SEI) of an aged 800H microstructure is shown in Figure 2.6.

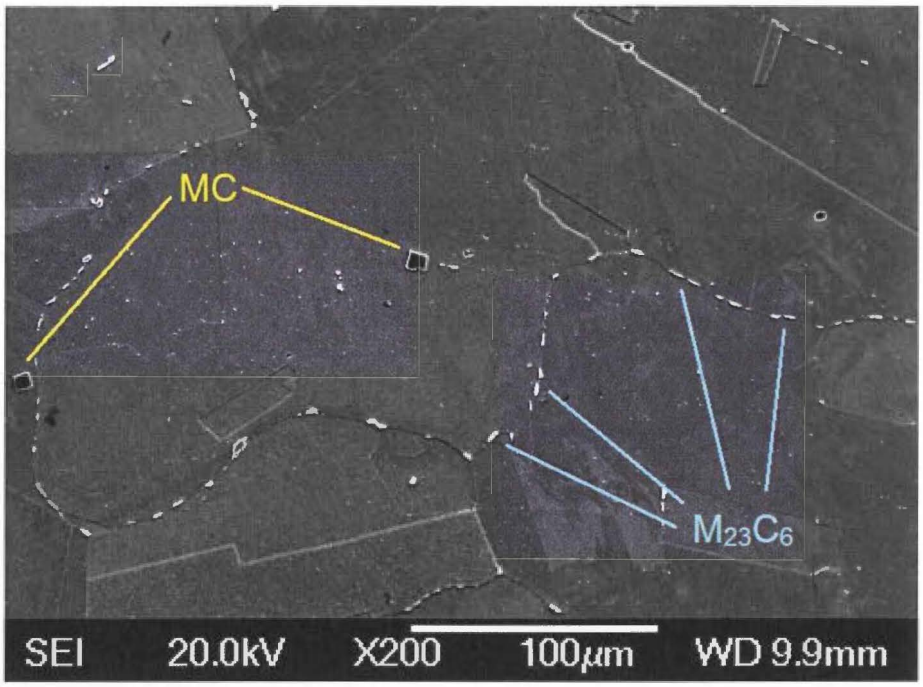

Figure 2.6 SEI image of ex-service 800H, indicating MC and $M_{23}C_6$ carbides

These carbides provide three principle functions [4]. First, grain boundary carbides strengthen the grain boundary, retard grain boundary sliding, and permit stress relaxation. Second, if fine carbides are precipitated in the matrix, this results in lattice strengthening. Finally, carbides also tie up certain elements that would otherwise promote phase instability during service.

MC carbides (mostly TiC) are distributed throughout the alloy, mainly in intragranular positions. It has been suggested that the presence of TiC as well as the coarse grain size leads

to the good creep rupture properties above 800°C [4]. Up to 0.1%C, the TiC has been shown to have little effect on creep ductility. MC carbides also act as a source of carbon for subsequent phase reactions during heat treatment and service, for example the dissociation of MC into $M_{23}C_6$ [4].

The $M_{23}C_6$ carbides form during lower temperature heat treatment and service (760-1050°C) [5], both from the degeneration of MC carbide and from soluble residual carbon in the alloy matrix. These carbides occur mainly in the grain boundaries, and the presence of these discrete particles improves the rupture strength of the alloy, believed to be through the inhibition of grain boundary sliding [3], while still allowing sufficient ductility in the surrounding grains.

2.5 Pigtail Stress State

The pigtail tubes are essentially cylindrical pressure vessels and therefore exhibit a triaxial stress state, as shown in Figure 2.7.

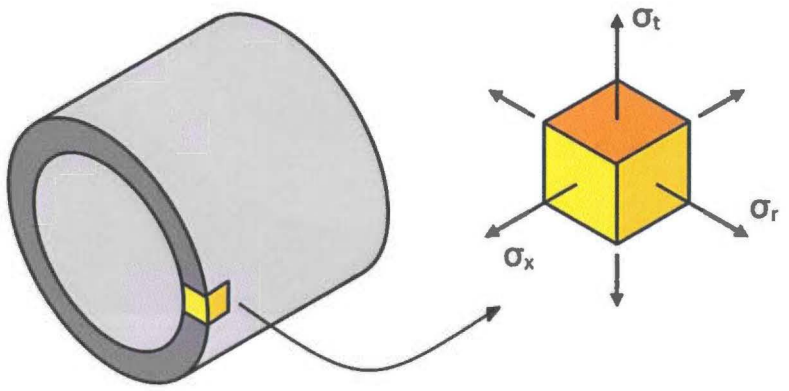

Figure 2.7 Triaxial stress state in a pigtail tube

The stresses σ_t (tangential), σ_x (longitudinal) and σ_r (radial) represent the three directional stresses experienced by each unit volume of material. The tangential (or hoop) stress is the largest of the three, which is calculated to be approximately 8MPa at the mid-wall, and approximately 9.5MPa at the inner surface, assuming a uniform temperature.

It is also important to note that the stress state differs in the bend sections of the pigtail. Due to the bending operation, the cross-sectional geometry of the pipe changes from circular to slightly oval-shaped within the bent sections. This adds an additional stress concentration under applied hoop stress. In order to determine the effect of this "out of round" condition, a finite element model of the pipe cross section was created using ANSYS. An example of the meshed area is shown in Figure 2.8.

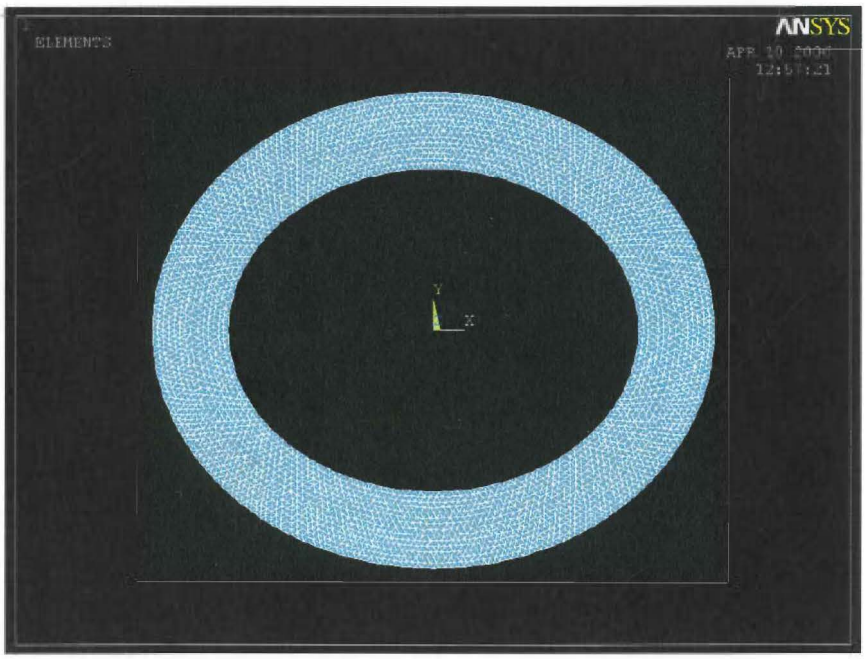

Figure 2.8 Example of meshed area for out-of-round analysis

A series of finite element simulations was performed on accurately size tubes with varying ratios of major axis to minor axis length (aspect ratio). An example of the resulting Von

Mises stress distribution in a tube with an aspect ratio of 1.2 is shown in Figure 2.9. The neutral axis is oriented horizontally.

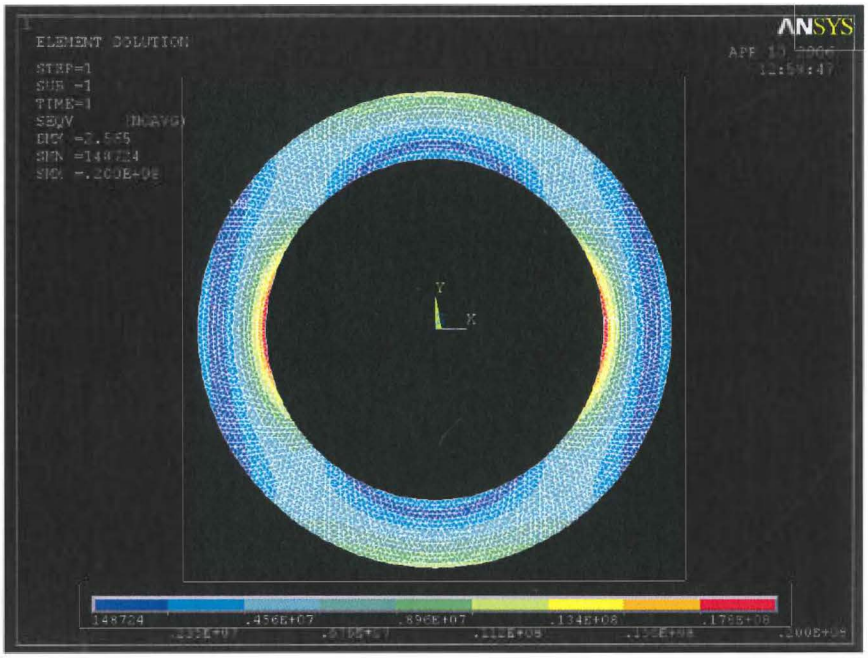

Figure 2.9 Von Mises stress distribution resulting from out-of-round condition

The maximum stress in the cross-section was recorded for seven aspect ratios ranging from 1.0 to 1.3, and the results are shown in Figure 2.10.

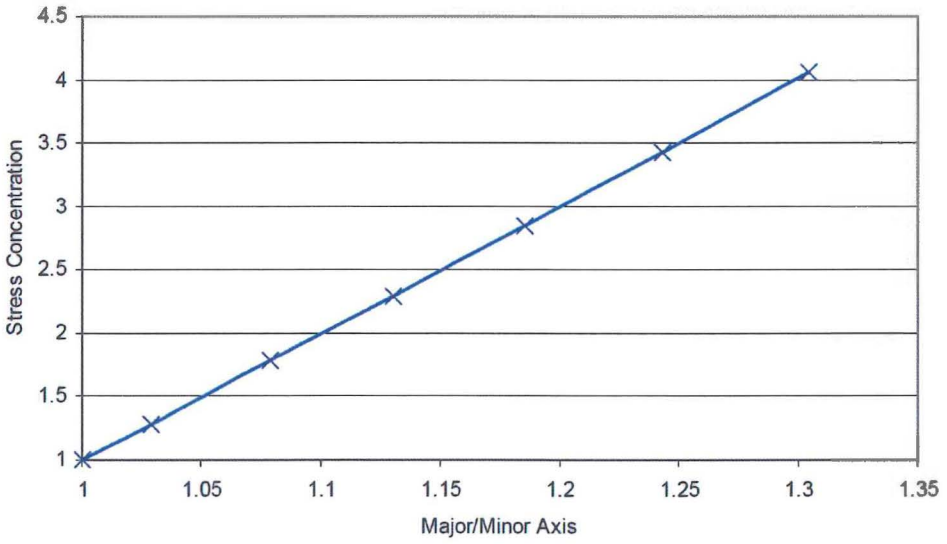

Figure 2.10 Stress concentration for varying degrees of out-of-round

The results show a significant stress concentration at the inner wall of the neutral axis of the bend. The cross-sectional dimensions of a sample bend, which was processed under the same conditions as the pigtail tubes, revealed an aspect ratio of up to 1.1. This measurement infers a stress concentration of two at the neutral axis. Further analysis is required to determine the degree to which the additional bending operation is detrimental to the life of the pigtails, although this analysis was considered outside the scope of the present project.

2.6 Major Damage Mechanism - Creep

2.6.1 Overview of Creep

Creep is a time-dependent deformation of a material subject to temperatures generally in excess of 40% of the melting point. Creep is a thermally activated phenomenon, which differentiates it from simple mechanical deformation in that there is no specific threshold stress at which the onset of plastic deformation begins. In fact, creep deformation occurs at stresses significantly below the yield point of the material. For example, the yield strength of the pigtail tubes at service temperature is approximately 100MPa [3], whereas the previously calculated stress of 8MPa eventually causes creep failure.

In order to determine the creep response of a material, a creep test is conducted. A creep test generally involves the application of a constant load to a tensile specimen, which is maintained at a constant temperature. The extension (or strain) of the specimen is measured as a function of time. The duration of such tests may range from several minutes to several years depending on the temperature and stress employed. The typical deformation-time relationship for a constant-load test is shown in Figure 2.11.

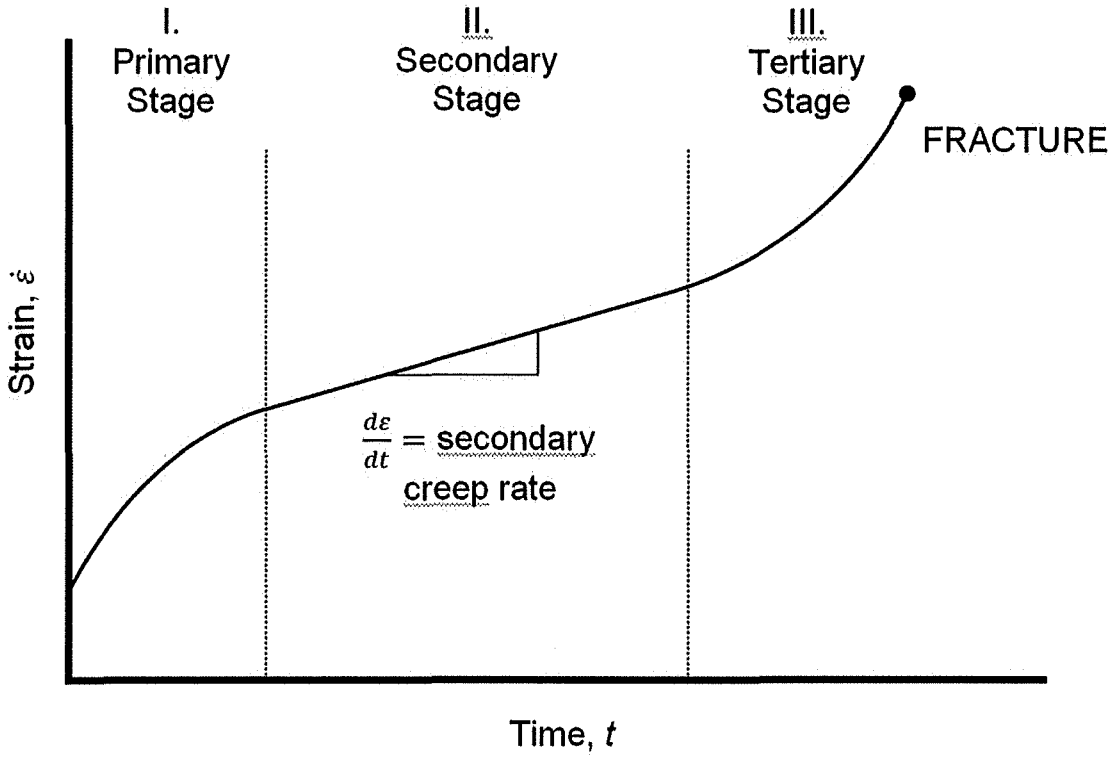

Figure 2.11 Typical creep curve showing the three stages of creep

At the beginning of the test, there is some initial strain due to the elastic (and perhaps plastic) deformation of the material. The strain rate $\dot{\varepsilon} = d\varepsilon/dt$ progressively decreases during the primary stage until it reaches a relatively constant value. This point marks the end of the primary creep stage and the beginning of the secondary creep stage. The slope of the curve during the secondary creep stage is called the secondary creep rate, but is often termed the steady-state creep rate, the minimum creep rate, or more simply, the creep rate. Finally the strain rate increases throughout a stage known as the tertiary stage, until the point of rupture. In general, it is the secondary creep stage which represents the largest fraction of the test duration, and hence it is the secondary creep rate which is normally used for design purposes.

Creep data are generally presented as plots of (secondary) creep rate versus stress for varying temperatures, as shown in Figure 2.12a. Alternatively, the time to rupture may be plotted in a similar manner, such as in Figure 2.12b.

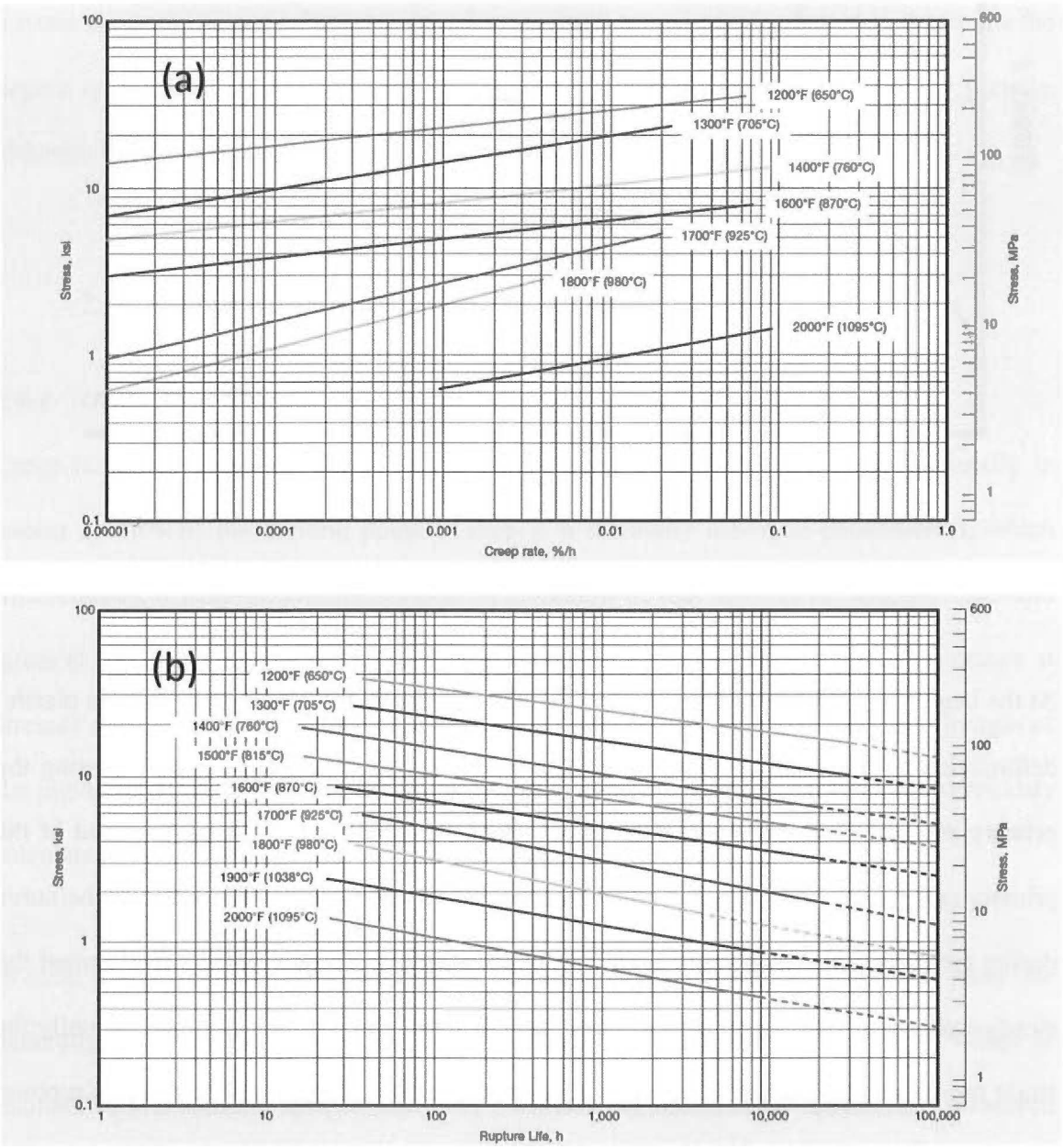

Figure 2.12 (a) Secondary creep rate data for 800H, (b) Creep rupture life data for 800H [3]

Extrapolation parameters such as the Shelby-Dorn and Larson-Miller parameters [6] are also used. Of these, the latter is commonly used with the design of reformer tubes and pigtails. The Larson-Miller parameter (*LMP*) is a combination of time and temperature given by the general equation $LMP = T(\log t_r + C)$, where T is the absolute temperature (K), t_r is the rupture time (hours) and C is a constant specific to the material. Once the constant, C, is calculated by experimentation, the time to rupture can then be estimated based on the test conditions.

For example, at a service temperature of 900°C and a surface stress of 9.5MPa, the rupture life can be calculated, given the constant, $C = 22.93$ [3]. From the manufacturer's specifications (Figure 2.13), the Larson-Miller Parameter at a stress of 9.5MPa (1.4ksi) is approximately 59.

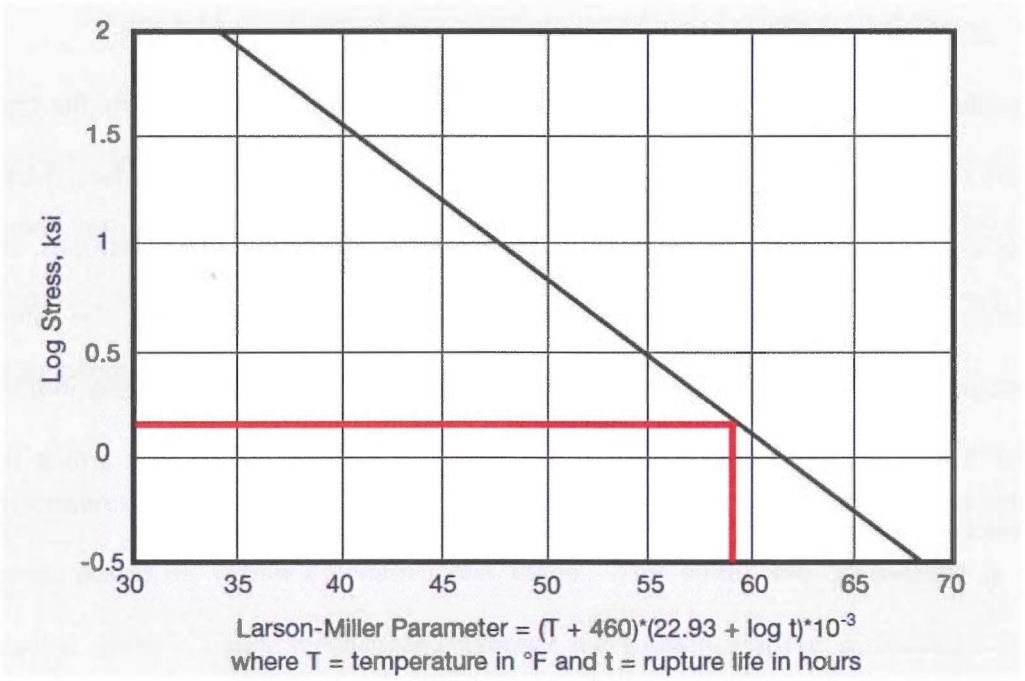

Figure 2.13 Larson-Miller data for 800H [3]

The corresponding rupture life can then be calculated from the formula (where T_F is the temperature in Fahrenheit:

$$LMP = (T_F + 460)(22.93 + \log t_r) \times 10^{-3} \quad (2.2)$$

$$59 = (1652 + 460)(22.93 + \log t_r) \times 10^{-3}$$

$$\log t_r = 27.94 - 22.93$$

$$t_r \approx 100\,000 \text{ hours}$$

This calculated design life is probably an overestimate for the pigtails because it considers only hoop stress, only one failure mode (creep), and does not take into account the stress concentration present at the neutral axis of the bends. However, reducing the temperature by 30°C increases the calculated design life to over 500,000 hours, illustrating the dependence of creep life on temperature.

2.6.2 Mechanisms of Creep

The mechanism by which creep deformation occurs is variable, influenced by the type and structure of the material, as well as the stress and temperature conditions. In fact, there are a number of deformation mechanisms which are active at any given set of conditions, leading to a deformation rate which is controlled by the dominant creep mechanism. The competing deformation mechanisms were arranged into graphical form by Frost and Ashby in their text entitled "Deformation Mechanism Maps" in 1984 [7]. An example of such a map for 316 stainless steel is shown in Figure 2.14 (no such map exists for 800H).

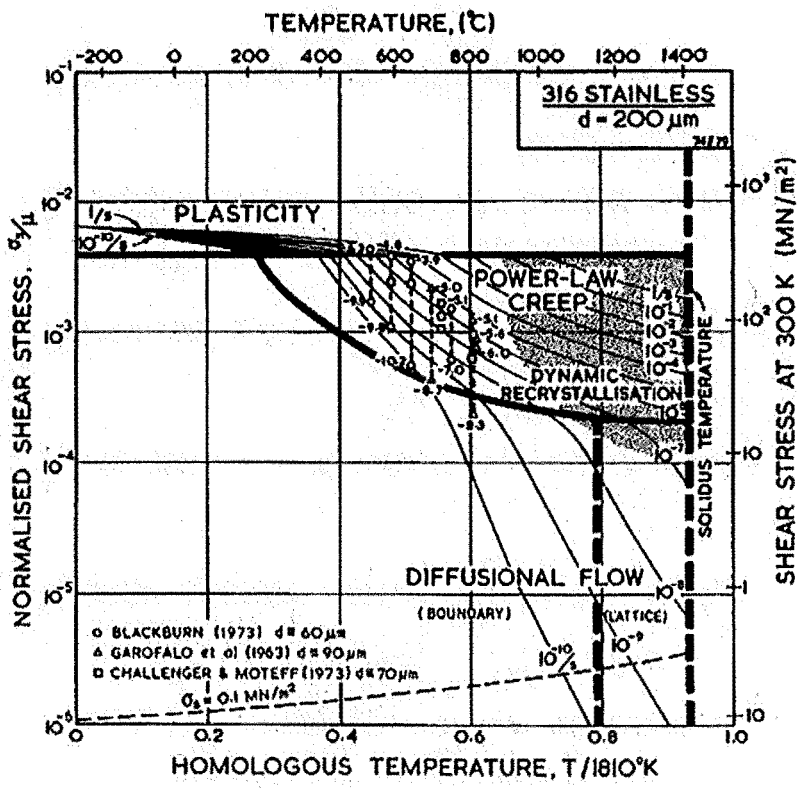

Figure 2.14 Deformation-mechanism map for 316 stainless steel [7]

The maps are unique to each alloy and also dependent on grain size. They provide a means to predict both the strain rate, and the dominant creep mechanism based on the known temperature and stress. The relevant creep mechanisms will be briefly discussed in the following paragraphs.

At temperatures above T_m=0.4 for most alloys, strain becomes proportional to stress raised to a constant power, *n*, within a certain stress range. This strain rate dependence is called "power-law creep". This mechanism involves the motion of free dislocations by the combined processes of climb and glide, and is defined according to Frost and Ashby by the equation:

$$\dot{\gamma}_{pl} = \frac{A_2 D_{eff} \mu b}{kT} \left(\frac{\sigma_s}{\mu}\right)^n \tag{2.3}$$

where A_2 represents a dimensionless constant,

D_{eff} is an effective diffusion coefficient which combines core and lattice diffusion,

μ is the temperature adjusted shear modulus,

b is the Burger's vector,

k is the Boltzmann constant,

T is the absolute temperature,

σ_s is the shear stress and

n is the stress exponent (typically between 3 and 10).

At high temperatures and low stresses, lattice diffusion dominates and the resulting field is often called "high-temperature creep" or "H.T. creep". Conversely, at lower temperatures and higher stresses, core diffusion dominates and the field is referred to as "low-temperature creep". Variations to this law also exist at sufficiently low stresses (Harper-Dorn creep) or at sufficiently high stresses (Power-Law breakdown). However, these latter mechanisms will not be covered as they are not thought to be applicable to the current material service conditions.

The competing mechanism to power-law creep which occurs at lower stresses is referred to as diffusional creep. Diffusional creep involves the movement of vacancies from areas of high vacancy concentration, such as the areas surrounding grain boundaries which are oriented normal to the applied stress, to areas of lower vacancy concentration. The rate equation is given as:

$$\dot{\gamma}_{diff} = \frac{42\sigma_s \Omega}{kTd^2} D_{eff} \tag{2.4}$$

using the same nomenclature as the previous equation and adding the atomic volume, Ω.

At very high temperatures ($0.8T_m$ in the case of Figure 2.14), lattice diffusion is dominant. This is known as Nabarro-Herring creep and strain rate scales with grain size as $(1/d^2)$. At lower temperatures, grain boundary diffusion is dominant. This mechanism is known as Coble creep, leading to a grain size dependence of $(1/d^3)$.

The explanation of creep mechanisms provided here is relevant to explain the restrictions which exist on the selection of creep testing conditions. Normally, the creep test is accelerated, as testing at actual service conditions is prohibitively time-consuming. Hence, test conditions generally involve an increase in either stress, or temperature, or both, compared to the design conditions, and the results are then extrapolated for design purposes. However, this extrapolation is flawed in that accelerating the creep test changes the relative contribution from each creep mechanism, and may well change the dominant mechanism. This leads to some uncertainty in whether or not such an extrapolation is valid. Information regarding the selection of test conditions for the current work is presented in Chapter 8, along with increased detail regarding the relevant creep mechanisms and their relative contributions to creep strain.

2.6.3 Creep Damage in Pigtails

Creep is believed to be responsible for the majority of damage seen in methanol pigtail tubes. Visual evidence for creep damage occurs in the form of voids, which begin isolated, but become oriented with each other as creep strain increases. Once enough voids coalesce, micro-cracks begin to form, which eventually leads to through-wall cracking and thus failure

of the component. An example of creep damage in a pigtail tube wall is shown as a montage of optical micrographs in Figure 2.15.

Figure 2.15 Creep damage in pigtail tube showing orientation of creep voids

As explained in Section 2.5, the greatest stress exists at the neutral axis of the pipe bends, where there is a stress concentration due to the non-circular section. Inevitably, this leads to significant creep damage at the inner wall of the neutral axis. An example of a 2mm crack located in this position is shown in Figure 2.16, from a pigtail tube that had been in service for approximately three years.

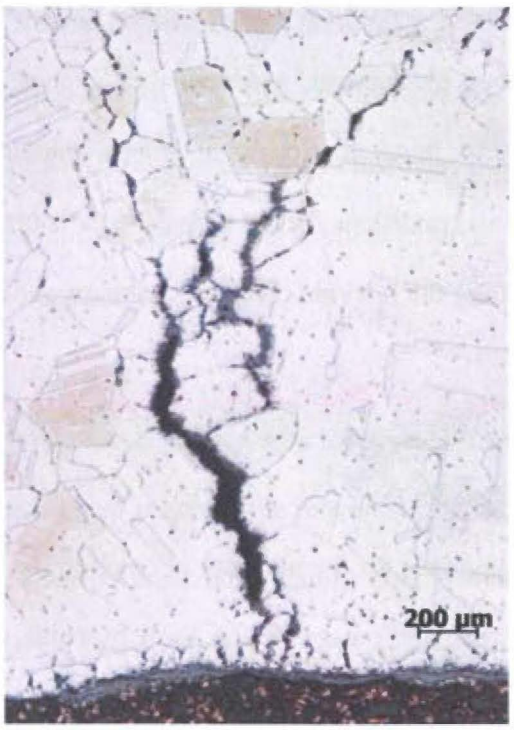

Figure 2.16 2mm crack located at the inner wall of the neutral axis of the pipe bend

In addition to the stress concentration, there is also a microstructural difference in the neutral axis of the bend. In some cases, the grain size has been observed to be 1-2 ASTM sizes larger in the neutral axis when compared to the extrados and intrados of the bend. This has been noted in pigtails previously [8-9] as well as by the current author. The reason for the grain size difference is currently unknown, although the variation in the level of cold work throughout the cross-section is a likely factor. In the areas surrounding the neutral axis, much lower levels of cold work are likely, compared to the intrados and extrados. This effect is also documented for alloy A-286 [4], which shows a grain size increase after annealing with cold work levels up to 5%, and then a decreasing grain size with increasing cold work. It is unknown whether this grain size difference is a contributor to the preferential damage at the neutral axis.

2.7 Additional Damage Mechanisms

Although creep is considered to be the major damage mechanism for pigtail tubes, other effects due to the high-temperature environment also act in combination with creep. These mechanisms are also briefly overviewed in the following sections.

2.7.1 Oxidation

Oxidation describes the degradation and loss of the material through reaction with oxygen, and is highly dependent on the material chemistry, the availability of oxygen in the environment and the temperature. Alloy 800H/HT contains 19-23% chromium, which is sufficient to develop a protective layer of α-chromia under oxidising conditions. Once this layer is established, the subsequent oxidation rate is determined by the effectiveness of the α-chromia layer as a barrier to inward diffusion of oxygen and as an outward barrier to metallic

ions. This α-chromia scale is protective at temperatures up to approximately 900°C, and is able to "heal" itself through the diffusion of chromium to the scale [8].

Surface oxidation (spinel and chromium oxide) and internal oxidation (aluminium or titanium oxide) at grain boundaries are both common in ex-service alloy 800H pigtails, as noted by Roumeau [10]. However, oxidation is generally only perceived as a damage contributor when combined with another damage mechanism, such as creep, the combination of which allows sub-surface oxidation within creep cracks. Therefore, improving the oxidation resistance of this alloy in this application is seen as less useful than improving its creep resistance.

2.7.2 Carburisation/Nitridation

Carburisation and nitridation are the terms used to describe the absorption of carbon and nitrogen respectively from the atmosphere. These elements normally take the form of precipitates, which may provide some strengthening but also result in a loss of ductility. Carburisation and nitridation both occur during service, as noted in [10]. Although this environmental degradation is considered in this case as a possible contributor to the material damage, it was noted that cracking occurred before the environmental attack. Therefore, the same conclusion must be drawn as with oxidation – that improving the creep resistance is of greater importance than improving the resistance to environmental attack.

2.7.3 Thermal Stresses

Some thermal stresses are present on plant shutdowns and restarts, and the pigtail tubes are designed to accommodate both their own thermal expansion, and also that of the reformer tube and manifold assembly. The design of the tube is such that this stress is minimised due to its geometry, and the fact that its endpoints are not fixed spatially. However, the highest

stresses again occur in the bend regions of the pigtail. This leads to the potential for preferential damage in this region, and thermal stress as a damage mechanism has been suggested in at least one investigation [9]. Further analysis is required to determine the exact contribution from thermal stress and the way in which thermal stresses act in conjunction with the creep damage which is typical of ex-service pigtails.

2.8 Conclusions

In conclusion, pigtail tubes in methanol reformer furnaces are constructed from alloy 800H/HT, a wrought iron-nickel based stainless steel known for its excellent ductility and creep strength. They are used as exhaust tubes from the reformer itself, and as such, experience a combination of high temperature (870°C) and stress (8-10MPa) due to the internal pressure. Because of the tube forming operations, a stress concentration also exists in the neutral axis of the pipe bends due to ovality of the cross-section. There is also evidence of large grains present at the neutral axis after re-annealing.

These service conditions result in a number of in-situ damage mechanisms such as creep, environmental attack, and thermal stresses. However, it is believed that creep is the major contributor to the material damage, as typical creep damage (void formation and cracking) is commonly found in ex-service pigtails. Therefore, it follows that improving the creep resistance of this alloy will result in longer service life, which is the underlying objective of this work.

2.9 References

[1] Methanex Corporation, *Environmental Report*, 2008.

[2] American Society of Mechanical Engineers, *Boiler and Pressure Vessel Code, Section VIII, Div 1, UNF-79*, 2007.

[3] Special Metals Corporation, *Technical Publication - Alloy 800H & 800HT*, 2004.

[4] ASM International, *Heat-Resistant Materials*, ASM International, 1997.

[5] Coppolecchia, V., Bryant, J., Hoffmann, F., Drefahl, K., *Loss of Creep Ductility in Alloy 800H with High Levels of Titanium and Aluminium*, P. Ganesan, Bradley, R.A., (Ed.) Performance of High Temperature Materials in Fluidized Bed Combustion Systems and Process Industries, ASM International, 1987, p. 201.

[6] Norman E. Dowling, *Mechanical Behaviour of Materials*, Prentice Hall, 1999.

[7] Frost H.J., Ashby M.F., *Deformation-Mechanism Maps*, Pergamon Press, 1982.

[8] Smith, G. D., *The role of protective scales in enhancing oxidation resistance*, Inco Alloys International Inc., 1996.

[9] Hoffman, J. J., Lai, G. Y., *Metallurgical Evaluation of Alloy 800HT Pigtails*, Corrosion 2005, 2005.

[10] Roumeau, X., *High-Temperature Cracking of 800HT Pigtails in a Hydrogen Unit*, NACE International, Corrosion 2010, San Antonio, 2010.

CHAPTER 3: GRAIN BOUNDARY ENGINEERING – A LITERATURE REVIEW

3.1 Introduction

The purpose of this chapter is to provide a comprehensive literature review on the topic of grain boundary engineering. However, in order to make this review more useful, it is first necessary to provide some background information regarding the structure of grain boundaries and the relevant geometric model used to describe a "special" subset of these boundaries. The concept of a special grain boundary is then investigated, followed by an overview of the successful implementations of grain boundary engineering, both commercially and in laboratory experimentation. In particular, the work of Watanabe, Randle and co-workers is covered in detail, as these authors are considered seminal in the field.

3.2 Structure of a Grain Boundary

The interface between two adjacent ordered crystals (grains) in a polycrystalline material is known as a grain boundary. In general, grain boundaries are treated as planar discontinuities, with structures characterised by their excess free volume [1] and elastic strain fields [2] compared to the lattice. It is these features of grain boundaries which confer properties that differ from those of the lattice. Such properties include increased diffusion rates, chemistry/compositional differences, strain and defect accommodation and nucleation phenomena [3]. For example, Gust et al showed that diffusion rates could be several orders of magnitude higher through the grain boundary network, as compared to the lattice [4]. A

representation of the geometry of a grain boundary separating two crystals, is shown in Figure 3.1. For simplicity, the boundary normals are displayed as coincident in this figure, although in a general boundary, this is not necessarily the case.

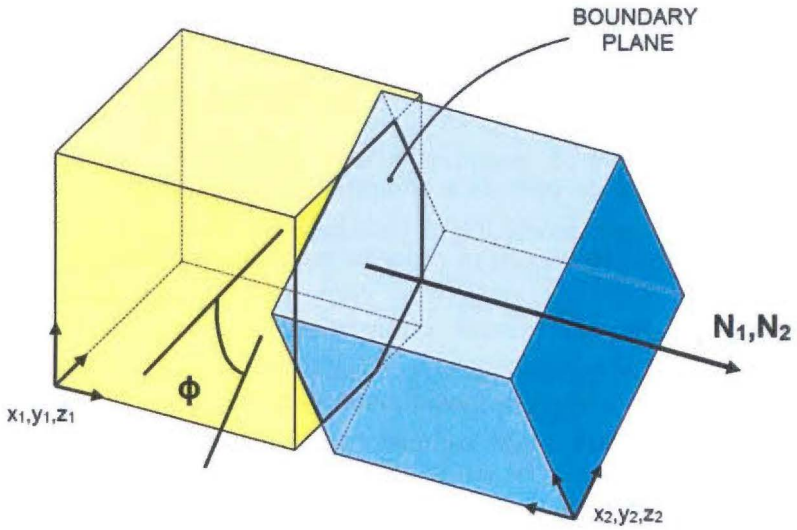

Figure 3.1 Geometry of a grain boundary

Any planar grain boundary may be described according to five macroscopic degrees of freedom, as labelled in the preceding figure. Two degrees of freedom are required to define each vector, N_1 and N_2, which represent the normals to the GB plane in each crystallographic reference orientation (the plane normals are actually defined by three direction cosines but only two are independent). A further degree of freedom is necessary to define the twist angle, ϕ, between the two lattices. Defining the geometry of a grain boundary in this way is known as the interface-plane scheme [5].

An alternative and more common method of defining grain boundary geometry is known as the misorientation scheme. In this scheme, the relative misorientation between the two grains defines three degrees of freedom. This is normally specified as both an axis of rotation,

UVW (two degrees of freedom), and the angle of rotation, θ (one degree of freedom). This is shown in Figure 3.2.

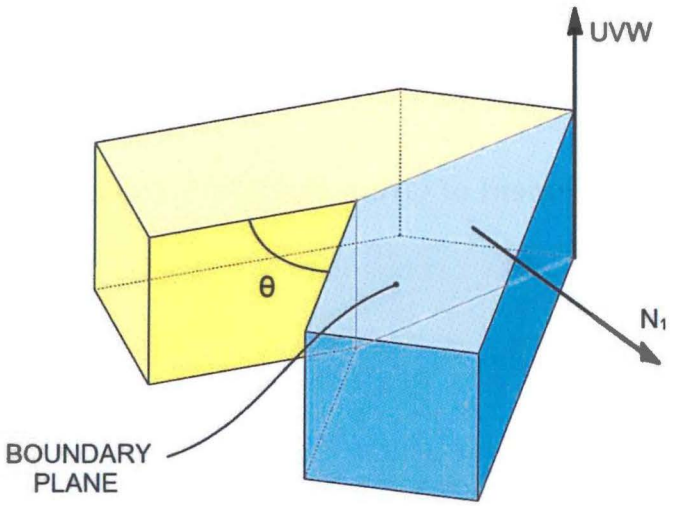

Figure 3.2 Illustration of the misorientation scheme for a grain boundary

However, the angle/axis pair only describes the misorientation between the two lattices and hence does not indicate the position of the grain boundary plane itself. Two further degrees of freedom are therefore required to indicate the normal of the plane with respect to either lattice, N_1 or N_2.

3.3 Classification of Grain Boundaries

Grain boundaries can be classified into four types based on the interface-plane scheme (Figure 3.1). Recall that under this scheme, a boundary is defined by each boundary plane $h_1k_1l_1$ and $h_2k_2l_2$ (or their normals N_1 and N_2), as well as the twist angle, θ, about either plane normal. This gives rise to the following conditions:

1) $\{h_1k_1l_1\} = \{h_2k_2l_2\}$ and θ=0. This indicates a symmetrical tilt boundary, or STB.
2) $\{h_1k_1l_1\} \neq \{h_2k_2l_2\}$ and θ=0. This indicates an asymmetrical tilt boundary, or ATB.

3) $\{h_1k_1l_1\} = \{h_2k_2l_2\}$ and $\theta \neq 0$. This indicates a twist boundary, or TWB.

4) $\{h_1k_1l_1\} \neq \{h_2k_2l_2\}$ and $\theta \neq 0$. This indicates a general boundary.

This nomenclature will be used throughout the following sections.

3.4 The Measurement of Grain Boundary Geometry

The geometry of a grain boundary can be measured in a number of ways, such as X-ray techniques, or transmission electron microscope (TEM) diffraction methods such as selected area diffraction (SAD) or convergent beam electron diffraction (CBED). However, by far the most common measurement tool for grain boundary identification and measurement is electron backscatter diffraction (EBSD), coupled with a scanning electron microscope (SEM). As this is the technique utilised in the current project, EBSD will be briefly overviewed.

Kikuchi diffraction patterns are generated by the interaction of the electron beam with a tilted sample of material, as shown in Figure 3.3. These diffraction patterns are then projected onto a phosphor screen and captured using a low-light TV camera.

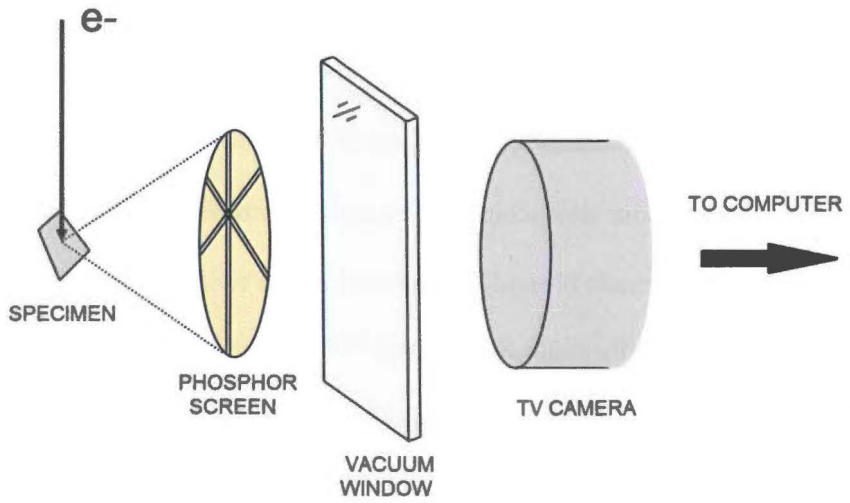

Figure 3.3 General setup of electron backscatter diffraction

The Kikuchi pattern obtained is unique to a specific lattice within the interaction volume, which typically extends approximately 20nm below the material surface. Through computer software, the pattern may then be indexed, or traced back to the specific lattice parameters and orientation by which it was generated. This process is illustrated in Figure 3.4 for a sample of austenite.

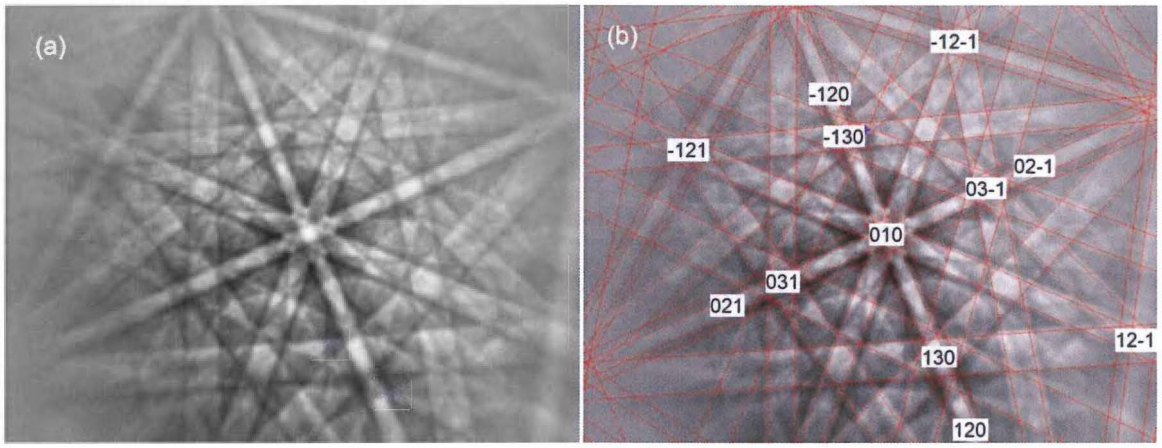

Figure 3.4 (a) raw Kikuchi diffraction pattern (b) diffraction pattern indexed as f.c.c steel (austenite)

Indexing such a pattern not only determines the lattice parameters, which allows EBSD to be used as a phase identification tool, but also the rotation of the impinged lattice with respect to the sample axes. The diameter of the electron beam can be tuned as low as 0.5μ in a conventional W-filament electron microscope, or significantly smaller in a field-emission-gun microscope (FEGSEM). Therefore, the beam may be "stepped" across the sample surface in a user-defined grid, and the crystal orientation calculated at each grid point to within a precision of 0.5-1.0° [6]. The change in crystal orientation between two adjacent grid points, called the misorientation, can also be calculated through various mathematical methods [3]. If the calculated misorientation is greater than a user-defined threshold and the two grid points represent the same phase, this indicates the position of a grain boundary.

Stepping the beam through a grid-pattern in this way creates what is called an EBSD map. An example of an EBSD map for 800H is shown in Figure 3.5.

Figure 3.5 Example EBSD map for 800H with high-magnification inset in lower-right

In this figure, each grain boundary segment is shown as a black, pixellated line (see the inset in the lower-right corner). Creating an EBSD map therefore allows data such as grain boundary length per unit area, or average grain size to be extracted (more detail on the measurement of average grain size is provided in Chapter 4). However, because the crystal orientation is known at points either side of the grain boundary, the misorientation across each grain boundary segment may also be calculated. This information provides three of the five degrees of freedom necessary to fully define grain boundary geometry, and is the basis for a common boundary classification model called the coincidence site lattice (CSL) model, which is explained in the following section.

3.5 The Coincidence Site Lattice Model

3.5.1 Description of the CSL Model

The coincidence site lattice geometry was first described in 1949 [7], and represents a common method of classifying certain types of grain boundaries which have the potential to exhibit periodicity in the boundary plane. In order to understand this classification, it is necessary to consider two lattices which intersect each other and produce a theoretical "superlattice", where the atomic positions of one lattice are superimposed onto the atomic positions of the other grain. This is shown in Figure 3.6.

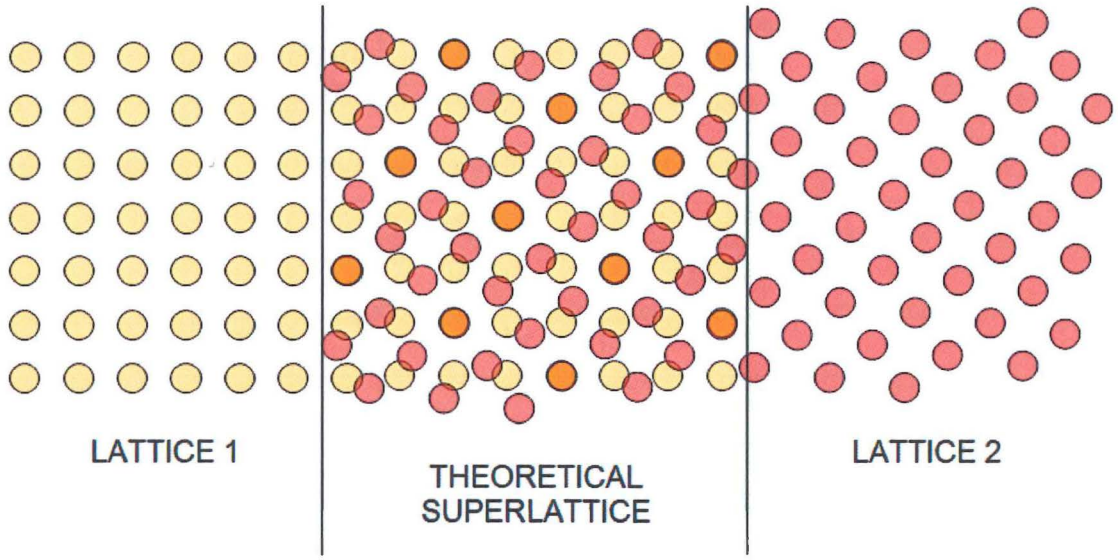

Figure 3.6 Illustration of the CSL model

Within the volume of the theoretical superlattice, some of the atomic positions from lattice 1 also match with lattice 2. These atomic positions are called coincident sites, and are shown in orange in Figure 3.6. The proportion of lattice sites from either grain which are coincident with the opposing grain is denoted $1/\Sigma$, and therefore Σ represents the reciprocal of the fraction of coincident sites within the superimposed lattice. For example, in the preceding figure, it is apparent that one in five sites is coincident, making it a $\Sigma 5$ boundary. It is

important to note that the superlattice does not actually exist at a grain boundary, rather the grains are truncated at the boundary plane. The CSL model is merely an indicator of the relative orientation between the two lattices.

Each Σ value has one or more specific lattice misorientations which satisfies its necessary geometric conditions. The first few Σ values and their relevant misorientations are listed in Table 3.1.

Table 3.1 Specific lattice misorientations for Σ3 to Σ15

Σ Value	**Misorientation Angle, θ**	**Misorientation Axis, UVW**	**Allowable Deviation, v_m***
3	60°	<111>	8.67°
5	36.87°	<100>	6.71°
7	38.21°	<111>	5.67°
9	38.94°	<110>	5.00°
11	50.48°	<110>	4.52°
13a	22.62°	<100>	4.16°
13b	27.80°	<111>	4.16°
15	48.19°	<210>	3.87°

* based on the Brandon criterion

Table 3.1 also lists the maximum allowable deviation, v_m, from the ideal misorientation. This is based on a criterion known as the Brandon criterion [8], and is calculated by the formula:

$$v_m = {}^{15}/_{\sqrt{\Sigma}} \tag{3.1}$$

The Brandon criterion is based on the fact that certain deviations from the exact CSL misorientation could be accommodated by arrays of dislocations. Other, generally more restrictive criteria such as those proposed by Ishida and McLean [9] or, more commonly, the

Palumbo and Aust criterion [10], are also used in the literature and have shown some correlation with special boundary properties. However, the Brandon criterion is by far the most commonly reported in the literature, and hence it has also been applied in the current work in order to retain continuity with previous studies. For comparison, the Palumbo-Aust criterion allows a maximum deviation of 6.0° from a Σ3 boundary compared to the 8.67° allowed by the Brandon criterion. Applying the Palumbo-Aust criterion to fully annealed 800H in the present work typically causes the detected length fraction of Σ3 boundaries to fall by less than 5% compared with the Brandon criterion, showing that the vast majority of Σ3 boundaries are acceptable by both criteria.

The periodicity in the superlattice denoted by a low-Σ boundary enables the possibility of similar periodicity in the grain boundary plane itself. Such periodicity in the boundary plane leads to low bond distortion (i.e. good "atomic fit") across the boundary. This, in turn, confers low free volume compared to random boundaries with no periodicity. It is this low free volume which infers "special" properties compared with random, high-angle boundaries.

3.5.2 Advantages of the CSL Model

With the relatively recent development of EBSD, which became prevalent in the late 1990's and early 2000's, the CSL model has become even more useful as a tool for the characterisation of the geometry of grain boundaries. Because the model is based only on the misorientation across a boundary, it can be applied automatically to EBSD data sets, without the need for user inputs. EBSD software can rapidly identify CSL boundaries, and then provide key statistics such as the length fraction of each CSL boundary type compared to the total grain boundary length. This statistic is used frequently in the grain boundary engineering field as a measure of how "engineered" a microstructure is [11-13].

The CSL model is also utilised in the identification of annealing twins for the purpose of calculating grain size in f.c.c metals. The annealing twin is a subset of the Σ3 classification, and in fact comprises almost all Σ3 boundaries in conventionally processed materials. More detail regarding the measurement of grain size using EBSD is provided in Chapter 4.

3.5.3 Limitations of the CSL Model

The major drawback of the CSL model is that, as explained in the previous sections, a grain boundary requires five degrees of freedom to be described in order to be fully defined. The CSL model is based on misorientation alone, which only provides three degrees of freedom. Therefore, the CSL notation is an incomplete description of the structure of a grain boundary.

This fact is not so much a limitation of the model itself, but rather a limitation of its applicability. It was originally proposed that the CSL model might explain observed anisotropy in grain boundary properties which are sensitive to boundary structure. However, the use of the CSL model to directly predict grain boundary properties is scientifically lacking, due to its inability to fully describe the boundary [14-15]. In order to make direct structure-property correlations, one must also obtain boundary plane information through a method such as serial sectioning. However, serial sectioning remains an extremely time-consuming and difficult method. Boundary plane data can also be estimated from single-section trace analysis [16], which is less laborious than serial sectioning, but still leaves one degree of freedom undefined. Another more recent method [17] allows the collection of boundary plane information for a large data set, through the collection of a statistically relevant number of boundary traces and their geometric relationship with the adjacent crystals (typically 50,000+ traces are required). However, the limitation is that the information cannot be traced back to individual boundaries, and so can only be reported as probability distributions. Hence the CSL model is still widely used in the field of grain boundary

engineering, although it is often supplemented with other information such as CSL deviation data (e.g [18]) or boundary plane information (e.g [19]) in order to make correlations with grain boundary properties.

3.6 Special Grain Boundaries

3.6.1 History of Special Boundaries

When the CSL model was first formalised [8], it was thought the non-random geometry of low-Σ grain boundaries may correlate with observations of anisotropic boundary properties. This led to a series of experiments using bicrystals, such as those performed by Aust and Rutter [20], and Viswanathan and Bauer [21], which showed that the energy and mobility of a grain boundary could be linked to its Σ-value. Further evidence was developed which suggested that low-Σ boundaries showed improvements compared to random high-angle boundaries (HABs) such as lower diffusivity [22], lower susceptibility to solute segregation [23], greater resistance to sliding [24], and greater resistance to corrosion [25]. This evidence was based on the suggestion that low-Σ boundaries exhibited lower free volume, where free volume is the principal feature which controls boundary behaviour [26]. In fact, it was initially thought that all low-Σ boundaries were expected to show special properties. The fact that the CSL model did not fully describe the boundary structure was countered by the assumption that, in a low-Σ boundary, the boundary plane would orient itself in order to minimise its energy and hence adopt the plane of highest periodicity [8, 27]. However, later TEM investigations showed that this assumption was incorrect [28-29]. Sutton and Baluffi further showed that not all the low-Σ grain boundary energy cusps could be detected experimentally [30].

It is now known that not all low-Σ boundaries exhibit special properties. The CSL descriptor merely denotes the potential of a boundary to have special characteristics [31], provided the boundary plane is oriented favourably. However, this leaves the question of why the increase in the fraction of low-Σ boundaries has resulted in so many cases of improved material properties (such examples will be discussed in section 3.10).

There is a growing collection of evidence which suggests that special boundary properties are attributable not to the misorientation across the boundary, but to the presence of low-index planes at the boundary surface [17, 32-33]. There has been some suggestion that a 'special' grain boundary should be defined as one that is terminated by at least one low-index plane [34]. This theory is further supported by the fact that special properties have been observed at boundaries not described by any CSL misorientation [35].

3.6.2 The Σ3 Boundary

The Σ3 boundary is the boundary most commonly associated with special properties. There are several special configurations into which the Σ3 boundary category may be subdivided. Energies correspond to collation by Caul et al [14] in copper, which is based on atomistic calculations by authors such as Wolf et al [36]:

i) The {111/111} symmetrical tilt boundary (STB) (energy <0.02J/m^2)

ii) The {211/211} STB (energy 0.54J/m^2)

iii) Asymmetrical tilt boundaries (ATBs) on the <110> zone (energies 0.02-0.60J/m^2)

iv) Other ATBs and twist boundaries (TWBs) (energy >0.60J/m^2)

The {111/111} STB is the coherent annealing twin and is thought to have an energy approximately 1/50th of a random boundary [37]. The {211/211} STB is referred to as the 'incoherent twin' and is also expected to have lower energy than a random boundary,

although significantly higher than the coherent twin. For example, the boundary energies of the coherent twin, the incoherent twin and a random HAB in 304 stainless steel were determined as 19, 209 and 835mJ/m^2 respectively by Murr [38]. The third group, namely ATBs on the <110> zone, is significant in that these boundaries lie in an energy valley [39]. In other words, they have lower energies than other ATBs in the Σ3 classification. All of the ATBs with at least one low-index plane, as well as the two low-energy STBs are on the <110> zone [15]. The fourth category also includes the {111/111} TWB which is known to have low energy [40].

There is significant evidence behind the fact that the vast majority of Σ3 boundaries contain at least one low-index plane [15, 19, 39, 41-44]. From this, it is generally accepted within the literature that the large majority of Σ3 boundaries exhibit special properties. It is therefore the primary aim of GBE to increase the relative fraction of Σ3 boundaries, compared to random HABs. In fact, in order to be referred to as grain boundary engineered commercially, a material is required to have more than 50% Σ3 boundaries [45], due to the relative low-energy of these boundaries.

3.6.3 The Σ9 and Σ27 Boundaries

Of the CSL boundaries present in a GBE material, it is only the Σ3, Σ9 and Σ27 boundaries that are present in levels significantly above a random distribution. Throughout this thesis, the term $\Sigma 3^n$ is used to refer to this group (i.e. $0<n<4$). The Σ9 and Σ27 represent a geometric necessity between Σ3 boundaries and hence it is useful to know whether these boundaries are also special.

There are several configurations of Σ9 in particular which are calculated to have lower than average energy, including the low-index ATB {111}/{115} [46]. There is also evidence to

suggest that Σ9 boundaries, and to a lesser extent, Σ27 boundaries in general show special properties experimentally. Shimada [47] showed that corrosion of 304 stainless steel by ferric sulphate-sulphuric acid was significantly reduced at Σ9s and Σ27s. Skidmore et al [48] showed that the energy of Σ9 and Σ27 boundaries was lower than random HABs, through the use of thermal groove and orientation imaging microscopy (OIM) correlation. Fang et al [49] showed that some Σ9 boundaries exhibited good corrosion resistance compared to HABs, which were almost all susceptible to intergranular corrosion.

Recently, the development of the technique mentioned previously [17] for extracting boundary plane information from a large data set has allowed the structure of boundaries to be investigated for individual subsets such as the Σ9 and Σ27 groups [44]. The plane normal distribution for all boundaries close to the Σ9 misorientation in GBE copper was calculated by Coleman and Randle [50], and is reproduced in Figure 3.7, in terms of multiples of random distribution (MRD).

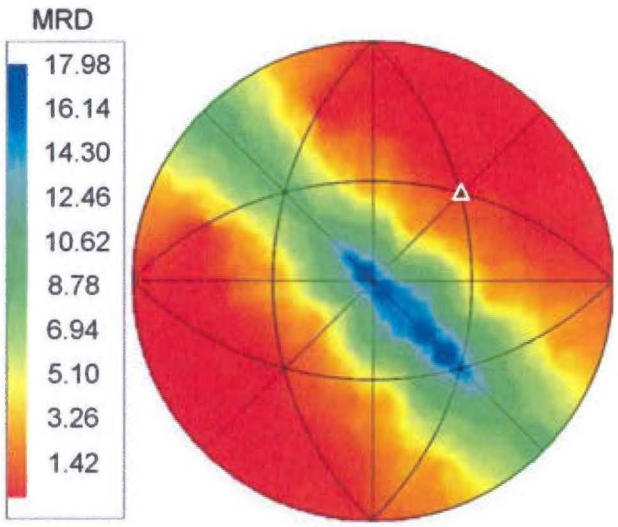

Figure 3.7 Σ9 plane distribution in GBE copper [50], plotted in stereographic projection along [001]. The triangle indicates the position of the [111] direction.

The results show a definite preference for asymmetric tilt boundaries along the [110] zone, up to eighteen times the expected random distribution. These boundaries have been shown to

have lower energy than random boundaries [39], as mentioned previously. Therefore, it is expected that a large proportion of Σ9 boundaries do possess low energy, and, in general, the group may be considered to be special.

The same information was presented for the two Σ27 boundaries [19], shown in Figure 3.8, again as multiples of random distribution (MRD).

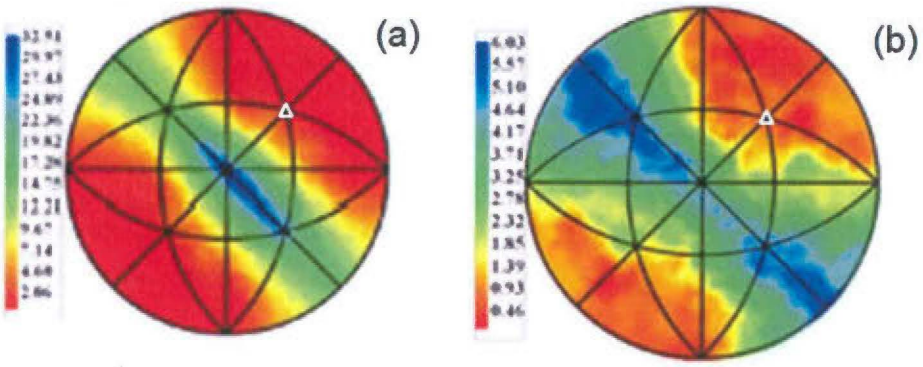

Figure 3.8 (a) Σ27a plane distribution in GBE copper (b) Σ27b plane distribution [19]. Plotted in stereographic projection along [001] with a triangle indicating the [111] direction.

Again, the data show a preference for boundary planes to orient along the [110] zone, indicating a lower than average boundary energy, even for the case of Σ27b where the misorientation will not produce a pure tilt boundary.

3.6.4 Summary

In summary, although the existence of special boundary properties cannot be attributed directly to the misorientation-based Σ value, experimentation has shown that almost all Σ3 boundaries, as well as a significant fraction of Σ9 and Σ27 boundaries are expected to show low energy. These are the three boundary types which are promoted by grain boundary engineering, and hence may explain the correlation between material properties and low-Σ boundary fraction. It is therefore reasonable to believe that the CSL model, and thus single

section EBSD statistics, are sufficient as guides to predicting improved properties in many cases, albeit indirectly.

3.7 Aim of Grain Boundary Engineering

The primary aim of GBE processing is to increase the relative fraction of low-energy grain boundaries ($\Sigma 3^n$) in the microstructure, as originally proposed by Watanabe [51], under the term 'grain boundary design'. A concomitant effect of increasing the fraction of $\Sigma 3^n$ boundaries is the breaking up of the interconnected network of randomly oriented HABs. This situation is well represented as a percolation problem, although the percolation dynamics of three-dimensional grain boundary networks in GBE materials have not yet been determined. The implications of the reduction in random HAB connectivity are that damage mechanisms which depend on this network, such as intergranular stress corrosion, grain boundary sliding or Coble creep will be retarded.

3.8 Grain Boundary Engineering Methods

The process of grain boundary engineering (also called iterative thermomechanical processing) generally involves a number of cycles of thermomechanical processing, each constituting a deformation step followed by an annealing step. This cycle is then normally repeated up to seven times, although grain boundary engineered conditions have been reported after a single cycle in some cases (e.g. [52]).

Typically the starting material condition is plate or sheet stock, as this lends itself easily to uniform plastic deformation under laboratory conditions. The most common deformation method reported in the literature is plate rolling, although other deformation methods such as

mechanical compression [53] and shot-peening [54] have also been utilised. Plate rolling is invariably performed cold to prevent dynamic recrystallisation, and induces plastic deformation typically in the range 5–30%.

Annealing is normally performed in box or tube furnaces for periods between a few minutes and a few hours. A protective atmosphere is sometimes employed to prevent external oxidation, although often the outer layer is either ignored in microstructural analyses, or mechanically removed in the machining of test specimens, in order to eliminate surface effects from the rolling process. Cooling is then performed either by air cooling or quenching, depending on the material.

3.9 The Mechanism of Grain Boundary Engineering

Although the methodology of grain boundary engineering is well documented in the literature, the metallurgical reasons for the increase in the $\Sigma 3^n$ boundary fraction are not well understood. In fact, there have been relatively few attempts at isolating the microstructural changes, which has potentially slowed the development of GBE as an industrial processing method.

GBE processing routes were initially divided into two fields [55], initially named 'strain-recrystallisation' for processes involving higher strains per cycle, and 'strain-annealing' for lower strains. However, it was noted later [56] that the term 'strain-recrystallisation' may be a misnomer as it is unlikely that complete recrystallisation occurs in any successful GBE process. In support of this theory, Kumar [57] pointed out that recrystallisation, where the network of existing boundaries is effectively replaced rather than modified, is unable to produce microstructures where the interconnectivity of random grain boundaries is

substantially changed. In recent successful studies [58-60], the annealing conditions are deliberately chosen so that conventional recrystallisation does not occur, and instead the formation of $\Sigma 3^n$ boundaries relies on the strain-induced boundary migration (SIBM) induced by the low deformation levels. This boundary migration offers two potential ways in which the relative fraction of $\Sigma 3^n$ boundaries may be increased.

First, as twin boundaries are a subset of the $\Sigma 3$ group, it follows that new twinning results in an increase in the relative fraction of $\Sigma 3$ boundaries. Ideas relating to the formation of new twins in GBE processing have mainly been centred around the ideas of grain boundary migration velocity, and the optimum boundary velocity for the creation of new twins. The migration velocity of a grain boundary is generally described by the equation [61]:

$$v = MF$$

where v is the boundary velocity, M is the boundary mobility (which varies according to temperature), and F is the driving force for migration, which is affected mainly by the strain energy.

Owen and Randle [62] suggested that a low boundary velocity is more suitable for the nucleation of annealing twins, in accordance with the observed trend that low deformation levels are generally more successful in increasing the fractions of $\Sigma 3^n$ boundaries. There is some experimental evidence to support this, such as [63], in which a rapidly-heated specimen of nickel was compared with a partner specimen which was slowly heated to the same temperature. The rapidly-heated sample was found to have a $\Sigma 3$ number fraction of 25%, compared to the slow-heated sample (which was expected to have a lower average boundary velocity due to the driving force being expended at comparatively low temperature), which exhibited 50% number fraction. Horton [64] suggested two reasons in support of the idea

that a low boundary velocity is more suitable for the generation of annealing twins. First, twinning may be a less favourable mechanism when compared energetically to fast grain growth at high boundary velocities, and hence may become redundant as boundary migration speed increases. Second, the kinetics of twin formation may be a limiting factor at high boundary velocities, where less time is available for nucleation.

In contrast however, Mahajan [65] proposed a respected model for the formation of annealing twins in f.c.c. crystals, in which it was suggested that higher boundary migration velocities result in higher twin densities, due to the higher probability of growth accidents on consecutive {111} planes. As such, the evidence which exists in either case is somewhat inconclusive, and the optimum conditions for twin generation, as well as the relative contribution of new coherent twins to the $\Sigma 3^n$ fraction, remains largely unknown.

The second way in which the $\Sigma 3^n$ is thought to be increased, probably in combination with the first, is as a result of interactions between existing CSL boundaries. The 'Σ3 regeneration mechanism', which was originally proposed by Randle [55], may describe how incoherent Σ3 boundaries and higher order twin variants are introduced according to the geometrical constraints which exist at triple points. These triple points are governed by the relation [66]:

$$\Sigma_{CA} = \Sigma_{AB}\Sigma_{BC}/d^2$$

In this equation, d represents a common divisor of Σ_{AB} and Σ_{BC}. For example, at a triple point where a mobile migrating Σ9 boundary meets a Σ3 boundary, the resultant third boundary is geometrically constrained (according to the above equation) to be a Σ3 ($d = 3$) or a Σ27 ($d = 1$) in the probability ratio 1:2 (there is one Σ3 boundary and two Σ27s – Σ27a and Σ27b). Similar encounters may occur between mobile (incoherent) and immobile Σ3 boundaries, or amongst any of the $\Sigma 3^n$ family to produce an increase in the relative fraction in

these boundaries. Importantly however, it was pointed out by Reed and Kumar [67] that although the Σ3 regeneration mechanism may be responsible for some increase in the relative fraction of $\Sigma 3^n$ boundaries, it cannot be responsible for the large scale disruption to the HAB network, but must be localised within a twin-related domain.

In summary therefore, the existing literature is incomplete in its ability to describe the microstructural changes during GBE, although the ideas of boundary migration and interactions have been recently introduced. Unfortunately, because EBSD is a surface technique, it is not possible to observe these changes during heating. However, future experiments involving the classification of coherent versus incoherent Σ3 boundaries and their relative fractions throughout processing may prove useful in confirming the present theories regarding the interactions of grain boundaries. Details of the present results and relations to these factors are presented in Chapter 6.

3.10 Successful Applications of Grain Boundary Engineering

Since its inception, there have been many reports of improved material properties based on the process of GBE. A selection of these studies is summarised here, categorised according to the specific properties which were altered.

3.10.1 Mechanical Properties

Room-temperature mechanical properties are generally not the target of GBE processing, though some studies report effects in this area. For example, Thaveeprungsriporn and Was [11] reported a slight increase in yield strength and ultimate tensile strength of Ni-16Cr-9Fe alloys at 360°C after GBE. Randle and Davies [68] report increases in the ductility of alpha-brass with no appreciable loss of tensile strength through GBE. Furthermore, Watanabe [69-

70] has reported increases in fracture toughness of brittle materials such as Ni_3Al and molybdenum. Gao [71] later reported increases in fatigue resistance of the nickel alloy ME3 at high temperatures, where intergranular fracture is seen to dominate. No significant difference was noticed at low temperatures, where transgranular fracture occurs.

3.10.2 Creep and Cracking

The work of Lehockey and Palumbo [12], and Thaveeprungsriporn and Was [11] showed that grain boundary engineering could have an extremely significant effect on creep rate. In the former study, the secondary creep rate of as-cast nickel was reduced by approximately 16x, which resulted from the fraction of low-Σ boundaries being increased from 13% to 66%. In the latter, the secondary creep rate of Ni-16Cr-9Fe in 360°C argon was reduced by more than twenty-fold, commensurate with an increase in the special boundary fraction by a factor of two compared with the solution-annealed (SA) condition. The results of this study are reproduced in Figure 3.9.

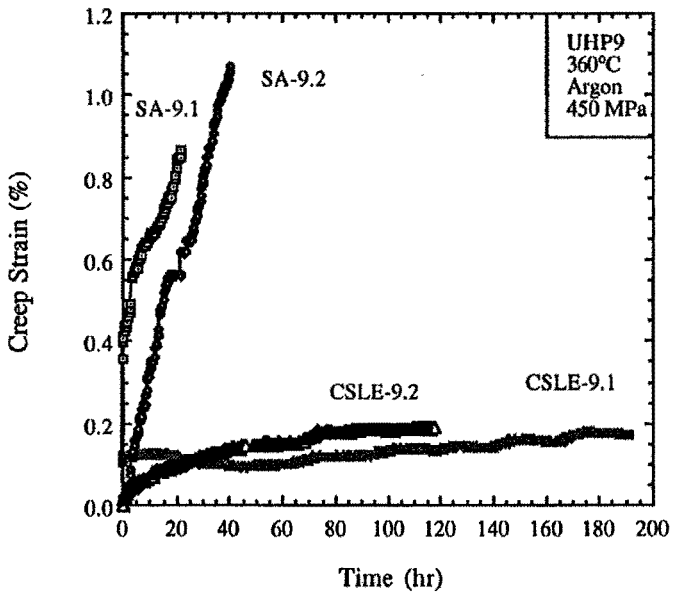

Figure 3.9 Reduction in steady-state creep rate in Ni-16Cr-9Fe by GBE [11]

A 15x reduction in secondary creep rate, accompanied by a large reduction in primary creep strain, was also achieved by GBE processing of alloy V-57, a common turbine rotor material [72]. Boehlert [73] et al also showed that the secondary creep rate was reduced by four cycles of 10% reduction in Udimet alloy 188, compared to four cycles of 35% reduction which reflects a non-GBE case. They also noticed that less than 15% of cracks were located on LABs or CSL boundaries.

3.10.3 Segregation and Precipitation

In 2008, Jones et al investigated the precipitation of $M_{23}C_6$ carbides in an overaged 316 stainless steel with respect to the grain boundary planes [74]. They found a high percentage of {111} boundary planes, including {111} twist boundaries and <110> asymmetric tilt boundaries which had one {111} plane. They showed that coherent twins were immune to precipitation, and also that boundaries containing {111} planes were more resistant to precipitation. Schlegel et al investigated similar precipitation in alloy 617 during creep deformation [75]. They concluded that the precipitation of intergranular carbides is suppressed on low-Σ CSL boundaries compared to general HABs, and that the HABs were more likely to have a higher length fraction of precipitate coverage than special boundaries.

Bechtle et al investigated the susceptibility of commercially pure nickel to hydrogen embrittlement, in both the base state and a GBE state [76]. Through processing, they increased the fraction of "special" boundaries from 46 to 75%. This resulted in an increase of almost 100% in the tensile ductility in the presence of high hydrogen concentrations. The fracture toughness was also increased by 20-30% compared to the base state. The property improvements were attributed to the lower degree of segregation at special boundaries.

Kobayashi et al then investigated the brittleness of ultrafine-grain nickel associated with sulphur segregation to grain boundaries [77]. The fracture toughness in sulphur-bearing conditions was increased from 1.1MPam$^{1/2}$ to 2.5MPam$^{1/2}$ by increasing the fraction of special boundaries, without a significant change in grain size.

3.10.4 Corrosion

The most well-known use of grain boundary engineering to mitigate corrosion damage is in its use in lead-acid battery grids, now commercially produced by Banner GmBh [78]. A grain boundary engineered battery grid was tested after 40 charge-discharge cycles in H_2SO_4 at 70°C, and compared to a non-GBE grid. The test showed that the GBE grid exhibited far superior performance under these conditions. The results are shown in Figure 3.10, reproduced from [79].

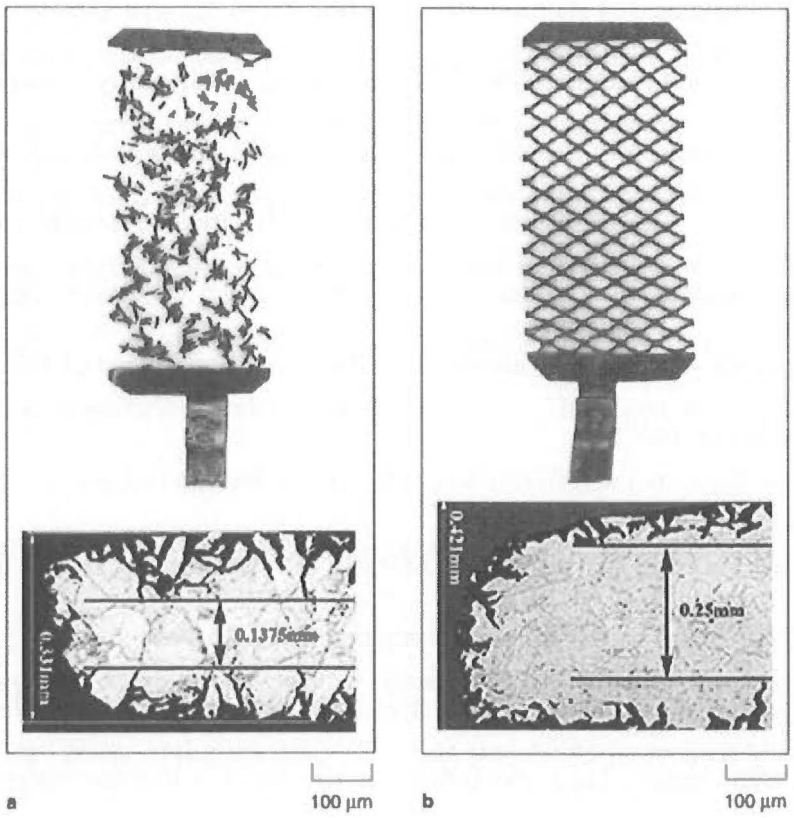

Figure 3.10 Condition of (a) conventional and (b) GBE processed Pb-Ca-Sn-Ag lead-acid positive battery grids following 40 cycles in H_2SO_4 at 70°C

A second significant result was achieved in alloy 600, an alloy widely used in nuclear-steam-generator tubing in pressurised water reactors [80]. The alloy suffers from intergranular stress-corrosion cracking (IGSCC) in this application. However, after GBE processing, alloy 600 C-rings exposed to 10% NaOH at 350°C for 3000 hours were noted to be completely immune to stress-corrosion cracking.

Bi et al investigated the sensitisation behaviour of 304 stainless steel, and found that chromium depletion along twin-related low-energy boundary segments was less prominent than along random boundaries [81]. They concluded that the introduction of such low-energy segments disrupts the continuity of chromium depletion in the boundary network, and arrests the percolation of intergranular corrosion.

Kokawa et al also studied 304 stainless steel, specifically in the heat-affected-zone (HAZ) of a weld [52]. They found that grain boundary engineering significantly reduced the degree of sensitisation and subsequently reduced the corrosion rate by approximately 40% compared with the base material. The same authors found that a GBE treatment could also suppress the formation of intergranular and cellular nitrides in the HAZ of a high-nitrogen austenitic stainless steel during welding [82], attributed to the "strong resistance of CSL boundaries to intergranular deteriorations".

Shimada showed that the corrosion rate of GBE 304 stainless steel in ferric sulphate-sulphuric acid was significantly reduced compared with the base state [47]. Similar tests were later performed on GBE 316 stainless steel in the same solution by Michiuchi et al [83], who found the same result. Fang concluded that $\Sigma 3$s and $\Sigma 9$s in these materials were more resistant to corrosion than HABs [49].

There are also results obtained for corrosion of alloy 800H, the alloy of concern in the present work. In the same study on alloy 600 mentioned previously [80], alloy 800 was also tested and the corrosion rate was found to decrease from 2.2mm/yr to 0.2mm/yr with an increase in special boundary fraction from 43 to 83%. Tan et al tested the oxidation behaviour of 800H in supercritical water [84], and found that GBE processing was able to mitigate the oxide spallation which occurred extensively on control samples. Tan later tested the same alloy under cyclic oxidation in air [85], and found that oxide spallation was again reduced in the GBE condition.

3.11 Conclusions

In conclusion, it is known that grain boundaries show anisotropic behaviour, depending on their geometrical structure. It was originally proposed that these properties could be associated with their misorientation, as denoted by the CSL model. However, this was later disproven [29], and current thinking [43] is that special properties may be associated with the presence of low-index planes at the boundary. It has since been shown [50] that a large proportion of the CSL boundaries which are promoted by GBE (i.e. the $\Sigma 3^n$ family) also fit with this definition of a special boundary, and may explain the correlations between the fractions of these boundaries, and material properties. Therefore, the CSL $\Sigma 3^n$ boundary fraction may still be used as an indication of the level of GBE in a microstructure, although it must be remembered that the correlation is indirect.

Grain boundary engineering has yielded improvements to many properties, including strength, ductility, creep, and corrosion. The fact that 800H is an f.c.c alloy and has low levels of precipitation means that GBE represents an opportunity to improve the high-temperature properties of methanol reformer pigtails, and in doing so, increase their service

life. However, it should be noted that the vast improvements in creep properties achieved by Thaveeprungsriporn and Lehockey were exhibited under very high stress conditions (84-300MPa). These conditions are far from representative of typical service conditions (ie. the Methanex pigtails have a wall stress of approximately 10MPa). No research currently exists regarding the effect of GBE on creep properties at test conditions which are applicable to material service, namely stress levels in the range 5-20MPa. Therefore, it was proposed to investigate both the microstructural aspect of GBE on this alloy, and also the resulting changes in properties including mechanical properties, and specifically the creep properties under test conditions which be reasonably extrapolated to the pigtail service conditions. The ultimate aim of the work was therefore to create a processed version of 800H which is better suited for this specific application.

3.12 References

[1] Qian, X. R., Chou, Y. T., Kamenetzky, E. A., *The structure dependence of grain boundary corrosion in niobium bicrystals*, Less Comm. Met. 134 (1987) 179-185.

[2] Sutton, A. P., Vitek, V., *On the Structure of Tilt Grain Boundaries in Cubic Metals*, Phil. Trans. of the Royal Soc. 309 (1983) 1-68.

[3] Randle, V., *The Measurement of Grain Boundary Geometry*, IOP Publishing Ltd., 1993.

[4] Gust, W., Mayer, S., Bogel, A., Predel, B., *Generalised representation of grain boundary self-diffusion data*, J. de Phys. 46 (1985) C4: 537-544.

[5] Wolf, D., Lutsko, J. F., *On the relationship between tilt and twist grain boundaries*, Zeit. Kristall. 189 (1989) 239-262.

[6] Randle, V., Engler, O., *Introduction to Texture Analysis: Macrotexture, Microtexture and Orientation Mapping*, Gordon and Breach, London, 2000.

[7] Kronberg, M. L., Wilson, F. H., *The role of grain boundary character distribution in secondary recrystallization of electrical steels*, Met. Trans. 185 (1949) 501-516.

[8] Brandon, D. G., *The structure of high-angle grain boundaries*, Acta Metall. 14 (1966) 1479-1484.

[9] Ishida, Y., McLean, M., *Burgers vectors of boundary dislocations in ordered grain boundaries of cubic metals*, Phil. Mag. 27 (1973) 1125-1134.

[10] Palumbo, G., Aust, K. T., *Structure-dependence of intergranular corrosion in high-purity nickel*, Acta Metall. 38 (1990) 2343-2352.

[11] Thaveeprungsriporn, V., Was, G.S., *The role of coincidence-site-lattice boundaries in creep of Ni-16Cr-9Fe at 360C*, Metall. and Mat. Trans. A 28A (1997) 2101-2112.

[12] Lehockey, E. M., Palumbo, G., *On the creep behaviour of grain boundary engineered nickel*, Mat. Sci. & Eng. A 237 (1997) 168-172.

[13] Was, G. S., Thaveeprungsriporn, V., Crawford, D.C., *Grain boundary misorientation effects on creep and cracking in Ni-based alloys*, J. of Mat. 50 (1998) 44-49.

[14] Caul, M., Fiedler, J., Randle, V., *Grain-boundary plane crystallography and energy in austenitic steel*, Scripta Mater. 35 (1996) 831-836.

[15] Randle, V., *Relationship between coincidence site lattice, boundary planes indices and boundary energy in nickel*, Mat. Sci. & Tech. 15 (1999) 246-252.

[16] Randle, V., *A methodology for grain-boundary plane assessment by single-section trace analysis*, Scripta Mat. 44 (2001) 2789-2794.

[17] Saylor, D. M., El-Dasher, B. S., Adams, B. L., Rohrer, G. S., *Measuring the five-parameter grain boundary distribution from observations of planar sections*, Metall. & Mater. Trans. 35A (2004) 1981-1989.

[18] Thomson, C. B., Randle, V., *Fine tuning at sigma 3 boundaries in nickel*, Acta Mat. 45 (1997) 4909-4916.

[19] Randle, V., Rohrer, G. S., Miller, H. M., Coleman, M., Owen, G. T., *Five-parameter grain boundary distribution of commercially grain boundary engineered nickel and copper*, Acta Mater. 56 (2008) 2363-2373.

[20] Aust, K. T., Rutter, J. W., *Grain boundary diffusion in high-purity lead and dilute lead-tin alloys*, Trans. AIME 215 (1959) 119-127.

[21] Viswanathan, R., Bauer, C. L., *Kinetics of grain boundary migration in copper bicrystals with [001] rotation axes*, Acta Metall. 21 (1973) 1099-1109.

[22] Priester, L., *Geometrical speciality and special properties of grain boundaries*, Rev. Phys. Appl. 24 (1989) 419-438.

[23] Bouchet, D., Priester, L., *Grain boundary plane and intergranular segregation in nickel-sulfur system*, Scripta Met. 21 (1987) 475-478.

[24] Kokawa, H., Watanabe, T., Karashima, S., *Sliding behaviour and dislocation structures in aluminium grain boundaries*, Phil. Mag. A 44 (1981) 1239-1254.

[25] Palumbo, G., King, P. J., Lichtenberger, P. C., Aust, K. T., Erb, U., *Grain boundary structure control for intergranular stress-corrosion resistance*, Mater. Res. Soc. Symp. Proc. 238 (1992) 311-316.

[26] Mehta, S. C., Smith, D. A., *Grain Boundary Engineering*, Canadian Inst. Mining, Metallurgy and Petroleum, Montreal, 1994.

[27] Brandon, D. G., Ralph, B., Ranganathan, S., Wald, M. S., *A field ion microscope study of atomic configuration at grain boundaries*, Acta Metall. 12 (1964) 813-821.

[28] Tweed, C. J., Ralph, B., Hansen, N., *The pinning of particles of low and high angle grain boundaries during grain growth*, Acta Metall. 32 (1984) 1407-1414.

[29] Dechamps, M., Marrouche, A., Barbier, F., Revcolevschi, A., *T.E.M. study of the texture and preferential orientation of grain boundaries in polycrystalline NiO prepared by metal oxidation*, J. Phys (Orsay) 46 (1985) 435-440.

[30] Sutton, A. P., Balluffi, R. W., *Overview No. 61: On geometric criteria for low interfacial energy*, Acta Metall. 35 (1987) 2177-2201.

[31] Goodhew, P. J., Smith, D. A., *Can the CSL model fail?*, Scripta Met. 14 (1980) 59-61.

[32] Saylor, D. M., Morawiec, A., Rohrer, G. S., *Distribution of grain boundaries in magnesia as a function of five macroscopic parameters*, Acta Mater. 51 (2003) 3663-3674.

[33] Miyamoto, H., Ikeuchi, K., Mimaki, T., *The role of grain boundary plane orientation on intergranular corrosion of symmetric and asymmetric [110] tilt grain boundaries in directionally solidified pure copper*, Scripta Met. 50 (2004) 1417-1421.

[34] Rohrer, G. S., Saylor, D. M., El-Dasher, B. S., Adams, B. L., Rollett, A. D., Wynblatt, P., *The distribution of internal interfaces in polycrystals*, Z Metallkd. 95 (2004) 197-214.

[35] Field, D. P., Adams, B. L., *Interface cavitation damage in polycrystalline copper*, Acta Metall. Mater. 40 (1992) 1145-1157.

[36] Wolf, U., Ernst, F., Muschik, T., Finnis, M. W., Fischmeister, H. F., *The influence of grain boundary inclination of the structure and energy of sigma 3 grain boundaries in copper*, Phil. Mag A 66 (1992) 991-1016.

[37] Randle, V., *The Role of the Coincidence Site Lattice in Grain Boundary Engineering*, The Institute of Materials, London, 1996.

[38] Murr, L. E., *Interfacial Phenomena in Metals and Alloys*, Addison-Wesley, Reading, 1975.

[39] Wolf, U., Ernst, F., Muschik, T., Finnis, M. W., Fischmeister, H. F., *The energy of sigma 3 boundaries in copper*, Philos. Mag. A 66 (1992) 991-1016.

[40] Merkle, K. L., Wolf, D., *Low energy configurations of symmetric and asymmetric tilt boundaries*, Phil. Mag A 65 (1992) 513-530.

[41] Chang-Soo, K., Yan, H., Rohrer, G. S., Randle, V., *Five-parameter grain boundary distribution in grain boundary engineered brass*, Scripta Mater. 52 (2005) 633-637.

[42] Randle, V., Davies, H., *A comparison between three-dimensional and two-dimensional grain boundary plane analysis*, Ultramicroscopy 90 (2002) 153-162.

[43] Saylor, D. M., El Dasher, B. S., Rollett, A. D., Rohrer, G. S., *Distribution of grain boundaries in aluminum as a function of five macroscopic parameters*, Acta Mater. 52 (2004) 3649-3655.

[44] Rohrer, G. S., Randle, V., Kim, C.-S., Hu, Y., *Changes in the five-parameter grain boundary character distribution in alpha-brass brought about by iterative thermomechanical processing*, Acta Mater. 54 (2006) 4489-4502.

[45] Palumbo, P., *International Patent Classification C21D 8/00 8/10 C22F 1/10 1/08, no. WO 94/14986*, 1994.

[46] Wolf, D., *Ceramic Microstructures '88*, Plenum, New York, 1988.

[47] Shimada, M., Kokawa, H., Wang, Z. J., Sato, Y. S., Karibe, I., *Optimization of grain boundary character distribution for intergranular corrosion resistant 304 stainless steel by twin-induced grain boundary engineering*, Acta Mater. 50 (2002) 2331-2341.

[48] Skidmore, T., Buchheit, R. G., Juhas, M. C., *Grain boundary energy vs. misorientation in Inconel 600 alloy as measured by thermal groove and OIM analysis correlation*, Scripta Mat. 50 (2004) 873-877.

[49] Fang, X., Wang, W., Guo, H., Zhang, X., Zhou, B., *Corrosion behaviours of random and special grain boundaries in a sensitized 304 stainless steel*, Sino-Swedish Structural Materials Symposium, 2007, pp. 339-343.

[50] Coleman, M., Randle, V., *Changes in interface parameters and tensile properties in copper as a consequence of iterative processing*, Metall. & Mater. Trans. A 39 (2008) 2175-2183.

[51] Watanabe, T., *An approach to grain boundary design for strong and ductile polycrystals*, Res. Mech. 11 (1984) 47-84.

[52] Kokawa, H., Shimada, M., Michiuchi, M., Wang, Z. J., Sato, Y. S., *Arrest of weld-decay in 304 austenitic stainless steel by twin-induced grain boundary engineering*, Acta Mater. 55 (2007) 5401-5407.

[53] Gupta, G., Alexandreanu, B., Was, G. S., *Grain boundary engineering of ferritic-martensitic alloy T91*, Metall. & Mater. Trans. 35 A (2004) 717-718.

[54] Alyousif, O. M., Engelberg, D. L., Marrow, T. J., *Surface grain boundary engineering of shot-peened type 304 stainless steel*, J. of Mater. Sci. 43 (2008) 1270-1277.

[55] Randle, V., *Mechanism of twinning-induced grain boundary engineering in low stacking-fault energy materials*, Acta Mater. 47 (1999) 4187-4196.

[56] Randle, V., *Twinning-related grain boundary engineering*, Acta Mater. 52 (2004) 4067-4081.

[57] Kumar, M., Schwartz, A. J., King, W. E., *Microstructural evolution during grain boundary engineering of low to medium stacking fault energy fcc materials*, Acta Mater. 50 (2002) 2599-2612.

[58] Fang, X., Zhang, K., Guo, H., Wang, W., Zhou, B., *Twin-induced grain boundary engineering in 304 stainless steel*, Mat. Sci. & Eng. A 487 (2008) 7-13.

[59] Engelberg, D. L., Newman, R. C., Marrow, T. J., *Effect of thermomechanical process history on grain boundary control in an austenitic stainless steel*, Scripta Mater. 59 (2008) 554-557.

[60] Li, Q., Guyot, B. M., Richards, N. L., *Effect of processing parameters on grain boundary modifications to alloy Inconel 718*, Mat. Sci. & Eng. A 458 (2007) 58-66.

[61] Poirier, J., *Creep of Crystals - High Temperature Deformation Processes in Metals, Ceramics and Minerals*, Cambridge University Press, 1985.

[62] Owen, G., Randle, V., *On the role of iterative processing in grain boundary engineering*, Scripta Mat. 55 (2006) 959-962.

[63] Coppolecchia, V., Bryant, J., Hoffmann, F., Drefahl, K., *Loss of Creep Ductility in Alloy 800H with High Levels of Titanium and Aluminium*, P. Ganesan, Bradley, R.A., (Ed.) Performance of High Temperature Materials in Fluidized Bed Combustion Systems and Process Industries, ASM International, 1987, p. 201.

[64] Horton, D., Thomson, C. B., Randle, V., *Aspects of twinning and grain growth in high purity and commercially pure nickel*, Mat. Sci. & Eng. A A203 (1995) 408-414.

[65] Mahajan, S., Pande, C. S., Imam, M. A., Rath, B. B., *Formation of annealing twins in f.c.c. crystals*, Acta Mater. 45 (1997) 2633-2638.

[66] Miyazawa, K., Iwasaki, Y., Ito, K., Ishida, Y., *Combination rule of sigma values at triple junctions in cubic polycrystals*, Acta Cryst. A52 (1996) 787-796.

[67] Reed, B. W., Kumar, M., *Mathematical methods for analyzing highly-twinned grain boundary networks*, Scripta Mater. 54 (2006) 1029-1033.

[68] Randle, V., Davies, H., *Evolution of microstructure and properties in alpha-brass after iterative processing*, Metall. & Mater. Trans. A 33 (2002) 1853-1857.

[69] Watanabe, T., Tsurekawa, S., *The control of brittleness and development of desirable mechanical properties in polycrystalline systems by grain boundary engineering*, Acta Mater. 47 (1999) 4171-4185.

[70] Watanabe, T., Tsurekawa, S., *Toughening of brittle materials by grain boundary engineering*, Mat. Sci. & Eng. A 387-389 (2004) 447-455.

[71] Gao, Y., Kumar, M., Nalla, R. K., Ritchie, R. O., *High-cycle fatigue of nickel-based superalloy ME3 at ambient and elevated temperatures: Role of grain-boundary engineering*, Metall. & Mater. Trans. A 36 (2005) 3325-3333.

[72] Lehockey, E. M., Palumbo, G., Lin, P., *Improving the weldability and service performance of nickel- and iron-based superalloys by grain boundary engineering*, Metall. & Mater. Trans. A 29 A (1998) 3069-3079.

[73] Boehlert, C. J., Longanback, S.C., Bieler, T.R., *Effect of thermomechanical processing on the creep behaviour of Udimet alloy 188*, Phil. Mag A 88 (2008) 641-664.

[74] Jones, R., Randle, V., Owen, G., *Carbide precipitation and grain boundary plane selection in overaged type 316 austenitic stainless steel*, Mat. Sci. & Eng. A 496 (2008) 256-261.

[75] Schlegel, S., Hopkins, S., Young, E., Cole, J., Lillo, T., Frary, M., *Precipitate redistribution during creep of alloy 617*, Metall. & Mater. Trans. A 40 (2009) 2812-2823.

[76] Bechtle, S., Kumar, M., Somerday, B. P., Launey, M. E., Ritchie, R. O., *Grain-boundary engineering markedly reduces susceptibility to intergranular hydrogen embrittlement in metallic materials*, Acta Mater. 57 (2009) 4148-4157.

[77] Kobayashi, S., Tsurekawa, S., Watanabe, T., Palumbo, G., *Grain boundary engineering for control of sulfur segregation-induced embrittlement in ultrafine-grained nickel*, Scripta Mater. 62 (2010) 294-297.

[78] Banner GmbH, *www.bannerbatterien.com*.

[79] Palumbo, G., Lehockey, E.M., Lin, P., *Applications for grain boundary engineered materials*, J. of Mater. 50 (1998) 40-43.

[80] Palumbo, G. e. a., *Interfacial Engineering for Optimised Properties*, Pittsburgh, PA: MRS, 1997.

[81] Bi, H. Y., Kokawa, H., Wang, Z. J., Shimada, M., Sato, Y. S., *Suppression of chromium depletion by grain boundary structural change during twin-induced grain boundary engineering of 304 stainless steel*, Scripta Mat. 49 (2003) 219-223.

[82] Kokawa, H., Jin, W. Z., Wang, Z. J., Michiuchi, M., Sato, Y. S., Dong, W., Katada, Y., *Grain boundary engineering of high-nitrogen austenitic stainless steel*, Mater. Sci. Forum 539-543 (2007) 4962-4967.

[83] Michiuchi, M., Kokawa, H., Wang, Z. J., Sato, Y. S., Sakai, K., *Twin-induced grain boundary engineering for 316 austenitic stainless steel*, Acta Mater. 54 (2006) 5179-5184.

[84] Tan, L., Sridharan, K., Allen, T. R., *The effect of grain boundary engineering on the oxidation behavior of INCOLOY alloy 800H in supercritical water*, J. of Nuclear Mater. 348 (2006) 263-271.

[85] Tan, L., Sridharan, K., Allen, T. R., Nanstad, R. K., McClintock, D. A., *Microstructure tailoring for property improvements by grain boundary engineering*, J. of Nuclear Mater. 374 (2008) 270-280.

CHAPTER 4: MICROSTRUCTURAL ANALYSIS

4.1 Introduction

The literature in the field of grain boundary engineering contains many examples of successful GBE processing on several different materials including copper, brass, nickel and some stainless steels. In order to arrive at these GBE microstructures, there has been some investigation into the combination of adjustable parameters (number of cycles, deformation per cycle, annealing temperature/time) which optimises the structure in terms of certain measures such as the $\Sigma 3^n$ boundary fraction. However, the optimal GBE process for one material may not provide the same results in another material. Therefore, it is necessary to investigate the optimal combination of GBE parameters for each new material. The main aim of this section of work was to determine the optimum GBE processing route through experimentation and analysis.

This chapter covers the microstructural aspect of the analysis of samples of grain boundary engineered 800H. First, the specific method of GBE that was used in this work is described. It is then necessary to explain how such microstructures are analysed, including sample preparation, and the techniques used to derive the various parameters (deformation percentage, annealing temperature/time) referred to in this document. The results are then presented in two stages; first an initial set of results, followed by a refinement of those parameters and a second set of results. The effect of sample texture is then briefly discussed for the general GBE case.

4.2 Grain Boundary Engineering Method

Material (800H) was obtained from Thyssenkrupp VDM Australia [1], in sections of plate measuring 300x150mm, and in thicknesses varying between 3.5mm and 8mm. The plates were then cut by slow-speed band-saw into strips measuring approximately 150x25mm, ready for deformation.

The grain boundary engineering procedure used in this work is illustrated in Figure 4.1.

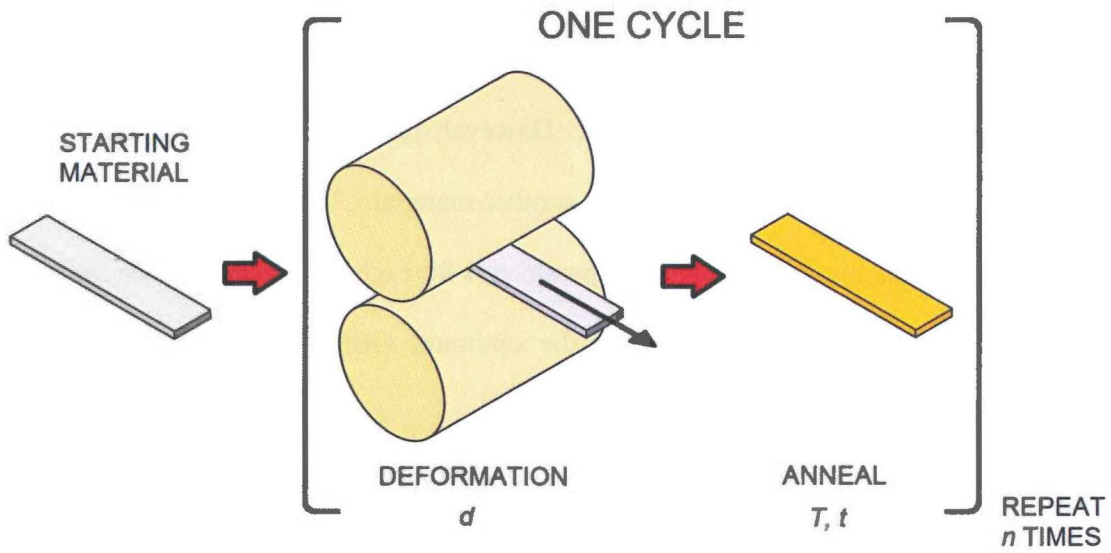

Figure 4.1 Illustration of grain boundary engineering process

The process is divided into a number of cycles, which are each divided into two steps. In this work, the same conditions were used in each cycle, leaving four GBE parameters which could be altered:

- *d*, the deformation level per cycle (%)
- *T*, the annealing temperature (°C)
- *t*, the annealing time per cycle (min)
- *n*, the number of cycles

Deformation was performed by plate rolling in a conventional rolling mill. The final reduction was achieved through the accumulation of several passes at a reduction of approximately 0.2mm per pass. The sample was also flipped over for each pass ensuring a relatively flat final state. The deformation level was measured at each pass by digital callipers, and the final reductions for each step were within 0.05mm of the target thickness.

Annealing was performed in a box furnace coupled with a K-type thermocouple and controller. The temperature was also verified before each anneal using a second K-type or N-type thermocouple and an appropriate reader. The accuracy of the temperatures used is expected to be approximately ±10°C, based on the temperature distribution within the furnace. Annealing time was controlled by stopwatch and was controlled to ±15 seconds. The samples were then water-quenched after each anneal to prevent microstructural changes such as the formation of γ' phase during cooldown.

4.3 Method of Sample Preparation

Metallographic samples were cut from the strips, initially both parallel to the rolling direction and also perpendicular to the rolling direction. When it was found that there was no discernable difference between the two, all subsequent samples were only taken perpendicular to the rolling direction. It was also ensured that the surface of interest was at least 25mm away from the ends of the strip. The surface of interest is shown in Figure 4.2, relative to the sample strip.

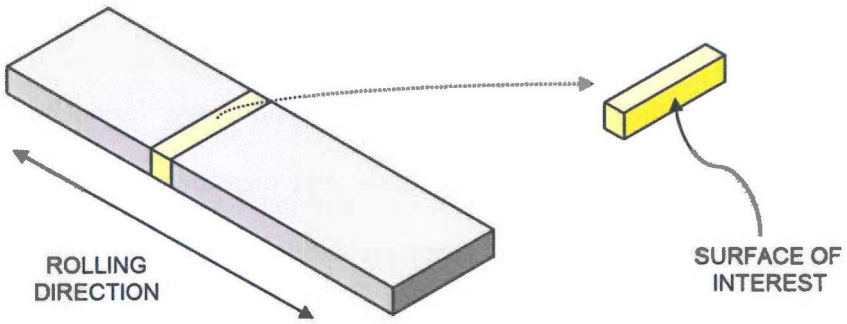

Figure 4.2 Geometry of the metallographic sample

Each sample was ground with progressively finer silicon carbide paper (240, 320, 400 and 600-grit) for 1-3 minutes per step. The samples were then polished with 9μ diamond solution, followed by 3μ diamond solution for approximately 3 minutes each. They were then washed in water and detergent to remove any residue. Final polishing was performed by a Buehler Minimet Automatic Polisher, using a solution of 75% 0.05μ colloidal silica suspension (Buehler Mastermet) and 25% water. Typical polishing times were on the order of 120 minutes in order to remove the sub-surface deformation induced by the grinding stages.

For EBSD analysis, it was found that a light etch was extremely useful in removing any remaining deformation and optimising pattern quality during EBSD analysis. This was performed either by submersion in glyceregia (10ml glycerol, 15ml HCl, 5ml HNO_3) for 1-2 minutes, or by electropolishing in a 10% oxalic acid solution at 1.5V for 12 seconds. For optical microscopy, the sample was etched completely in glyceregia for 3-4 minutes or until grain boundaries were fully revealed. In both cases, the samples were then washed in ethanol and dried before analysis.

4.4 EBSD Setup

EBSD analysis was performed in a JEOL JSM 6100 Scanning Electron Microscope, coupled with an HKL Channel 5 EBSD package. The accelerating voltage used was 20kV, with the specimen surface tilted at 70° relative to the incident beam. Linear dimensions were calibrated initially through the use of copper grids to ensure that the use of tilt correction within the software did not alter the scale or aspect ratio of the EBSD maps. Further details of the scanning electron microscope (SEM)/EBSD setup can be found in Appendix A.

In general, six EBSD maps were created from each sample at dimensions of 2mm x 2mm (except where sample thickness prevented this), meaning a total of 24mm^2 was scanned. The step size used was 10μ for the initial study (Section 4.8), which was then reduced to 5μ for the refined study (Section 4.9). More detail about the mapping procedure and the selection of these parameters is also provided in Appendix A, though it is reasonable to state here that the mapping conditions were chosen to provide a balance of speed and accuracy, and resulted in typical successful Kikuchi pattern identification rates of 95-98%. The remaining points were located almost exclusively in the grain boundaries, where pattern quality is sometimes poor due to the change in crystal orientation. Noise reduction was then applied to these points using the Channel 5 algorithm, which involves assigning an unindexed point the average orientation of its successfully identified neighbouring pixels.

4.5 Analysis Method for $\Sigma 3^n$ Boundary Fraction

From the original data set, the misorientation between neighbouring pixels is calculated within the Channel 5 software. If the misorientation is within the acceptable angle from a CSL misorientation (according to the Brandon criterion [2] in this work), that section of boundary is designated as a CSL boundary, as explained in the previous chapter. If the

misorientation is not close to a CSL misorientation, but exceeds a user-defined threshold angle for a high-angle boundary (HAB), it is designated as a random HAB. In the present work, the threshold was set at 10°.

The ratio between the total length of each Σ boundary, and the total length of all boundaries within an EBSD map is called the Σ length fraction. The calculation of this length fraction is performed automatically within the HKL Channel 5 software, according to the equation:

$$f_{\Sigma a} = n_{\Sigma a}/n_{HAB} \tag{4.1}$$

where $f_{\Sigma a}$ is the length fraction of Σa boundaries, $n_{\Sigma a}$ is the number of neighbouring pixel-pixel misorientations which meet the Brandon criterion for a Σa boundary, and n_{HAB} is the total number of neighbouring pixel-pixel misorientations which exceed the angular threshold (10°) for a high-angle boundary (note that $n_{\Sigma a}$ is a subset of n_{HAB})[1].

There is another method for calculating the Σ fraction, namely using the relative number fraction of boundaries rather than the relative length fraction. The number fraction has been used in several GBE studies [3-6], although it is less commonly reported than the length fraction. This process involves identifying each boundary segment, from triple point to triple point, and then summing the number of each type of segment compared to the total number of boundary segments.

The advantage of using the number fraction is that it allows differentiation between the introduction of new sections of Σ boundary, and the lengthening of existing Σ boundaries during GBE processing. However, using the number fraction also has its disadvantages. First, the number fraction is much more sensitive to small errors in the pattern acquisition and

[1] This calculation was confirmed by the analysis of small subsets of EBSD data involving 5-10 pixels.

solving procedure. These errors often result in small 1-2 pixel "false grains" being identified. The number fraction will weight such false grain boundaries equal to any other, whereas the length fraction will reduce their significance due to their small size. Therefore, much more care must be taken in the noise reduction stages where the number fraction of boundaries is to be measured. This normally has to be done manually, and is often a time-consuming process. Second, the length fraction intuitively has more correlation with properties than the number fraction. For example, the resistance of a boundary segment to diffusion is calculated by the product of its diffusivity and its length. For these reasons, the length fraction of $\Sigma 3^n$ boundaries is specified in this work, as calculated within the Channel 5 software.

4.6 Analysis Method - Grain Size

4.6.1 Current Optical Method

The conventional method of grain size measurement by optical microscopy is detailed in ASTM Standard E-112 [7]. The method normally involves obtaining a micrograph of known magnification, and superimposing a template such as a circle of known diameter (Circle-Intercept Procedure) or a line (Linear-Intercept Method) onto the image. An example of the circular-intercept procedure is shown in Figure 4.3.

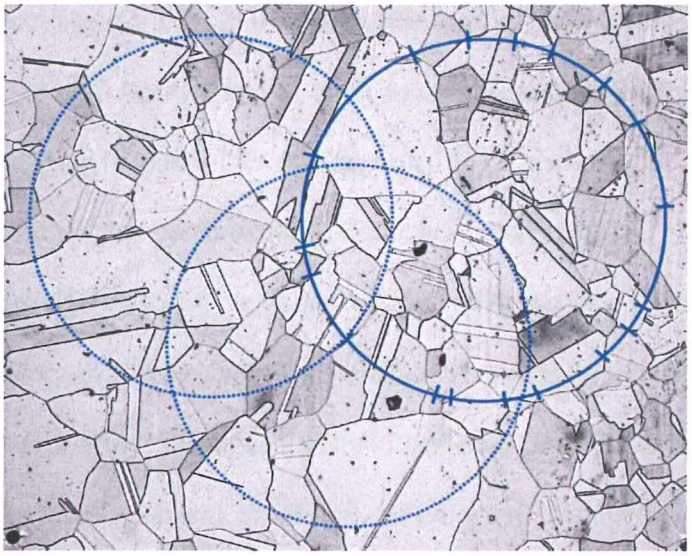

Figure 4.3 Example of the circular-intercept procedure

The template is marked at each point that it crosses a relevant grain boundary, and the number of intercepts per mm, N_L, is then calculated. An important point to note is that twin boundaries are not included, according to E112. In the case of the circular intercept procedure, the ASTM grain size number, G, is given by the formula:

$$G = (6.643856 \log_{10} N_L) - 3.288 \tag{4.2}$$

The ASTM grain size number is based on an inverse-logarithmic scale, and can be related to the mean grain diameter. This relationship is shown for reference in Figure 4.4.

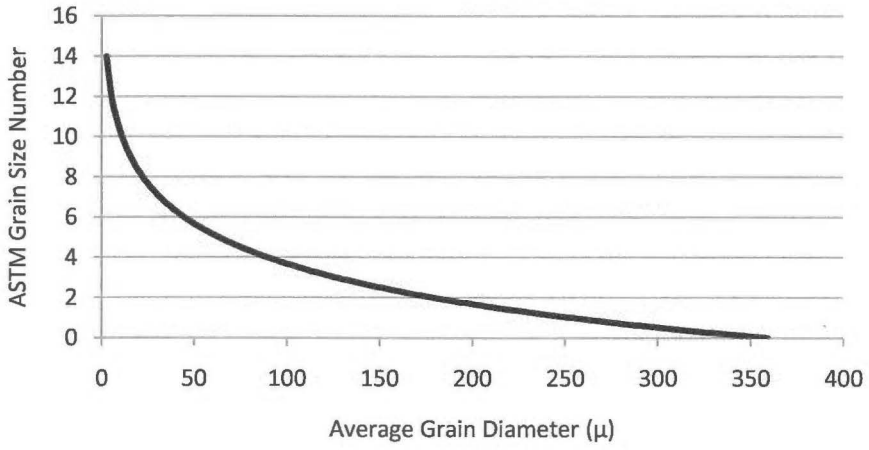

Figure 4.4 Relationship between ASTM grain number and mean grain diameter

4.6.2 EBSD Methods

The development of EBSD mapping in the past decade has presented an opportunity to improve the method by which grain size is measured. However, at present there is no accepted standard governing the use of EBSD for grain size measurement, and so there are a number of different methods currently used. The two most common methods are presented here.

4.6.2.1 Flood-Fill

In order to determine the location of grain boundaries, the EBSD software determines the lattice misorientation between each pixel and its neighbouring pixels. Therefore, a single grain may be identified automatically by defining a region of contiguous pixels where the pixel-pixel misorientation does not exceed the threshold for a grain boundary (ie. the crystal orientation is approximately equal among the entire region). Twin boundaries are identified by the software as boundaries within 5° of a 60°/<111> misorientation, and therefore may be automatically excluded.

This method can be described as a "flood-fill" approach, where a starting pixel is chosen, and each of its neighbouring four pixels (above, below, left, right) is checked to determine whether it is also part of the same grain. If so, it is included, and its neighbours are subsequently checked. This process continues until all neighbouring pixels to the current grain have been identified as part of other grains (in other words, the current grain is completely encircled by high-angle grain boundaries). An example of this process is shown in Figure 4.5 for material in the as-received condition. The first image, (a), shows the original EBSD map, with high-angle boundaries shown in black and twin boundaries shown in red. The second image, (b), shows the same area, processed by a flood-fill algorithm and with each identified grain shown in a different colour.

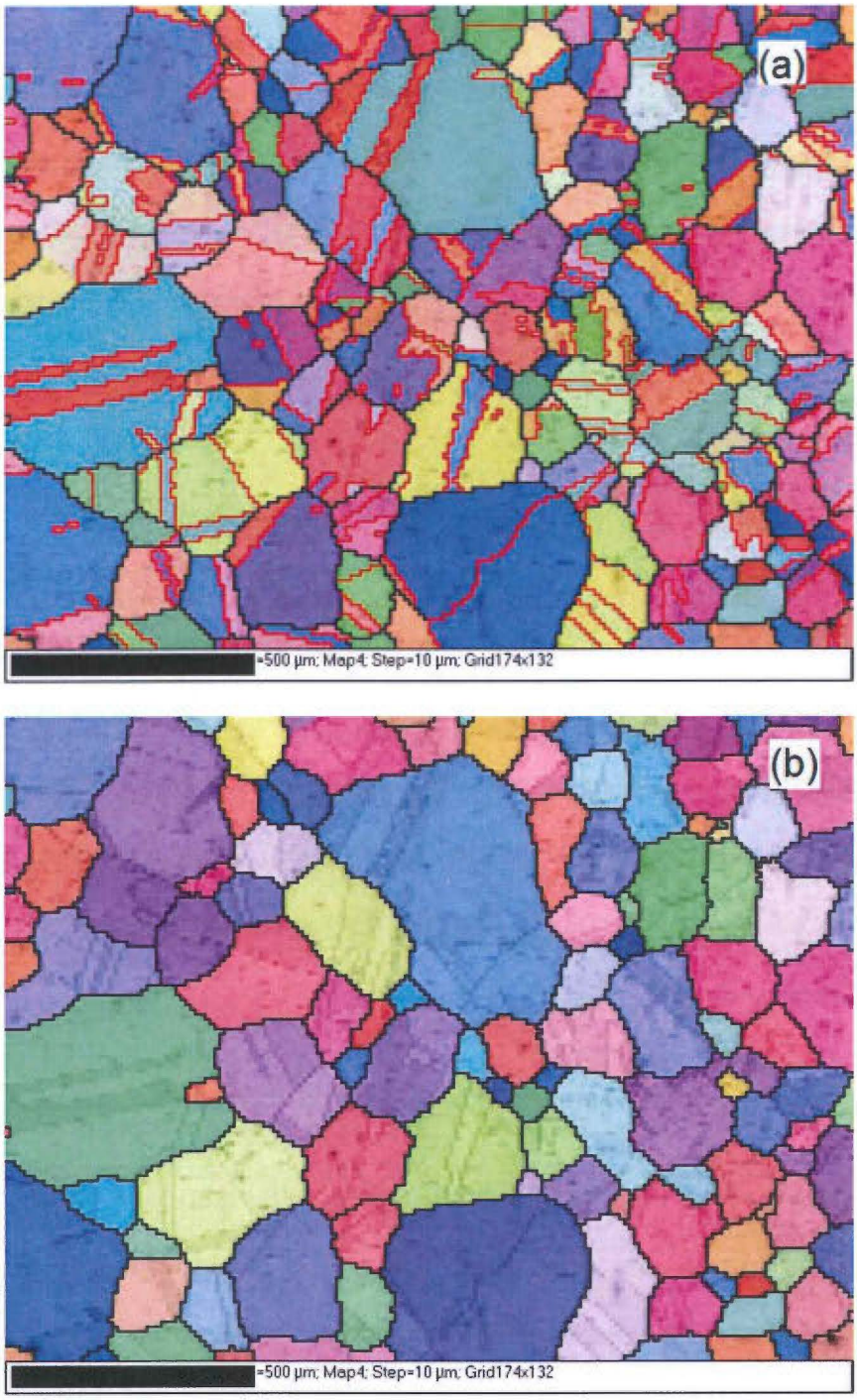

Figure 4.5 Example of "flood-fill" grain detection on an as-received microstructure. (a) shows the raw EBSD data, and (b) shows how grains are identified by this approach. High-angle boundaries are shown in black and twin boundaries are shown in red.

This figure shows that the processing algorithm delivers a result that is easy to interpret. Because each grain has a defined area, this method also provides information about the statistical distribution of grain size. For example, the upper and lower quartiles or largest

grain may be extracted from this data set if required. However, when grain boundary engineered microstructures are investigated in the same way, the results are surprising. An example of this is shown in Figure 4.6.

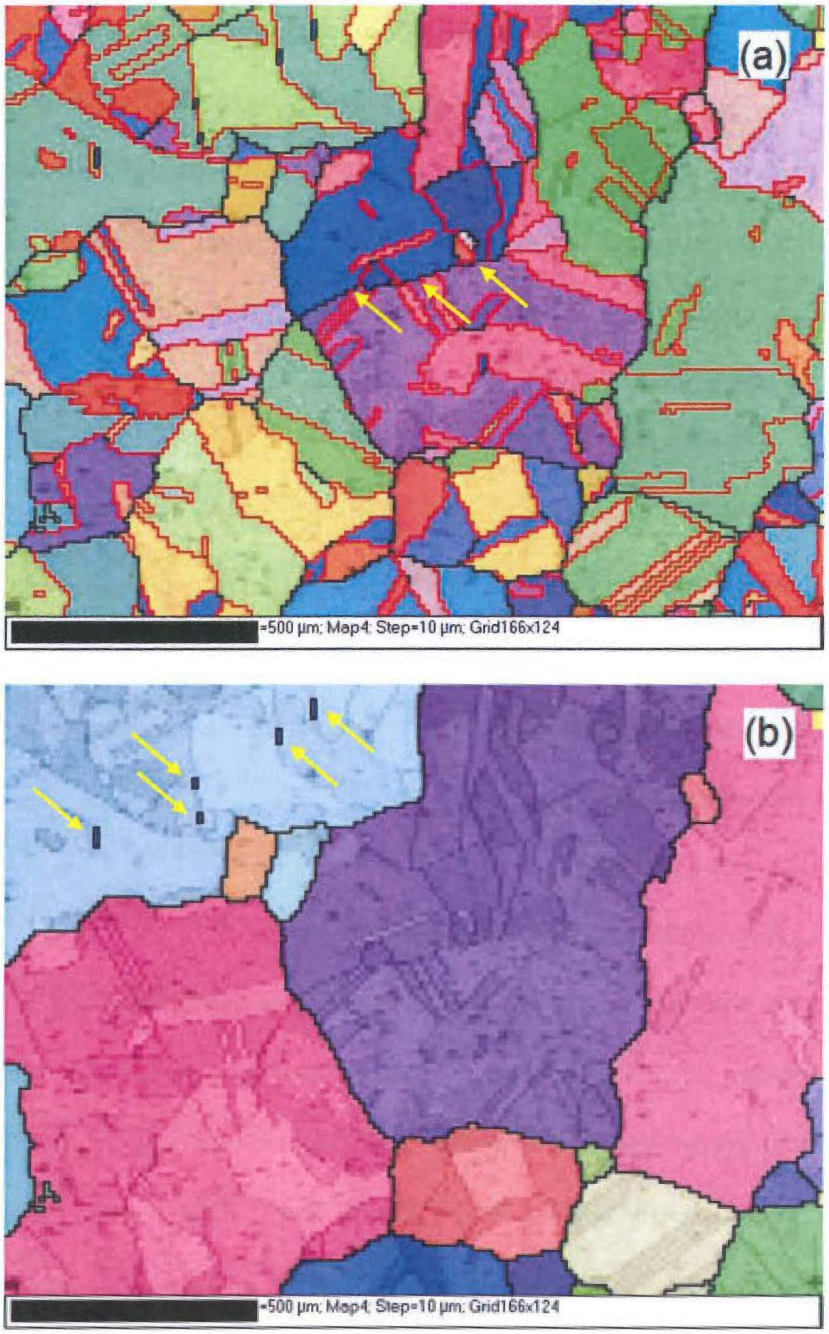

Figure 4.6 Example of "flood-fill" grain detection on a GBE microstructure. (a) shows the raw EBSD data, and (b) shows how grains are identified by this approach. High-angle boundaries are shown in black and twin boundaries are shown in red. Arrows in (a) indicate a HAB boundary which is ignored by the processing algorithm, and "false grains" in (b).

The processed map in (b) shows a grain size that appears to be an overestimate compared with the raw data in (a). This is due to the prolific twinning in GBE materials. Many grains become merged in such an analysis because they are linked by small sections of Σ3 boundary. It is important to note that these Σ3 boundaries are not necessarily annealing twins, and in fact it has been suggested that the Σ3 boundaries introduced by GBE are primarily incoherent [8], meaning they should not be ignored in grain size calculations. However, because the misorientation is largely indistinguishable between coherent and incoherent Σ3s, even sections of incoherent Σ3 boundary will be ignored by the flood-fill algorithm, leading to the large grain sizes seen in Figure 4.6(b).

It should be noted that this problem with the flood-fill approach is highly exacerbated for GBE materials, where the Σ3 fraction is increased significantly and where such boundaries become incorporated into the network. As a method for determining grain size in recrystallised, equiaxed structures, it is a relatively accurate measurement with the advantage of providing a complete data set.

4.6.2.2 Mean-Intercept-Length Method

The other method used is a combination of the optical methods described in Section 4.6.1, and EBSD mapping. An EBSD map is generated in the same way as the method described above, but the intercept procedures (either the circular-intercept or the linear-intercept methods) are then manually applied to the EBSD map. This method generates what is referred to as a mean-intercept-length between boundaries, and does not ignore HABs that do not completely encircle a grain. For an example of this, see the HAB indicated by arrows in Figure 4.6(a), which is then ignored when the flood-fill processing algorithm is applied (Figure 4.6(b)). Many properties such as strength are dependent on the mean spacing between grain boundaries, and hence the combined method described here is a better

indicator for such properties, for the case of GBE materials. For this reason, this mean-intercept-length method is used exclusively in this work.

4.6.3 Comparison Between Optical and EBSD Methods

As part of this project, the three methods of grain size measurement (optical, combined EBSD+optical, EBSD automatic) were directly compared and summarised. The conclusions are briefly summarised here.

- EBSD methods determine the location of grain boundaries from actual crystallographic data, as opposed to an optical image of the microstructure. Therefore, EBSD methods eliminate problems of preferential etching in optical analyses, which can lead to some grain boundaries not being revealed, and therefore causes inaccurate counts.
- The identification of twin boundaries is based on the crystallographic relationship between twinned grains (i.e. a 60°/<111> misorientation), and therefore is more accurate than optical methods, where there is no crystallographic data.
- EBSD methods are entirely repeatable, and not subject to the human biases associated with optical methods.

The disadvantage to using EBSD for grain size measurement, apart from the fact that an SEM and EBSD detector are required, is that no standard currently exists governing its use, and therefore slightly different methods/parameters are used by different researchers. However, the creation of an ASTM standard for grain size measurement using EBSD is currently in progress [9], and EBSD may well become the industrially accepted method for the measurement of grain size in the coming years.

4.6.4 Treatment of "False" Grains

Occasionally, an EBSD pattern is misindexed, normally due to a reduction in pattern quality associated with a second phase particle, or an unclean surface etc. These misindexed patterns commonly appear as "island grains" within other grains. For example, several of these false grains are indicated with arrows in Figure 4.6(b). These false grains are normally not more than one or two contiguous pixels, but have an influence on the calculated grain size if they are not removed. Therefore, in this work, these grains were filtered out of such calculations by applying a lower limit threshold of $300\mu^2$ (corresponding to 1-4% of the average grain area in the microstructures measured). Any grains equal to or below this threshold area were marked as false and excluded from the intercept count.

4.6.5 Treatment of Twin Boundaries

Although methods exist to determine which Σ3 boundaries are coherent annealing twins [10-11], they are currently not practical for large data set collection such as is necessary for the determination of average grain size. Evidence [12] suggests that coherent annealing twins are typically closer to the reference misorientation of 60°/<111> than incoherent Σ3s. Therefore, although the Brandon criterion sets a maximum of 8.67° deviation for a Σ3 boundary, the maximum angular deviation for a coherent twin is typically set at 5° [13]. However, this is far from a robust rule, and the precise identification of twin boundaries by EBSD remains an issue in the analysis of GBE materials in particular.

Although the ASTM standard for determination of grain size (E-112) [7] states that twin boundaries should be ignored, there is mounting evidence to suggest that even coherent annealing twins in fact do have some effect on material properties [14-19]. Therefore, in this work, and in some other GBE studies (e.g.[6]), two grain sizes are reported. One grain size is reported excluding twins (technically: excluding boundaries within 5° of the 60°/<111>

misorientation, whether or not they are actually annealing twins) in the vein of ASTM E-112. A second grain size, reported as a "crystallite size" occasionally in the literature [6, 20], includes all grain boundaries in the intercept count. Presenting both grain sizes helps to alleviate some of the problems with determining which boundaries are true, coherent annealing twins, in that correlations may then be drawn with either one.

4.7 Characterisation of As-Received Material

In order to determine the differences to the microstructure caused by GBE, the 4.5mm as-received material was initially characterised by EBSD, in terms of $\Sigma 3^n$ length fraction and grain size. A representative EBSD map is shown in Figure 4.7. In this image, HABs are shown in black, Σ3s in red, Σ9s in yellow and Σ27s in blue.

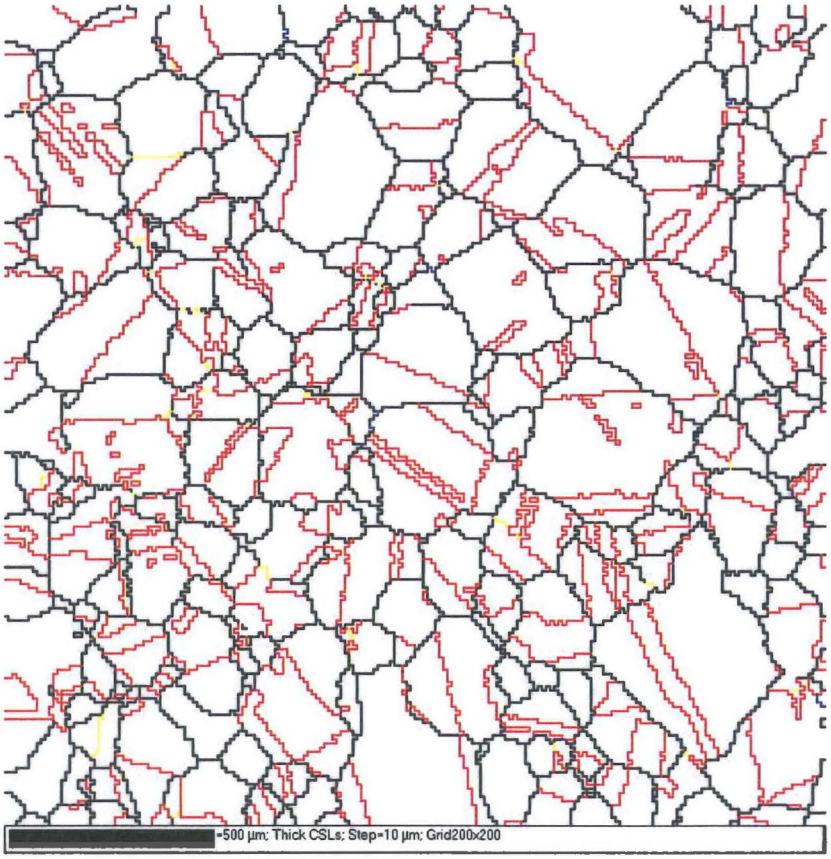

Figure 4.7 Representative EBSD map for as-received condition. HABs are shown in black, Σ3s in red, Σ9s in yellow, Σ27s in blue. Bar at lower-left corner indicates 500µ.

The length fraction of each of the $\Sigma 3^n$ boundaries was calculated as described in Section 4.6. The grain size, both excluding and including twins, was also calculated, and the results are shown in Table 4.1.

Table 4.1 $\Sigma 3^n$ boundary fractions and grain size for 4.5mm as-received sample

Boundary Length Fraction			**Grain Size**	
Σ3 Boundary	Σ9 Boundary	Σ27 Boundary	Excluding Twins	Including Twins
44.1%	1.0%	0.1%	151.5μ	81.7μ

The as-received microstructure shows a starting total $\Sigma 3^n$ boundary fraction of approximately 45%, reasonably consistent with a previous study on the same material [21]. The average grain size was found to be 151.5μ (ASTM 2.5), well within the material requirements [22] of ASTM 5 or coarser.

It is also interesting to note the morphology of the Σ3 boundaries. Figure 4.8(a) shows a representative EBSD map for the as-received condition, where the map has subsequently been processed in order to show only Σ3 boundaries (Figure 4.8(b)).

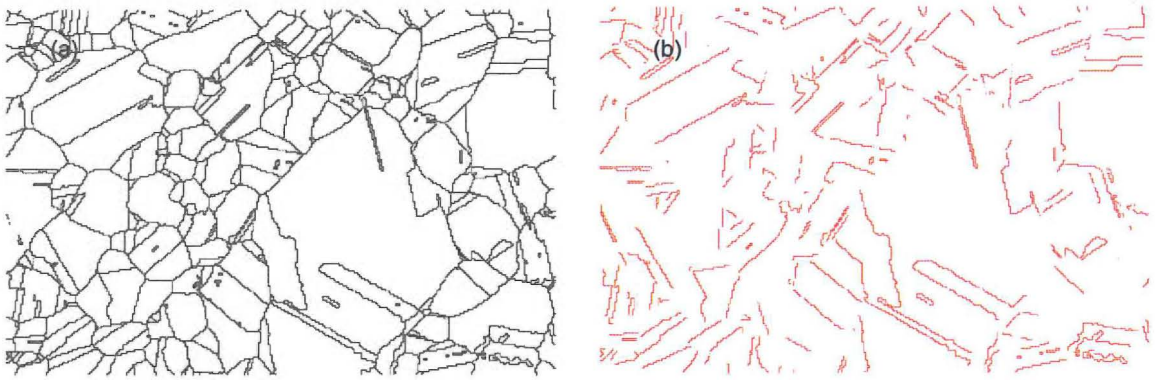

Figure 4.8 EBSD maps for as-received condition showing (a) all grain boundaries (including Σ3s), and (b) Σ3 boundaries only

The vast majority of the Σ3 boundaries in Figure 4.8(b) exhibit classic signs of annealing twins. They are predominantly straight, occasionally stepped, and often occur in pairs. Therefore, it is likely that the majority of the Σ3 boundaries present in the as-received material are coherent annealing twins with {111} boundary planes.

4.8 Results of GBE – Initial Study

As an initial study into the effects of various process parameters (deformation level, annealing conditions etc), ten samples of 800H plate were grain boundary engineered according to the methods described in Section 4.2. The plate thickness was initially 4.5mm in all cases. The combinations of processing parameters and associated sample names are shown in Table 4.2. Labels are also assigned for reference in future figures.

Table 4.2 GBE conditions for initial samples

Number of Cycles	Deformation per Cycle	Annealing Temperature	Annealing Time	Sample Name	Sample Label
AS RECEIVED				[AR]	(a)
1	50%	1150°C	30 min	[1x50,1150,30]	(b)
1	6%	1100°C	60 min	[1x6,1100,60]	(c)
1	6%	1115°C	300 min	[1x6,1115,60]	(d)
4	6%	1100°C	10 min	[4x6,1100,10]	(e)
4	6%	1100°C	30 min	[4x6,1100,30]	(f)
4	6%	1100°C	90 min	[4x6,1100,90]	(g)
4	6%	1150°C	10 min	[4x6,1150,20]	(h)
4	6%	1150°C	30 min	[4x6,1150,30]	(i)
4	15%	1115°C	10 min	[4x15,1115,10]	(j)
4	15%	1115°C	30 min	[4x15,1115,30]	(k)

Some success has been shown in creating GBE materials with the use of one cycle and comparatively long annealing times [23]. Therefore, three samples were subject to just one cycle of processing. The remainder were subject to four cycles, which is fairly common in the GBE literature. A previous study on this material [21] concluded that a GBE condition could be achieved using a 6% deformation percentage, and so this claim was investigated by creating seven samples with this deformation percentage, and varying the other conditions. Deformation levels of 15% and 50% were also investigated.

Example EBSD maps from the as-received condition, and selected GBE conditions, are shown in Figure 4.9 (overleaf). In these figures, high-angle boundaries are shown in black, Σ3s in red, Σ9s in yellow, and Σ27s in blue. The size of each map is 2mm x 2mm (micron marker indicates 500μ), except for the deformation levels 15% and higher, which measure 2mm x 1mm (micron marker indicates 200μ).

It is visually apparent from these images that the majority of the different GBE procedures exhibit measurable increases in the relative fractions of $\Sigma 3^n$ boundaries, compared to the as-received microstructure, labelled (a). The $\Sigma 3^n$ length fractions were calculated for all samples and are subsequently shown in Figure 4.10.

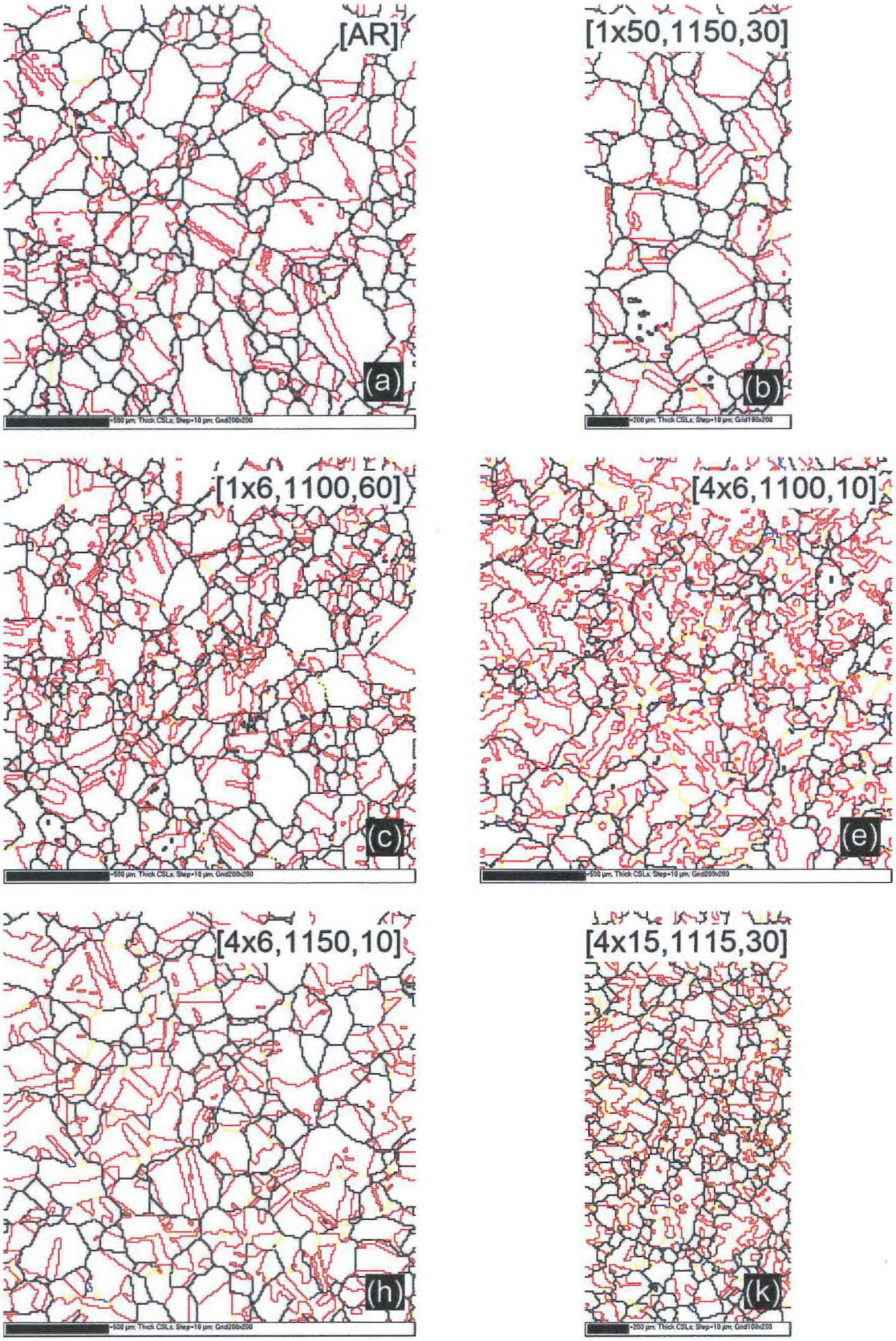

Figure 4.9 Example microstructures for selected GBE samples. Σ3 boundaries are shown in red, Σ9s in yellow, Σ27s in blue and HABs in black.

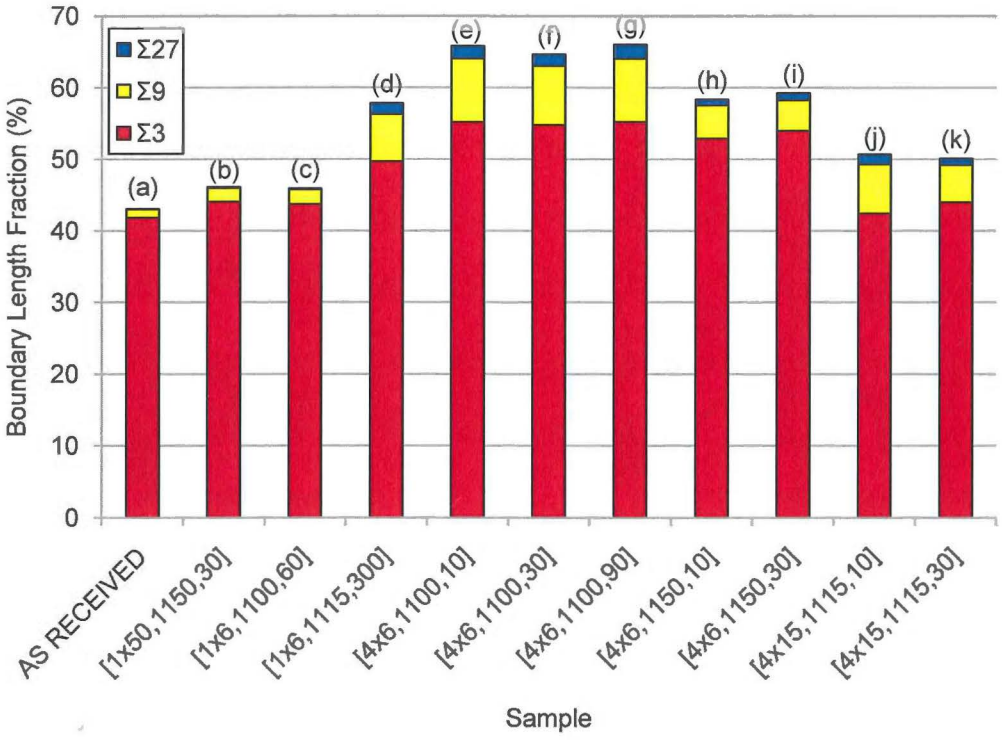

Figure 4.10 $\Sigma 3^n$ length fractions for initial GBE samples

Of the single cycle samples (b-d), only sample (d) showed any significant increase in $\Sigma 3^n$ fraction. It is possible that increasing the annealing time further may result in higher $\Sigma 3^n$ boundary fractions. However, the highest $\Sigma 3^n$ fractions were obtained using four cycles of 6% deformation and annealing at 1100°C (e-g), representing an increase of approximately 55% in total $\Sigma 3^n$ fraction compared to the as-received sample. Increasing the annealing temperature to 1150°C (h,i) resulted in an increased $\Sigma 3^n$ fraction compared to the as-received condition, but a reduction compared to the 1100°C anneal. Similarly, using 15% deformation per cycle (j,k) resulted in a relatively equiaxed structure and comparatively low $\Sigma 3^n$ fractions.

The grain size of all samples was calculated as described in Section 4.6, and the results are shown in Figure 4.11.

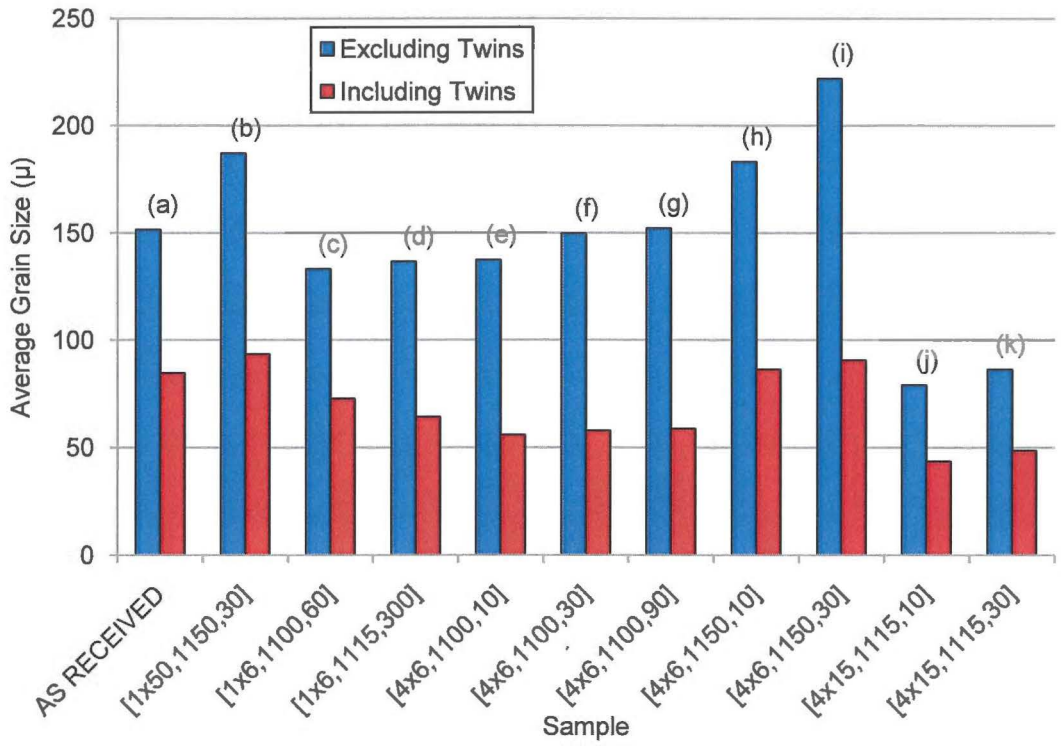

Figure 4.11 Grain size for initial GBE samples

If the grain size is measured in the conventional way and twin boundaries are excluded, it is apparent that many of the processing seqences have no significant effect on grain size. The most successful samples in terms of $\Sigma 3^n$ boundary fraction (e-g) have a grain size which is similar to the as-received sample. It is only when the annealing temperature is increased to 1150°C that the grain size begins to increase. When the deformation level is increased to 15%, the grain size halves, indicating that recrystallisation has taken place without much grain growth.

If the grain size is measured including twins as grain boundaries, it is apparent that in many cases, the grain size decreases as a result of GBE. The ratio of twin-excluded to twin-included grain sizes has increased from approximately 1.8 in the as-received condition, to

nearly 2.6 in the case of [4x6,1100,30] and [4x6,1100,90]. This increase is consistent with the increase in relative length fraction of Σ3 boundaries.

The effectiveness of the GBE procedure can also be estimated using a combination of Σ3 length fraction and the Σ9/Σ3 boundary ratio, as used in [20]. These results are shown in Figure 4.12.

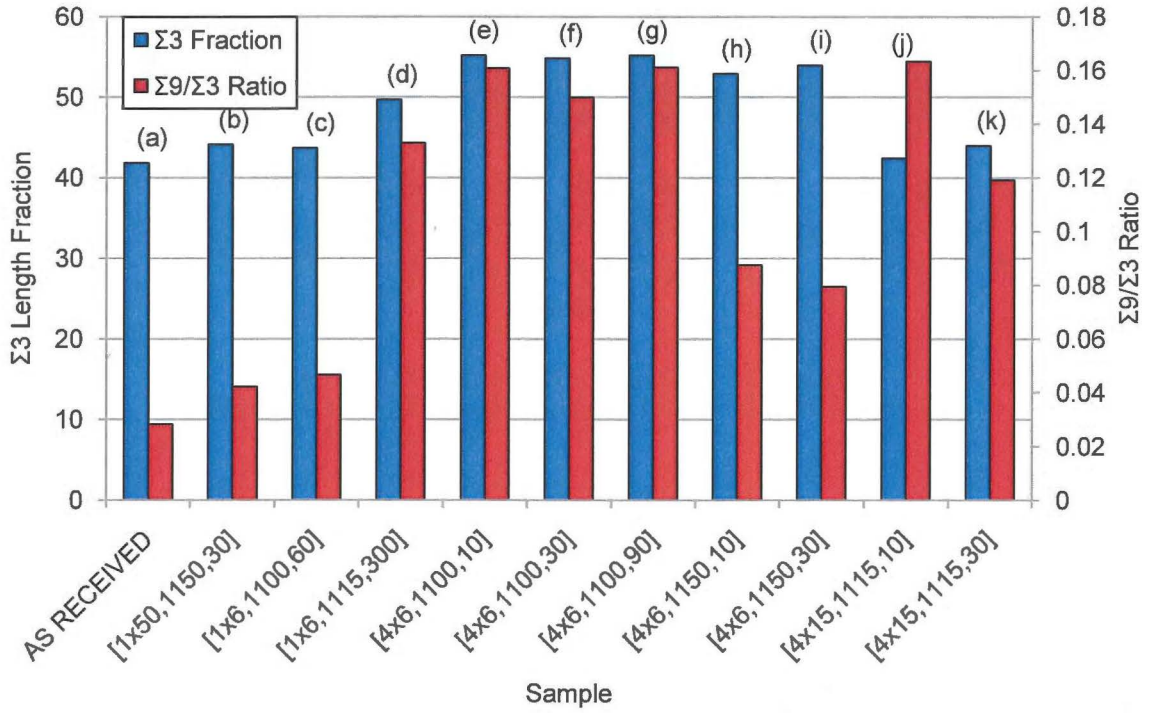

Figure 4.12 Σ3 length fraction and Σ9/Σ3 boundary ratio for initial GBE samples

This figure confirms that the "most grain boundary engineered" samples are the three samples subjected to four cycles of 6% deformation and 1100°C anneals (e-g). These samples show both the highest $\Sigma 3^n$ fractions and the most consistent grain size. Therefore, the 6% deformation/1100°C anneal combination was selected for further study, as detailed in the following section.

4.9 Results of GBE – Refinement of Initial Study

In the second iteration of the GBE study, the material used was 8mm thickness, as opposed to 4.5mm used for the first iteration. Part of the reason for this was that the 8mm thickness better replicated the 6.25mm pigtail wall thickness once it had been engineered (four reductions at 6% each then result in a final thickness of exactly 6.25mm). The second reason for this was that a thin layer of very small grains was observed directly on top of each strip of material (ie. the surfaces that had been in contact with the rollers). This is shown by EBSD map in Figure 4.13, as a comparison between the cross-section and top of a material strip.

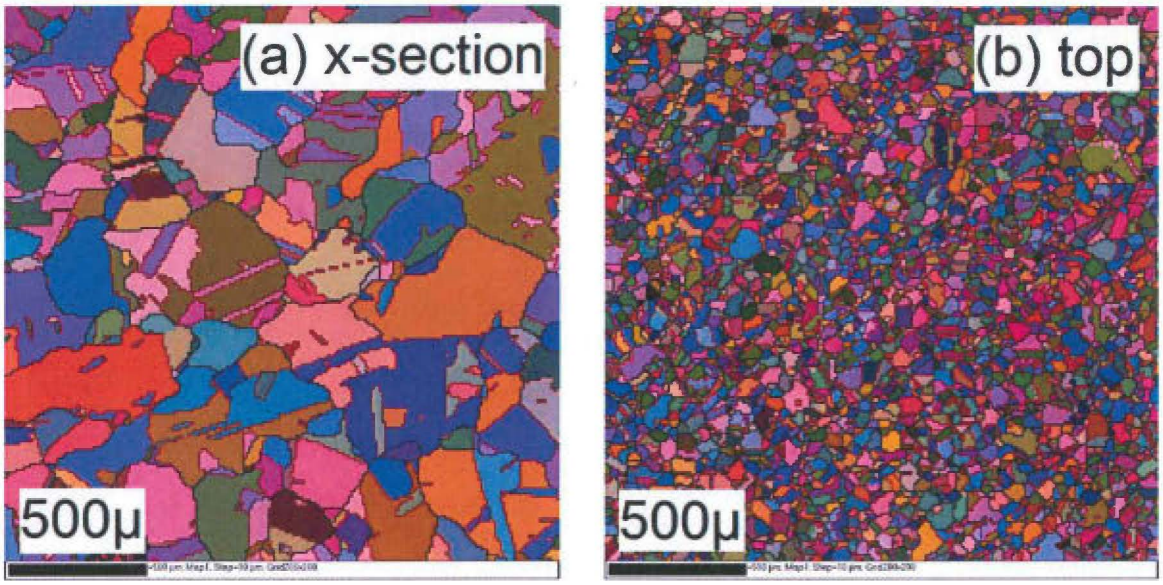

Figure 4.13 Comparison between (a) cross-section and (b) top of material strip

According to the results obtained for the initial GBE study, this layer is probably consistent with a locally higher deformation at the surface of the material. As a result, it was decided that the surface layer should be mechanically removed for subsequent tensile and creep samples.

A second matrix of parameters for the refined GBE study was selected and is shown in Table 4.3.

Table 4.3 GBE conditions for refined samples

Number of Cycles	Deformation per Cycle	Annealing Temperature	Annealing Time	Sample Name
4	6%	1075°C	10 min	[4x6,1075,10]
4	6%	1075°C	20 min	[4x6,1075,20]
4	6%	1100°C	10 min	[4x6,1100,10]
4	6%	1100°C	20 min	[4x6,1100,20]
4	6%	1100°C	30 min	[4x6,1100,30]
4	10%	1100°C	20 min	[4x10,1100,20]
4	10%	1100°C	30 min	[4x10,1100,30]

The matrix was based around the successful [4x6,1100,*x*] conditions explored previously. It was necessary to determine whether the increase from 4.5mm initial thickness to 8mm initial thickness had any effect on $\Sigma 3^n$ fraction or the grain size, and hence some of the conditions were repeated from the previous iteration. The [4x6,1100,90] sample was not repeated as the previous results showed that the increase in annealing time from 30 to 90 minutes made very little difference to the $\Sigma 3^n$ boundary fractions.

Four cycles of processing were used in all cases, as the previous results, plus several studies in the literature (e.g.[8, 24]), led to the conclusion that the $\Sigma 3^n$ boundaries become more incorporated into the grain boundary network when cyclic processing is used. A lower annealing temperature, 1075°C was selected as two temperatures higher than 1100°C had already been tested. Finally, a new deformation level, 10%, was also investigated. It had been shown that 15% deformation was too high, however this left a large range between 6 and 15% without any data. 10% was selected as it was approximately halfway in this range. EBSD maps were again constructed from each of the sample conditions listed in Table 4.3. However, the resolution was changed from 10μ per step to 5μ per step, in order to better resolve some of the finely-spaced boundaries. Selected maps are shown in Figure 4.14.

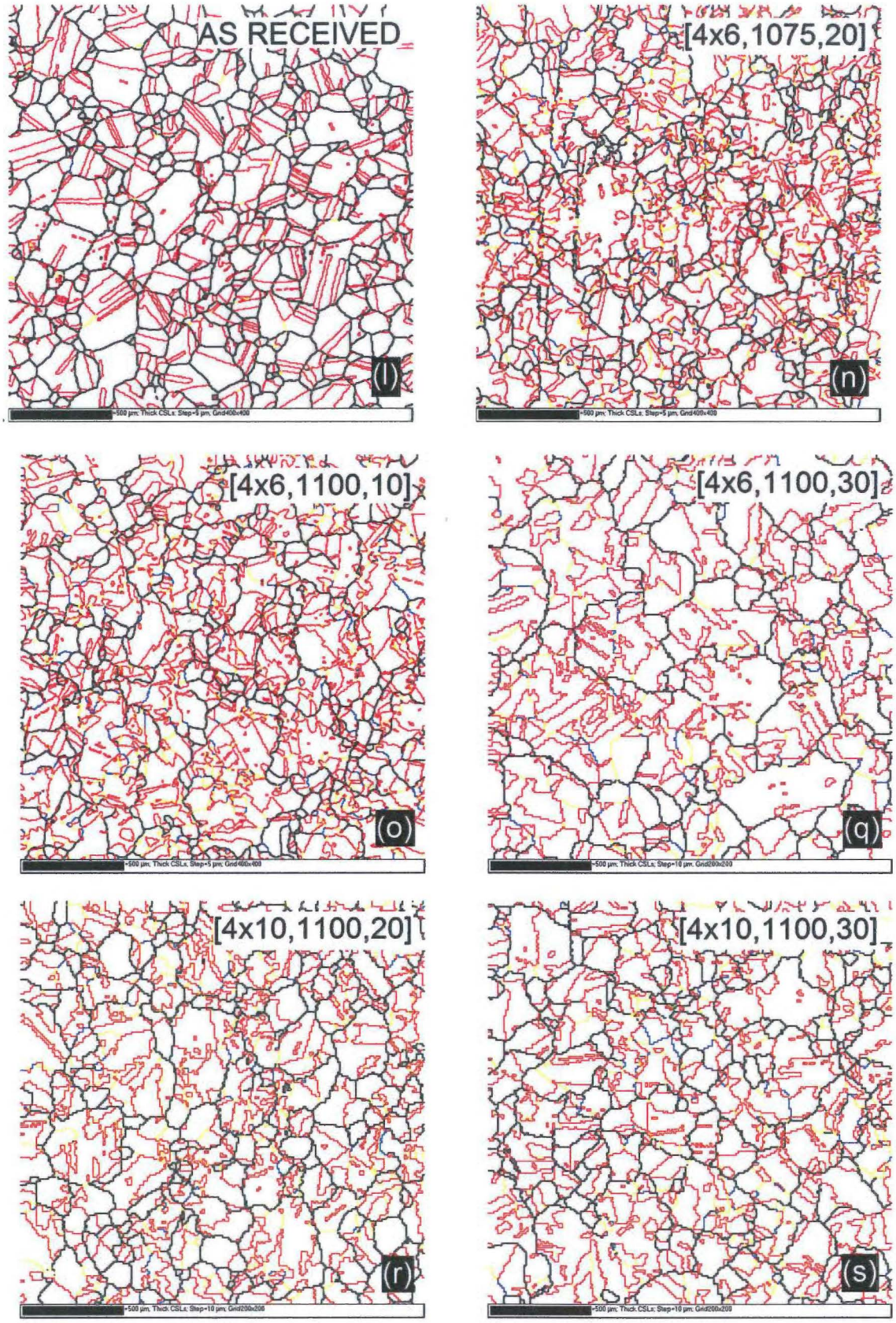

Figure 4.14 Example microstructures for refined GBE samples. Σ3 boundaries are shown in red, Σ9s in yellow, Σ27s in blue and HABs in black. Bar in lower-left represents 500μ.

The length fractions of $\Sigma 3^n$ boundaries were calculated from these EBSD maps, and are shown in Figure 4.15.

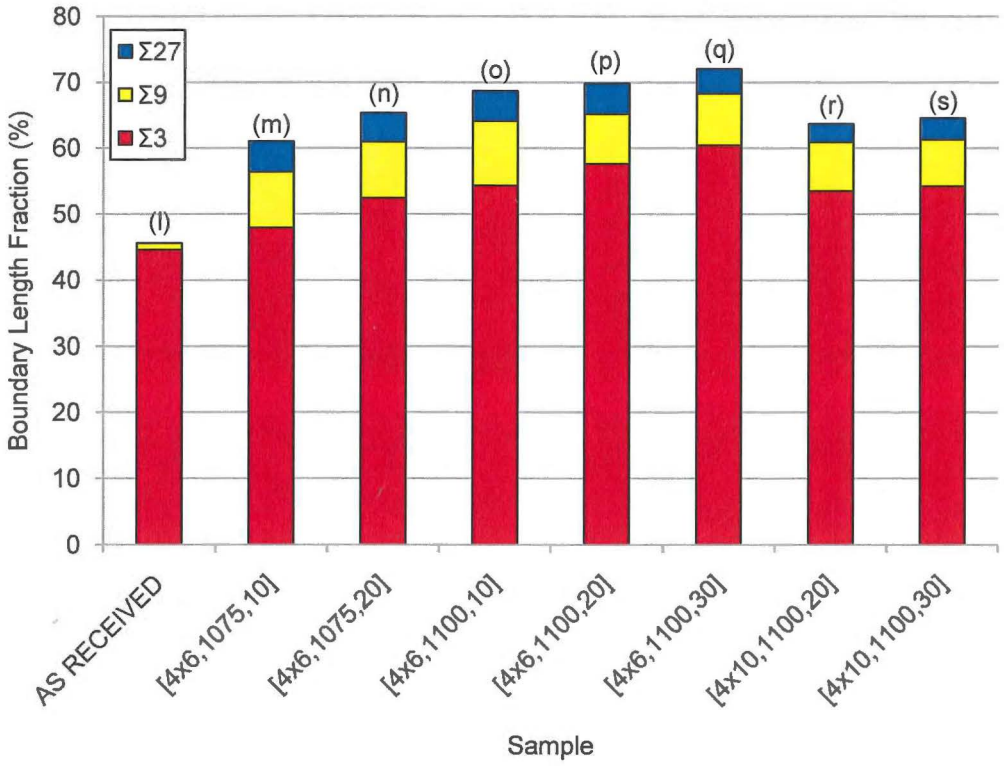

Figure 4.15 $\Sigma 3^n$ length fractions for refined GBE samples

It is apparent from this figure that all of the refined GBE conditions produced large increases in $\Sigma 3^n$ boundary fractions, although noticeably, it is once again the [4x6,1100,*x*] samples which show the greatest fractions. In particular, sample (q) showed an increase of 60% in total $\Sigma 3^n$ fraction compared to the as-received sample.

The grain size, excluding and including twins, was also calculated and is shown in Figure 4.16.

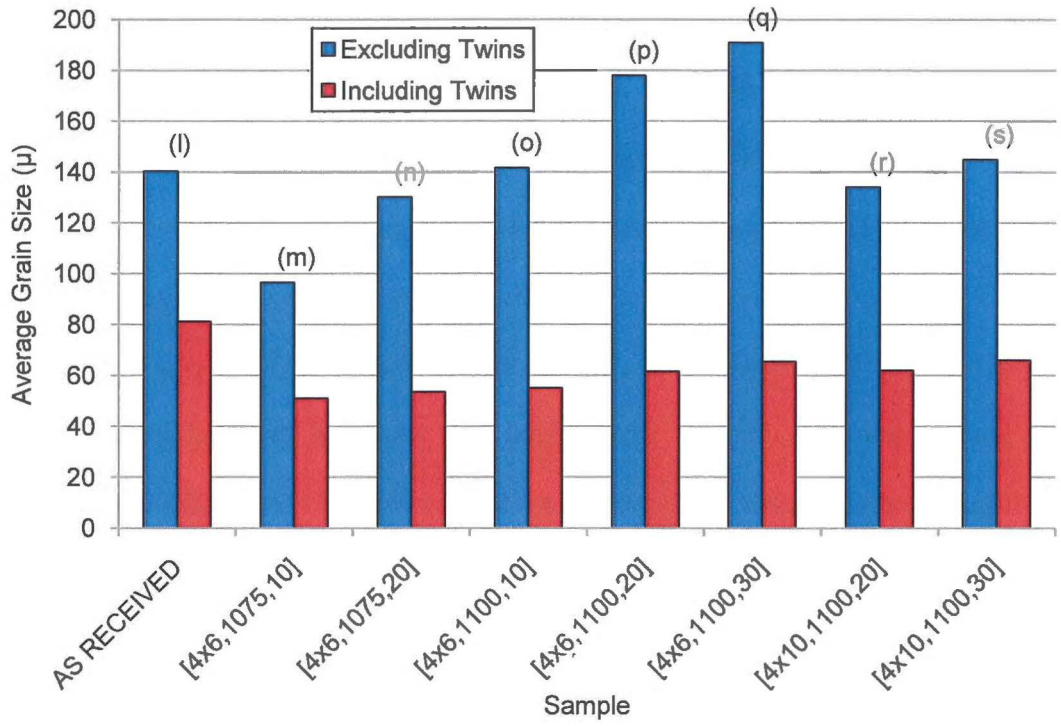

Figure 4.16 Grain size for refined GBE samples

Similar trends are observable in the grain size as were apparent in the previous iteration of processing. For the 1100°C annealed samples, there is some grain growth after 20 minutes, which continues up to 30 minutes. However, the twin-included grain size has actually decreased, suggesting that new Σ3 boundaries have been generated. Again the ratio between twin-excluded grain size and twin-included grain size has increased from approximately 1.7 to 2.9 in the case of [4x6,1100,30]. It is also likely that the 10% deformation level has not caused recrystallisation, as the grain size has not changed. Combined with the results from Figure 4.15, it is apparent that this deformation is also suitable for creating a GBE state.

4.10 Effects of Processing Parameters

From this study, it is not possible to determine the effects of a change in any single parameter under all conditions. For example, choosing three states for each parameter would result in a

testing matrix of 81 samples, which was considered prohibitively time-consuming. However, it was possible to separate the effects of one parameter under at least one condition in all cases. These effects are explained in the following paragraphs, excluding the number of cycles, which is investigated in much greater detail in Chapter 6.

4.10.1 Initial Sample Thickness

The initial sample thickness may be investigated by comparing the [4x6,1100,10] and [4x6,1100,30] samples from each starting thickness (e-f and o,q). The total $\Sigma 3^n$ fractions for these two samples are 65.8% and 64.6% for the 4.5mm samples, and 69.9% and 72.1% for the 8mm samples, showing a slight increase for the 8mm samples. However, the resolution of the EBSD scans was increased from 10μ per pixel to 5μ per pixel, and this allowed finer twin grains to be resolved. An increase in Σ3 fraction from 41.8% to 44.6% was also noticed in the as-received sample. This change in resolution could well explain the minor increases in special boundary fraction in the 8mm samples, and hence it was concluded that initial sample thickness is likely to have no significant effect.

The grain sizes of each sample were 137.4μ and 149.7μ for the 4.5mm samples, and 141.5μ and 190.9μ for the 8mm samples. This suggests that increasing the initial sample thickness, at least in this range, allowed the grains to grow larger in the centre of the sample. The reasons for this result are not currently known.

4.10.2 Deformation Percentage

Four different deformation percentages were used in this work (6%, 10%, 15%, 50%) at annealing temperatures between 1100°C and 1115°C. The 50% deformation produced no increase in $\Sigma 3^n$ boundary fraction and produced a microstructure very similar to that of the as-received sample, which is likely to have had a large deformation and anneal as part of its

prior processing. The 15% deformation level produced a small increase in $\Sigma 3^n$ boundary fraction but caused the grain size to decrease from approximately 150μ to 75-85μ. The 10% deformation level produced a GBE material (ie. increased $\Sigma 3^n$ fractions) with little effect on grain size, however the increases in $\Sigma 3^n$ boundary fraction were lower than those introduced by the lowest deformation (6%). Therefore, it may be concluded that the 6% deformation level is the most suitable to create a GBE material, within the range tested.

This conclusion is consistent with several studies in the literature, such as the work by Guyot and Richards [25], who tested 5% deformation and 20% deformation in commercially pure nickel, and found the 5% level to produce approximately 50% more special boundaries when annealed at 900°C. Similarly, Kokawa et al concluded that the optimum deformation percentage for creating a GBE 304 stainless steel was 5% [26]. This was also observed by Engelberg et al [27] for the same material, and by Li et al [28] in their study of Inconel 718. In general, strains higher than 20% have caused recrystallisation and not resulted in a GBE state [29].

4.10.3 Annealing Temperature

Four different annealing temperatures between 1075°C and 1150°C were used throughout the GBE processing. In general, it was found that the 1150°C treatment was higher than optimal and resulted in low $\Sigma 9/\Sigma 3$ ratios and large grain sizes. Incidentally, this is also the temperature used to promote grain growth in alloy 800H. The temperatures between 1075°C and 1115°C were all found to be suitable for increasing the special boundary fraction, and 1050°C was also found to be successful for this material by other authors [21]. However, in this work, a temperature of 1100°C was found to be optimal for both special boundary fraction and consistency in grain size. The expected trend of increasing grain size with increasing annealing temperature was also found.

4.10.4 Annealing Time

The effect of annealing time can be compared directly by considering the samples (o-q) in Figure 4.15 and Figure 4.16. The results show a slight increase in $\Sigma 3^n$ fraction with increasing annealing time, which is also noticeable in other samples (e.g. m-n and r-s). This trend has also been noted previously by Tan and Allen [21], who made the same conclusion based on annealing times up to 90 minutes. Li et al showed that the special boundary fraction increased slowly with annealing times up to 10 minutes, and then rapidly between 10 and 20 minutes after 6% strain in pure nickel [29]. Annealing times of longer than 20 minutes were shown to have no significant added effect, which is consistent with the present results in that increasing the annealing time from 30 to 90 minutes did not alter the $\Sigma 3^n$ boundary fraction. Again, the trend of increasing grain size with increasing annealing time was noted in all cases.

4.10.5 Summary

In summary of the GBE conditions tested, there appears to be a local maximum in $\Sigma 3^n$ boundary length fraction near the 6% deformation and 1100°C anneal conditions. Small deviations from these parameters, such as increasing the strain to 10%, or altering the annealing temperature in the range 1075-1115°C, are shown to still result in GBE, but with reduced $\Sigma 3^n$ fractions compared to the maximum. Possible reasons for this are investigated in Chapter 6, where the mechanism of GBE is examined in more detail.

4.11 Analysis of GBE Microstructure

It is useful at this point to make a comparison between a GBE microstructure and the as-received microstructure. Such a comparison is shown in Figure 4.17.

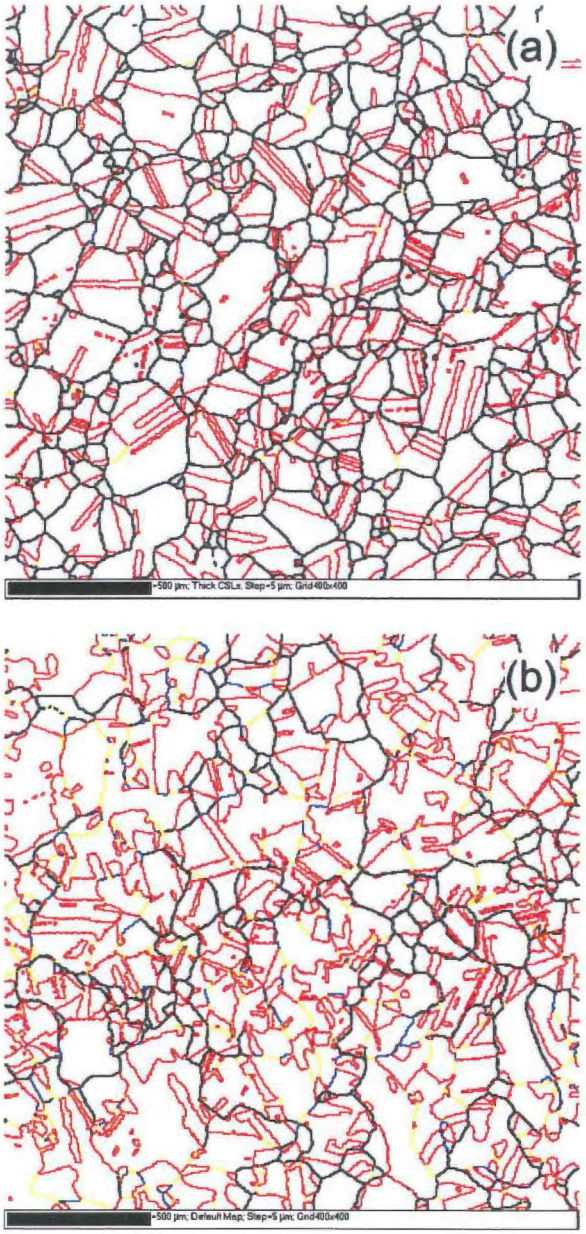

Figure 4.17 Comparison between (a) as-received and (b) GBE microstructures

There are several differences between these two microstructures. First, the relative fractions of the Σ3, Σ9 and Σ27 boundaries are all greater in the GBE structure, as calculated in the previous section. These large $\Sigma 3^n$ fractions are the most common feature associated with a GBE microstructure. Second, the morphology of the grain boundaries has changed significantly. From the relatively equiaxed grain structure of the as-received material, the grain structure has become much less defined. This is due to the fact that $\Sigma 3^n$ boundaries

have become incorporated into the GB network. To illustrate this, these EBSD maps have also been processed to show only the Σ3 boundaries, and the result is shown in Figure 4.18.

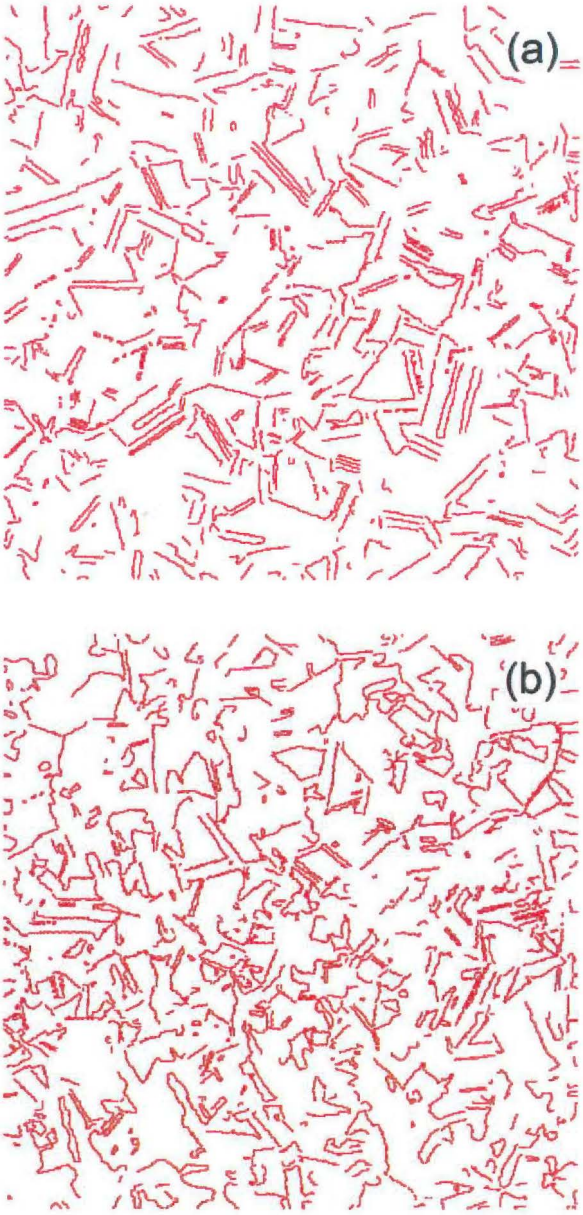

Figure 4.18 Comparison between (a) as-received and (b) GBE microstructures showing Σ3 boundaries

As mentioned previously, the vast majority of the Σ3 boundaries present in the as-received microstructure show the classic morphology of annealing twins, indicating that most of them are likely to be coherent. Although the GBE microstructure still contains a large proportion of linear Σ3s, many of which are likely to be coherent twins, it also contains a greatly

increased fraction of Σ3s which are not linear. This indicates that they are incoherent, and it is mainly these incoherent Σ3 boundaries which are thought to be responsible for breaking up the connected HAB network [30]. Many studies in the literature have indicated that incoherent Σ3s are introduced in the microstructure via GBE [8, 24, 31-32], which is consistent with the results achieved in this work.

4.12 Sample Texture

In order to compare the as-received and GBE conditions in creep tests, it was also necessary to determine the microtexture of each sample. It is well known that rolling and annealing a material may induce an annealing texture, or certain preferred crystallographic orientations. It is also known that texture can have an effect on creep rates, although it is thought to be more influential at high strain rates [33]. In order to determine the effect on texture from the GBE processing, the texture of two samples ([AR] and [4x6,1100,30]) was calculated. This was performed using the HKL software, based on six EBSD maps totalling 24mm^2, and the results are presented as inverse pole figures (IPF) in Figure 4.19. The rolling direction corresponds with the *z* direction as shown.

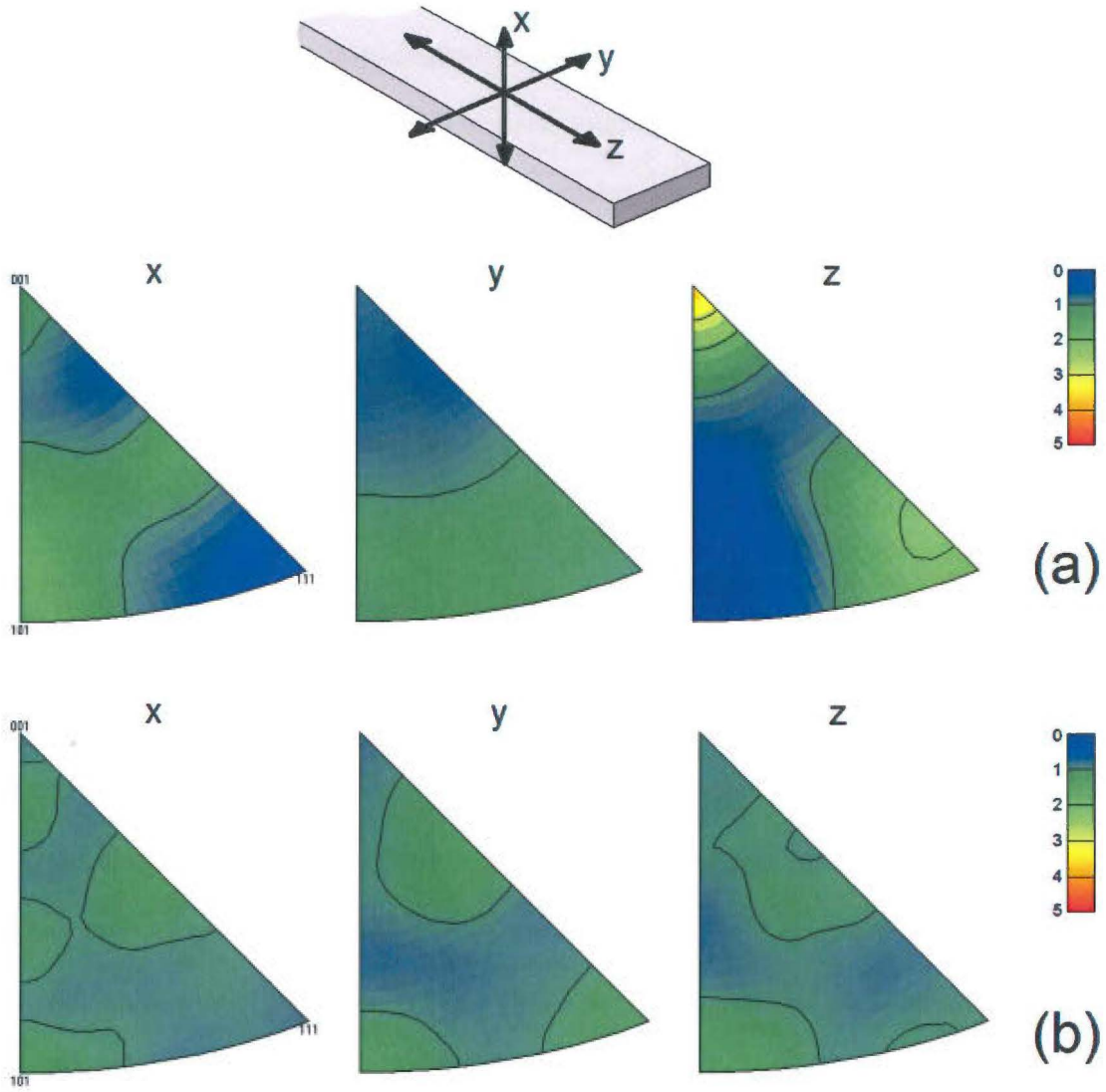

Figure 4.19 Comparison of microtexture between (a) as-received and (b) GBE samples

The previous working direction of the 800H plate is unknown, and therefore the way in which the as-received texture relates to its previous working also cannot be determined exactly. However, the major component is possibly the Goss orientation {110}/<100>, which is typically found in austenitic steels [34] and nickel [35]. This would suggest the working direction was consistent with the *z* direction as shown, and explain the pole at <001>||*z* and <101>||*x*. However, with a maximum multiple of uniform density (MUD) of less than four, the as-received texture can be classified as weak.

After the GBE processing, the texture becomes essentially random, showing a MUD of less than two. This has been reported several times in the literature [35-36], and is due to the fact that multiple twinning operations, such as those active during the GBE process, serve to weaken the texture [37].

Neither of the conditions shows significant texture, and combined with the extremely low strain-rates used for creep testing, the effect of microtexture was considered to be negligible in this work.

4.13 Conclusions

In conclusion, the majority of the combinations of GBE parameters tested were successful in increasing the length fraction of $\Sigma 3^n$ boundaries. The best conditions examined were four cycles of 6% deformation and 1100°C annealing for times between 10 and 30 minutes. The longer annealing times also resulted in small increases in twin-excluded grain size, however the twin-included grain size was reduced in all cases, consistent with the introduction of new $\Sigma 3$ boundaries.

The microstructure appears consistent with other GBE microstructures reported in the literature. In particular, the grain structure is difficult to define where random HABs are concerned, and the $\Sigma 3$ morphology has become much more convoluted, consistent with the introduction of incoherent $\Sigma 3$ boundaries. The microtexture has also evolved towards a uniform distribution.

Overall, the creation and analysis of a grain boundary engineered microstructure in alloy 800H was achieved successfully, as measured by $\Sigma 3^n$ boundary length fraction and $\Sigma 9/\Sigma 3$

ratio. Further analysis of the microstructure and its effects on mechanical and creep properties are described in the following chapters.

4.14 References

[1] Thyssenkrupp VDM Australia, *www.vdmaustralia.com.*

[2] Brandon, D. G., Ralph, B., Ranganathan, S., Wald, M. S., *A field ion microscope study of atomic configuration at grain boundaries*, Acta Metall. 12 (1964) 813-821.

[3] Rohrer, G. S., Randle, V., Kim, C.-S., Hu, Y., *Changes in the five-parameter grain boundary character distribution in alpha-brass brought about by iterative thermomechanical processing*, Acta Mater. 54 (2006) 4489-4502.

[4] Kumar, M., King, W., Schwartz, A. J., *Modifications to the microstructural topology in f.c.c. materials through thermomechanical processing*, Acta Mater. 48 (2000) 2081-2091.

[5] Randle, V., Davies, H., *Evolution of microstructure and properties in alpha-brass after iterative processing*, Metall. & Mater. Trans. A 33 (2002) 1853-1857.

[6] Coleman, M., Randle, V., *Changes in interface parameters and tensile properties in copper as a consequence of iterative processing*, Metall. & Mater. Trans. A 39 (2008) 2175-2183.

[7] ASTM, *E-112: Standard test methods for determining average grain size*, ASTM International, 1996.

[8] Randle, V., *Mechanism of twinning-induced grain boundary engineering in low stacking-fault energy materials*, Acta Mater. 47 (1999) 4187-4196.

[9] Vander Voort, G. F., *personal communication*, 2009.

[10] Randle, V., *A methodology for grain-boundary plane assessment by single-section trace analysis*, Scripta Mat. 44 (2001) 2789-2794.

[11] Saylor, D. M., El-Dasher, B. S., Adams, B. L., Rohrer, G. S., *Measuring the five-parameter grain boundary distribution from observations of planar sections*, Metall. & Mater. Trans. 35A (2004) 1981-1989.

[12] Randle, V., Davies, P., *Deviation from reference planes and reference misorientation for Σ3 boundaries*, Interface Sci. 7 (1999) 5-13.

[13] HKL Technologies, *HKL Channel 5 User Manual*, 2004.

[14] Pande, C. S., Rath, B. B., Imam, M. A., *Effect of annealing twins on Hall-Petch relation in polycrystalline materials*, Mat. Sci. & Eng. A 367 (2004) 171-175.

[15] Babyak, W. J., Rhines, F. N., *Relationship between boundary area and hardness of recrystallized cartridge brass*, Trans. AIME 218 (1960) 21-23.

[16] Pande, C. S., Imam, M. A., Rath, B. B., *Study of annealing twins in FCC metals and alloys*, Met. Trans. A 21 (1990) 2891-2896.

[17] Pestman, B. J., De Hasson, J., Vitek, T. M., Schaping, F. W., *Interaction between lattice dislocations and grain boundaries in FCC and ordered compounds: a computer simulation*, Phil. Mag. A 64 (1991) 951-969.

[18] Thaveeprungsriporn, V., Was, G.S., *The role of coincidence-site-lattice boundaries in creep of Ni-16Cr-9Fe at 360C*, Metall. and Mat. Trans. A 28A (1997) 2101-2112.

[19] Lu, L., Shen, Y., Chen, X., Qian, L., Lu, K., *Ultrahigh strength and high electrical conductivity in copper*, Science 304 (2004) 422-426.

[20] Randle, V., Coleman, M., *A study of low-strain and medium-strain grain boundary engineering*, Acta Mater. 57 (2009) 3410-3421.

[21] Tan, L., Allen, T. R., *An electron backscattered diffraction study of grain boundary-engineered INCOLOY alloy 800H*, Metall. & Mater. Trans. A 36A (2005) 1921-1925.

[22] Special Metals Corporation, *Technical Publication - Alloy 800H & 800HT*, 2004.

[23] Michiuchi, M., Kokawa, H., Wang, Z. J., Sato, Y. S., Sakai, K., *Twin-induced grain boundary engineering for 316 austenitic stainless steel*, Acta Mater. 54 (2006) 5179-5184.

[24] Randle, V., Jones, R., *Grain boundary plane distributions and single-step versus multiple-step grain boundary engineering*, Mat. Sci. & Eng. A 524 (2009) 134-142.

[25] Guyot, B. M., Richards, N. L., *A preliminary model to predict the special grain boundary fraction in commercial-purity nickel*, J. of Mat. Proc. Tech. 189 (2007) 162-168.

[26] Kokawa, H., Shimada, M., Michiuchi, M., Wang, Z. J., Sato, Y. S., *Arrest of weld-decay in 304 austenitic stainless steel by twin-induced grain boundary engineering*, Acta Mater. 55 (2007) 5401-5407.

[27] Engelberg, D. L., Newman, R. C., Marrow, T. J., *Effect of thermomechanical process history on grain boundary control in an austenitic stainless steel*, Scripta Mater. 59 (2008) 554-557.

[28] Li, Q., Guyot, B. M., Richards, N. L., *Effect of processing parameters on grain boundary modifications to alloy Inconel 718*, Mat. Sci. & Eng. A 458 (2007) 58-66.

[29] Li, Q., Cahoon, J. R., Richards, N. L., *Effects of thermo-mechanical processing parameters on the special boundary configurations of commercially pure nickel*, Mat. Sci. & Eng. A 527 (2009) 263-271.

[30] Wang, W. G., Guo, H., *Effects of thermo-mechanical iterations on the grain boundary character distribution of Pb-Ca-Sn-Al alloy*, Mat. Sci. & Eng. A 445 (2007) 155-162.

[31] Kumar, M., Schwartz, A. J., King, W. E., *Microstructural evolution during grain boundary engineering of low to medium stacking fault energy fcc materials*, Acta Mater. 50 (2002) 2599-2612.

[32] Fang, X., Zhang, K., Guo, H., Wang, W., Zhou, B., *Twin-induced grain boundary engineering in 304 stainless steel*, Mat. Sci. & Eng. A 487 (2008) 7-13.

[33] Estrin, Y., Heilmaier, M., Drew, G., *Creep properties of an oxide dispersion strengthened nickel-base alloy: the effect of grain orientation and grain aspect ratio*, Mat. Sci. & Eng. A 272 (1999) 163-173.

[34] Chowdhury, S. G., Singh, R., *The influence of recrystallized structure and texture on the sensitization behaviour of a stable austenitic stainless steel (AISI 316L)*, Scripta Mater. 58 (2008) 1102-1105.

[35] Horton, D., Thomson, C. B., Randle, V., *Aspects of twinning and grain growth in high purity and commercially pure nickel*, Mat. Sci. & Eng. A A203 (1995) 408-414.

[36] Kowalska, J., Ratuszek, W., Chrusciel, K., *Texture and microstructure of annealed AISI302 steel wires*, Arch. of Metall. and Mat. 53 (2008) 131-137.

[37] Wilbrandt, P. J., *Recrystallization texture in terms of multiple twinning*, Phys. Stat. Solidi 61A (1980) 411-418.

CHAPTER 5: MODELLING GRAIN BOUNDARY CONNECTIVITY

5.1 Introduction

One way in which grain boundary engineering is thought to improve material properties is by the break-up of the connected random high-angle boundary (HAB) network, through the introduction of low-energy boundary segments. Ultimately, grain boundary connectivity exists in three-dimensions, though the difficulty of data collection in three dimensions has so far prevented such analyses within the GBE field. Instead, trends must be extracted from planar microstructures (i.e. two-dimensions) and then extrapolated (at least qualitatively) to the three-dimensional case. Although this is undoubtedly a compromise, the extrapolation is to the three-dimensional case is not unreasonable, due to the isotropy of GBE materials. Such models exist for the quantification of the grain boundary network connectivity from two-dimensional microstructures, however all of the current models have limitations on their accuracy or use.

The purpose of this chapter is to discuss an alternative method for analysing GBE materials, by modelling the connectivity of the grain boundary network directly from EBSD maps. The grain boundary connectivity has been emphasised as important throughout the literature, and several attempts have been made to quantify it through microstructural analysis. These attempts are examined and compared in this chapter. A new method of grain boundary analysis has been designed and utilised in this work, which offers advantages over the existing models. This model is presented and discussed, followed by the analysis of the GBE microstructures examined in Chapter 4 using this new method. The model allows the degree

of special boundary incorporation to be quantified and hence the various thermomechanical processing routes are compared in terms of this new parameter.

5.2 Importance of Grain Boundary Connectivity

One of the aims of grain boundary engineering is the disruption of the grain boundary network through the introduction of boundary segments which exhibit improved properties. Certain damage mechanisms such as intergranular stress corrosion, cracking, and Coble creep (which is of high importance in this study) rely on the grain boundary network as a connected "pathway". In these cases, it is the geometry and connectivity of this pathway which controls the rate of damage. Increasing the fraction of damage-resistant, or special, boundaries is a necessary condition to improve the resistance of material to such attack, however it is not a sufficient criterion in itself. On this basis, designing a measure of grain boundary connectivity has become increasingly important in the GBE field. Several attempts have been made to make such quantifications, as will be described in the following section.

5.3 Existing Methods for Analysing Grain Boundary Connectivity

5.3.1 Neutral-Twin Concept

Although the neutral twin concept proposed by Lehockey et al [1] is not directly a measure of grain boundary connectivity, it was probably the first study in which it was attempted to divide the Σ3 group into two groups: those which disrupted the random HAB network, and those which did not. The calculation of special boundary fraction subsequently excluded those Σ3 boundaries which were not expected to disrupt the GB network. These boundaries were termed "neutral twins".

The neutral twins were not classified individually, but rather their fraction was estimated based on the fractions of the twin-variants Σ9 and Σ27, and the geometrical constraints imposed at triple junctions. The equation for effective special boundary fraction was given as:

$$f_{sp}^{eff} = f_{\Sigma 1} + f_{\Sigma 3}^{eff} + f_{3<\Sigma<29}\,, \tag{5.1}$$

where $f_{\Sigma 3}^{eff}$ was considered the effective fraction of Σ3 boundaries (i.e. excluding neutral twins), and was calculated according to the equation:

$$f_{\Sigma 3}^{eff} = -\frac{f_{\Sigma 27}+f_{\Sigma 9}}{2} \pm \sqrt{\left(\frac{f_{\Sigma 27}+f_{\Sigma 9}}{2}\right)^2 - 2(f_{\Sigma 1}f_{\Sigma 9} + f_{\Sigma 1}f_{\Sigma 27} - f_{\Sigma 27} - f_{\Sigma 9})} \tag{5.2}$$

In the analysis of the concept, the authors showed a very good correlation between the fraction of effective special boundaries and the depth of intergranular stress-corrosion cracking (IGSCC) measured in ex-service Alloy 600 steam generator tubing. The correlation with total special boundary fraction was found to be very poor. Similar results were also obtained with brass, a material which exhibits a high fraction of twin boundaries. Four-fifths of these twin boundaries in brass were estimated to be neutral, and the intergranular stress corrosion cracking (IGSCC) depth measurements showed much better correlation when these neutral twins were excluded.

The concept of excluding boundaries which do not disrupt the random HAB network is certainly useful for grain boundary-based mechanisms such as IGSCC, which is analysed in this work. The main limitation of the analysis is the way in which these boundaries are identified. Very generally, a Σ3 is considered effective in this study if it results in Σ9s and Σ27s being introduced into the network. However, such boundaries may not necessarily break up the existing HAB network. Consider an example from an 800H EBSD map, shown in Figure 5.1.

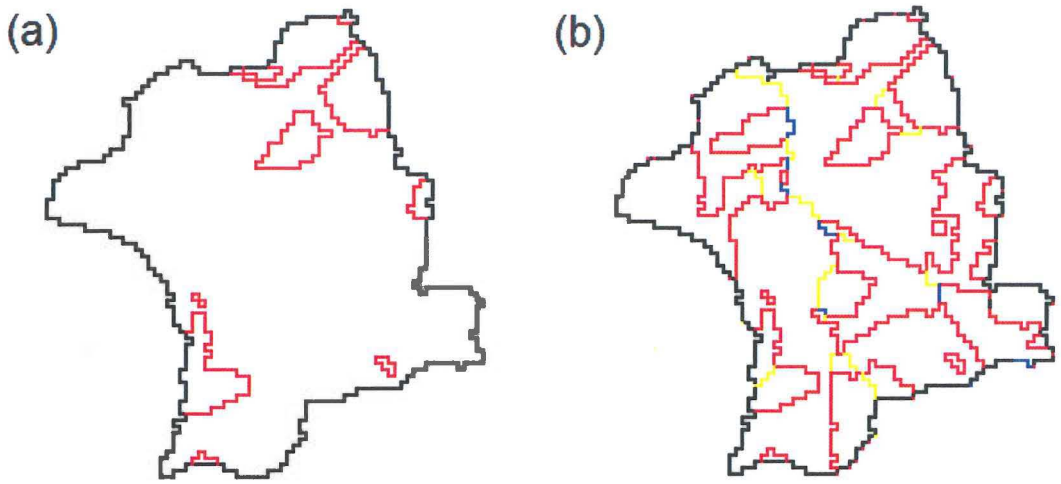

Figure 5.1 Portion of EBSD map showing (a) an area with most twin-related boundaries removed and (b) original map with twin-related boundaries included

The figure shows a comparison between an area where most of the twin-related boundaries have been manually removed by image processing (while still ensuring geometric constraints are met at triple junctions, and therefore the data represent an entirely realistic microstructure) (Figure 5.1a), to the original area, as mapped (Figure 5.1b). In these figures, Σ3s are shown in red, Σ9s in yellow, Σ27s in blue and HABs in black. It is clear from Equation 5.2 that the microstructure in (b) will contain a greater fraction of effective twins than that of (a), and therefore the neutral-twin model will predict improved properties. Importantly however, the extra $\Sigma 3^n$ boundaries present in (b) do not actually disrupt the original HAB network (the black outline). Provided this HAB network remains intact (ie. it is not disrupted by $\Sigma 3^n$ boundaries), it is reasonable to expect that the grain boundary-based properties will be very similar, as the special boundaries become somewhat irrelevant. One may argue that by introducing new Σ9 and Σ27 boundaries, the grain boundary network has been altered to include these boundaries and hence it may be disrupted by segments of Σ3. Although this statement is valid, the microstructure in (b) is still unlikely to show any property improvements compared with the microstructure which contains no Σ9 and Σ27

boundaries, and hence property correlations become somewhat difficult. Such a model requires a more detailed determination of which boundaries actually are expected to confer improved material properties, which is a limitation of this analysis method.

5.3.2 Triple Junction Geometry

The analysis of triple junctions in a GBE material was proposed by Kumar et al [2], and involves assigning each triple junction a category based on the number of low-Σ CSL boundaries which meet at each triple junction. Kumar used the terms 0,1,2 or 3-CSL to describe triple junctions adjoining zero, one, two or three special boundaries respectively. The aim of the analysis was to "quantify the effects of the improvement in the grain boundary character distribution (GBCD) on the spatial connectivity of the grain boundaries". In other words, the study provided a way to compare the boundary connectivity of different samples (in two-dimensions) on numerical grounds.

The authors showed that as a result of GBE, the relative fraction of triple junctions containing zero special boundaries (i.e. three random HABs) decreased sharply, and that the fraction containing three special boundaries increases as a result of processing. Results from GBE copper are reproduced in Figure 5.2, showing the triple junction distribution (TJD) as a function of processing cycle.

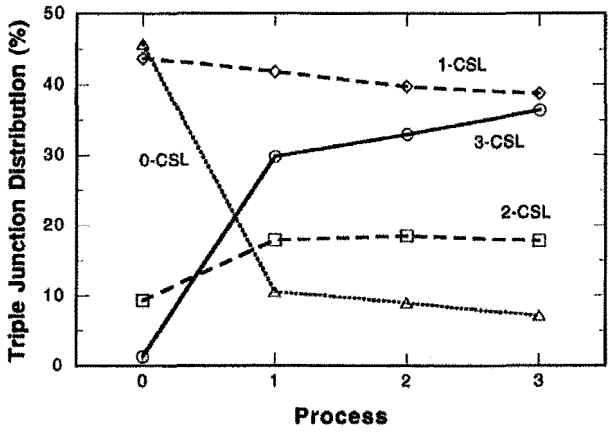

Figure 5.2 Triple junction distribution for GBE Cu, reproduced from [2]

It was also noted that the distribution did not match a random distribution. This was explained using the crystallographic constraints at each junction, which state that the Σ-values of adjoining boundaries must follow the rule [3]:

$$\Sigma_{CA} = \Sigma_{AB}\Sigma_{BC}/d^2 \tag{5.3}$$

where d is a common divisor of Σ_{AB} and Σ_{BC}.

The triple junction distribution was determined in some other studies [4-5] in the same way, and an increase in the fraction of 3-CSL junctions (and decrease in the fraction of 0-CSL junctions) was generally said to be correlated with the increased disruption of the HAB network. However, such an analysis is flawed. Consider again the EBSD maps shown previously in Figure 5.1. The map on the right (Figure 5.1(b)) has a of 3-CSL fraction of 0.48, whereas the map on the left (Figure 5.1(a)) has no 3-CSL junctions. According to the triple junction analysis [2, 4-5] therefore, the microstructure in (b) is more disrupted than the microstructure in (a). However, if one considers grain boundary diffusion for example, it is expected that the microstructure in (b) will not be better than that of (a), because the original HABs remain. In fact, the extra paths within the twin-related domain are effectively acting as

parallel paths, and may actually increase the diffusivity of the network. Therefore, the triple junction analysis also fails to distinguish special boundaries which are incorporated into the original GB network from those which are located entirely within random high-angle grain boundaries, which is the major limitation of this analysis method.

5.3.3 Percolation Theory

Percolation theory has an interesting application to a grain boundary engineering network and has been reported several times in the literature in conjunction with GBE experiments [2, 6-10]. In one application, it has been used to estimate the fraction of random boundaries required in simulated microstructures to achieve percolation behaviour (ie. to ensure an infinitely connected path of random boundaries). The general consensus seems to be approximately 0.65 number fraction [9, 11-12].

The second application, and the one directly related to GB connectivity measurements, is also known as cluster analysis, and involves assigning the interconnected clusters of each boundary type (binary classification is used exclusively based on low-Σ CSL criterion) a "mass" based on the combined total length of grain boundary which is self-connected (ie. part of a cluster). For example, a study of annealed René 41 [10] showed that over 95% of the random HABs were in clusters larger than 500 grain diameters. This percentage was then reduced to zero in the GBE microstructures, indicating that the percolating network of HABs was disrupted by the GBE process. This method is a much more direct measure of grain boundary connectivity than the previous two described.

Percolation theory has also shown correlation with material properties by extracting a parameter such as mean free path, which shows correlation with intergranular damage [5]. However, such a correlation remains an indirect measure of material properties, which is a

slight limitation of this analysis type. A more significant limitation of cluster analysis was pointed out by Chen and Schuh [9] in the case of diffusion-controlled properties, and involves the treatment of what are termed "dangling branches". An example of this is shown in Figure 5.3.

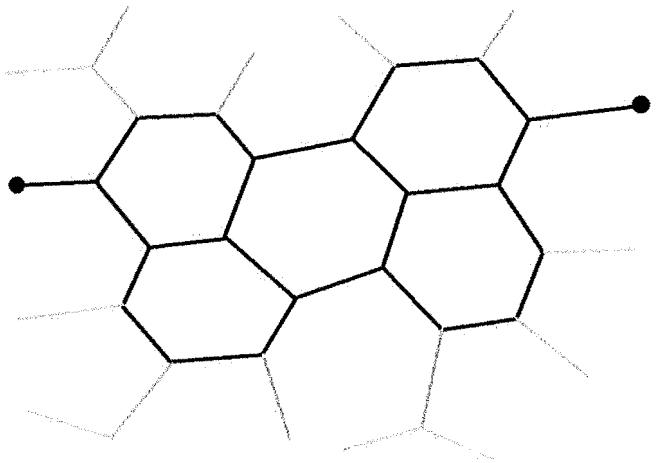

Figure 5.3 Example of dangling branches in cluster analysis showing the fast-diffusion pathway in black, and dangling branches in grey

The figure shows a simulated grain boundary network adjoining two points. The fast-diffusion pathway is coloured black and comprises the backbone of the cluster. This backbone ultimately controls the rate of grain boundary transport. However, the dangling branches of the network, indicated in grey, form part of the cluster and therefore count towards the cluster mass, despite the fact that they are non-contributing to the diffusional properties of the network. This situation ultimately leads to discrepancies when attempting to correlate with such properties. Therefore, although this method is useful in quantifying grain boundary connectivity, it loses some its usefulness in a situation such as the present study into the diffusion-controlled regime of Coble creep.

5.4 Requirements for a New Model

As investigated in the previous section, existing models for connectivity analysis have limitations in how they can predict material properties. Therefore, it was proposed that a new method be created for the purposes of this work. The requirements of such a model are listed below:

- The model must be able to used in the analysis of actual grain boundary networks, as derived from EBSD mapping
- The model must be able to determine which boundaries are expected to contribute to improved material properties, through both grain boundary structure and boundary topology
- The model must be able to be linked directly to material properties (ideally to creep, which is relevant for the case of reformer pigtails)
- The model must incorporate a binary classification of grain boundaries (e.g. special/non-special), but ideally has the ability for this classification to be refined further
- The model should be able to determine the extent of grain boundary engineering, and compare samples of differing thermomechanical history

5.5 A New Method for Connectivity Analysis

Based on these requirements, a method of grain boundary connectivity analysis was created which incorporates all of the design elements. This method is discussed in the following paragraphs.

5.5.1 Description of Method

Coble creep, which is likely to be a significant contributor to the creep rate of pigtail tubes, involves the transport of matter throughout the grain boundary network. Further details regarding this mechanism are provided in Chapter 8, however it is useful to consider the grain boundary diffusion dependence of this creep mechanism [13], where d represents the (twin-excluded) average grain size:

$$\dot{\gamma} \propto {}^{D_b}/_{d^3} \tag{5.4}$$

The grain boundary diffusivity term, D_b, is intended as a single constant suitable for describing the average grain boundary diffusivity. However, with the development of GBE, the topology of the GB network is also able to be significantly altered, which also has an effect on the diffusivity of the material, in that high diffusivity paths may be disrupted by low-diffusivity segments of boundary. The effect of boundary topology therefore needs to be incorporated into the rate equation when GBE materials are considered.

This was achieved by considering the grain boundary diffusion rate of a finite two-dimensional section of microstructure. By treating each grain boundary segment as a "resistor" to diffusion, the two-dimensional network becomes perfectly analogous to an electric circuit with a complex geometry of resistors [14]. In the electrical analogy, the mass flow rate, J, becomes analogous to the current flow, i, and the concentration gradient, C, is analogous to the voltage, V.

It should be noted at this point that such an analysis has been performed previously by Chen and Schuh [9]. However, the microstructures used in that study were simulated, made up of perfect hexagons in a grid pattern where the fraction of special boundaries could be adjusted to simulate various degrees of grain boundary engineering. The major difference between

the analysis performed by Chen and Schuh, and the analysis presented here, is that in the present case, the microstructures being analysed are real microstructures, digitised by EBSD analysis. This is believed to be the first time such an analysis has been carried out.

In this work, 24 EBSD maps measuring 1mm x 1mm were examined. The digitised images were used to construct a network or resistors with the aim of determining the effective resistivity of a standard section of microstructure. An analogous "voltage", V^+, was applied to any resistors which terminated at the left-hand side of the image, and the set of terminating nodes on the right were assigned voltage zero. The (diffusion) resistance of a grain boundary segment (or resistor) j is given by equation 5.5:

$$R_j = l_j \rho_j \tag{5.5}$$

where l_j is the length of the boundary segment, and ρ_j is the resistivity. The resistivity is determined solely by grain boundary character, and is classified as either $\rho_{(\Sigma 3^n)}$ or $\rho_{(HAB)}$ according to a binary system. A study in 2003 of an austenitic Ni-16Cr-9Fe alloy [15] concluded that, on average, the low-Σ (Σ<29) grain boundary diffusion coefficient was approximately 12x lower than that of the HABs. In the 2003 study, the low-Σ network consisted primarily of Σ3s, as do the present microstructures. Therefore, the resistivity ratio of $\frac{\rho_{(\Sigma 3^n)}}{\rho_{(HAB)}} = 12$ was also used in this analysis, although it is recognised that there is potential for further refinement of the model to include information based on boundary type and boundary plane configurations.

At any internal node, j, Kirchhoff's Current Law (KCL) states that the sum of currents flowing into the node is equal to the sum of the currents flowing out of the node (the analogy in the diffusion case is conservation of mass). This can be rewritten as equation 5.6.

$$\sum_k a_{jk} i_k = 0 \tag{5.6}$$

where $a_{jk} = \pm 1$ for resistors transporting current to/from the node, j, and $a_{jk} = 0$ for all others. This provides n linearly independent equations, where n is the total number of internal nodes in the network.

Assuming there are m resistors in the network, a further $n - m$ equations are therefore required in order to solve the system. These equations arise from Kirchhoff's Voltage Law (KVL), which states that the total voltage drop across any path connecting two nodes must be equal to the voltage difference between them (the same statements holds true if one considers the concentration in the diffusion case). Applying KVL combined with Ohm's Law yields equations of the form:

$$\sum_k c_{jk} R_k i_k = V^+ \tag{5.7}$$

where $c_{jk} = 1$ for resistors in the j^{th} path and $c_{jk} = 0$ for all others. In this case, paths were determined from the left hand edge of the image to the right hand edge of the image, meaning the voltage drop is equal to the applied voltage, V^+.

These two equations (5.5 and 5.6) completely describe the system, and therefore the current in each path was solved according to the matrix equation:

$$\boldsymbol{A}\boldsymbol{i} = \boldsymbol{b} \tag{5.8}$$

where $\boldsymbol{A}$ is the $m \times m$ matrix of coefficients, $\boldsymbol{i}$ is the $m \times 1$ vector of currents, and $\boldsymbol{b}$ is an $m \times 1$ vector. The net current flow, i_{net}, is simply a sum of the current flowing from the left hand side of the image, or alternatively, the sum of the current flowing into the right hand side. The effective resistance of the network is termed R_{eff}, and is calculated according to equation 5.9:

$$R_{eff} = \frac{V^+}{i_{net}} \tag{5.9}$$

As the resistance of a unit length of grain boundary must be arbitrarily chosen, the absolute value of R_{eff} is meaningless. However, the ratio of R_{eff} for a GBE sample to R_{eff} for a non-GBE sample represents an excellent way of comparing the two microstructures in terms of two-dimensional grain boundary connectivity. This ratio has been denoted $\bar{R}_{eff}$, and the results of the analysis in Section 5.6 are presented using this ratio.

5.5.2 Normalisation of Grain Size

The effective resistance determined in this way is not only dependent on the two-dimensional topology of the grain boundary network, but also on the grain size of a fixed unit area. While this is not a problem when attempting to correlate with material properties (i.e. grain boundary diffusion is dependent on the grain size anyway), it is desirable in this analysis to isolate the effect of changes in boundary topology through the use of normalisation. An example of the grain size dependence of R_{eff} is shown in Figure 5.4 for two honeycomb lattices.

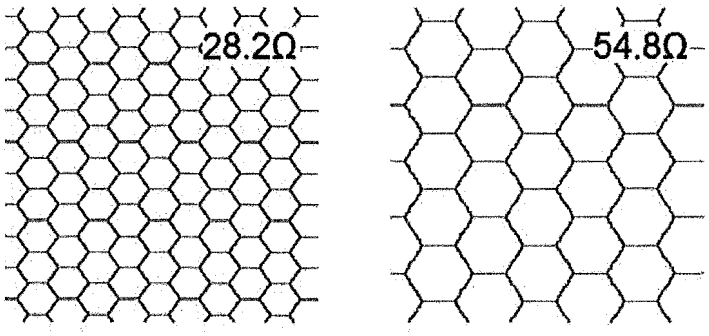

Figure 5.4 Dependence of $\boldsymbol{R_{eff}}$ on grain size for two example honeycomb lattices

The reason for this dependence is that for a fixed area, increasing the grain size results in fewer parallel paths, which therefore increases $\boldsymbol{R_{eff}}$. However, for a self-similar

microstructure such as those pictured in Figure 5.4, there exists an exact analytical solution which describes this dependence, and therefore may be used to decouple the effect of grain size, leaving only the effect of topological differences.

Consider a network of resistors arranged in a hexagonal grid, as shown in Figure 5.5(a).

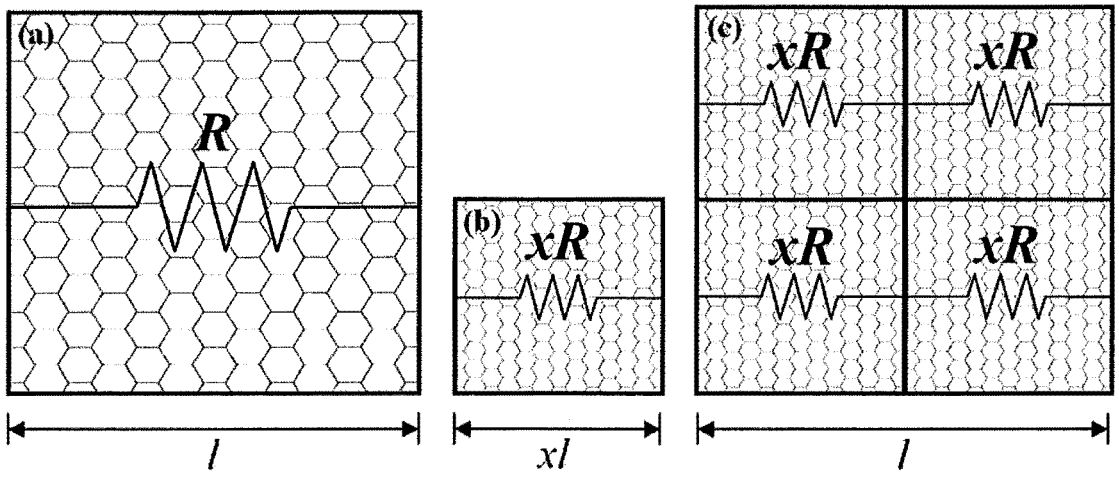

Figure 5.5 Honeycomb microstructure showing (a) initial microstructure, (b) initial microstructure scaled by factor x (0.5 as shown), (c) scaled microstructure repeated to restore initial geometry

Recall from equation **5.8** that the matrix equation is in the form $\boldsymbol{i} = \boldsymbol{A}^{-1}\boldsymbol{b}$, and that $\boldsymbol{A}$ and $\boldsymbol{b}$ consist of some equations from Kirchhoff's Current Law, and some from Kirchhoff's Voltage Law, as shown:

$$\boldsymbol{A} = \begin{bmatrix} a_{jk} & a_{jk} & \cdots & a_{jk} \\ a_{jk} & a_{jk} & \cdots & a_{jk} \\ \vdots & \vdots & \vdots & \vdots \\ c_{jk}R_k & c_{jk}R_k & \cdots & c_{jk}R_k \\ c_{jk}R_k & c_{jk}R_k & \cdots & c_{jk}R_k \end{bmatrix}, \quad \boldsymbol{b} = \begin{bmatrix} 0 \\ 0 \\ \vdots \\ V^+ \\ V^+ \end{bmatrix} \tag{5.10}$$

Scaling the microstructure in Figure 5.5(a) by a factor x results in a microstructure shown in Figure 5.5(b). The resistance of each boundary segment is therefore reduced linearly according to equation 5.5. Denoting the scaled versions of $\boldsymbol{A}$, $\boldsymbol{i}$, and $\boldsymbol{b}$ as $\boldsymbol{A_x}$, $\boldsymbol{i_x}$, and $\boldsymbol{b_x}$ and adjusting the resistances by the factor x leads to the equation:

$$\begin{bmatrix} a_{jk} & a_{jk} & \dots & a_{jk} \\ a_{jk} & a_{jk} & \dots & a_{jk} \\ \vdots & \vdots & \vdots & \vdots \\ c_{jk}xR_k & c_{jk}xR_k & \dots & c_{jk}xR_k \\ c_{jk}xR_k & c_{jk}xR_k & \dots & c_{jk}xR_k \end{bmatrix}_x \begin{bmatrix} i_k \\ i_k \\ \vdots \\ i_k \\ i_k \end{bmatrix}_x = \begin{bmatrix} 0 \\ 0 \\ \vdots \\ V^+ \\ V^+ \end{bmatrix}_x \tag{5.11}$$

Note that the first n rows of $\boldsymbol{A_x}$ (the KCL equations) may also be freely multiplied by the non-zero scale factor x without affecting the solution of the matrix equation. Hence equation 5.11 may also be written as:

$$\begin{bmatrix} xa_{jk} & xa_{jk} & \dots & x\,a_{jk} \\ xa_{jk} & xa_{jk} & \dots & xa_{jk} \\ \vdots & \vdots & \vdots & \vdots \\ c_{jk}xR_k & c_{jk}xR_k & \dots & c_{jk}xR_k \\ c_{jk}xR_k & c_{jk}xR_k & \dots & c_{jk}xR_k \end{bmatrix}_x \begin{bmatrix} i_k \\ i_k \\ \vdots \\ i_k \\ i_k \end{bmatrix}_x = \begin{bmatrix} 0 \\ 0 \\ \vdots \\ V^+ \\ V^+ \end{bmatrix}_x \tag{5.12}$$

Because x is a constant, it can therefore be factored out of $\boldsymbol{A_x}$, leading to the equation:

$$x \begin{bmatrix} a_{jk} & a_{jk} & \dots & a_{jk} \\ a_{jk} & a_{jk} & \dots & a_{jk} \\ \vdots & \vdots & \vdots & \vdots \\ c_{jk}R_k & c_{jk}R_k & \dots & c_{jk}xR_k \\ c_{jk}R_k & c_{jk}R_k & \dots & c_{jk}xR_k \end{bmatrix}_x \begin{bmatrix} i_k \\ i_k \\ \vdots \\ i_k \\ i_k \end{bmatrix}_x = \begin{bmatrix} 0 \\ 0 \\ \vdots \\ V^+ \\ V^+ \end{bmatrix}_x \tag{5.13}$$

Comparing $\boldsymbol{A_x}$ from equation 5.13 to the original $\boldsymbol{A}$ from equation 5.10 therefore gives the relation:

$$\boldsymbol{A_x} = x\boldsymbol{A} \tag{5.14}$$

Therefore, it follows that the effective resistance of the scaled microstructure, $R_{eff,x}$ is related to the effective resistance of the original microstructure, R_{eff}, according to the equation:

$$\frac{R_{eff,x}}{R_{eff}} = x \tag{5.15}$$

This result shows that scaling the microstructure by a factor x causes the effective resistance of the new microstructure, $R_{eff,x}$, to be scaled linearly by the same factor. In order to then calculate the resistance per unit cross sectional length for square images, the effective resistances in the scaled hexagonal grid must be repeated $1/x$ times in both the vertical and

horizontal directions to fill the same space as the original network of resistors (as shown in Figure 5.5(c)).

This construction corresponds to a circuit with $1/x$ resistors in parallel, where each of those resistors corresponds to a series arrangement of resistors, each with resistance $R_{eff,x} = xR_{eff}$. Due to its symmetry, it does not make a difference whether the paths are also connected vertically or not, as there is no voltage difference between two paths in vertical alignment. Hence, there would be no current flow if such a path was introduced. The effective resistance of the construction in Figure 5.5(c) is denoted $R_{eff,total}$, and is calculated according to the combination of resistors in parallel:

$$R_{eff,total} = \left[\left(\frac{1}{x}\right)\frac{1}{\left(\frac{1}{x}\right)xR_{eff}}\right]^{-1} = xR_{eff} \tag{5.16}$$

This equation shows that for a honeycomb grid, altering the grain size by a factor x results in the effective resistance of a unit area also being multiplied by x. Therefore, to decouple the effect of grain size when comparing two samples, the effective resistance of second sample is multiplied by $1/x$, where x is the ratio of the grain size between the two. This normalisation effectively isolates the effect of differences in grain boundary topology, and therefore allows the comparison of samples with differing grain sizes, as per the requirements of the model.

The relationship obtained in equation 5.16 was also confirmed for the case of honeycomb lattices by digitising a number of these lattices and analysing them according to the model described in Section 5.5.1. The results are shown in Figure 5.6.

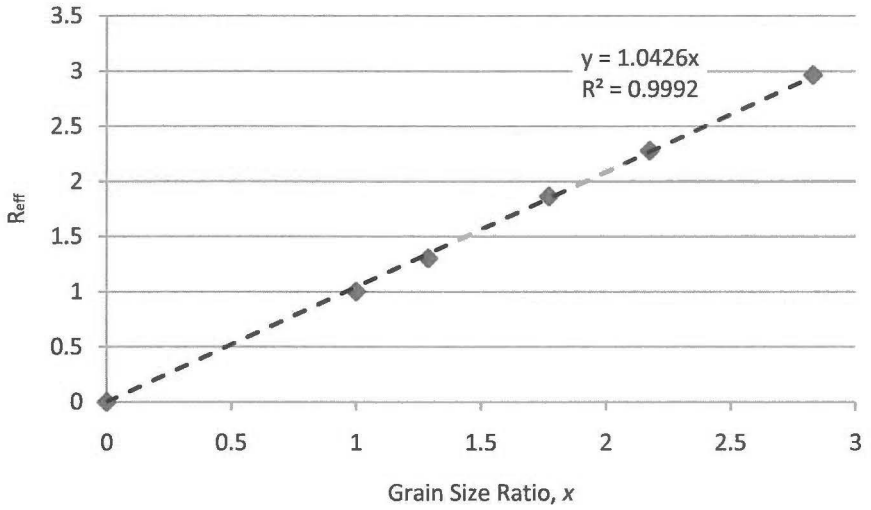

Figure 5.6 Modelled relationship between R_{eff} and grain size for honeycomb lattices

The results show a correlation with grain size ratio, x, that is very close to the $y = x$ relationship predicted by equation 5.16, and therefore confirm that this relationship is correct. The extremely small deviations from the analytical solution are likely to be due to the effects of digitising the images, and the truncation effects associated with the edges of the image.

In the present analysis, the twin-excluded grain size is considered for normalisation, as opposed to the twin-included grain size. The justification is that in a parallel system, it is the low-resistance boundaries which dominate the resistance of the network. For example, for the resistivity ratio $\rho_{\Sigma 3^n}/\rho_{HAB} = 12$, adding a similar $\Sigma 3^n$ boundary in parallel with an HAB will decrease the resistance of the system by approximately 7.7%. Adding a similar HAB will decrease the resistance of the system by 50%.

5.5.3 Model Benefits/Limitations

The main benefit of the analysis technique presented in this work is that it is directly linked to material properties (ie. grain boundary diffusion). It does not suffer from the limitations of

the models presented in Section 5.3, in that special boundaries are only considered beneficial provided they are incorporated into the random HAB network. If special boundaries only exist within twin-related domains inside the original HAB framework, they do not contribute to diffusional resistance, and therefore they are not counted as beneficial in this model (in fact, they are considered to be slightly detrimental as they offer parallel paths). The comparison of the four models presented can be summarised by Table 5.1, in which the outcome of each model for the case in Figure 5.1 is qualitatively compared with the predicted result from Fick's first law and mass balance requirements (ie. that diffusion occurs in the direction of high-to-low concentration gradient, and no mass accumulates at triple junctions).

Table 5.1 Summary of models for the case found in Figure 5.1

Model Type	**Parameter Analysed**	**Comparison of Figure 5.1(b) with Figure 5.1(a) and Diffusion Rate Predictions**
Neutral Twin Model [1]	Special boundary fraction excluding neutral twins	(b) has a higher fraction of effective special boundaries than (a), and therefore would exhibit a lower diffusion rate
Triple Junction Distribution [2]	Number fraction of triple junctions with 0,1,2 and 3 CSL boundaries	(b) has a higher fraction of 3-CSL triple junctions and a lower fraction of 0-CSL triple junctions, and therefore would exhibit a lower diffusion rate
Percolation Theory [6]	"Mass" of connected HAB clusters	The HAB cluster is of equal mass in (a) and (b), and therefore both microstructures would exhibit equal diffusion properties
Effective Resistance Model	Grain boundary diffusion in a unit area of microstructure	The microstructure in (b) contains the original HAB network from (a), plus several other low-diffusivity parallel paths. Therefore, the diffusion rate in (b) would be slightly greater than (a).
Diffusion Theory	*Grain boundary diffusion*	*The diffusion rate of (b) cannot be less than that of (a), as the microstructure contains the original HAB network, plus the additional parallel paths. Therefore, the diffusion rate in (b) must be greater than (a). The magnitude of the difference is dependent on the ratio of diffusivity between special and general boundaries.*

From this table, it is clear that both the neutral twin model and the triple junction distribution model predict reduced grain boundary diffusion properties for the microstructure in Figure 5.1(b), as compared to (a). In fact, the situation must be reversed, as the additional special boundaries in (b) are not actually incorporated into the original HAB network. Percolation theory is the best of the three existing connectivity models in this situation, predicting equal diffusion rates between (a) and (b). However, the microstructure (Figure 5.1(b)) contains no dangling branches. If dangling branches were present, further inaccuracies would be introduced. Therefore, the major benefit of the effective resistance model proposed in this work is the ability to automatically distinguish whether special boundaries are incorporated into the network or not. In the case of grain boundary diffusion and its related damage mechanisms (eg. Coble creep), this is a vital point when property correlations are required. The effective resistance model also inherently has the ability to compare boundary topology between different samples in terms of a direct material property. Therefore, it was used to analyse the GBE samples presented in Chapter 4 as a measure of the level of grain boundary engineering.

The limitations of the present model are consistent with limitations of the existing models. First, the classification of grain boundaries into special and non-special masks a wide range of boundary properties [16]. However, extracting boundary plane information for a large enough data set is currently unfeasible due to the inherent inaccuracies and time required for a method such as serial sectioning. Should the extraction of boundary plane information become feasible in the future, the model is equipped to deal with an almost infinite number of different boundary classifications and associated properties. Currently though, it is necessary to classify boundaries according to their geometry (such as low-Σ etc.) as an indirect predictor of boundary properties.

The other limitation of this model is the fact that it is based on two-dimensional sections, and therefore does not describe connectivity in three dimensions. Differences between GBE and non-GBE materials in three-dimensions must therefore be inferred from the two-dimensional differences, as with the previous models described. However, the determination that a low-energy boundary forms part of the GB network, as is possible with the present model, is perfectly valid in three dimensions and will also serve to increase the resistance to GB diffusion. Therefore, it is assumed that the three-dimensional case and the two-dimensional case are correlated.

5.6 Results and Discussion

Eight samples were chosen to be analysed for grain boundary connectivity, comprising two deformation levels (6%, 10%), two annealing temperatures (1100°C, 1150°C), and three annealing times (10, 20, 30 mins). The selected samples are shown in Table 5.2. The aim of the analysis was to use the connectivity parameter as a measure of how disrupted the random HAB network was in each case.

Table 5.2 Samples selected for GB connectivity analysis

Sample Label	Number of Cycles	Deformation per cycle	Annealing Temperature	Annealing Time
[AS RECEIVED]	-	-	-	-
[4x6,1100,10]	4	6%	1100°C	10 min
[4x6,1100,20]	4	6%	1100°C	20 min
[4x6,1100,30]	4	6%	1100°C	30 min
[4x6,1150,10]	4	6%	1150°C	10 min
[4x6,1150,30]	4	6%	1150°C	30 min
[4x10,1100,20]	4	10%	1100°C	20 min
[4x10,1100,30]	4	10%	1100°C	30 min

The analysis was performed on 24 microstructures for each sample, measuring 1mm x 1mm. The images were also rotated 90° and the analysis repeated, giving 48 results for effective resistance, which were then averaged. The results are shown in Figure 5.7, as a ratio of the as-received R_{eff} in each case (the ratio is denoted $\bar{R}_{eff}$). The "normalised" column indicates the results have been normalised against the as-received sample for changes in grain size, as detailed in Section 5.5.2.

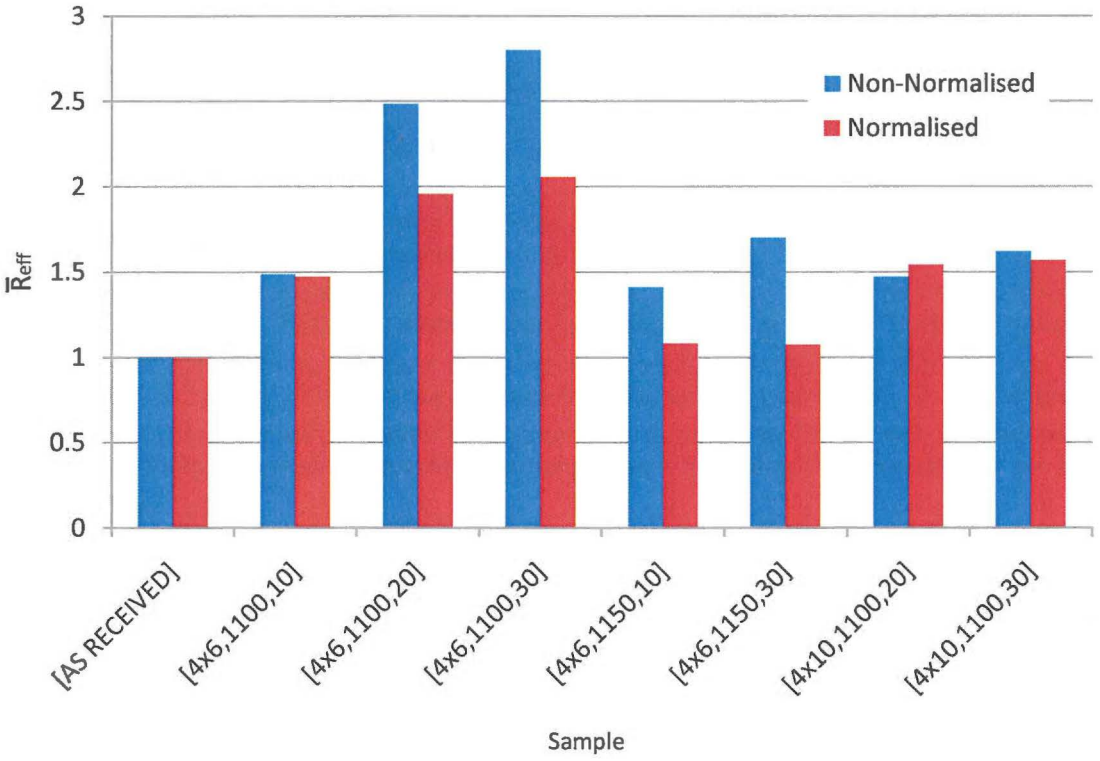

Figure 5.7 Results of grain boundary connectivity analysis

Considering first the non-normalised data, it is apparent that all of the GBE samples exhibit at least some increase in effective resistance to diffusion. It would be expected on this basis that all of the GBE samples analysed would exhibit a decreased bulk grain boundary diffusion rate compared to the as-received sample. The largest increase in effective resistance occurs in the samples [4x6,1100,20] and [4x6,1100,30], which are the two samples

with the highest $\Sigma 3^n$ boundary fractions. However, a fraction of the increase in R_{eff} in these two samples is attributable to the increased grain size. Normalisation removes this effect, isolating the boundary connectivity.

Considering the normalised results now, Figure 5.7 shows that even when the effect of increased grain size is ignored in the two samples mentioned previously, the effective resistance of the 2D GBE microstructure is still significantly higher than that of the as-received microstructure in the case of the [4x6,1100,20] and [4x6,1100,30] samples. This result confirms that the random HAB network is most disrupted by this set of processing conditions. Another way to visualise this result is by processing an EBSD map to show only the random HAB network (ie. removing the $\Sigma 3^n$ family). The [4x6,1100,30] sample is compared to the as-received sample in this way in Figure 5.8.

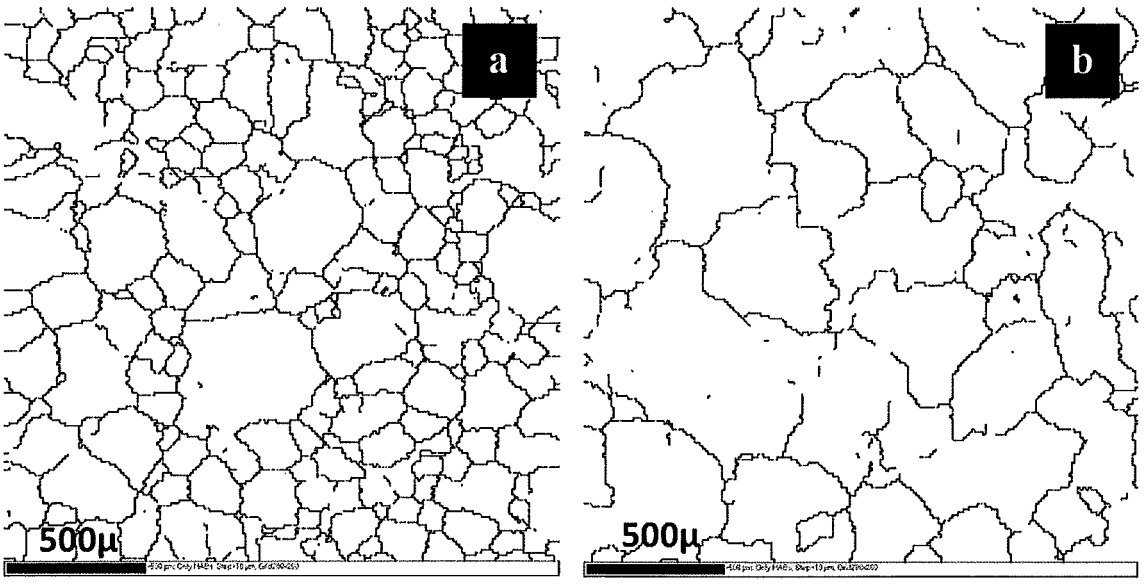

Figure 5.8 Comparison of random HAB networks between (a) as-received and (b) [4x6,1100,30] samples

Visually, this disruption is obvious and not entirely attributable to the grain size increase (which was calculated according to the mean-intercept length method described in Section 4.6.2.2) from approximately 140µ to 190µ. Figure 5.7 also suggests that this HAB boundary

disruption is time-dependent, as the normalised effective resistance, $\bar{R}_{eff}$, increases with annealing time within the [4x6,1100,x] series. Combining the measures (ie. $\Sigma 3^n$ boundary fraction, $\Sigma 9/\Sigma 3$ ratio, and the connectivity analysis) of the level of GBE, it was concluded that the [4x6,1100,20] and [4x6,1100,30] samples were the "most engineered".

Other interesting results are also apparent in Figure 5.7. First, the $\Sigma 3^n$ boundary fractions suggested that the 10% deformation level was also suitable for creating a GBE condition, although the $\Sigma 3^n$ fractions were not as high as the 6% samples. This finding is confirmed by the connectivity analysis, which shows that the normalised effective resistance has increased by approximately 50% and therefore suggests that $\Sigma 3^n$ boundaries are disrupting the HAB network. However, in line with the boundary fraction results, the 10% deformation conditions were not considered to be as "well engineered" as the [4x6,1100,20] and [4x6,1100,30] samples mentioned previously.

Second, the [4x6,1150,x] samples show an increase of 40-65% in their non-normalised effective resistance compared to the as-received condition. However, the normalised results show that this increase is almost entirely due to the grain size difference. This is an important finding for GBE studies, and shows that the special boundary fraction may be increased (in this case from ~42% to ~59%) without causing disruption to the network. This result is consistent with twin and twin variants being introduced internally within the existing HAB network, and thus would not result in reduced transport properties. Therefore, a model of connectivity, such as the one used in this work, is required to determine whether the increased fraction of special boundaries can be expected to confer improved material properties.

5.7 Comparison with Triple Junction Geometry

As such a model has not been presented in the literature previously, it also seems useful to present the GBE results in terms of an existing model, in order to allow some comparison between the two. Therefore, the triple junction distribution was extracted from the EBSD data for the same eight samples, and is shown in Figure 5.9.

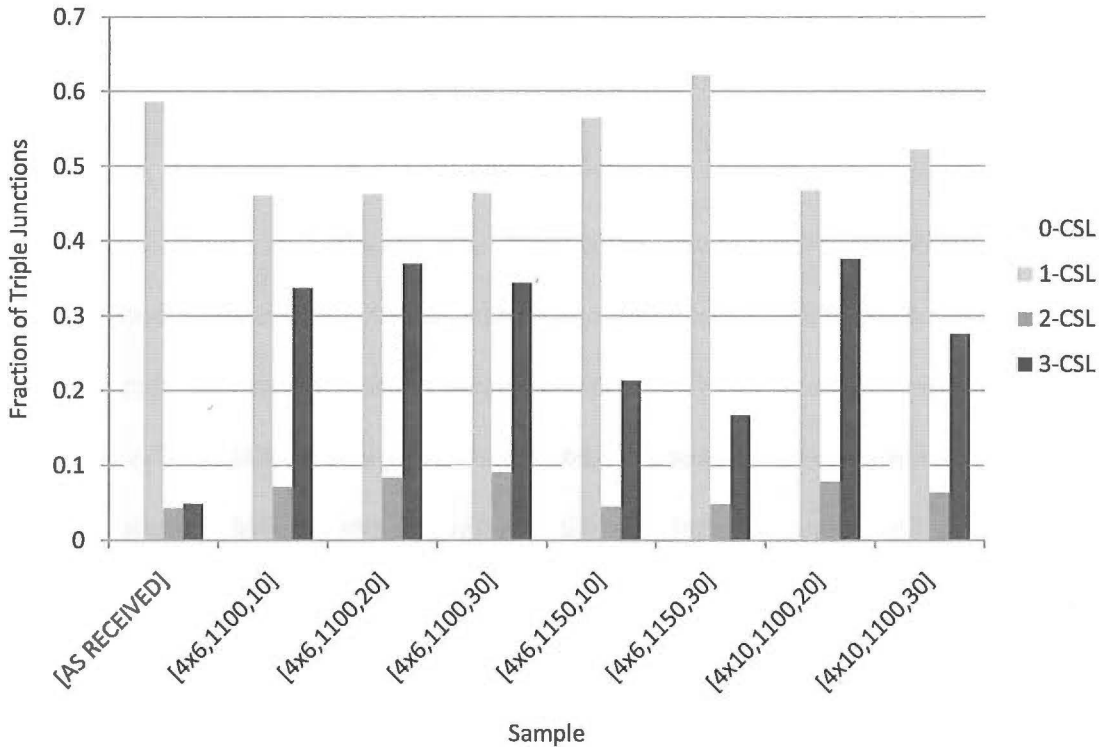

Figure 5.9 Triple junction distribution for selected GBE samples

This figure shows that 32% of the triple junctions in the as-received sample show only random HABs (0-CSL), and approximately 5% join three $\Sigma 3^n$ boundaries (3-CSL). In the highest $\Sigma 3^n$ fraction samples ([4x6,1100,20] and [4x6,1100,30]), the number of 0-CSL triple junctions decreases to 10-12% and the number of 3-CSL junctions increases to 34-37%. For these samples, the $\Sigma 3^n$-only fraction is predominantly made up of the $\Sigma 3$-$\Sigma 3$-$\Sigma 9$ junction (~66%) and the $\Sigma 3$-$\Sigma 9$-$\Sigma 27$ junction (~33%). When the 1150°C samples are considered, similar trends are observed, but to a lesser extent than the 1100°C annealed samples. In this

case, the 3-CSL fraction (0.17-0.21) is made up of the same two junctions (Σ3-Σ3-Σ9 and Σ3-Σ9-Σ27) but in the ratio ~73% to ~27%. This result is consistent with their lower Σ9 and Σ27 fractions illustrated in the previous chapter. Importantly however, these 1150°C annealed samples show the major limitation of the triple junction analysis. The decrease in 0-CSL junctions and increase in 3-CSL junctions could be misinterpreted as a disruption to the HAB network. However, the effective resistance model shows that the $\Sigma 3^n$ boundaries are not effectively incorporated into the GB network.

5.8 Conclusions

Measuring the connectivity of the grain boundary network has increasingly become a focus of grain boundary engineering investigations, especially when the controlling properties are related to the grain boundary network. Existing models for connectivity analysis have been shown to have limitations, especially in the way they distinguish incorporated from non-incorporated special boundaries. Therefore, a new model for the quantification of two-dimensional grain boundary connectivity has been presented here, which does not suffer from these limitations.

The analysis of GBE samples using the resistivity model has shown that the samples with the highest $\Sigma 3^n$ fractions also show the highest degree of special boundary incorporation in the random HAB network. An important point has also been confirmed by this analysis, which proved that the increase in $\Sigma 3^n$ fraction is necessary, but not a sufficient criterion on which to expect improved material properties. In the case of the 1150°C annealed samples, the increase in effective resistance was attributed entirely to the increased grain size compared to the as-received condition, despite the large increase in special boundary fraction for these

samples. Therefore, it may be concluded that a grain boundary connectivity analysis is an important part of a GBE investigation where property correlations are required.

5.9 References

[1] Lehockey, E. M., Brennenstuhl, A. M., Thompson, I., *On the relationship between grain boundary connectivity, coincident site lattice boundaries, and intergranular stress corrosion cracking*, Corrosion Sci. 46 (2004) 2383-2404.

[2] Kumar, M., King, W., Schwartz, A. J., *Modifications to the microstructural topology in f.c.c. materials through thermomechanical processing*, Acta Mater. 48 (2000) 2081-2091.

[3] Miyazawa, K., Iwasaki, Y., Ito, K., Ishida, Y., *Combination rule of sigma values at triple junctions in cubic polycrystals*, Acta Cryst. A52 (1996) 787-796.

[4] Schuh, C. A., Kumar, M., King, W. E., *Universal features of grain boundary networks in FCC materials*, J. of Mat. Sci. 40 (2005) 847-852.

[5] Schuh, C. A., Kumar, M., King, W. E., *Analysis of grain boundary networks and their evolution during grain boundary engineering*, Acta Mater. 51 (2003) 687-700.

[6] Wells, D. B., Stewart, J., Herbert, A. W., Scott, P. M., Williams, D. E., *Use of percolation theory to predict the probability of failure of sensitized, austenitic stainless steels by intergranular stress corrosion cracking*, Corrosion 45 (1989) 649-660.

[7] Pan, Y., Olson, T., Adams, B. L., *Applications of orientation imaging analysis to microstructural control of intergranular stress corrosion cracking*, Can. Metall. Q. 34 (1995) 147-154.

[8] Frary, M., Schuh, C. A., *Grain boundary networks: Scaling laws, preferred cluster structure, and their implications for grain boundary engineering*, Acta Mater. 53 (2005) 4323-4335.

[9] Chen, Y., Schuh, C. A., *Diffusion on grain boundary networks: Percolation theory and effective medium approximations*, Acta Mater. 54 (2006) 4709-4720.

[10] Gao, Y., Stölken, J. S., Kumar, M., Ritchie, R. O., *High-cycle fatigue of nickel-base superalloy René 104 (ME3): Interaction of microstructurally small cracks with grain boundaries of known character*, Acta Mater. 55 (2007) 3155-3167.

[11] Stauffer, D., Aharony, A., *Introduction to percolation theory*, Taylor & Francis, London, 1992.

[12] Isichenko, M. B., *Percolation, statistical topography, and transport in random media*, Rev. Mod. Phys. 64 (1992) 961-1043.

[13] Frost H.J., Ashby M.F., *Deformation-Mechanism Maps*, Pergamon Press, 1982.

[14] Kirkpatrick, S., *Percolation and conduction*, Rev. Mod. Phys. 45 (1973) 574-588.

[15] Alexandreanu, B., Spencer, B. H., Thaveeprungsriporn, V., Was, G. S., *The effect of grain boundary character distribution on the high temperature deformation behavior of Ni-16Cr-9Fe alloys*, Acta Mater. 51 (2003) 3831-3848.

[16] Palumbo, G., Aust, K. T., *Materials Interfaces*, Chapman and Hall, London, 1992.

CHAPTER 6: MICROSTRUCTURAL EVOLUTION THROUGHOUT GBE PROCESSING

6.1 Introduction

Despite the large number of GBE studies in the literature, there is a disproportionately low number of studies which seek to interpret the actual mechanism by which grain boundary engineering occurs. For this reason, the evolution of the microstructure was studied in this work, as a function of processing cycle, in order to track the progress of the microstructure throughout the GBE process and to determine the minimum number of cycles required to achieve a sufficiently GBE state.

It is first necessary to introduce some useful parameters which are also tracked throughout the GBE process. These parameters are introduced in Section 6.2, and their calculation is subsequently explained. The experimental method and results are then presented, in terms of $\Sigma 3^n$ length fraction, grain size, and measures of internal strain. Finally, these results are then compared to the other studies presented in the literature, and the contribution of the present study to the determination of a GBE mechanism is evaluated and discussed.

6.2 Other Useful Parameters

There are several ways in which GBE processes may affect the crystallography of individual grain boundaries, including twinning, grain growth, grain rotation, local lattice rotation and grain boundary rotation and recovery [1]. The contribution of twinning and grain growth can be estimated from the $\Sigma 3$ fraction and grain size respectively. Grain rotation is primarily a

surface effect, and therefore not relevant in this case (where the surface layer is removed mechanically). However, evaluating the effect of local lattice rotation, and grain boundary recovery requires the use of additional parameters.

Each grain boundary segment may be classified according to its deviation from any specific CSL misorientation (the calculations of this are detailed in the next section). Therefore, if a boundary segment is identified as a CSL boundary by a criterion such as the Brandon criterion [2] used in this work, it also has a deviation from the ideal CSL misorientation angle, which is termed v. For example, if a grain boundary is found to have a misorientation of 59° about a <111> axis, it is classified as a Σ3 boundary because it is within the allowable deviation according to the Brandon criterion of 8.7° away from 60°/<111> (the ideal Σ3 misorientation), and is said to have a deviation angle, v, of 1°. The ratio between v and the allowable deviation, v_m, for a CSL boundary is termed the deviation from ideal, or more commonly, the v/v_m ratio.

The significance of the v/v_m value is twofold. First, v/v_m has shown some correlation with boundary energy for CSL boundaries [3], which indicates that the closer a boundary is to the exact CSL reference, the more likely it is to have periodicity in the boundary plane, and therefore exhibit special properties. In particular, the {111} symmetrical tilt boundary (STB) in the Σ3 system (the coherent annealing twin), has generally been shown to exhibit low v/v_m in nickel and copper [3-4]. Hence, the evaluation of v/v_m provides an estimate of the boundary planes in this system.

Also, v/v_m is used as a measure of how much strain is retained in the microstructure [1, 5]. The lattice dislocations introduced by the plate rolling operation can reduce their energy by interacting with a grain boundary [6]. The result of this interaction is an extrinsic grain

boundary dislocation (EGBD). The presence of EGBDs near grain boundaries introduces local lattice rotations, which in turn affects the misorientation across the boundary. Evidence exists [7-8] to suggest the subsequent absorption of the EGBD into the boundary (which reduces its energy further) is retarded at low-Σ grain boundaries compared to random boundaries, and also that absorption becomes more difficult as the boundary becomes more ordered. Therefore, the measurement of v/v_m at Σ3 boundaries in particular is an effective method of determining whether strain is retained at these boundaries, and offers insight into the driving force for boundary migration during processing.

The other useful parameter is similarly a measure of retained strain in the lattice, namely the low-angle boundary (LAB) fraction. A low angle boundary is classified in this work as any boundary which exhibits more than 2°, but less than 10° misorientation. The fraction of these boundaries in the network has been correlated with the amount of strain energy in the microstructure [9-10], and therefore this fraction is used as confirmation of the v/v_m measurement, allowing the retained strain levels to be evaluated as a function of processing cycle.

6.3 Calculating the Deviation from Ideal (v/v_m)

The deviation from ideal parameter was not able to be exported from the HKL Channel 5 software package, although it must be calculated internally in order to classify CSL boundaries. Therefore, a program was written in MATLAB [11] to take the raw EBSD data (a large matrix of positional Euler angles) and calculate this parameter. In order to present this calculation, it is first necessary to explain the calculation of boundary misorientation, shown in the following section.

6.3.1 Calculation of Boundary Misorientation

The first step in converting raw EBSD data into useful form is to determine the position of each grain boundary. This process involves evaluating the misorientation between all neighbouring pixels. Two methods (matrix multiplication and quaternions) were used in this work, in order to confirm the accuracy of the calculation. The matrix method is presented first.

Any three-dimensional rotation in space can be described by a rotation matrix. When the rotation matrix describes the rotation from crystal axes in a grain to the relevant crystal axes in a neighbouring grain, this rotation matrix is also referred to as a misorientation matrix. This matrix is denoted $\boldsymbol{M}$, and comprises three columns which each represent the direction cosines of the crystal axes of one grain with respect to the other. The rotation matrix may be converted to other descriptions such as the angle-axis pair using mathematical relationships [12]. For example, the Σ9 misorientation may be described as 38.9°/<110>, or as the matrix:

$$\boldsymbol{M}_{\Sigma 9} = \begin{bmatrix} 0.889 & 0.111 & 0.444 \\ 0.111 & 0.889 & -0.444 \\ -0.444 & 0.444 & 0.778 \end{bmatrix} \tag{6.1}$$

Because the raw EBSD data is in the form of Euler angles, which do not allow direct evaluation of the angle between two data points, each point was first converted into a rotation matrix according to standard methods available in [12]. The difference in rotation between two neighbouring lattice points is described as a rotation difference matrix, $\boldsymbol{M_d}$, and is given by the matrix equation:

$$\boldsymbol{M_d} = \boldsymbol{M_2} \times \boldsymbol{M_1}^{-1} \tag{6.2}$$

This misorientation matrix therefore describes the rotation from grain 1 to grain 2. However, in a cubic crystal system, there are 24 equivalent descriptions of a rotation, because the

crystal axes in this system may be chosen in several equivalent ways. Each of these 24 equivalent rotations produces a different rotation angle and axis, and hence it is necessary to find the minimum angle which completes the rotation. The misorientation which contains the smallest rotation angle is called the "disorientation".

The disorientation is calculated from $\boldsymbol{M_d}$ by systematically calculating all of the 23 other equivalent rotation matrices, according to the equation:

$$\boldsymbol{M'_d = T_i M_d} \tag{6.3}$$

where $\boldsymbol{T_i}$ represents the i^{th} symmetry operator matrix. These symmetry operator matrices are not reproduced here for the sake of brevity, but are also available in [12]. The disorientation matrix is the one with the largest trace. Once this has been found, the angle and axis pair are extracted from the disorientation matrix using the formulas:

$$\cos\theta = (a_{11} + a_{22} + a_{33} - 1)/2 \tag{6.4}$$

$$U{:}V{:}W = [a_{32} - a_{23}{:}\, a_{13} - a_{31}{:}\, a_{21} - a_{12}] \tag{6.5}$$

This process is illustrated in Figure 6.1, showing three symmetrically equivalent rotation matrices and their corresponding angle/axis pairs. It is clear that the largest trace corresponds to the smallest angle (as per equation 6.4).

$$\boldsymbol{M'_d} = \begin{bmatrix} 0.933 & 0.067 & 0.354 \\ 0.067 & 0.933 & -0.354 \\ -0.354 & 0.354 & 0.866 \end{bmatrix} = \begin{bmatrix} 0.354 & -0.067 & 0.933 \\ -0.354 & -0.933 & -0.067 \\ 0.866 & -0.354 & -0.354 \end{bmatrix} = \begin{bmatrix} 0.933 & -0.354 & 0.067 \\ 0.067 & 0.354 & 0.933 \\ -0.354 & -0.866 & 0.354 \end{bmatrix}$$

$\theta =$ 30° 165° 71°

$< UVW > = < 0.707, 0.707, 0 >$ $< -0.421, 0.067, -0.287 >$ $< -1.799, 0.421, 0.421 >$

Figure 6.1 Three selected symmetrically equivalent rotation descriptions

The disorientation angle, θ, is then checked against the threshold for a grain boundary (in this work, the threshold was 10°). If it exceeds this threshold, a grain boundary exists between these two data points with the misorientation given by $\theta/< UVW >$.

The second method of calculating boundary misorientation is through quaternions, and was employed as the primary method in the MATLAB program due to its increased speed of calculation. The calculation is very similar to the one described previously, however, each data point is represented by a unit quaternion instead of a matrix. The raw Euler angles at each point are converted to quaternions using the in-built MATLAB function 'angle2quat' along with the specification of the sequence of Euler angles output by the EBSD software (in this case, 'XZX'). The difference between neighbouring crystal orientations is then calculated according to the equation:

$$\boldsymbol{q_d} = \boldsymbol{q_2} \times \boldsymbol{q_1^{-1}} \tag{6.6}$$

Again, there are 24 symmetrically equivalent rotation quaternions within the cubic crystal system. However, if the quaternion $\boldsymbol{q_d}$ is ordered such that $e_4 > e_3 > e_2 > e_1$ and all components are positive (the justification for this process is available in [13]), the quaternion containing the disorientation angle can be found by calculating just three of the symmetrical equivalents [13]:

$$\boldsymbol{q_{d,1}} = [e_1, e_2, e_3, e_4] \tag{6.7}$$

$$\boldsymbol{q_{d,2}} = \left(1/\sqrt{2}\right) \times [e_1 - e_2, e_2 + e_1, e_3 - e_4, e_4 + e_3] \tag{6.8}$$

$$\boldsymbol{q_{d,3}} = (1/2) \times [e_1 - e_4 - e_2 + e_3, e_2 - e_4 - e_3 + e_1, e_3 - e_4 - e_1 + e_2, e_4 + e_1 + e_2 + e_3] \tag{6.9}$$

The disorientation is given by the quaternion with the largest fourth component, and extracted from the quaternion according to the equation:

$$\theta = 2 \times \cos^{-1}(e_4) \tag{6.10}$$

The disorientation axes can also be calculated from this quaternion, according to:

$$U{:}V{:}W = [e_1, e_2, e_3] \tag{6.11}$$

Therefore, given the raw matrix of Euler angle data, the MATLAB program calculated the misorientation between each pixel, and thereby located each segment of grain boundary. The results from both methods proved exactly the same, although the quaternion method was more than twice as fast due to the reduced memory requirements of four variables per quaternion as opposed to nine per matrix, and the simplified symmetry analysis.

6.3.2 Calculating Deviation from a CSL Misorientation

Once the misorientation of each grain boundary segment was calculated, it was then necessary to determine whether each misorientation was close to that of a CSL boundary. The four CSL boundaries tested were Σ3, Σ9, Σ27a and Σ27b. Each of these misorientations can be described as an angle/axis pair, a misorientation matrix, or a quaternion, as shown in Table 6.1 for the case of a Σ3 boundary. Naturally, there are 24 symmetrical equivalents for each. For example, the 60°/<111> misorientation may also be described as a 70.5°/<110> misorientation.

Table 6.1 Example representations of a Σ3 boundary

Angle/Axis Pair	Misorientation Matrix	Quaternion
60°/<111>	$\begin{bmatrix} 0.667 & -0.333 & 0.667 \\ 0.667 & 0.667 & -0.333 \\ -0.333 & 0.667 & 0.667 \end{bmatrix}$	[0.289 0.289 0.289 0.866]

Therefore, it was then possible to find a second difference matrix (or difference quaternion), between a boundary segment misorientation and its closest symmetrically equivalent CSL orientation. Alternatively, the angle between the original misorientation quaternion and the

closest symmetrically equivalent CSL quaternion (these must be stepped through to find the smallest deviation angle) may be calculated according to the equation:

$$v = 2\cos^{-1}(\boldsymbol{q_d} \cdot \boldsymbol{q'_\Sigma}) \tag{6.12}$$

where $\boldsymbol{q_d}$ represents the original misorientation quaternion, and $\boldsymbol{q'_\Sigma}$ represents the quaternion description of the CSL rotation.

Again, both matrix methods (equations 6.2 to 6.5) and quaternion methods (equation 6.12) were programmed in order to confirm the results, although the quaternion method was once again used after this confirmation was complete due to its increased speed. The angle between a boundary misorientation and each CSL misorientation, v, was then checked against the Brandon criterion for each boundary segment. If the angle was within the allowable deviation, that boundary segment was classified according to its Σ value, and its length recorded, along with its deviation from ideal, v/v_m.

In order to present these results, it is necessary to use a weighted mean deviation parameter, $\bar{v}$, which is defined as follows:

$$\bar{v} = \frac{\sum_i^n v_i L_i}{v_m \sum_i^n L_i} \tag{6.13}$$

where n is the number of Σ3 boundaries present, v_i is the angular deviation from ideal of Σ3 boundary segment i, L_i is the length of Σ3 boundary segment i, and v_m is the maximum allowable deviation from the Brandon criterion (~8.7° for a Σ3 boundary).

6.4 Experimental Method

In order to track the progress of the microstructure throughout the GBE procedure, two sets of GBE parameters were selected for further investigation. The combinations selected were

6% deformation, 1100°C anneal and either a 10 minute or a 30 minute anneal per cycle. A total of five cycles was performed, and the microstructure was analysed after each cycle by removing approximately 20mm of the strip and preparing the internal surface. Each sample was analysed using the methods described in Chapter 4, and the $\Sigma 3^n$ boundary length fraction and grain size (both excluding and including twins) were calculated along with the v/v_m and LAB fraction.

6.5 Evolution of $\Sigma 3^n$ Boundary Length Fraction and Grain Size

The $\Sigma 3^n$ boundary length fractions are shown for both samples in Figure 6.2.

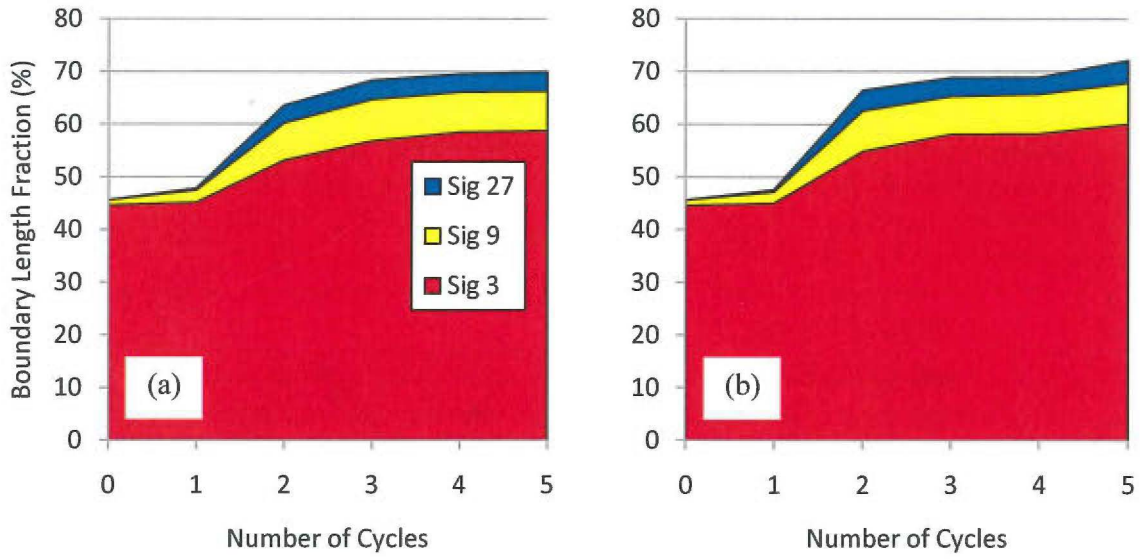

Figure 6.2 $\Sigma 3^n$ length fractions as a function of processing cycle for (a) [6%,1100,10] and (b) [6%,1100,30] processing conditions

Firstly, it is noticeable that both samples show a similar trend. The $\Sigma 3^n$ fraction could be described as a "diminishing return" trend as a function of processing cycle, however there is an important point to note. For both samples, if the $\Sigma 3^n$ fractions after one cycle are compared to the as-received values (zero cycles), it is apparent that there has been no significant improvement. Therefore, the diminishing return trend actually begins in cycle

two. This result has been noted previously in the literature [5, 9, 14], and will be discussed further in Section 6.7.

The grain size has also been measured after each cycle and the results are shown in Figure 6.3.

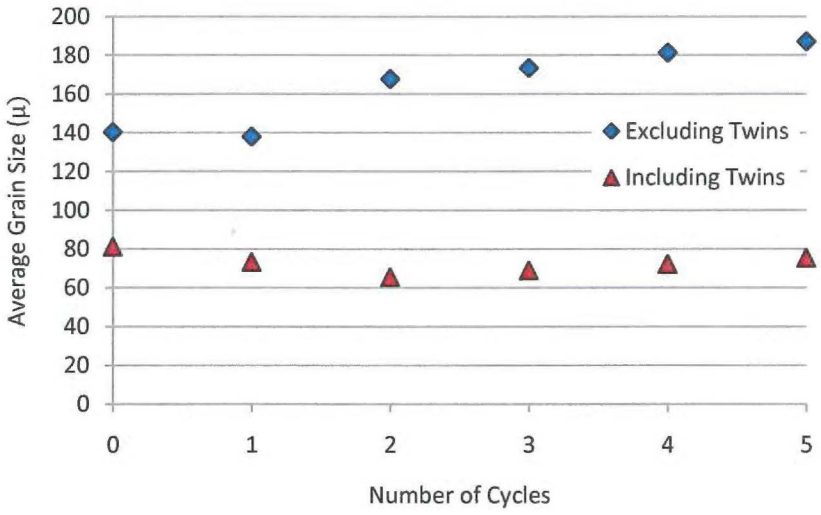

(a) [6%,1100,10]

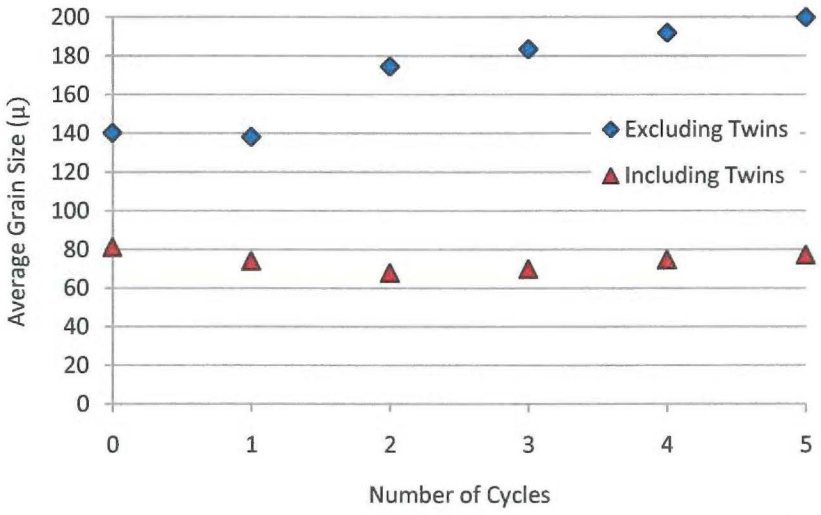

(b) [6%,1100,30]

Figure 6.3 Grain size (excluding and including twins) as a function of processing cycle for (a) [6%,1100,10] and (b) [6%,1100,30]

The results show that no significant change is evident in grain size after the first cycle. The largest increase in twin-excluded grain size occurs during cycle two, where the average grain size increases by approximately 25% in both samples. During cycles 3-5, the grain size increases slightly to a final size of up to 200μm. However, the twin-included grain size decreases slightly during the first cycle, and does not match the twin-excluded grain size increase in cycle two. This result is again consistent with the introduction of new Σ3 boundaries during this cycle. The final twin-included grain size of 75-80μ matches well with the as-received grain size, despite the large increase in twin-excluded grain size.

6.6 Evolution of v/v_m and Low-Angle Boundary Fraction

The mean deviation parameter, $\bar{v}$, is plotted as a function of processing cycle for both samples, shown in Figure 6.4. In this figure, the points are joined as a guide to the eye.

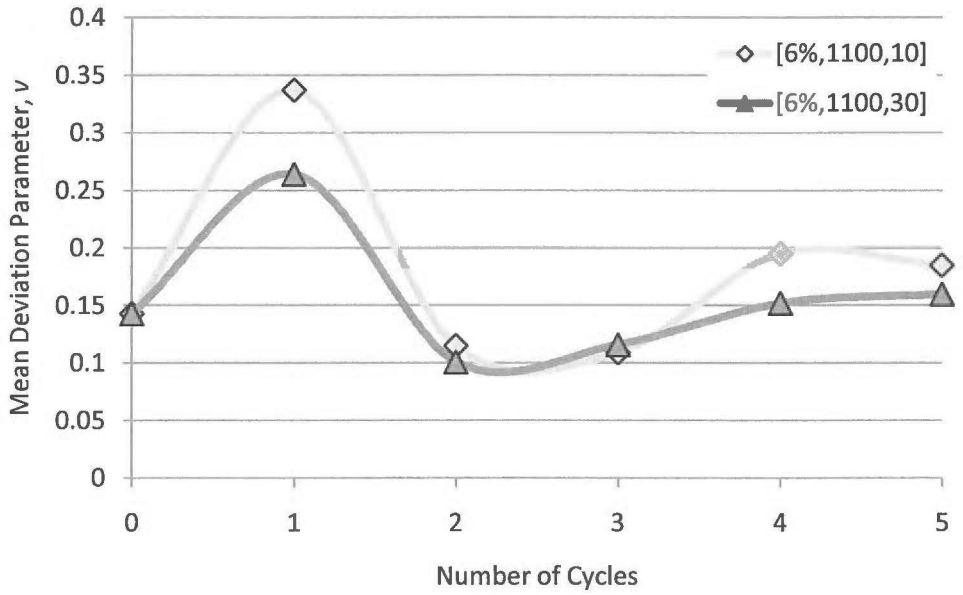

Figure 6.4 Mean deviation parameter as a function of processing cycle for [6%,1100,10] and [6%,1100,30] processing conditions

It is apparent from this figure that the deviation from the ideal Σ3 arrangement increased sharply in both samples after one cycle. This implies an increase in the strain retained in the microstructure at Σ3 boundaries, due to the introduction of new dislocations which have not been re-absorbed during the annealing treatment. The slightly lower $\bar{v}$ value for the [6%,1100,30] sample after one cycle is consistent with the increased energy available for dislocation absorption compared to the 10 minute anneal. During the second cycle, the deviation parameter then decreases to a level below that of the as-received sample, indicating that the retained strain has been largely removed from the microstructure. A $\bar{v}$ value of 0.1 shows that the Σ3 boundaries are, on average, very close to the exact reference structure. During the subsequent cycles 3-5, the retained strain levels then increase, although the increase is much less significant than the changes observed in the first two cycles.

These trends are confirmed by plotting the LAB fraction in both samples, shown in Figure 6.5. Again, the points are joined as a guide to the eye only.

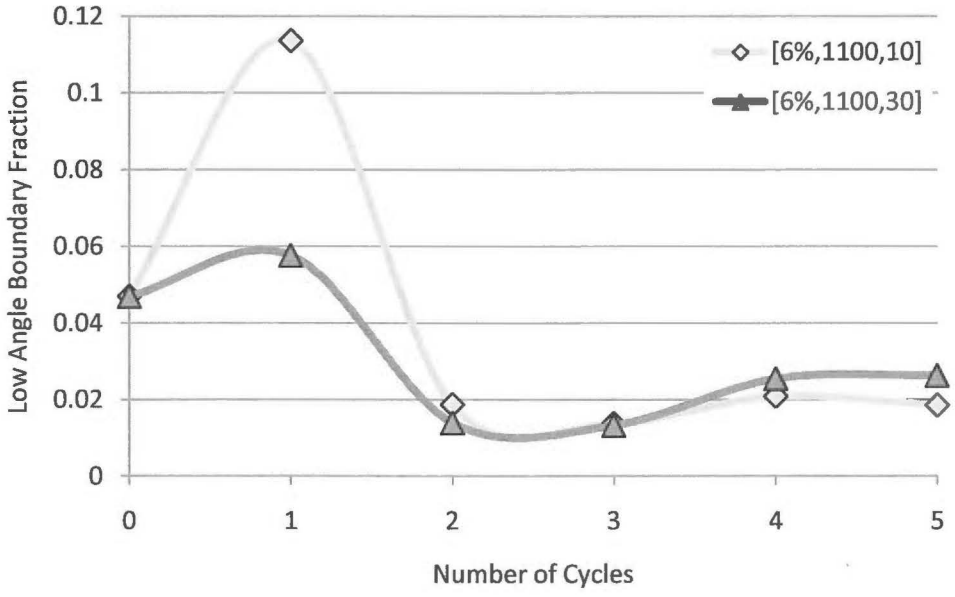

Figure 6.5 Low-angle boundary fraction as a function of processing cycle for [6%,1100,10] and [6%,1100,30] samples

Once again, the increase in retained strain is noticeable during the first cycle of processing for both samples, although this increase is definitely more significant for the 10 minute anneal. In both cases, there is a sharp decrease in LAB fraction after the second cycle, and the level drops below the level of the as-received material. There is also a slight increase throughout the remaining cycles, as seen with the deviation parameter.

6.7 Discussion

Although the exact mechanism by which GBE increases the fraction of $\Sigma 3^n$ boundaries is not well agreed upon in the literature, there are several trends which occur consistently whenever the evolution of a GBE microstructure is studied. For example, the present results showed that during the first cycle of processing, there was no significant increase in $\Sigma 3^n$ boundary fraction or grain size, and that the retained strain in the microstructure has increased. It follows therefore that the annealing conditions (temperature, time) were not sufficient to completely remove the deformation introduced during the plate rolling step for either sample. As expected, the longer annealing time was shown to yield lower retained strain levels.

This result is important in that in shows that, under these specific conditions, more than one processing step is required in order to achieve a GBE state. This statement is in general agreement with the majority of work in the GBE field [15-19], although there are occasional instances of GBE states being reported after a single cycle. For example, Kokawa et al [20] report very high length fractions of $\Sigma<29$ boundaries in an austenitic 304 stainless steel after one cycle of 5% rolling and annealing at 1200-1240K. However, the annealing time used was 72 hours, which is very long compared to the majority of GBE conditions. Coleman and Randle [21] also showed that in copper, a single GBE cycle increased the fraction of $\Sigma 3$s,

although these new Σ3s were mainly not incorporated into the GB network until subsequent processing cycles.

The absence of change in the $\Sigma 3^n$ boundary fraction during the initial stages of processing has been noted previously in the majority of previous studies. In 2002, Randle and Davies [5] performed five cycles of GBE on alpha-brass and measured the special boundary fraction after each cycle. They showed that the Σ3 fraction initial decreased slightly during the first two stages of processing, before increasing throughout the final three. Also, the average v/v_m was shown to increase during these first two cycles, which is consistent with the present results. In a study of Inconel 600 by Schuh et al [22], the fraction of special boundaries decreased from approximately 44% to 40% during the first cycle, before increasing to more than 52% during the second cycle and then increasing up to 61% after four cycles. A similar trend was noticed by Owen and Randle [14] in 316 stainless steel, and Engelberg et al [9] in 304 stainless steel.

An explanation of the initial stability in Σ3 fraction was suggested by Owen and Randle [14]. During the early GBE cycles, dislocation pile-ups increase the amount of strain which is retained in the lattice either side of Σ3 boundaries. There is indirect evidence for this claim, in the form of the increasing Σ3 v/v_m parameter noticed by Randle and Davies [5], and Engelberg [9], and the same result achieved in the present experiments. In addition, Kumar [23] illustrated planar arrays of dislocations after 5% strain in alloy 600 by transmission electron microscopy (TEM). The LAB fraction also matches the v/v_m parameter in the above mentioned cases.

During the initial annealing steps therefore, the retained strain is high, indicating there is a comparatively large driving force for grain boundary migration. In [14], Owen and Randle

continue to explain that because of this, mobile boundaries move through the microstructure, and may annihilate twins as they do so, causing a reduction in Σ3 fraction. In fact, there is also another possible way in which the increased strain results in fewer Σ3 boundaries. Because the average deviation parameter for Σ3s is increasing throughout these early cycles, more Σ3 boundaries would be pushed outside the maximum allowable deviation (i.e. their v/v_m becomes greater than one). Therefore, some boundaries which were previously classified as Σ3 could instead be classified as random HABs, decreasing the relative fraction of Σ3s in the network. In the present work, the mean Σ3 deviation parameter increased from 0.15 to 0.34, which is lower than the 0.56 measured by Randle in the alpha-brass study, and may explain why there was no reduction in Σ3 fraction detected in the present case.

During the second cycle in the present study, both samples exhibited a concurrent increase in $\Sigma 3^n$ boundary fraction, and twin-excluded grain size. The increases during this cycle were the largest measured throughout the entire five cycles of processing. Simultaneously, the strain retained at Σ3 boundaries was significantly reduced, indicated by a large decrease in $\bar{v}$, as well as the LAB fraction. These results could be explained by migration of mobile grain boundaries during this cycle, which resulted in the absorption of dislocations and a decrease in the stored strain energy. The connectivity of the random HAB network was most influenced by this step, as illustrated in Figure 6.6, which shows the HAB network only after 0-2 cycles for the 30-minute annealed sample.

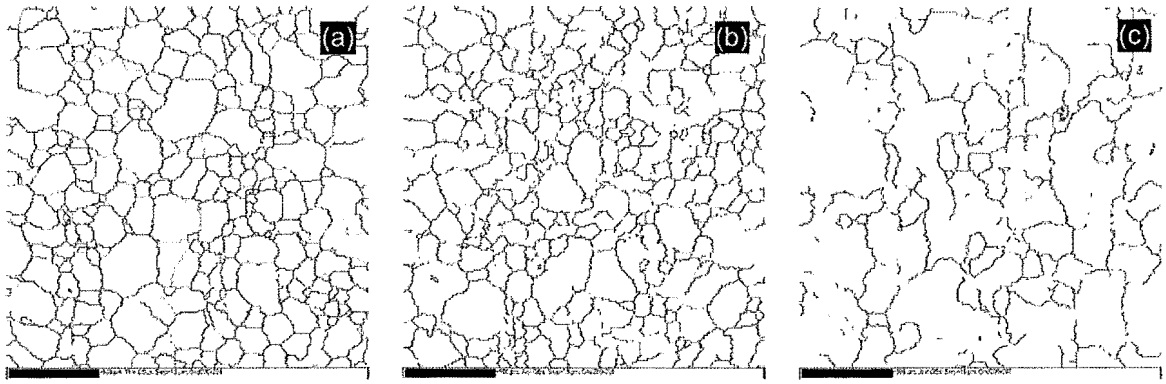

Figure 6.6 Random high-angle boundary networks after (a) no cycles, (b) one cycle and (c) two cycles for the sample [6%,1100,30]

The changes in $\Sigma 3^n$ fraction are also entirely consistent with previous studies. For example, other studies showed that immediately following one or two cycles of little change in $\Sigma 3$ fraction, there is an increase from 19 to 26% number fraction of $\Sigma 3$s in alpha-brass [5], and increases in total $\Sigma 3^n$ fraction from 40 to 52% in Inconel 600 [22], and 28 to 55% in 304 stainless steel [9]. One could describe the cycle in which the $\Sigma 3^n$ significantly increases as "the grain boundary engineering cycle", although it is important to remember that the initial cycles appear to be a necessary precursor. A description of the microstructural changes during this cycle was first offered by Randle and Davies [5], who suggested that new twinning is a result of boundary migration, once the retained strain has been absorbed. As stated in Chapter 3.9, Owen and Randle attempted to add to this explanation by suggesting that once this retained strain has been removed in the later cycles, that boundary migration proceeds more slowly, and that this slower migration velocity is more suitable for the nucleation of annealing twins, although evidence for this claim is currently inconclusive.

In these studies mentioned, the largest increase in $\Sigma 3$ fraction was observed in either (a) the same cycle as the largest decrease in $\Sigma 3$ deviation parameter (as in the present study, and also [5]), or (b) the cycle immediately following the largest decrease in $\Sigma 3$ deviation parameter [14]. In case (a), it is possible that the absorption of retained strain, requiring a relatively

high boundary velocity, and the new Σ3 generation (which may require a low boundary velocity) occur consecutively within the same annealing step. Therefore, it is possible that case (a) and case (b) are equivalent, and therefore the present results do not disprove the theory that low boundary velocity is more suitable for new Σ3 generation. In fact, the result that as-received condition was not in a GBE state after its manufacturing process of heavy deformation and high-temperature annealing also suggests that very high boundary velocities are not suitable for GBE. Essentially, however, the overall increase in $\Sigma 3^n$ boundaries throughout the later GBE cycles it is thought to be due to a combination of new twinning, plus the interaction of existing CSL boundaries, possibly according to a mechanism suggested by Randle [19] which was detailed in Chapter 3.9.

Turning now to the remaining three cycles of five total, in this work, in which the $\Sigma 3^n$ fraction increased slightly throughout, it is likely that the interactions between $\Sigma 3^n$ boundaries continued. There is further evidence for boundary migration in that the grain size increased each cycle, and therefore it is also possible that new twinning occurred as a result. Interestingly, Randle and Coleman suggested that there may be a cyclic nature to GBE processing [24], as they observed the retained strain levels increase again after the step in which the majority of $\Sigma 3^n$ boundaries were introduced, as was also the case in the present work. It is possible the retained strain could build high enough again to allow a second "GBE cycle", although this was not investigated in this work because it was not considered feasible industrially.

With knowledge of the theories regarding the mechanism of GBE, it is useful to revisit the effects of individual processing parameters on the $\Sigma 3^n$ fraction and grain size which were initially described in Chapter 4. For example, the results of this work showed that the higher deformation levels (15% and 50%) were not as suitable for creating a GBE material as low

deformation levels (<10%). This statement is also generally supported in the literature [23, 25-26]. The reason for this may be that the mechanism of GBE is entirely different to conventional recrystallisation, which occurs preferentially at high deformation levels. Transmission electron microscope (TEM) work by Kumar et al in 2002 [23] showed that the dislocation distribution during GBE in Inconel 600 is relatively uniform compared with microstructures after large deformations.. After annealing, no evidence of recrystallisation was observed, but instead Kumar suggested boundary migration based on the curvature of the boundaries. This theory indicates that although some cold work is required in order to facilitate boundary migration, the level of cold work in GBE must be insufficient to cause recrystallisation. This is consistent with the present results, which showed a peak in $\Sigma 3^n$ boundary fraction at the deformation level 6%, which then decreased through 10, 15 and 50% cold work.

The effect of annealing conditions can therefore also be implied. Because the migration of mobile boundaries is a requisite for the GBE process, the thermal energy must be sufficient to allow this, indicating that there is a threshold temperature below which GBE will not occur. In this instance, the retained strain will not be removed from the microstructure. If the temperature is too high however, recrystallisation may be activated preferentially to selective boundary migration (provided there is a threshold level of cold work), causing a new boundary network to develop in place of the existing network. In the case where recrystallisation does not occur, the migration velocity of grain boundaries increases with temperature, and as discussed, it is possible that the boundary velocity becomes too great for the nucleation of new annealing twins. This description therefore predicts a maximum in the relationship between $\Sigma 3^n$ boundary fraction and annealing temperature, which is consistent with the local maximum showed at approximately 1100°C in the present work.

6.8 Conclusions

The evolution of the microstructure has been studied for two of the more successful sets of GBE conditions, comprising a 6% deformation and 1100°C at each cycle at two different annealing times. Both samples showed that during the first cycle, the $\Sigma 3^n$ fraction remained approximately constant, as did the grain size. However, the retained strain in the material, as measured by the mean deviation from ideal misorientation for $\Sigma 3$ boundaries and the LAB fraction, increased during the first cycle.

During the second cycle, both samples exhibited a significant decrease in their retained strain levels, and concurrently showed a large increase in the relative fractions of $\Sigma 3^n$ boundaries and the twin-excluded grain size. These results suggest boundary migration and interaction of $\Sigma 3^n$ boundaries during this cycle. This trend also continued throughout the final three cycles.

These results are consistent with several other studies of microstructural evolution in the literature, which generally show an initial stage of $\Sigma 3$ fraction stability or decreases, before significant increases in the $\Sigma 3^n$ fraction in the later cycles. The present results have been found to be consistent with an existing theory [14] regarding the boundary velocity dependence of new twin generation.

6.9 References

[1] Thomson, C. B., Randle, V., *Fine tuning at sigma 3 boundaries in nickel*, Acta Mat. 45 (1997) 4909-4916.

[2] Brandon, D. G., Ralph, B., Ranganathan, S., Wald, M. S., *A field ion microscope study of atomic configuration at grain boundaries*, Acta Metall. 12 (1964) 813-821.

[3] Randle, V., Davies, P., *Deviation from reference planes and reference misorientation for Σ3 boundaries*, Interface Sci. 7 (1999) 5-13.

[4] Randle, V., Davies, P., Hulm, B., *Grain-boundary plane reorientation in copper*, Phil. Mag. A 79 (1999) 305-316.

[5] Randle, V., Davies, H., *Evolution of microstructure and properties in alpha-brass after iterative processing*, Metall. & Mater. Trans. A 33 (2002) 1853-1857.

[6] Randle, V., *Refined approaches to the use of the coincidence site lattice*, J. of Mat. 50 (1998) 56-59.

[7] Kokawa, H., Watanabe, T., Karashima, S., *Sliding behaviour and dislocation structures in aluminium grain boundaries*, Phil. Mag. A 44 (1981) 1239-1254.

[8] Kegg, G. R., Horton, C. A. P., Silcock, J. M., *Grain boundary dislocations in aluminium bicrystals after high-temperature deformation*, Phil. Mag A 17 (1973) 1041-1055.

[9] Engelberg, D. L., Humphreys, F. J., Marrow, T. J., *The influence of low-strain thermo-mechanical processing on grain boundary network characteristics in type 304 austenitic stainless steel*, J. of Microscopy (2008) 435-444.

[10] Alyousif, O. M., Engelberg, D. L., Marrow, T. J., *Surface grain boundary engineering of shot-peened type 304 stainless steel*, J. of Mater. Sci. 43 (2008) 1270-1277.

[11] The Mathworks Inc., *MATLAB*, 1994.

[12] Randle, V., *The Measurement of Grain Boundary Geometry*, IOP Publishing Ltd., 1993.

[13] Hanson, A. J., *Visualising Quaternions*, Morgan Kaufmann Publishers, San Francisco, 2006.

[14] Owen, G., Randle, V., *On the role of iterative processing in grain boundary engineering*, Scripta Mat. 55 (2006) 959-962.

[15] Kumar, M., King, W., Schwartz, A. J., *Modifications to the microstructural topology in f.c.c. materials through thermomechanical processing*, Acta Mater. 48 (2000) 2081-2091.

[16] Gao, Y., Stölken, J. S., Kumar, M., Ritchie, R. O., *High-cycle fatigue of nickel-base superalloy René 104 (ME3): Interaction of microstructurally small cracks with grain boundaries of known character*, Acta Mater. 55 (2007) 3155-3167.

[17] Thaveeprungsriporn, V., Sinsrok, P., Thong-Aram, D., *Effect of iterative strain annealing on grain boundary network of 304 stainless steel*, Scripta Mat. 44 (2001) 67-71.

[18] Krupp, U., Kane, W. M., Liu, X., Dueber, O., Laird, C., McMahon Jr, C. J., *The effect of grain-boundary-engineering-type processing on oxygen-induced cracking of IN718*, Mat. Sci. & Eng. A 349 (2003) 213-217.

[19] Randle, V., *Mechanism of twinning-induced grain boundary engineering in low stacking-fault energy materials*, Acta Mater. 47 (1999) 4187-4196.

[20] Kokawa, H., Shimada, M., Michiuchi, M., Wang, Z. J., Sato, Y. S., *Arrest of weld-decay in 304 austenitic stainless steel by twin-induced grain boundary engineering*, Acta Mater. 55 (2007) 5401-5407.

[21] Coleman, M., Randle, V., *Changes in interface parameters and tensile properties in copper as a consequence of iterative processing*, Metall. & Mater. Trans. A 39 (2008) 2175-2183.

[22] Schuh, C. A., Kumar, M., King, W. E., *Analysis of grain boundary networks and their evolution during grain boundary engineering*, Acta Mater. 51 (2003) 687-700.

[23] Kumar, M., Schwartz, A. J., King, W. E., *Microstructural evolution during grain boundary engineering of low to medium stacking fault energy fcc materials*, Acta Mater. 50 (2002) 2599-2612.

[24] Randle, V., Coleman, M., *A study of low-strain and medium-strain grain boundary engineering*, Acta Mater. 57 (2009) 3410-3421.

[25] Fang, X., Zhang, K., Guo, H., Wang, W., Zhou, B., *Twin-induced grain boundary engineering in 304 stainless steel*, Mat. Sci. & Eng. A 487 (2008) 7-13.

[26] Engelberg, D. L., Newman, R. C., Marrow, T. J., *Effect of thermomechanical process history on grain boundary control in an austenitic stainless steel*, Scripta Mater. 59 (2008) 554-557.

CHAPTER 7: MECHANICAL PROPERTIES OF GRAIN BOUNDARY ENGINEERED ALLOY 800H

7.1 Introduction

Although the major aim of this project is to improve the creep properties of alloy 800H, it is important that such an increase does not come at the expense of the mechanical properties of the alloy. Therefore, in this chapter, the hardness and tensile properties of several different GBE conditions are compared to the as-received condition.

Initially, some background information regarding the mechanical testing methods and the microstructural changes throughout plastic deformation is provided, in order to relate the test results to existing theory. The methods and results of both hardness tests and tensile tests are then presented and discussed in turn.

7.2 Overview of Mechanical Testing

Hardness testing provides a means of measuring a material's resistance to deformation. In the present work, the Vickers hardness test is used, which involves making an indentation into the polished surface with a set load and indenter geometry. The Vickers hardness (VHN) is then defined as the load divided by the surface area of the indentation, according to the formula [1]:

$$VHN = \frac{2P\sin(\theta/2)}{L^2} = \frac{1.854P}{L^2} \tag{7.1}$$

where P is the applied load in kg,

L is the average length of diagonals in mm, and

θ is the angle between opposite faces of the diamond indenter = 136°

The lengths of diagonals in the indentation are calculated from measurements taken through a low-power optical microscope, and therefore are subject to some user uncertainties. At least three measurements are taken of each sample, and the results are normally specified as a mean hardness, or occasionally also as a range of hardness values.

The tensile test requires more sample preparation than the hardness test, as it involves applying a uniformly increasing extension to a standard tensile specimen, and measuring the required load. The output is a stress-strain curve, an example of which is shown in Figure 7.1.

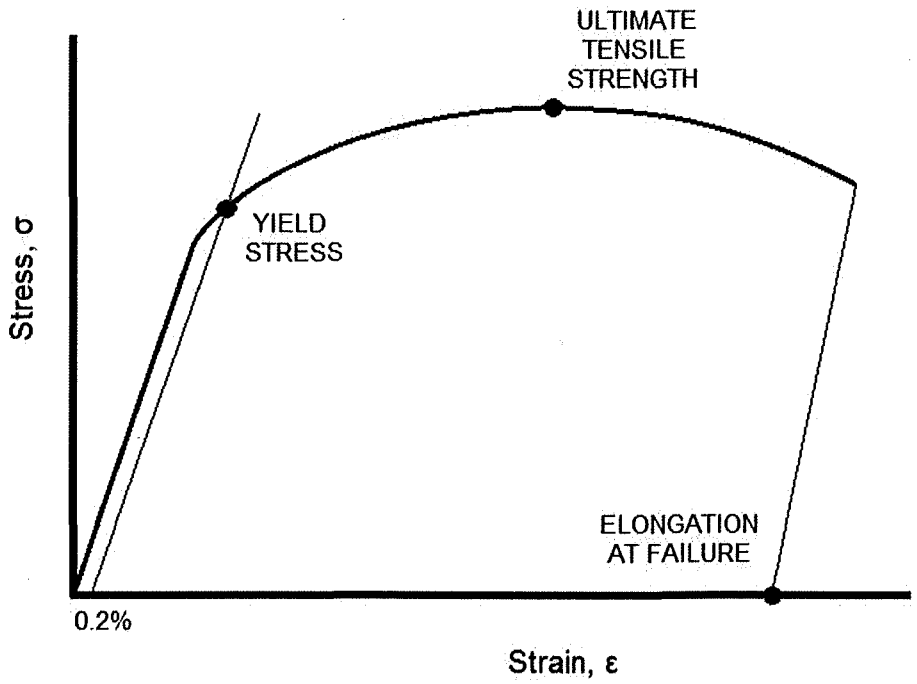

Figure 7.1 Example stress-strain curve

The advantage of tensile testing over hardness testing is the increased information provided by a tensile test. While the hardness of a material is correlated only with its strength, the tensile test provides information such as the elastic modulus, the yield strength, the ultimate tensile strength (UTS) and the ductility at failure. The yield strength is normally calculated according to the 0.2% offset method (shown in Figure 7.1), which involves constructing a line from the 0.2% strain mark parallel with the elastic region of the stress-strain curve. The intercept between this line and the curve is known as the 0.2% offset yield strength, or just the offset yield strength.

Plastic deformation occurs due to the generation, interaction and motion of dislocations, which occurs along specific slip planes (primarily {111} in f.c.c. materials), and is driven by the applied stress (for more detail regarding dislocation theory, [1] is recommended). The critical resolved shear stress at which dislocation motion is activated in a single crystal signifies the yield stress. In polycrystals, the yield stress is affected by several microstructural factors, including the amount of retained strain present in the material and the grain size. Increasing the amount of retained strain in the microstructure increases the density of dislocations present, and decreases their relative mobility due to the interactions between their relative strain fields. Increasing the grain size causes a decrease in yield strength, as grain boundaries act as obstacles to dislocation motion. Dislocations pile-up at obstacles such as grain boundaries, creating a back stress which limits the mobility of further dislocations within the stress field. Therefore, increasing the spacing of grain boundaries by increasing grain size reduces this back stress, and enables dislocations to move at lower applied stresses.

7.3 Hardness Test Method

In total, seven combinations of GBE parameters were selected for hardness testing in addition to the as-received sample, as shown in Table 7.1. Each condition is denoted by a name and a numeric label in future figures.

Table 7.1 Samples selected for hardness testing

Number of Cycles	Deformation per Cycle	Annealing Temperature	Annealing Time	Sample Name	Sample Label
-	-	-	-	[AR]	(1)
4	6%	1075°C	10 min	[4x6,1075,10]	(2)
4	6%	1075°C	20 min	[4x6,1075,20]	(3)
4	6%	1100°C	10 min	[4x6,1100,10]	(4)
4	6%	1100°C	20 min	[4x6,1100,20]	(5)
4	6%	1100°C	30 min	[4x6,1100,30]	(6)
4	10%	1100°C	20 min	[4x10,1100,20]	(7)
4	10%	1100°C	30 min	[4x10,1100,30]	(8)

Specimens were cut from each GBE sample, with the surface oriented perpendicular to the rolling direction. They were then mounted and ground using standard metallographic techniques [2], as described in Chapter 4. The final polishing step was performed with colloidal silica, and the surface was tested in the as-polished condition.

Specimens were tested using a pyramidal diamond Vickers Hardness tester at a load of 10 kilograms. Five tests were carried out on each specimen, and the results presented as the mean of the five results. Experimental uncertainty is represented by the standard deviation of the result set.

7.4 Hardness Test Results

The Vickers hardness and twin-excluded grain size for each sample is plotted in Figure 7.2.

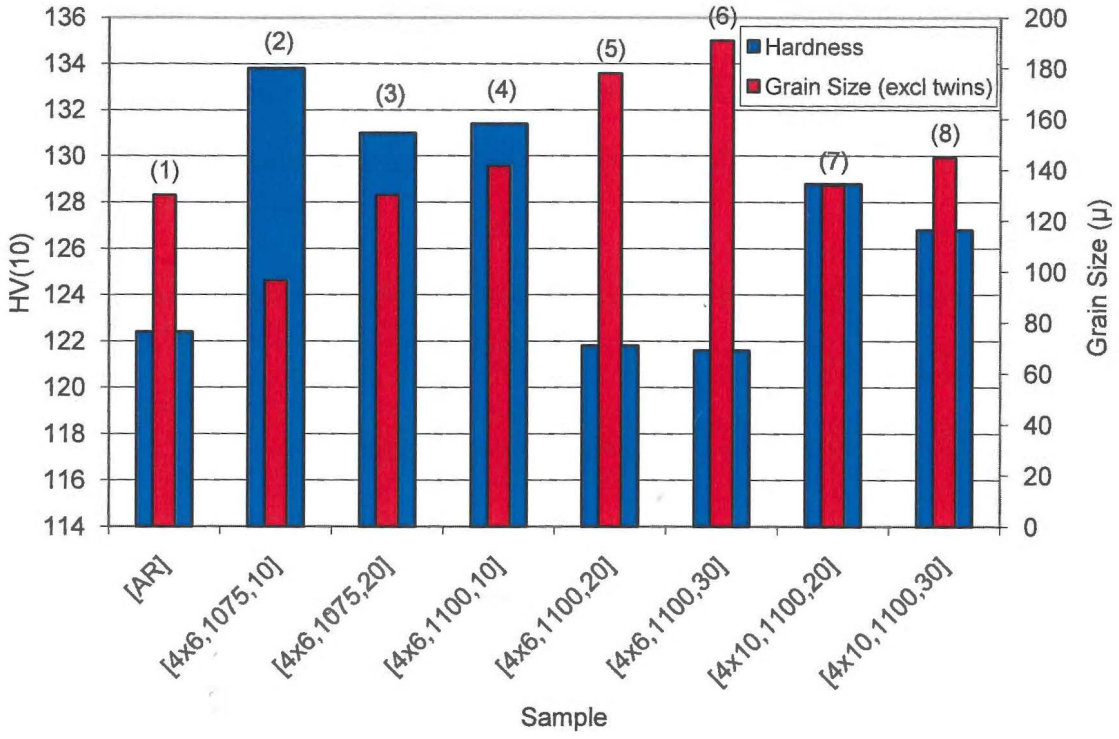

Figure 7.2 Vickers hardness and average grain size for each of the GBE conditions. Twin boundaries were excluded in the measurement of grain size.

The figure shows that most of the GBE processes have caused an increase in hardness compared to the as-received sample. It is also noticeable that the increases in hardness cannot be attributed to a decrease in grain size, as the grain size is not significantly reduced by any set of processing conditions. In fact, samples 3 and 4 show large increases in hardness despite having approximately the same grain size as the as-received condition. Furthermore, samples 5 and 6 show a similar hardness to the as-received sample, even though the grain size has increased by up to 45% in the case of the 30-minute annealed condition.

The Hall-Petch equation [3-4] is used to relate hardness to grain size, and can be stated as follows (by substitution of hardness for yield strength):

$$H = H_0 + \frac{K}{\sqrt{d}} \tag{7.2}$$

where H is the hardness, H_0 is a materials constant describing the theoretical hardness of a single crystal, K is a materials constant sometimes referred to as the strengthening constant, and d is the average grain diameter. It is important to note that this average grain diameter is measured according to ASTM E-112 [5] and twin boundaries are excluded in its calculation.

According to equation 7.2, plotting the material hardness, H, against the inverse root of the average grain size, $d^{-1/2}$, should yield a straight line with gradient, K, and y-intercept H_0. This relationship is plotted for the eight samples tested in Figure 7.3.

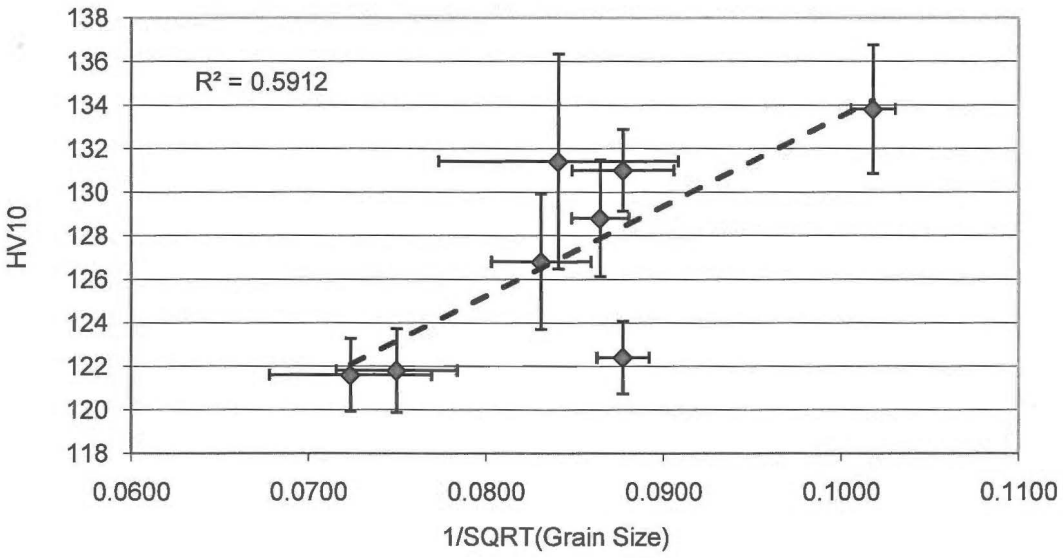

Figure 7.3 Hardness versus inverse square root of average grain diameter (excluding twins) for as-received and GBE samples

The trend line in this figure represents the Hall-Petch relationship. It is noticeable that the trend line does not pass through all data points, and the R^2 value of 0.59 shows that the fit is poor.

The most likely reason for the discrepancy between the Hall-Petch relation and the experimental observations lies in the definition of average grain size. Although the Hall-Petch relation is typically utilised according to the twin-excluded grain size (as defined by the ASTM standard E-112 [5]), there is mounting evidence [6-11] to suggest that twin boundaries have an effect on the motion of dislocations, and therefore should be included in structure-property correlations.

For these reasons, the Hall-Petch relationship is also plotted in Figure 7.4, where the twin-included grain size (also termed crystallite size in the literature [12]) has been calculated.

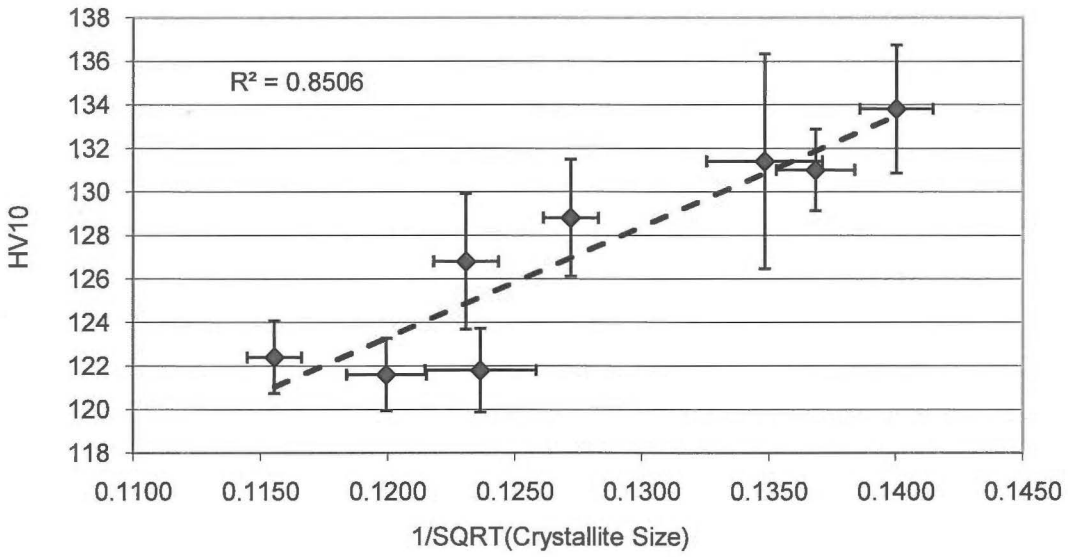

Figure 7.4 Hardness versus inverse square root of average grain diameter (including twins) for as-received and GBE samples

The R^2 value of 0.85 shows that the fit using the twin-included grain size is better than that of the twin-excluded grain size, and therefore these results add support to the claim that twin boundaries do in fact have an effect on mechanical properties. This result will be discussed further in conjunction with the tensile test results in Section 7.6.

7.5 Tensile Test Method

Eighteen tensile specimens were manufactured in total, comprising three different initial conditions (one as-received and two separate GBE conditions). Half of these samples were then aged, resulting in the testing matrix shown in Table 7.2. For convenience, the GBE conditions are referred to as [GBE10] and [GBE30] in this chapter, indicating a 10-minute or 30-minute anneal per cycle.

Table 7.2 Specimens for tensile testing

Number of Cycles	Deformation per Cycle	Annealing Temp.	Annealing Time	Aged?	Number of Samples	Sample Name
-	-	-	-	no	3	[AR]
4	6%	1100°C	10 min	no	3	[GBE10]
4	6%	1100°C	30 min	no	3	[GBE30]
-	-	-	-	yes	3	$[AR]_{aged}$
4	6%	1100°C	10 min	yes	3	$[GBE10]_{aged}$
4	6%	1100°C	30 min	yes	3	$[GBE30]_{aged}$

Aging was performed at 1000°C for 1000 hours in an inert Ar atmosphere, in order to eliminate environmental effects. At the conclusion of the aging period, the samples were water-quenched to eliminate the precipitation of γ' phase within the microstructure. The purpose of this aging was to simulate some evolution of the microstructure, to determine the changes in mechanical properties which may result from service. Metallographic samples were also removed from each material strip, and the microstructures were analysed by EBSD, using the methods described in Chapter 4. The total $\Sigma 3^n$ boundary length fractions and the grain size (excluding and including twins) were calculated from the resulting EBSD data sets.

Tensile specimens were then machined from each strip according to the dimensions in Figure 7.5.

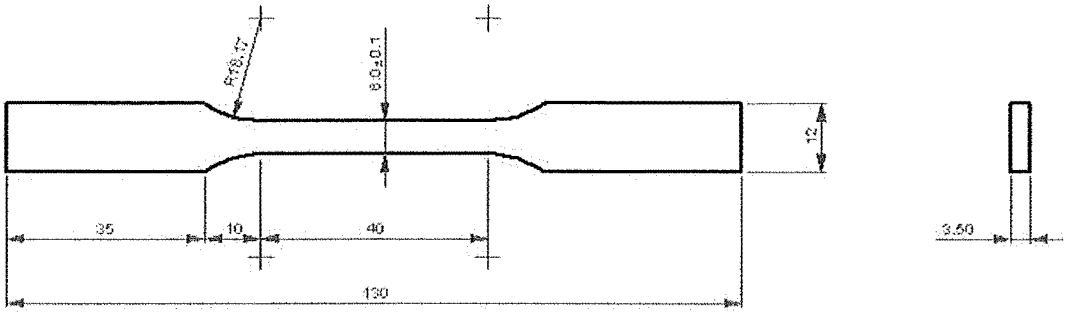

Figure 7.5 Dimensions for tensile test specimens (in mm)

The sample geometry was determined from ASTM E8 [13], the ASTM standard detailing tensile test methods. Material was removed equally from the faces of the starting strip, in order to avoid the fine-grained layer at the surfaces. The gauge length of each specimen was then ground to a 1200-grit finish using SiC paper before testing.

Each specimen was tested in an MTS 810 hydraulic test machine with a capacity of 100kN. Elongation was measured during the first part of each test using an Epsilon Technologies miniature axial extensometer. The elongation at failure was measured using fiducial marks at an initial spacing of 25mm, and the applied strain rate during the test was 1mm/s.

7.6 Tensile Test Results

7.6.1 Non-Aged Condition

Representative stress-strain curves for the three different non-aged samples are shown in Figure 7.6.

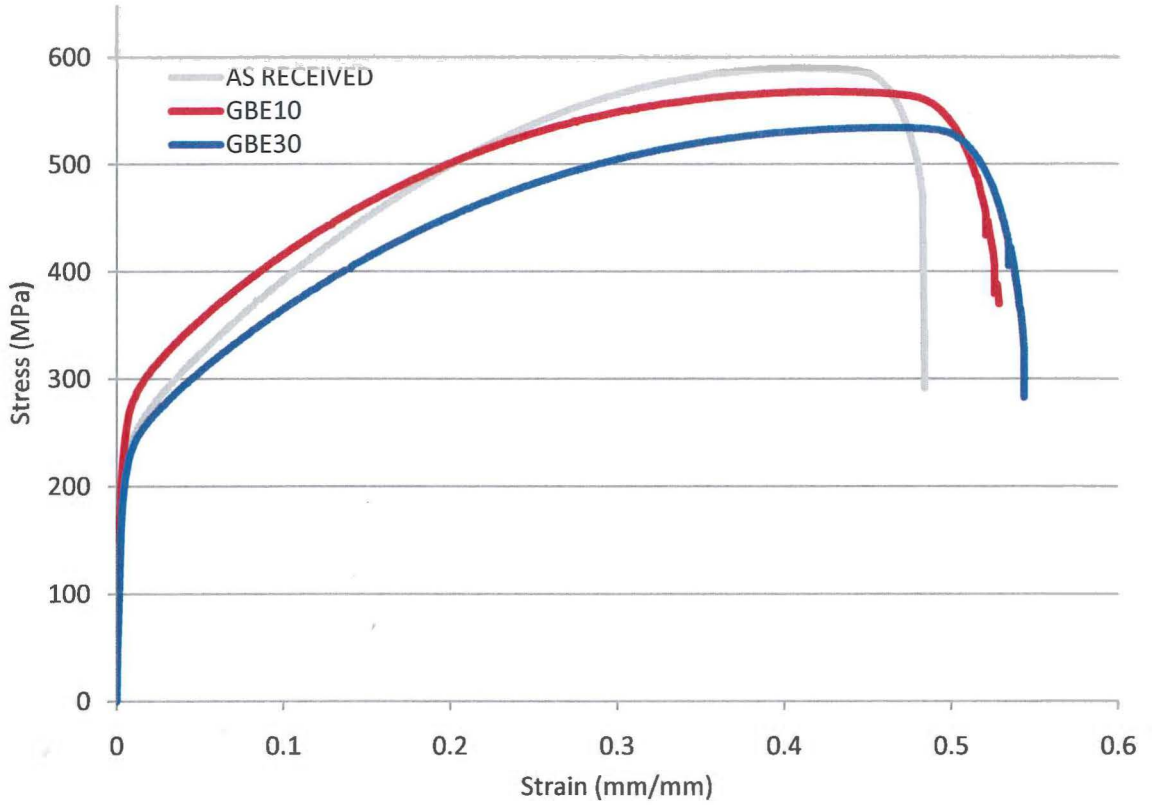

Figure 7.6 Representative stress-strain curves for non-aged samples

From these data, the mechanical properties were calculated and averaged for each sample, and are shown in Table 7.3. Experimental uncertainty is represented by the standard deviation from the three samples tested in each condition.

Table 7.3 Mechanical properties of non-aged samples

Sample	Elastic Modulus (GPa)	Yield Stress (MPa)	Ultimate Tensile Strength (MPa)	Elongation at Failure (%)
[AS RECEIVED]	212 ± 2	142 ± 4	586 ± 1	47.5 ± 1.6
[GBE10]	206 ± 14	147 ± 5	553 ± 9	51.5 ± 1.5
[GBE30]	209 ± 2	141 ± 5	540 ± 7	53.6 ± 1.1

As expected, the elastic modulus of all samples was approximately equal, and near the expected value of 196.5GPa [14]. The GBE10 sample showed a slightly higher yield stress

than the as-received sample and the GBE30 sample (as is also apparent in Figure 7.6), while the ultimate tensile strength was reduced in both GBE cases. However, the ductility of the GBE samples was improved by 8.5% in the GBE10 sample, and 13% in the GBE30 sample compared to the as-received condition.

The results of the microstructural analysis of the tensile samples are shown as averages in Table 7.4.

Table 7.4 Microstructural properties of non-aged tensile samples

Sample	Σ3 Fraction	Total $\Sigma 3^n$ Fraction	Grain Size (excluding twins)	Grain Size (including twins)
[AS RECEIVED]	44.9%	45.8%	117 ± 7μ	59 ± 4μ
[GBE10]	59.8%	71.5%	137 ± 9μ	49 ± 4μ
[GBE30]	62.7%	73.9%	207 ± 9μ	72 ± 5μ

The microstructural results therefore provide some interesting correlations. Firstly, the twin-excluded grain size of the GBE samples is significantly larger than that of the as-received condition, and therefore a corresponding decrease in yield stress may be expected according to the Hall-Petch relationship. However, Table 7.3 shows that this is not the case. The yield stress for all samples has been plotted against each measure of grain size in Figure 7.7, according to the $d^{-1/2}$ relationship described by the Hall-Petch equation.

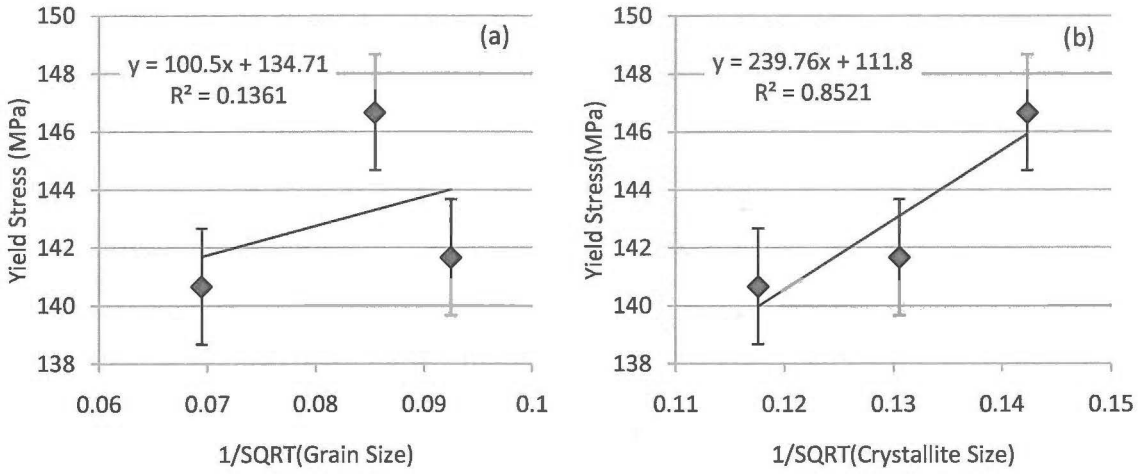

Figure 7.7 Relationship between yield stress and inverse root of the average grain size where (a) shows the twin-excluded grain size and (b) the twin-included grain size. Error bars represent standard error.

These results confirm the trend noticed in the hardness test; that the Hall-Petch equation predicts the dependence of yield stress more accurately where the twin-included grain size is considered, as opposed to the twin-excluded grain size which is more commonly used. There are two likely reasons for this discrepancy.

The first reason is due to the identification of twins by EBSD, which are classified according to boundary misorientation. Coherent annealing twins are a subset of the Σ3 classification, however twin boundaries cannot be entirely distinguished by misorientation alone. As explained in Chapter 4, any boundary within 5° of the 60°/<111> relationship is termed a "twin boundary" in the present work. However, this provides only an estimate, based on the correlation between coherency and low deviation from ideal [15]. In the case of the as-received material, it is likely from the linear morphology that the vast majority of Σ3 boundaries are coherent annealing twins. However, for GBE materials, it is thought that the GBE process introduces new segments of Σ3 boundary into the microstructure, which are not necessarily coherent annealing twins, but may have a deviation angle of <5°. For example,

Randle et al [16] showed that the {111} plane density in nickel decreased from 5.30 multiples of random distribution (MRD) to 5.17MRD after a commercial GBE process, despite the fact that the Σ3 length fraction increased from 43% to 63%. Had the new Σ3 boundary length been situated on predominantly {111} planes, an increase in the {111} plane density would have been expected. Because some of the newly formed Σ3 boundary segments are not coherent twins ({111} planes), they are likely to contribute to mechanical properties in that they provide obstacles to the motion of dislocations, while possibly being excluded from the conventional grain size intercept count due to their classification as twin boundaries. Therefore, the yield strength may be expected to show a better correlation when these boundaries are included in the intercept count (ie. the twin-included grain size).

The second reason is that there is also some likelihood that even coherent twin boundaries offer some resistance to dislocation motion, and therefore should be included in some way in structure-property correlations. Twin boundaries were not originally considered in the Hall-Petch relationship, as the grain size correlation was conceived from independent experimental observations on mild steels [3-4], which do not exhibit annealing twins. Since then, work by Pande in particular [7, 9], but also other researchers [6, 8, 10-11] has indicated that twin boundaries act as barriers to dislocation motion, and therefore act to increase the yield strength. However, the effect of twin boundaries is difficult to isolate, as creating microstructures with vastly different twin densities is difficult. Grain boundary engineering, due to the associated prolific twinning, may offer a solution to this problem once coherent twin boundaries can be accurately distinguished from the Σ3 group in sufficiently large numbers to allow statistically relevant correlations. In the case of the present results, it is likely to be a combination of the two reasons provided here which explains the trends

observed in the mechanical testing of these samples. Further analysis is required in order to determine the relative effects of each factor.

It is also noticeable from Table 7.4 and Figure 7.6 that the GBE samples exhibit increased elongation to failure compared with the as-received condition. On average, the ductility is 11% higher for the GBE samples. This trend of increasing ductility with no loss in yield strength for GBE materials has been noted in the literature on previous occasions [17-19]. In a study on nanotwinned copper by Lu et al [11], the relatively high ductility of a nanotwinned sample compared to conventional coarse-grained copper was attributed to the extra absorption of dislocations at twin boundaries. It is also possible that the dislocation absorption by twin boundaries may account for the extra ductility of the GBE samples in the present study. Although studies (e.g. [20-21]) have suggested that low-Σ CSL boundaries are generally more resistant to the absorption of extrinsic grain boundary dislocations (EGBDs), it is likely that the special geometry at such boundaries eventually becomes disrupted by dislocation absorption, thus causing "special" boundaries to act more like random high-angle boundaries (HABs) at high levels of strain. However, from the present results, the effect of dislocation absorption rate cannot be decoupled from the effect of initial grain size, which varies significantly between the three conditions, and has also been shown to affect ductility in similar materials [22].

Also noticeable from Figure 7.6 is the decreased rate of work hardening of the GBE samples compared to the as-received condition. In order to evaluate this change, the engineering stress and strain were converted to true stress and true strain according to the formulas [1]:

$$\varepsilon = \ln(e + 1) \tag{7.3}$$

$$\sigma = s(e + 1) \tag{7.4}$$

where ε and σ represent the true strain and stress respectively, e represents the engineering strain, and s the engineering stress. The value of the work hardening exponent, n, is given by the formula:

$$\frac{d\sigma}{d\varepsilon} = n\frac{\sigma}{\varepsilon} \tag{7.5}$$

The slope of the stress-strain curve was evaluated at each point using a linear least-squares fit, and hence n was calculated as a function of true strain. This relationship is shown in Figure 7.8 for strains up to the maximum load, where equation 7.4 breaks down due to necking effects.

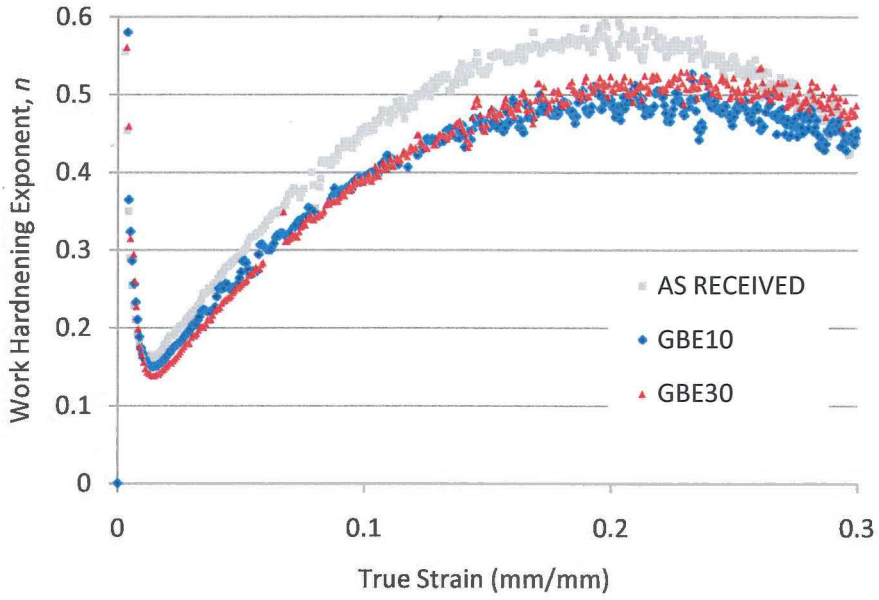

Figure 7.8 Work hardening exponent, n, as a function of true strain for all conditions

The results show that the work hardening exponent is not constant over the strain range and therefore cannot be evaluated as a single value. However, the conclusion that may be drawn from this analysis is that the work hardening exponent of the as-received sample is significantly higher than those of the GBE samples for almost the entire duration of the plastic region.

In summary of this information, the properties of most concern in industrial applications of this material are the the yield stress and the elongation at failure (ductility). The results of this testing show that grain boundary engineering provides a method to improve the ductility of this material, whilst simultaneously retaining or even improving the yield stress. Therefore, any changes in the high-temperature properties of this alloy do not come at the expense of the mechanical properties, which is an important result for this study.

7.6.2 Aged Condition

As stated previously, three samples of each condition were subjected to an aging procedure at 1000°C for 1000 hours in a pure Ar atmosphere, followed by a water-quench. The aged samples were analysed using EBSD, and the results are shown in Table 7.5.

Table 7.5 Microstructural properties of GBE samples after aging

Sample	Σ3 Fraction	Total $\Sigma 3^n$ Fraction	Grain Size (excluding twins)	Grain Size (including twins)
[AS RECEIVED]	44.9%	45.8%	131 ± 6μ	66 ± 3μ
[GBE10]	59.8%	71.5%	150 ± 8μ	58 ± 6μ
[GBE30]	62.7%	73.9%	234 ± 9μ	86 ± 5μ

Representative stress-strain curves for the three different conditions after aging in Ar at 1000°C for 1000 hours are shown in Figure 7.9.

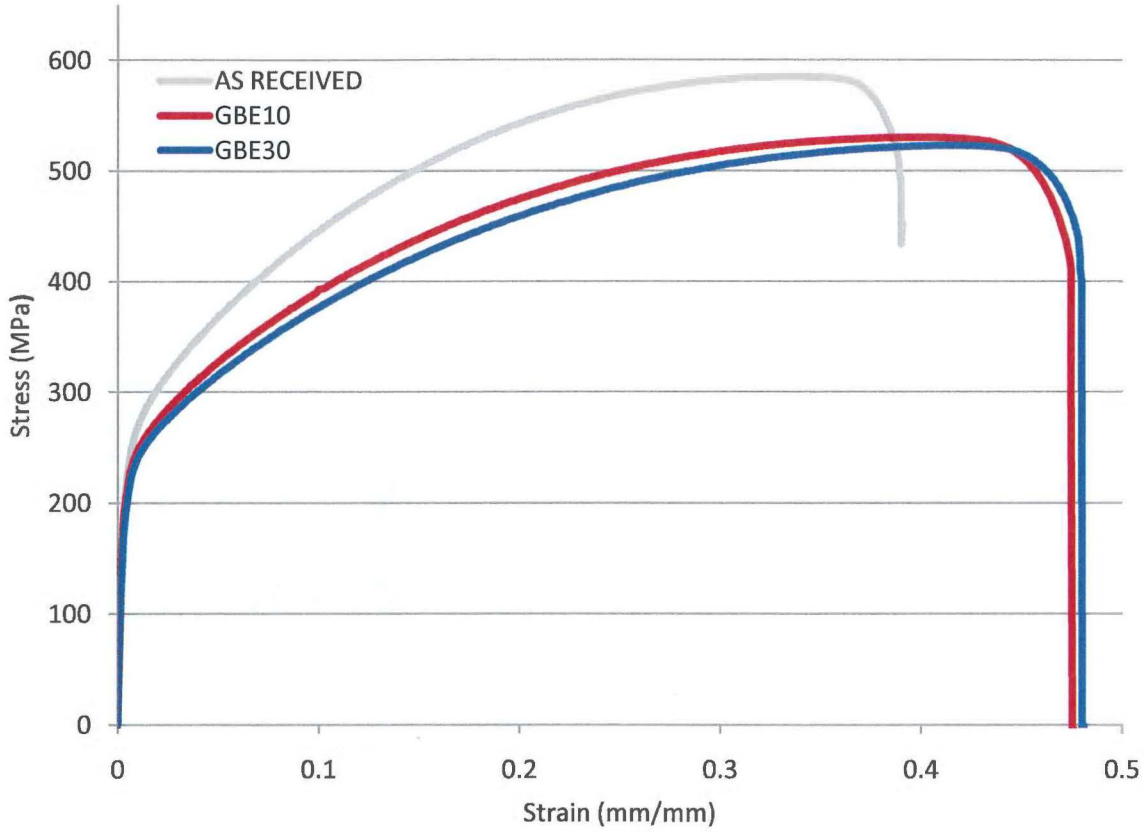

Figure 7.9 Representative stress-strain curves for aged samples

The average mechanical properties of these conditions are also summarised in Table 7.6.

Table 7.6 Mechanical properties of samples after aging

Sample	Elastic Modulus (GPa)	Yield Stress (MPa)	Ultimate Tensile Strength (MPa)	Elongation at Failure (%)
$[AR]_{aged}$	214 ± 2	147 ± 6	586 ± 5	41.9 ± 3.9
$[GBE10]_{aged}$	211 ± 5	143 ± 9	537 ± 7	47.6 ± 0.8
$[GBE30]_{aged}$	208 ± 3	127 ± 3	525 ± 3	47.8 ± 1.4

After aging, the as-received sample exhibits the highest yield stress and ultimate tensile stress of the three samples. However, the elongation at failure is significantly lower than that of the

two GBE samples, showing that the increased ductility of the GBE samples remains after the aging process.

The effect of the aging process can be determined by comparing the properties before and after aging, as shown in Figure 7.10.

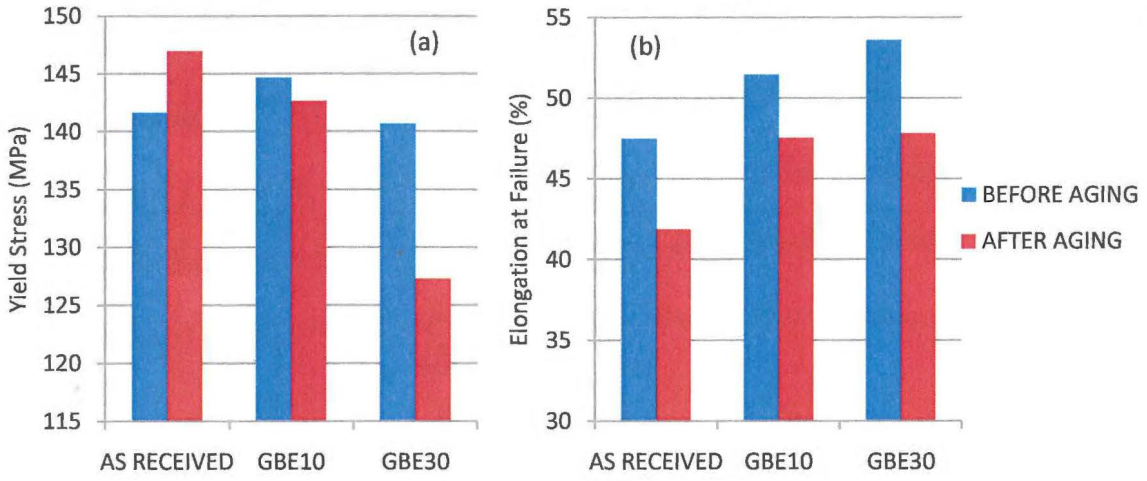

Figure 7.10 Comparison of properties for all samples before and after aging, showing (a) yield stress, and (b) elongation at failure

The yield strength has increased slightly in the as-received case, whereas there has been a moderate decrease in the [GBE30] sample. All three samples show reductions in ductility of between 7-12% compared with the pre-aged condition.

Secondary electron images (SEI) of the [GBE30] sample are shown in Figure 7.11, comparing the non-aged condition (a) to the aged condition (b).

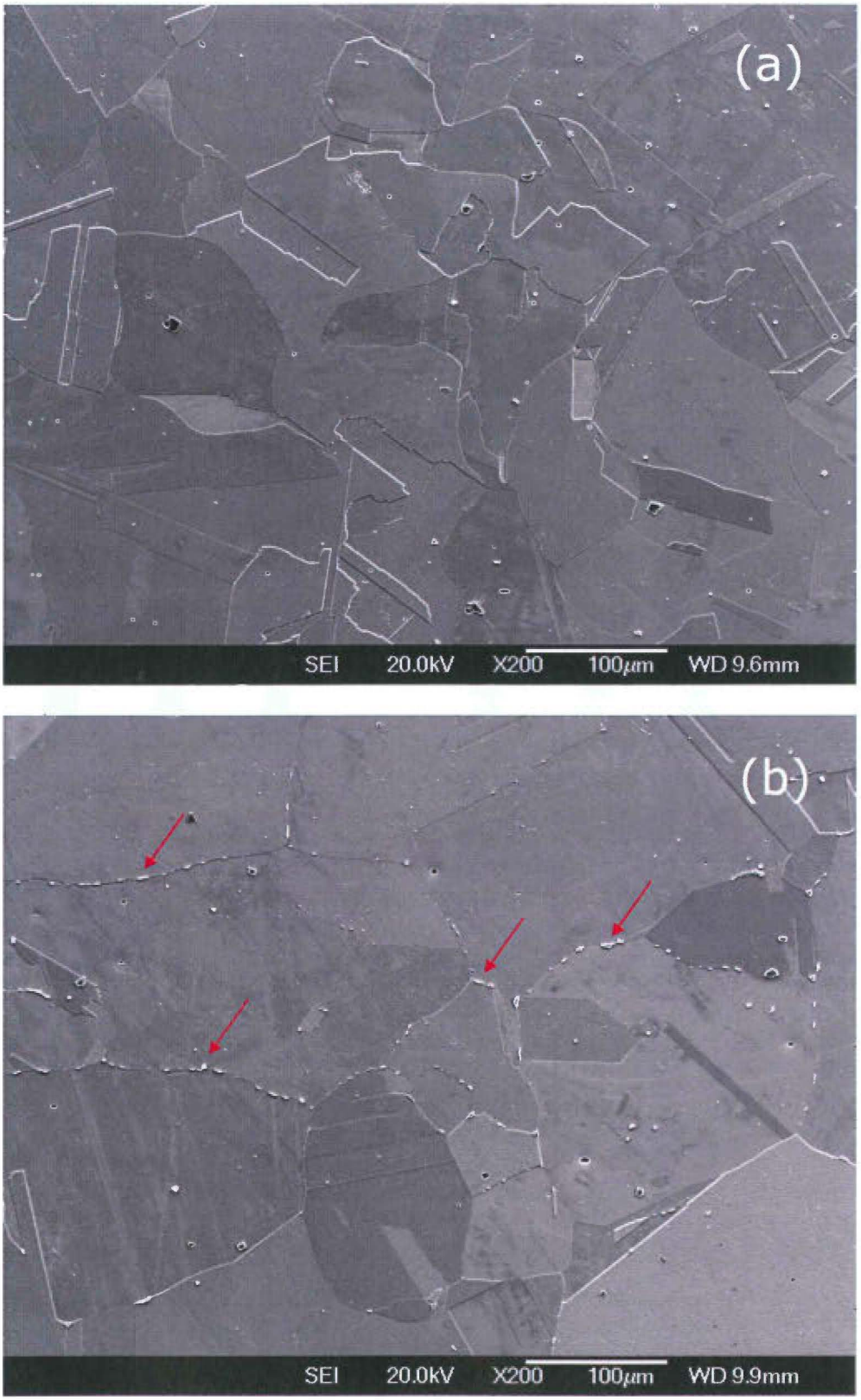

Figure 7.11 Scanning electron images of [GBE30] sample in (a) non-aged condition, and (b) after aging in Ar for 1000 hours at 1000°C. Arrows indicate chromium carbides.

The main difference between the two conditions is the formation of discrete precipitates in the high-angle grain boundary network during aging (indicated by arrows). These precipitates were confirmed as chromium carbides by Energy Dispersive Spectroscopy (EDS), shown in Figure 7.12.

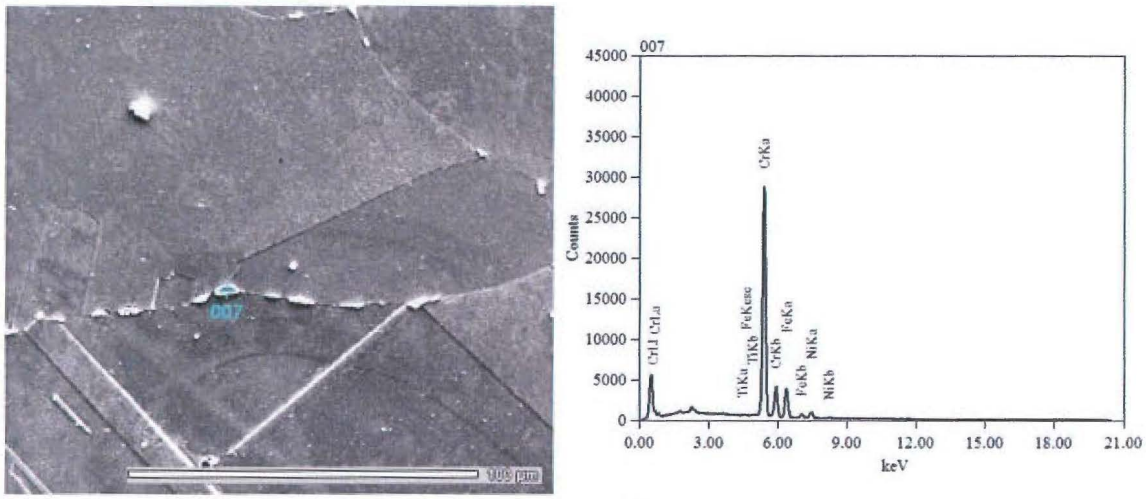

Figure 7.12 EDS spectrum of grain boundary carbide

This result is also consistent with the time-temperature-transformation (TTT) diagram for alloy 800H, which is reproduced from [23] in Figure 7.13.

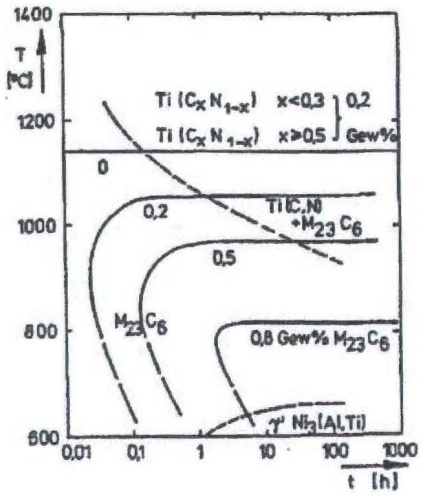

Figure 7.13 Time-temperature-transformation diagram for alloy 800H [23]

The formation of these chromium carbides is commonly associated with reduced ductility [24], and explains the decrease in elongation at failure noticed after aging in the present tests. The carbides may also provide a small amount of strengthening depending on their spacing (i.e the grain size), however this effect is countered by the fact that all samples also exhibited grain growth during the aging process. The grain size of each sample before and after aging is compared in Figure 7.14.

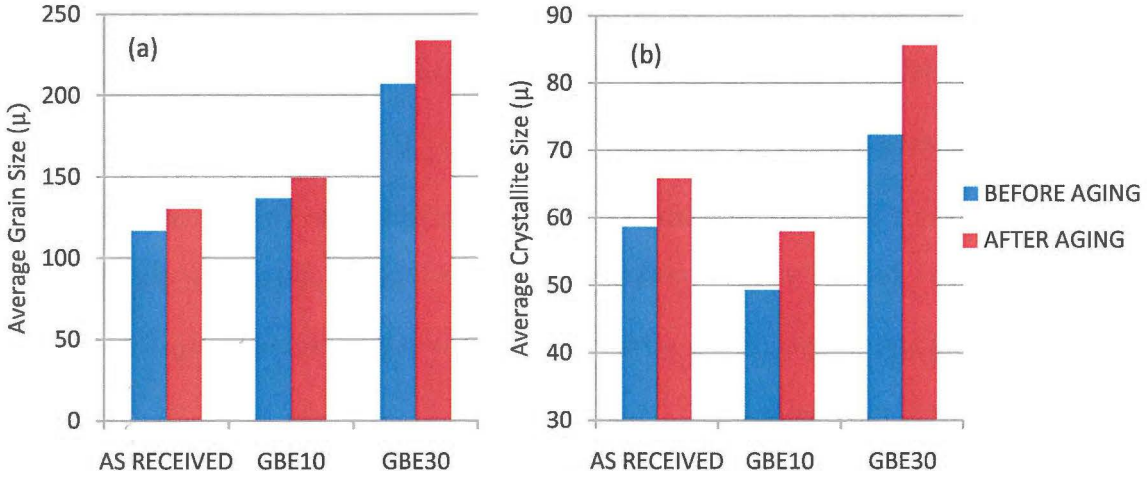

Figure 7.14 Grain size of tensile samples before and after aging showing (a) excluding twins and (b) including twins as grain boundaries

The largest decrease in yield strength ([GBE30]) is consistent with the largest amount of grain growth, which is logical according to the Hall-Petch relationship. Ultimately, these results show that the [GBE10] sample exhibits the best combination of yield strength and ductility, both before and after the aging process.

7.7 Conclusions

From the analysis of the mechanical properties of GBE 800H, several conclusions may be drawn. The grain boundary engineering process increased the ductility of the material by 8-12% compared with the as-received condition. This increase in ductility did not come at the

expense of yield strength, which was also shown to slightly increase in the case of [GBE10] and remain constant in the case of [GBE30].

It was also found that both hardness and yield strength showed a better correlation when twin boundaries were included in the calculation of grain size than when the grain size was measured in the conventional manner (excluding twins). The higher Σ3 density of the GBE samples therefore explains the higher hardness and yield strength of the GBE samples than is predicted by the Hall-Petch relationship, suggesting that twin boundaries do have an effect on the motion of dislocations.

In summary, grain boundary engineering provides a method of simultaneously increasing both the yield strength and ductility of a material, which improves its suitability for service in the Methanex pigtail tube application.

7.8 References

[1] Dieter, G. E., *Mechanical Metallurgy*, McGraw-Hill Inc., 1961.

[2] Vander Voort, G. F., *Metallography: Principles and Practice*, McGraw-Hill, New York, 1984.

[3] Hall, E. O., *Deformation and ageing of mild steel*, Phys. Soc. London 64B (1951) 747-753.

[4] Petch, N. J., *Cleavage strength of polycrystals*, J. Iron Steel Inst. London 174 (1953) 25-28.

[5] ASTM, *E-112: Standard test methods for determining average grain size*, ASTM International, 1996.

[6] Thaveeprungsriporn, V., Was, G.S., *The role of coincidence-site-lattice boundaries in creep of Ni-16Cr-9Fe at 360C*, Metall. and Mat. Trans. A 28A (1997) 2101-2112.

[7] Pande, C. S., Rath, B. B., Imam, M. A., *Effect of annealing twins on Hall-Petch relation in polycrystalline materials*, Mat. Sci. & Eng. A 367 (2004) 171-175.

[8] Babyak, W. J., Rhines, F. N., *Relationship between boundary area and hardness of recrystallized cartridge brass*, Trans. AIME 218 (1960) 21-23.

[9] Pande, C. S., Imam, M. A., Rath, B. B., *Study of annealing twins in FCC metals and alloys*, Met. Trans. A 21 (1990) 2891-2896.

[10] Pestman, B. J., De Hasson, J., Vitek, T. M., Schaping, F. W., *Interaction between lattice dislocations and grain boundaries in FCC and ordered compounds: a computer simulation*, Phil. Mag. A 64 (1991) 951-969.

[11] Lu, L., Shen, Y., Chen, X., Qian, L., Lu, K., *Ultrahigh strength and high electrical conductivity in copper*, Science 304 (2004) 422-426.

[12] Coleman, M., Randle, V., *Changes in interface parameters and tensile properties in copper as a consequence of iterative processing*, Metall. & Mater. Trans. A 39 (2008) 2175-2183.

[13] ASTM, *E8: Standard Test Methods for Tension Testing of Metallic Materials*, 1996.

[14] Special Metals Corporation, *Technical Publication - Alloy 800H & 800HT*, 2004.

[15] Randle, V., Davies, P., *Deviation from reference planes and reference misorientation for $\Sigma 3$ boundaries*, Interface Sci. 7 (1999) 5-13.

[16] Randle, V., Rohrer, G. S., Miller, H. M., Coleman, M., Owen, G. T., *Five-parameter grain boundary distribution of commercially grain boundary engineered nickel and copper*, Acta Mater. 56 (2008) 2363-2373.

[17] Lehockey, E. M., Palumbo, G., Lin, P., *Improving the weldability and service performance of nickel- and iron-based superalloys by grain boundary engineering*, Metall. & Mater. Trans. A 29 A (1998) 3069-3079.

[18] Watanabe, T., *An approach to grain boundary design for strong and ductile polycrystals*, Res. Mech. 11 (1984) 47-84.

[19] Randle, V., Davies, H., *Evolution of microstructure and properties in alpha-brass after iterative processing*, Metall. & Mater. Trans. A 33 (2002) 1853-1857.

[20] Kokawa, H., Watanabe, T., Karashima, S., *Sliding behaviour and dislocation structures in aluminium grain boundaries*, Phil. Mag. A 44 (1981) 1239-1254.

[21] Kokawa, H., Watanabe, T., Karashima, S., *Dissociation of lattice dislocations in coincidence boundaries*, J. of Mater. Sci. 18 (1983) 1183-1194.

[22] Mannan, S. L., Samuel, K. G., Rodriguez, P., *Influence of temperature and grain size on the tensile ductility of AISI 316 stainless steel*, Mat. Sci. & Eng. A 68 (1985) 143-149.

[23] Degischer, H. P., Aigner, H., Lahodny, H., Spiradek, K., *Proc. Petten Int. Conf. High Temperature Alloys*, J. B. Marriott (Ed.) Elsevier Applied Science, 1985, p. 487.

[24] Martin, J. W., *Concise encyclopedia of the structure of materials*, Elsevier, 2007.

CHAPTER 8: CREEP PROPERTIES OF GRAIN BOUNDARY ENGINEERED ALLOY 800H

8.1 Introduction

Improving the creep properties of alloy 800H through grain boundary engineering may be the most effective way of improving the service life of this alloy in the pigtail application. Previous work [1-4] has shown that improvements in creep properties are possible through GBE, however the test conditions in those experiments have been relatively high stress and relatively short rupture lives compared to the pigtail tubes. Therefore, it was desirable to test the GBE microstructures (described in Chapter 4) at conditions which were directly applicable to service conditions. Creep rates were therefore extracted for all samples under test conditions of 950°C and 12 MPa.

In this chapter, the importance of relevant test conditions is first explained, and the dominant creep mechanism of alloy 800H under service conditions is estimated based on previous experimental evidence. The creep test method is then explained, with emphasis on the test conditions and the extraction of minimum creep rate from extensometer data. Finally, the creep properties of as-received and grain boundary engineered samples are presented and analysed in accordance with the rate equations presented by Frost and Ashby [5]. The results are also compared to the significant reductions in creep rate achieved in previous GBE studies [1-4].

8.2 Creep Mechanism of Pigtail Tubes

As outlined in Chapter 2, there are several competing mechanisms by which creep deformation may occur in a material. At a specific set of conditions (temperature and stress), one mechanism will be dominant, although other mechanisms also contribute to the creep rate. In order to correlate creep testing results with expected service performance, it is desirable to ensure that the dominant creep mechanism is the same in the creep test as under service conditions. However, the previous creep experiments [1-3] in the GBE field typically exhibit rupture lives on the order of 100-1000 hours, whereas the design life of the Methanex pigtail tubes is 100,000 hours or greater. This significant discrepancy severely limits the usefulness of rupture tests in predicting creep properties at service conditions, as it implies a fundamental change in the mechanism of creep damage. Therefore, for the present analysis, the creep testing conditions were deliberately chosen in order to activate the same dominant creep mechanism as is probable during service. More detail regarding the selection of test conditions is provided in Section 8.3.1.

In order to determine the dominant creep mechanism for a given temperature and stress, creep rate equations for each creep mechanism must be evaluated. The regions of dominance for each mechanism can be viewed graphically in the form of a deformation-mechanism map. An example of a deformation map for pure iron is shown in Figure 8.1, reproduced from Frost and Ashby's "Deformation Mechanism Maps" [5].

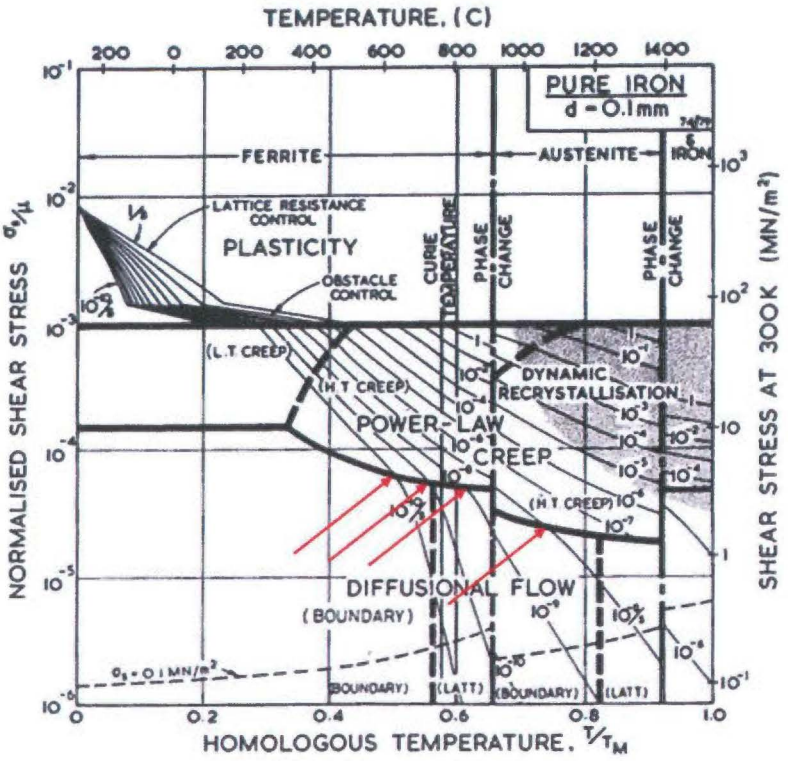

Figure 8.1 Example of a deformation map for pure iron [5]

The creation of a deformation-mechanism map experimentally involves creep testing a material at many different combinations of temperature and stress, and determining the resulting steady-state creep rate in each case. Where the steady-state creep rate is seen to change its dependence on temperature or stress, this implies a change in deformation mechanism. Such points are labelled with arrows in Figure 8.1. The rate equations for each creep mechanism are then empirically fitted to experimental data, and the map is constructed according to these equations.

Several deformation-mechanism maps were published by Frost and Ashby [5] in 1982. However, these maps were mostly presented for simple materials such as pure metals, and no such deformation map exists for alloy 800H. Instead, it is necessary in this work to make some assumptions based on the evidence available

It is a reasonable first step to consider the deformation mechanism map for 316 stainless steel, which is shown in Figure 8.2. 316 stainless steel is also an austenitic iron-nickel-based alloy, containing very similar levels of carbon and chromium to alloy 800H. The deformation map was constructed for a grain size of 200μ, which is similar to the grain size calculated in the present material.

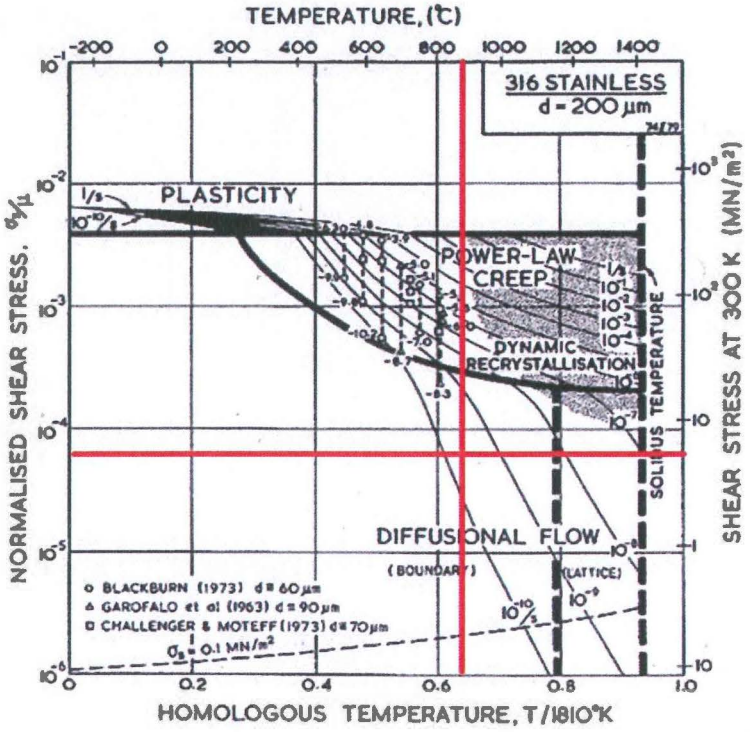

Figure 8.2 Deformation-mechanism map for 316 stainless steel [5] with Methanex pigtail service conditions given by the solid lines.

The approximate service conditions of the Methanex pigtails are marked by the crosshair (note the hoop stress has been converted into a shear stress using equation 1.5 in [5] - approximately 5.8MPa). It is apparent that the pigtail service conditions would result in a diffusion-based mechanism in this material. Diffusional creep involves the diffusion of vacancies within a non-hydrostatic stress field from areas of local tension to areas of local compression, and a corresponding flux of matter in the opposite sense [6]. If the diffusion occurs through the lattice, the mechanism is referred to as Nabarro-Herring creep [7-8], and

the strain rate varies with grain size according to d^{-2}. At lower temperatures or smaller grain sizes, diffusion instead occurs throughout the grain boundary network, in which case the mechanism is called Coble creep [9], and the strain rate varies according to d^{-3}.

From Figure 8.2, the transition temperature between grain boundary diffusion and lattice diffusion in 316 stainless steel is approximately 1200°C for the specified grain size of 200μ. This transition temperature is based on the relative diffusivity between the lattice and the grain boundary network (both are functions of temperature), and therefore is likely to be very similar in 800H for a similar grain size. For example, the transition temperature in 304 stainless steel and pure austenite [5] are also very close to 1200°C at grain sizes of 200μ and 100μ respectively. It is likely, therefore, that of the two diffusional mechanisms, Coble creep is more significant at the Methanex pigtail service temperature of 870°C.

Further support for a diffusional creep mechanism may be found in the work of Spiradek et al [10], who studied the relationship between the microstructure of 800H and the high-temperature creep properties at stresses between 25 and 80MPa and at a temperature of 800°C. They observed a minimum creep rate at stresses of 25-30MPa which was disproportionately lower than the creep rates at higher stresses. The stress exponent, n, was calculated according to the equation:

$$\dot{\varepsilon} \propto \left(\frac{\sigma}{\mu}\right)^n \tag{8.1}$$

where $\dot{\varepsilon}$ is the minimum creep rate, σ is the applied shear stress, and μ is the shear modulus. At the stresses in the range 25-30MPa, the stress exponent, n, was calculated to be approximately one, which coincides with the stress-dependence of diffusional creep according to the fundamental rate equation for diffusional flow, shown in equation 8.2.

$$\dot{\varepsilon} = \frac{42\sigma\Omega}{kTd^2} D_{eff} \tag{8.2}$$

where σ is the shear stress, Ω is the atomic volume, k is the Boltzmann constant, T is the absolute temperature, and D_{eff} is an effective diffusion coefficient which combines core and lattice diffusion.

At higher stresses, the stress exponent rose to approximately 8, signifying that power law creep was dominant under the higher-stress conditions. The rate equation for power law creep is given in equation 8.3.

$$\dot{\varepsilon} = \frac{A_2 D_{eff} \mu b}{kT} \left(\frac{\sigma_s}{\mu}\right)^n \tag{8.3}$$

using the same constants as equation 8.2 and adding a dimensionless constant, A_2, the Burger's vector, b, and the stress exponent, n. Typical values of n within the power-law regime range from 3 to 10.

From Figure 8.2, it is apparent that the transition between power-law creep and diffusional flow is relatively constant with temperature. Therefore, it is unlikely that the temperature difference between Methanex pigtail service (~870°C) and the Spiradek experiments (800°C) would result in a change in dominant mechanism. Spiradek [10] calculated the transition from power-law creep to diffusional creep to occur in the stress range 25-30MPa, and therefore it may be reasonably inferred that diffusional creep is likely to be significant at pigtail stresses of approximately 10MPa.

However, a significant contribution from power-law creep cannot be ruled out. Power-law creep involves the thermally-assisted glide and climb of dislocations, as opposed to point defects, and therefore requires higher stresses than diffusional creep. The term "power-law"

signifies a dependence of strain rate on stress raised to the n^{th} power, where n is an empirical constant normally between 3 and 10. In its simplest form, power-law creep shows no dependence on grain size [5]. It is impossible to theoretically determine the relative contributions from power-law creep and dislocation creep without accurate determination of several material constants, many of which vary as a function of temperature. In summary therefore, it must be concluded that the most likely creep mechanisms active at Methanex pigtail service conditions are Coble creep plus some contribution from power-law creep. The creep results are analysed in terms of the likely creep mechanisms further in Section 8.4.

8.3 Creep Test Method

8.3.1 Selection of Creep Testing Conditions

As explained in the previous section, it is likely that Coble creep, which involves the transport of matter through the grain boundary network, accounts for a significant fraction of creep strain at Methanex service conditions. Most creep tests are performed at much higher stresses, and in the case of 800H, these higher stresses could well activate the dislocation-based power-law creep mechanism. At the very least, the relative contribution from each mechanism is altered. Therefore, in order to retain continuity with service conditions, the creep test conditions were deliberately selected with the aim of ensuring a similar creep mechanism to that of service.

Figure 8.2 shows a much greater dependence on stress than temperature for the region dominated by diffusional creep. Therefore, the testing stress was limited to 12MPa, only approximately 2.5MPa higher than the inner wall stress in service (excluding the bend sections). The temperature was set at 950°C, which yielded a measurable expected creep rate of approximately 0.0004% per hour, according to Figure 8.3 (note the 950°C isotherm has

been linearly interpolated). This creep rate corresponds to a strain rate of approximately 11.1×10^{-10}/s.

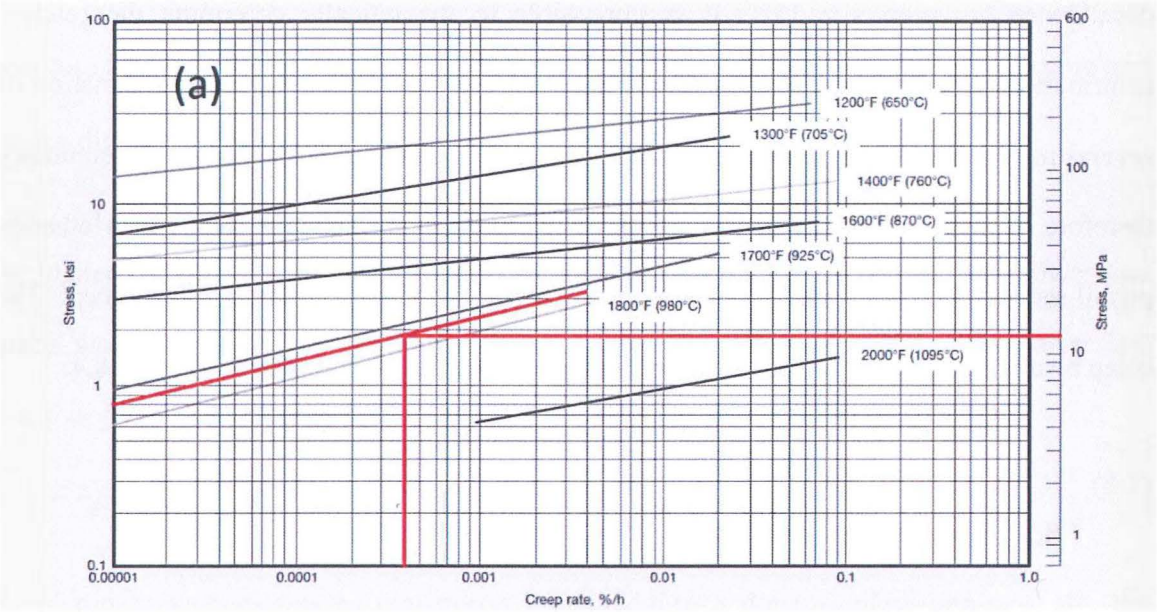

Figure 8.3 Expected creep rate for testing conditions, based on manufacturer's data [11]

Under the assumption that all of the strain is contained within the 35mm gauge length of the sample, the expected creep rate can be approximated as:

$$\dot{e} = l\varepsilon = 35 \times 0.0004/hr \approx 0.14\mu/hr \tag{8.4}$$

This calculated creep rate of 0.14μ/hr is reasonably close to the expected resolution limit of the test rig, and hence provides a good balance between ensuring the correct creep mechanism is active, and ensuring the resulting strains are measurable. All creep tests were therefore run at 950°C and 12MPa.

8.3.2 Creep Testing Method

Several GBE conditions were selected for creep testing against as-received samples, as shown in Table 8.1. Numeric sample labels are provided for reference in future figures.

Table 8.1 Conditions selected for creep testing

Number of Cycles	Deformation per cycle	Annealing Temperature	Annealing Time	Number of Samples	Sample Name	Sample Labels
AS RECEIVED				4	[AR]	(1-4)
4	6%	1100°C	10 min	2	[4x6,1100,10]	(5-6)
4	6%	1100°C	20 min	2	[4x6,1100,20]	(7-8)
4	6%	1100°C	30 min	2	[4x6,1100,30]	(9-10)
4	10%	1100°C	20 min	1	[4x10,1100,20]	(11)
4	10%	1100°C	30 min	1	[4x10,1100,30]	(12)

Creep specimens were machined from each material strip according to the dimensions in Figure 8.4. The geometry of the creep specimens was consistent with the guidelines given in ASTM E8 [12]. The approximate stress distribution within the sample may also be found in Appendix B.

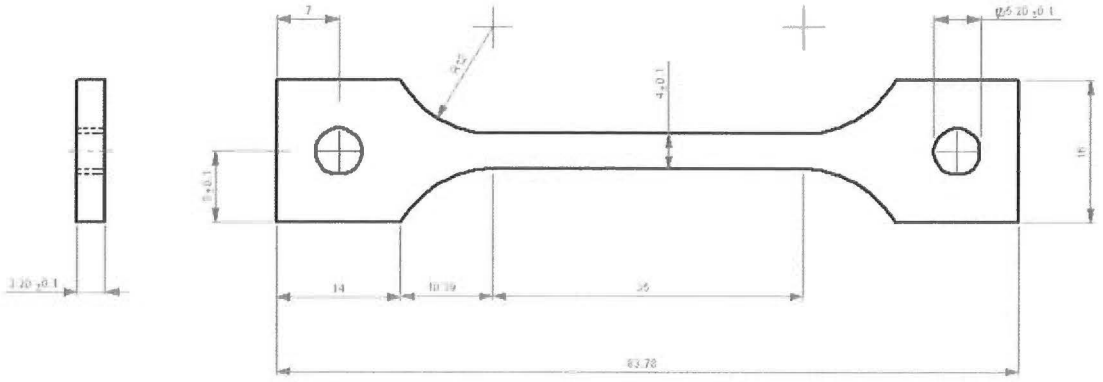

Figure 8.4 Creep sample dimensions (in mm)

Creep specimens were tested in series, with two specimens in the furnace simultaneously. The temperature of each sample was controlled by implementation of an isothermal furnace liner (IFL), which is claimed to provide an isothermal length to within 0.1°C. The IFL was built by ACT-1 [13], and consisted of two concentric pipes of an oxidation resistant stainless steel (Inconel 600), with the encapsulated space filled with a charge of pure sodium and

subsequently sealed. Local variations in temperature along the length of the pipe cause the local vapour pressure of sodium to increase, and therefore initiate heat transfer away from the hot-spot. The temperature distribution was measured prior to testing and was found to be within 1°C along the 300mm length. The absolute temperature during the testing was measuring using two independent N-type thermocouples, of which the mean was used to control the temperature throughout the test. The temperature was controlled to within 0.5°C throughout the entire test (a representative temperature log is shown in Appendix B.4.1). The two thermocouple readings did not differ by more than 2-3°C, and therefore this temperature range may be assumed to be the absolute temperature accuracy of the system.

Loading was applied by suspended dead-weight load of approximately 15.5kg, and therefore the test setup can be described as uniaxial tension under constant load. The extra loading of the top sample with respect to the bottom sample (due to the mass of the extra grip and specimen) was calculated to be approximately 0.1MPa, and thus considered negligible.

Specimen extension was measured by linear variable displacement transducer (LVDT) with an approximate resolution of ~1μ and a range of ±300μ. The minimum resolvable strain rate was considered to be approximately 4-5x10^{-10}/s. Further details regarding the creep test rig setup are provided in Appendix B.

The creep specimens were heated initially at 3°C/min to the test temperature of 950°C. This heating stage was performed under a load of approximately 10% of the final loading, as described in the ASTM standard for creep testing – ASTM E139 [14]. The temperature was then allowed to stabilise for a period of two hours before the load was applied. The measurement of extension was begun approximately 1-2 minutes after the load was applied, and so the elastic strain was not recorded.

The sample extension exhibited relatively linear behaviour after a period of approximately 150-200 hours in all cases. The measured creep rates also agreed well with the manufacturer's data [11] (as discussed in Section 8.4), and therefore the minimum creep rate was obtained from this linear region. A representative strain-time curve (after data averaging – see section 8.3.3 for details) is shown in Figure 8.5.

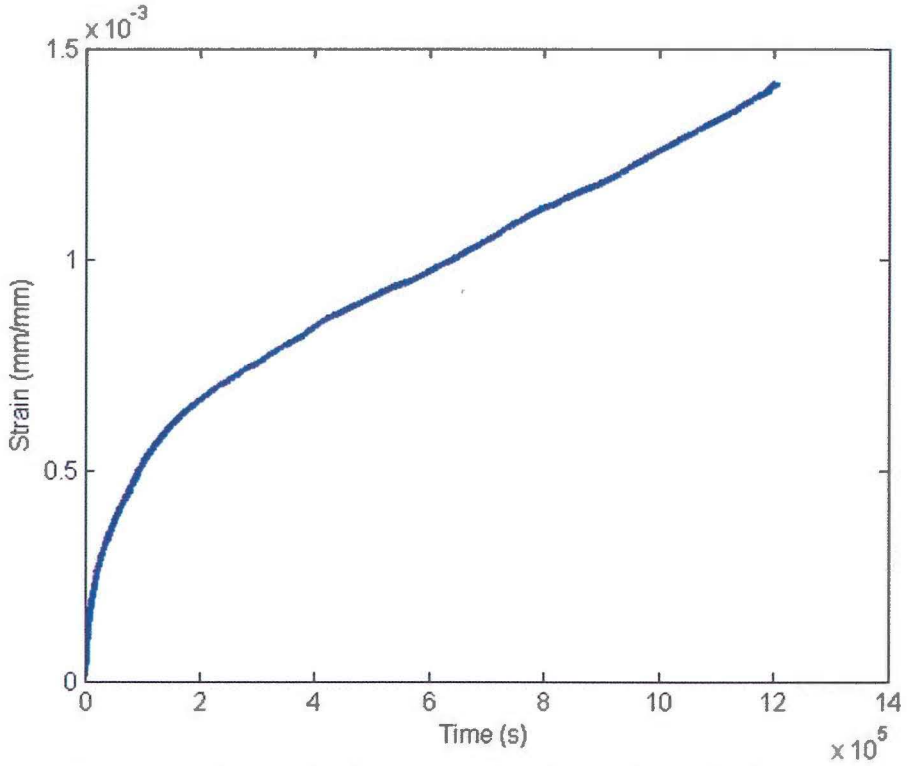

Figure 8.5 Representative strain-time curve showing regions of primary creep and steady-state creep.

Each test was therefore terminated after a period of 340-350 hours, once enough data was collected to determine the minimum creep rate. The advantage of interrupted creep testing is that the results are reasonably extrapolated to service conditions due to the similarities in temperature and stress, whilst ensuring the test duration remains reasonable. Measuring rupture life under these particular conditions would likely result in test durations of over three months per sample (850 days total), which was not considered feasible for the present study.

The specimens were cooled under load in order to preserve the microstructure, which was subsequently analysed by EBSD. The LVDT data were post-processed to remove noise, and the secondary creep rate was extracted, as detailed in the following sections.

8.3.3 Data Averaging Technique

The LVDT extension measurements exhibited some short-range noise, on the order of ±1.0μm, likely due to small variations in voltage measurement. This noise exhibited constant maximum amplitude, and therefore could be eliminated by a data smoothing operation.

A moving average operation was selected for application to the raw data. For each point, i, a range, R_i, was defined according to equation 8.5:

$$R_i = \{y_{i-n}\ y_{i-n+1}\ y_{i-n+2}\ \cdots\ y_{i+n}\} \tag{8.5}$$

where y_i is the data value at point i, and n is the span of the data range. For the present analysis, the minimum span was set at 40 hours either side of the central data point in order to remove the small fluctuations of the extensometer with ambient temperature (see Appendix B.4.3). For points within 40 hours of the beginning or end of the test, the range was shortened as per equation 8.6, where L denotes the total number of data points:

$$R_i = \begin{cases} y_1\ y_2\ \cdots\ y_{(2i-1)} & i < n \\ y_{(2i-L)}\ y_{(2i-L+1)}\ \cdots\ y_L & i > (L-n) \end{cases} \tag{8.6}$$

The smoothed data value at each point, denoted z_i, was then calculated as the mean of the range, as stated in equation 8.7:

$$z_i = \bar{R}_i \tag{8.7}$$

The total effect of the data smoothing is illustrated in Figure 8.6, which shows a comparison between raw data and smoothed data for an as-received sample.

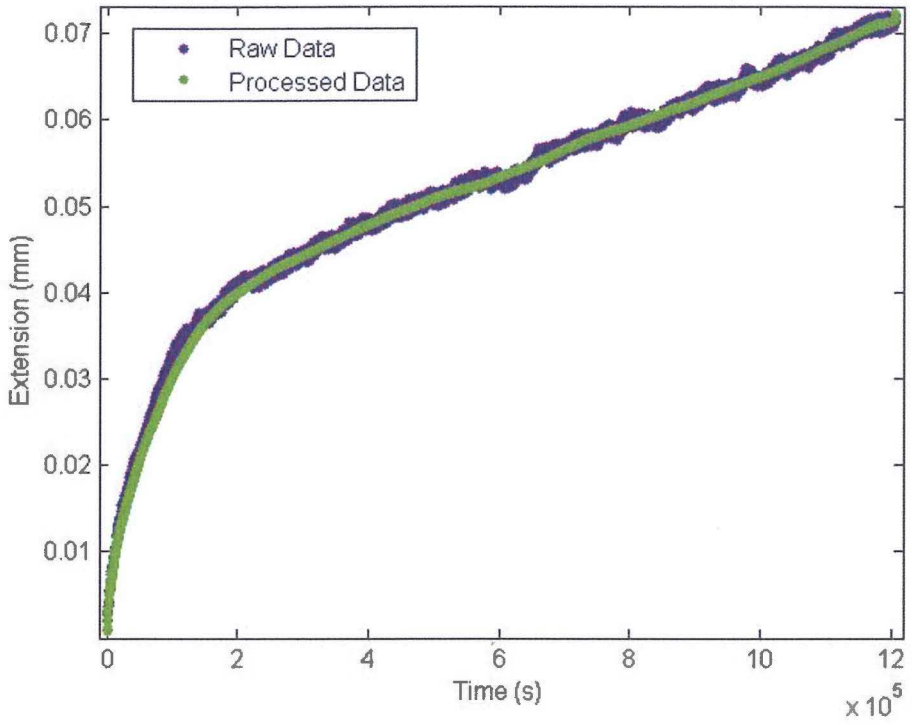

Figure 8.6 Creep curve showing the effect of the moving average data smoothing method

The smoothed data set was then used to extract the minimum creep rate, as explained in the following section.

8.3.4 Extracting the Minimum Creep Rate

The instantaneous creep rate was initially calculated at intervals of 30 seconds according to a linear least-squares fit with a span of 60 hours. An example creep rate curve is shown in Figure 8.7. Note the creep rate was not evaluated during the first 60 hours or the last 60 hours of the test as the data was insufficient to define the span.

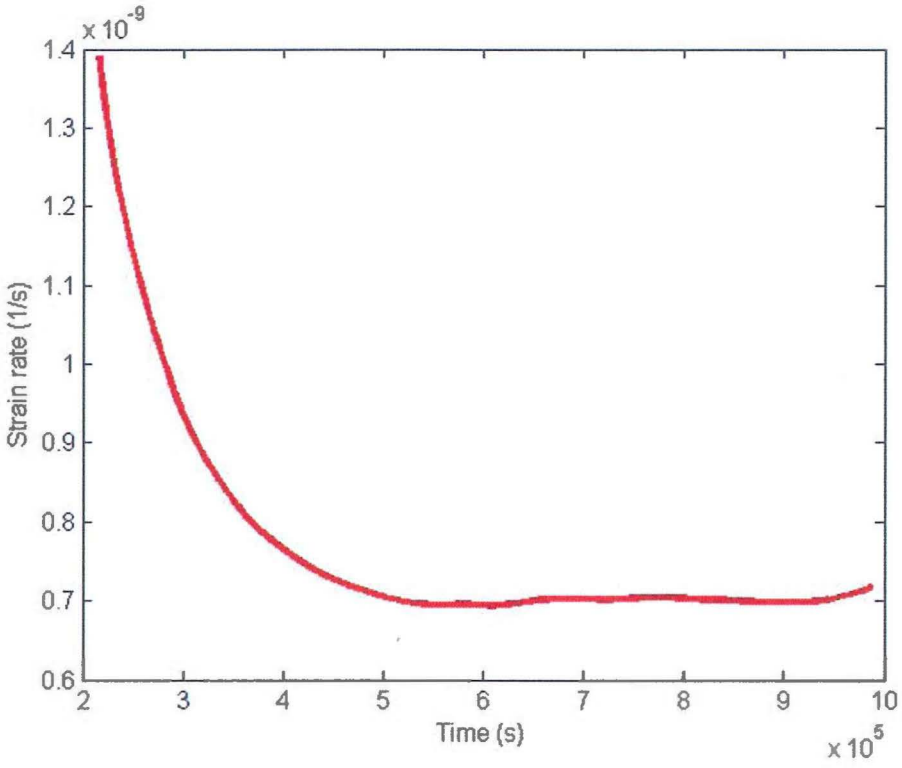

Figure 8.7 Example creep rate vs time curve

From the creep rate curves, it could be seen that the creep rate remained relatively constant in all cases over the final 5×10^5 seconds. Hence, a linear least-squares fit was applied to the smoothed data set throughout the final 5×10^5 seconds (approximately 40% of the total test period), according to the equation:

$$S = \sum_{i=1}^{2n+1} \left(z_i - (p_1 x_i + p_2)\right)^2 \tag{8.8}$$

where S is the residual term, x_i is the value of the independent variable (time) and p_1 and p_2 are the parameters defining the line of best fit. The minimum creep rate was then defined as the gradient (p_1 in equation 8.10) of the linear best fit line.

8.4 Creep Test Results and Discussion

The minimum creep rate was evaluated for each sample, and the results are shown in Figure 8.8.

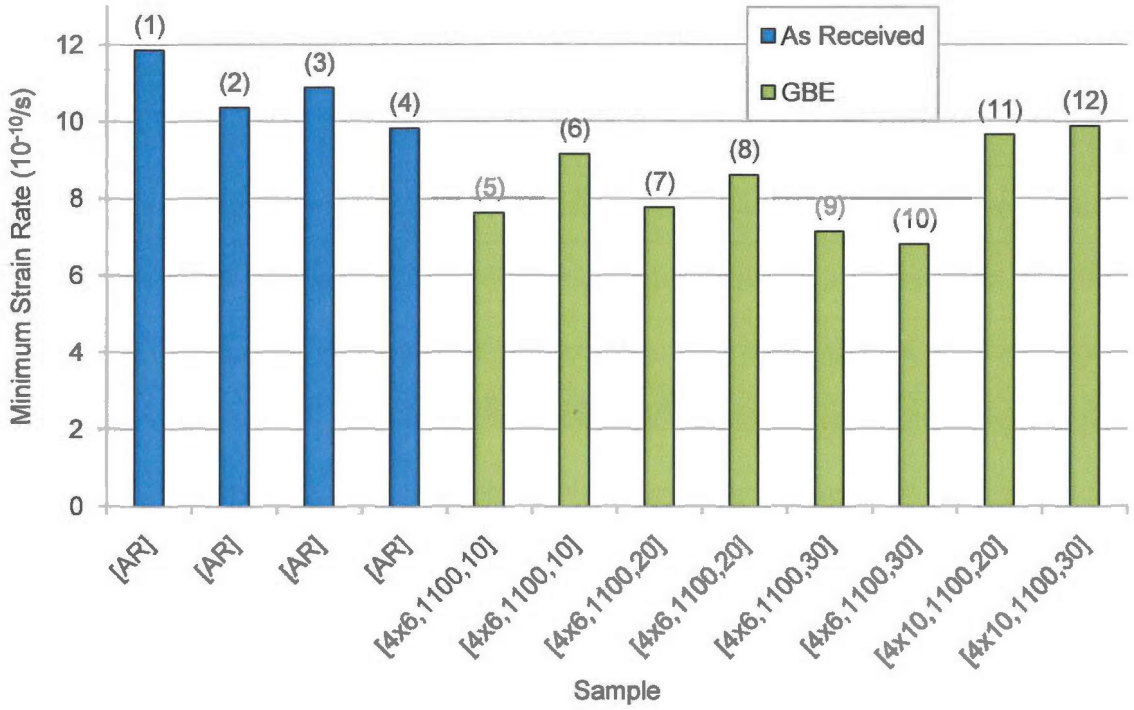

Figure 8.8 Minimum creep rates for all samples

It is apparent from Figure 8.8 that the highest minimum creep rates of all samples are those of the as-received samples, which exhibit an average minimum creep rate of $10.7 \times 10^{-10} s^{-1}$ over the four samples. This is consistent with the predicted creep rate of $11.1 \times 10^{-10} s^{-1}$ from the manufacturer's data [11], which was discussed in Section 8.3.1.

All of the 6% deformation samples (5-10) show decreased minimum creep rates compared to the as-received condition, of up to 30% in the case of samples 9 and 10. However, as creep rate is known to be affected by grain size, at least in the diffusional flow regime, it is more useful to plot the minimum creep rates as a function of initial grain size. This plot is shown in Figure 8.9.

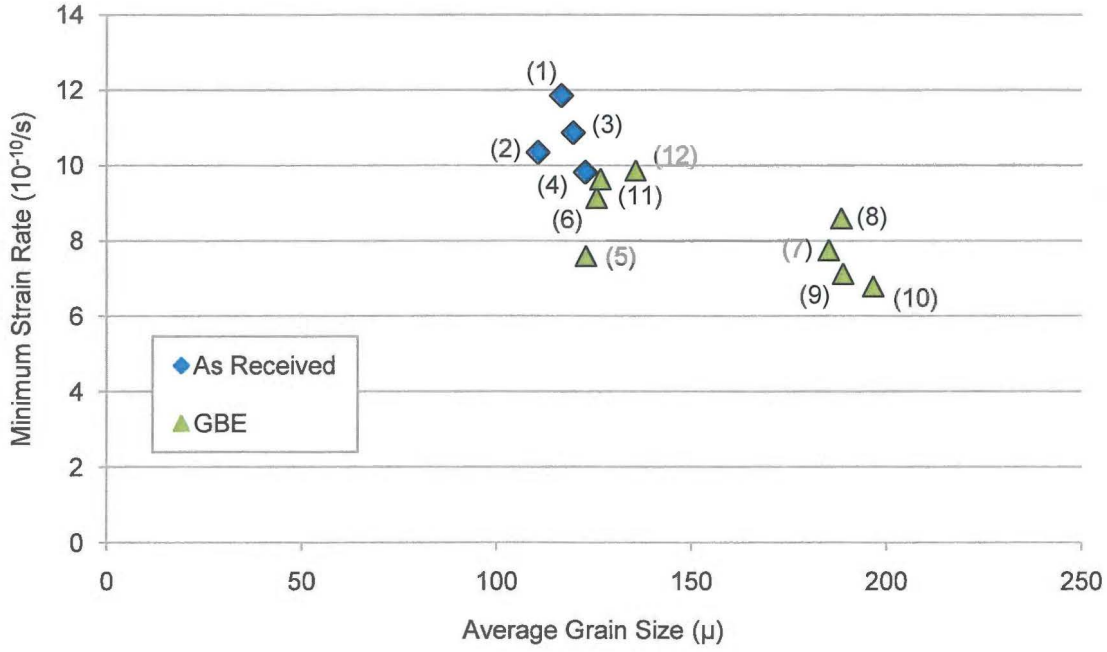

Figure 8.9 Minimum creep rates for all samples as a function of grain size

The results show a definite correlation with grain size, which makes it difficult to decouple the effects of the GBE processing. The dependence of creep rate on grain size cannot be calculated from the entire data set, as the samples exhibit fundamentally different microstructures. However, based on the GBE samples only (which were shown in Chapter 4 to have similar microstructures), and under the assumption that the two most significant creep mechanisms are power-law creep and Coble creep, the strain rate may be approximated in the following way:

$$\dot{\varepsilon}_{total} \approx \dot{\varepsilon}_{P-L} + \dot{\varepsilon}_{Coble} \tag{8.9}$$

From the rate equations in [5], the total strain rate may therefore be written as a function of grain size, d, as per equation 8.10:

$$\dot{\varepsilon}_{total} \approx A + bd^{-3} \tag{8.10}$$

where A represents the contribution from power-law creep (independent of grain size) and bd^{-3} represents the contribution from Coble creep. Calculating the average creep rate for the

GBE samples at each average grain size (combined to ~128μm and ~190μ) yields a set of simultaneous equations, which may be solved for the constants A and b, as per equation 8.11:

$$\varepsilon^1_{total} = A + b(128)^{-3} = 9.06 \times 10^{-10} \qquad (8.11)$$
$$\varepsilon^2_{total} = A + b(190)^{-3} = 7.57 \times 10^{-10}$$

Solving these equations for the constants A and b yields the result $A \approx 6.9 \times 10^{-10}$, suggesting that power-law creep may be responsible for 75-90% of the creep rate in the GBE samples, depending on the grain size. This result disagrees with the dominance of diffusional mechanisms at 25-30MPa predicted by Spiradek [10], albeit at a temperature of 800°C as opposed to 950°C, which was used in the present experiments. Figure 8.1 and Figure 8.2 show some dependence of dominant creep mechanism on temperature within this range, and therefore the temperature difference may explain part of the discrepancy. It is also possible that Coble creep has been retarded in the GBE samples by a reduction in diffusivity of the grain boundary network, which will be discussed further.

Of the samples which show a grain size of approximately 120-130μ, the GBE samples 7 & 8 exhibit the lowest minimum creep rate. On average, the creep rate of this GBE condition ([4x6,1100,10]) is 20% lower than that of the as-received samples. This decrease cannot be attributed to the grain size difference, as the difference in twin-excluded grain size is less than 10%, and Figure 8.9 and equation 8.11 suggests a much weaker dependence on grain size. Instead, it is the relative decrease in diffusivity of the grain boundary network as a whole which may account for the reduction in creep rate. The lower diffusivity of low-Σ boundaries compared to random HABs has been demonstrated on many occasions [15-19], although it is now thought that the lower diffusivity may be associated with favourable (ie. low energy) boundary plane configurations (which are indirectly associated with the $\Sigma 3^n$ family), as opposed to the CSL criterion. Nevertheless, equation 8.2 states that any reduction in the

diffusivity of the grain boundary network leads to a reduction in steady-state creep rate. It follows that introducing boundaries which, on average, exhibit reduced diffusivity compared to random HABs is one way to reduce the diffusivity of the network, and therefore reduce the steady-state creep response of the microstructure. However, it must be remembered that it is not only the number of low-diffusivity grain boundaries which must be considered, but their spatial distribution and the way in which the connectivity of high-diffusivity boundaries is interrupted by GBE processing. Hence, it is useful to revisit the grain boundary connectivity model (which was introduced in Chapter 5) at this stage and investigate the correlation between the connectivity parameter, $\bar{R}_{eff}$, and the steady-state creep rate. This analysis is provided in the following section.

8.5 Correlation Between Creep Rate and Boundary Connectivity

Recall from Chapter 5 that the parameter $\bar{R}_{eff}$ denotes a measure of the two-dimensional diffusion resistance of a unit microstructure, which contains a binary classification of grain boundaries (ie. high-diffusivity and low-diffusivity). The parameter encompasses not just the number of low-diffusivity boundaries which are present, but the way in which these boundaries become incorporated into, and disrupt the original boundary network.

While it may seem useful to compare the presented connectivity model with previous models described in Chapter 5 (such as the neutral twin model, the triple junction distribution model, or percolation theory) in terms of creep properties, it must be remembered that no previous model contains the ability to predict properties which are dependent on both grain size and grain boundary connectivity, as the present model is inherently able to. However, a reasonable test of the model exists in describing the correlation between steady-state creep rate and $\bar{R}_{eff}$, in comparison with the corresponding correlation with grain size. As the $\bar{R}_{eff}$

parameter has been shown to scale linearly with grain size (equation 5.15), it is possible to substitute $\bar{R}_{eff}$ for grain size, d, in equation 8.10, and analyse the creep data in terms of this equation using a residual least-squares approach. This analysis is shown in Figure 8.10 for (a) twin-excluded grain size, (b) twin-included grain size, and (c) $\bar{R}_{eff}$.

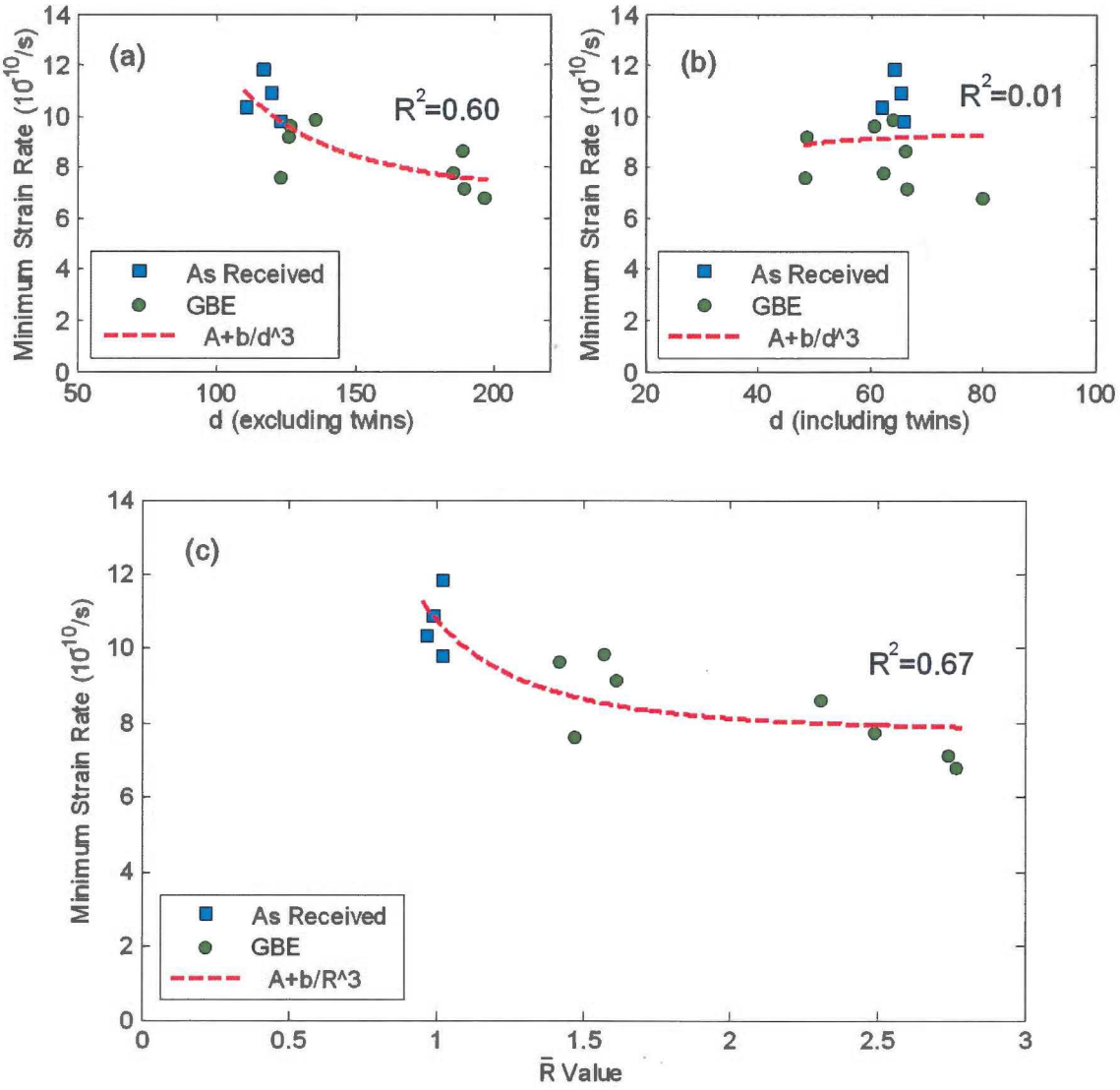

Figure 8.10 Minimum creep rates as a function of microstructural parameters: (a) twin-excluded grain size, (b) twin-included grain size, and (c) $\bar{R}_{eff}$.

Considering Figure 8.10(b) first, it is obvious that no correlation may be drawn between twin-included grain size and minimum creep rate. This result is not unexpected, as Σ3 boundaries may either act to reduce diffusion if they become incorporated into the network, or increase

diffusion if they simply exist as parallel paths within an existing network. Simply measuring their spacing therefore provides an incomplete picture. Where twin boundaries are excluded (Figure 8.10(a)), the creep data show a reasonable correlation with equation 8.10, exhibiting a coefficient of determination of 0.60.

When the $\bar{R}_{eff}$ parameter is used however (Figure 8.10(c)), it is apparent that the coefficient of determination increases, indicating a better "fit" to the experimental data. The most notable difference between (c) and (a) is that the scatter present in (a) in the 100-120μm grain size range is effectively separated when grain boundary connectivity is also considered. This result suggests some dependence on grain boundary connectivity under these test conditions, which is consistent with Coble creep as a contributor to creep rate. Furthermore, this trend supports the belief that analysis of grain boundary connectivity is an important part of GBE experiments, especially where dependent material properties are considered.

8.6 Comparison with Previous GBE Creep Studies

In comparison with previous GBE creep studies, it is apparent that the decrease in minimum creep rate of GBE samples (approximately 20-30% compared to the as-received condition), is well below those obtained by Lehockey and Palumbo [2] of 16x in cast nickel, and Thavesprungriporn and Was [3] of 20x in a Ni-16Cr-9Fe alloy. However, the conditions of testing in these two studies were significantly different to those of the present work. In the nickel study, specimens were tested at a temperature of 450°C and under a nominal stress of 84MPa. This was thought to activate a grain boundary sliding mechanism, according to [20]. The test conditions of the Ni-16Cr-9Fe alloy study were even higher stress, at 360°C and 300-450MPa, where grain boundary sliding was also thought to be significant. In a follow-up study by Lehockey et al [21] in 1998, a high-nickel alloy 625 was creep tested in a GBE state

under conditions of 700°C and 34MPa, which showed a 2x reduction in creep rate compared with the initial state. These results, combined with the present results, suggest that the large reductions in creep rate via GBE are most prominent at very high stresses, where dislocation-based and grain boundary sliding mechanisms are thought to dominate. Lehockey [21] suggested that ordered interfaces have limited "efficiency as sources and sinks for the absorption and re-emission of extrinsic, glissile, lattice dislocations required to promote grain boundary sliding".

It is difficult to distinguish between the relative effects of GBE processing and the increase in grain size of samples 7-10. It is recommended that the dependence of creep rate on grain size at the present test conditions is a subject of further study, in order to decouple these effects. Ultimately however, for industrial purposes, an increase in grain size is certainly acceptable provided it does not result in reduced yield stress or ductility. Achieving simultaneously a reduction in creep rate and improved mechanical properties is not possible by grain size adjustment alone. The present results indicate, however, that GBE can be utilised to decrease the creep rate by up to 30% in the [4x6,1100,30] condition, whilst retaining yield strength and improving the material ductility.

8.7 Effect of Creep Exposure on Microstructural Parameters

In order to determine the effect of the creep testing on the microstructural parameters, three further samples were analysed after being removed from the creep test. Specifically, the $\Sigma 3^n$ boundary length fractions and grain size were re-evaluated using EBSD.

The change in $\Sigma 3^n$ boundary length fraction for the three samples is shown in Figure 8.11.

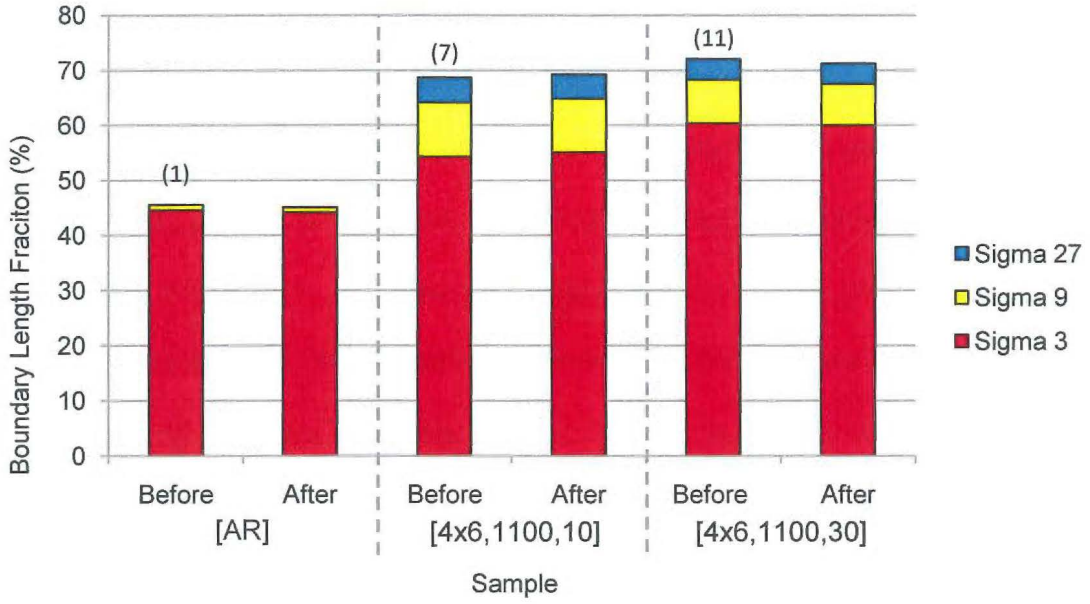

Figure 8.11 Change in boundary length fraction during creep test for selected samples

The analysis shows that the accumulated creep has not had measurably changed the $\Sigma 3^n$ boundary length fraction in either the as-received condition or the GBE conditions. Any differences are well within the experimental variation range. The change in grain size was also measured and is shown in Figure 8.12.

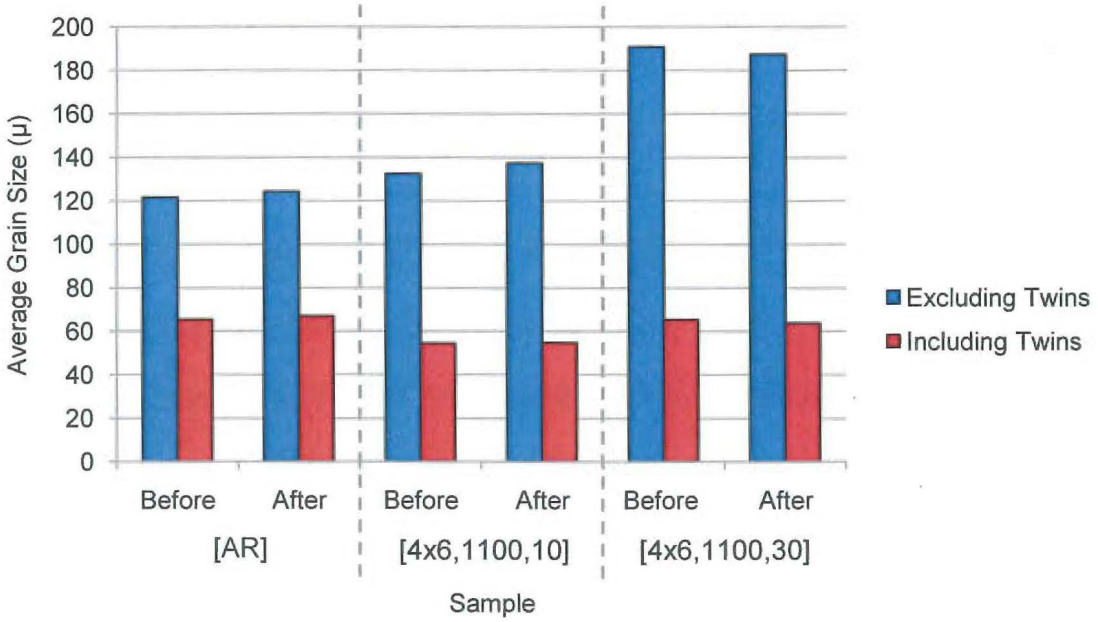

Figure 8.12 Change in grain size (both excluding and including twins as grain boundaries) during creep test for selected samples

The results show that no appreciable change in grain size has resulted after 300 hours at 950°C in any sample. This result is consistent with an investigation by Tan et al [22], who showed that the GBE microstructure of 800H was stable up to the highest temperature tested of 780°C. Tan also showed that the GBE microstructure of alloy 617 was stable up to 1000°C. It may be concluded from the present analysis that the microstructure is likely to be stable at the Methanex service temperature of approximately 870°C.

8.8 Conclusions

In conclusion, the results show that grain boundary engineering processing has resulted in minimum creep rates reduced by up to 30% compared with the as-received condition. This reduction is attributed to both an increase in the grain size of the material, and a decrease in the relative diffusivity of the grain boundary network which is independent of grain size. The present results are important in that they show the improvements in creep properties at such low-stress conditions, which are directly relatable to pigtail service conditions. The previous lowest stress tested in a GBE state was approximately 3x higher than the present study, which does not necessarily extrapolate to service conditions such as the Methanex pigtails.

Combined with the mechanical properties detailed in the preceding chapter, it has been shown that grain boundary engineering of alloy 800H is a viable approach for improving the creep properties and the ductility of the material, without sacrificing yield strength or ductility.

8.9 References

[1] Was, G. S., Thaveeprungsriporn, V., Crawford, D.C., *Grain boundary misorientation effects on creep and cracking in Ni-based alloys*, Journal of Materials 50 (1998) 44.

[2] Lehockey, E. M., Palumbo, G., *On the creep behaviour of grain boundary engineered nickel*, Materials Science and Engineering A 237 (1997) 168-172.

[3] Thaveeprungsriporn, V., Was, G.S., *The role of coincidence-site-lattice boundaries in creep of Ni-16Cr-9Fe at 360C*, Metallurgical and Materials Transactions A (Physical Metallurgy and Materials Science) 28A (1997) 2101.

[4] Boehlert, C. J., Longanback, S.C., Bieler, T.R., *Effect of thermomechanical processing on the creep behaviour of Udimet alloy 188*, Philosophical Magazine 88 (2008) 641.

[5] Frost H.J., Ashby M.F., *Deformation-Mechanism Maps*, Pergamon Press, 1982.

[6] Poirier, J., *Creep of Crystals - High Temperature Deformation Processes in Metals, Ceramics and Minerals*, Cambridge University Press, 1985.

[7] Nabarro, F. R. N., *Deformation of crystals by the motion of single ions*, The Physical Soc. (Ed.) Report of a Conference on Strength of Solids (Bristol), 1948, pp. 75-90.

[8] Herring, C., *Diffusional viscosity of a polycrystalline solid*, J. Appl. Phys. 21 (1950) 437-445.

[9] Coble, R. L., *A model for boundary-diffusion controlled creep in polycrystalline materials*, J. Appl. Phys. 34 (1963) 1679-1682.

[10] Spiradek, K., Degischer, H. P., Lahodny, H., *Correlation between microstructure and the creep behaviour at high temperature of Alloy 800 H*, High temperature metallic materials for gas-cooled reactors, International Atomic Energy Agency, Vienna, 18, IWGGCR, Cracow, 1988, pp. 51-62.

[11] Special Metals Corporation, *Technical Publication - Alloy 800H & 800HT*, 2004.

[12] ASTM, *E8: Standard Test Methods for Tension Testing of Metallic Materials*, 1996.

[13] Advanced Cooling Technologies Inc. (ACT), *http://www.1-act.com/products-/temperature-calibration-control/isothermal-furnace-liner.php.*

[14] ASTM, *E139 - 06: Standard test methods for conducting creep, creep-rupture and stress-rupture tests of metallic materials*, 1996.

[15] Priester, L., *Geometrical speciality and special properties of grain boundaries*, Rev. Phys. Appl. 24 (1989) 419-438.

[16] Mishin, Y., Herzig, C., *Grain boundary diffusion: recent progress and future research*, Mat. Sci. & Eng. A 260 (1999) 55-71.

[17] Budke, E., Herzig, C., Prokofjev, S., Shvindlerman, L. S., *Orientation dependence of Au and Cu diffusion along symmetric [001] tilt grain boundaries in Cu*, Mat. Sci. Forum 207-209 (1996) 465-468.

[18] Monzen, R., Takada, Y., Kita, K., *Misorientation dependence of diffusion of Bi in [001] symmetric tilt boundaries of Cu*, J. of Mat. Sci. Lett. 17 (1998) 283-284.

[19] Palumbo, G., Aust, K. T., *Structure-dependence of intergranular corrosion in high-purity nickel*, Acta Metall. 38 (1990) 2343-2352.

[20] Ashby, M., *A first report on deformation-mechanism maps*, Acta Metall. 20 (1972) 887-897.

[21] Lehockey, E. M., Palumbo, G., Lin, P., *Improving the weldability and service performance of nickel- and iron-based superalloys by grain boundary engineering*, Metallurgical and Materials Transactions A: Physical Metallurgy and Materials Science 29 A (1998) 3069-3079.

[22] Tan, L., Sridharan, K., Allen, T. R., Nanstad, R. K., McClintock, D. A., *Microstructure tailoring for property improvements by grain boundary engineering*, Journal of Nuclear Materials 374 (2008) 270-280.

CHAPTER 9: GRAIN BOUNDARY ENGINEERING – APPLICATION TO PIPE

9.1 Introduction

All of the experimentation so far has been performed on plate material, due to its relative ease of deformation by plate rolling. However, for the GBE process to be applicable to the intended application of Methanex pigtail tubes, it must be demonstrated that the process is adaptable from plate to pipe. Hence, a 100mm long section of pigtail pipe was grain boundary engineered using a swaging operation. The method of GBE is discussed in the following section, followed by a microstructural analysis of the resulting pipe by EBSD in terms of $\Sigma 3^n$ boundary length fraction and grain size.

9.2 Method

A section of as-received pipe measuring approximately 100mm by 43mm o.d., with a wall thickness of 4.5mm, was obtained to undergo GBE processing. The GBE parameters were selected on the basis of the successful results outlined in Chapter 4. A deformation per cycle of 6% was chosen, and the annealing temperature and time were chosen to be 1100°C and 20 minutes respectively. However, due to the aim of proving the industrial feasibility of the operation, the number of cycles was reduced in order to minimise processing cost. In Chapter 6, the evolution of the pipe microstructure was described as a function of the number of GBE cycles performed. It was found that one cycle was insufficient to achieve the desired result of increased $\Sigma 3^n$ boundary fractions, but that there was a large increase in $\Sigma 3^n$ fraction (approximately 0.20 or 45% of the one-cycle fraction) during the second cycle. The

following cycles yielded a maximum increase of 0.05 $\Sigma 3^n$ boundary length fraction. Hence, in order to achieve a balance between microstructure and processing time/cost, it was decided that two cycles of GBE processing would be performed.

The deformation operation was performed by Methanex New Zealand, using custom hardened mandrels and a hydraulic press, requiring an axial force of approximately 200kN. The process was performed as a free expansion, and consequently there was no measurable reduction in wall thickness. Instead, the strain resulted in a 6% reduction in axial length. The annealing steps were performed at the University of Canterbury, using the same box furnace as was utilised for the plate experiments. A separate length of as-received pipe was untreated and hence used as a control.

Microstructural samples were then taken, mounted, ground and polished as described in Chapter 4, and subsequently examined by EBSD. A total area of $16mm^2$ was analysed for each condition.

9.3 Results

A comparison between the microstructure of as-received pipe and GBE pipe is shown in Figure 9.1. High-angle boundaries (HABs) are indicated in black, and $\Sigma 3$, $\Sigma 9$ and $\Sigma 27$ boundaries are represented in red, yellow and blue respectively.

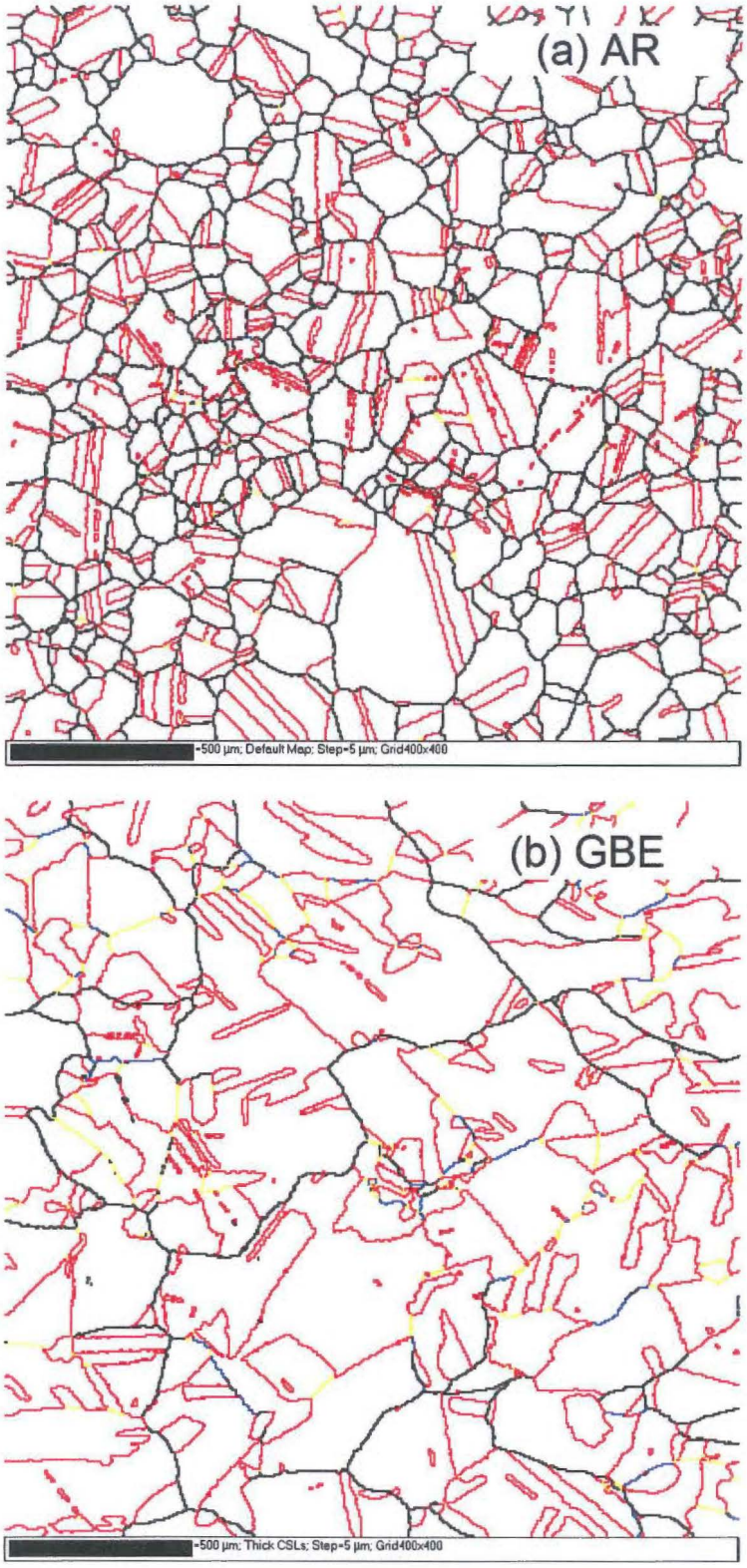

Figure 9.1 Comparison between microstructures of (a) as-received pipe and (b) GBE pipe. HABs are black, and Σ3, Σ9 and Σ27 boundaries are red, yellow and blue respectively. Bar at lower-left indicates 500µ.

These microstructures were evaluated in terms of the $\Sigma 3^n$ boundary length fraction, and the grain size (excluding and including twins). These results are discussed in the following sections.

9.3.1 $\Sigma 3^n$ Boundary Length Fraction

The $\Sigma 3^n$ boundary length fractions are compared in Figure 9.2.

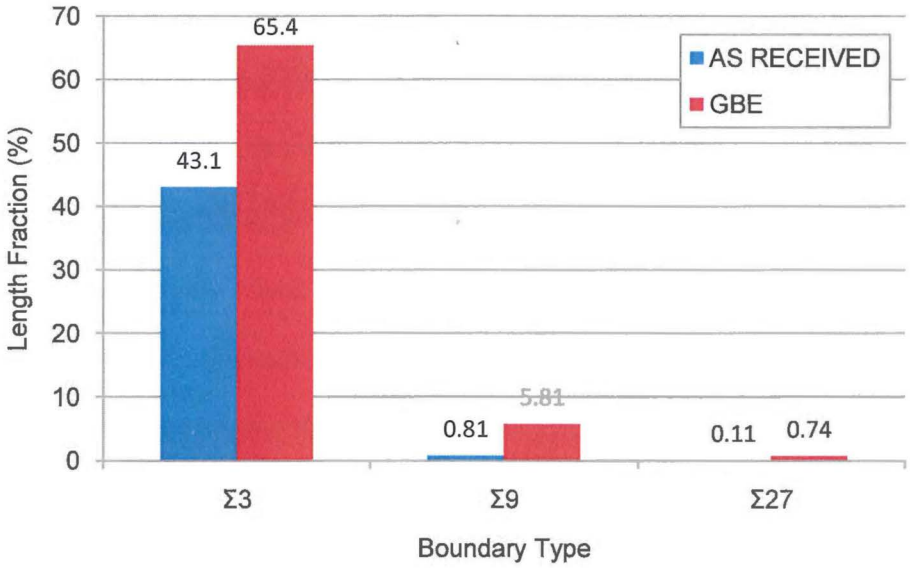

Figure 9.2 $\Sigma 3^n$ boundary length fraction comparison between as-received and GBE pipe

The results show that the $\Sigma 3$ fraction has increased by approximately 50% compared to the as-received pipe to a fraction of 65%. Concurrently, the $\Sigma 9$ fraction has increased from 0.8% to 5.8% and the $\Sigma 27$ fraction from 0.1% to 0.7%. These results indicate that the GBE processing has been successful in its aim of increasing the $\Sigma 3^n$ length fractions. Compared with the same processing conditions in the 8mm plate material (after four cycles), which showed $\Sigma 3$, $\Sigma 9$ and $\Sigma 27$ fractions of 57.6%, 7.6% and 4.7% respectively, it is apparent that the $\Sigma 9$ and $\Sigma 27$ fractions are slightly lower in the pipe. The $\Sigma 9/\Sigma 3$ ratio, which was used as a measure of the level of GBE in Chapter 4, is calculated as 0.09 for the pipe condition, compared with 0.13 after four cycles in the 8mm plate. Thus, it may be concluded that

although the pipe has been grain boundary engineered, it is in a "less engineered" state than the plate samples. This is likely due to the fact that the pipe received only two processing cycles instead of four.

9.3.2 Grain Size

The grain size was evaluated both including and excluding twin boundaries, and is shown in Figure 9.3.

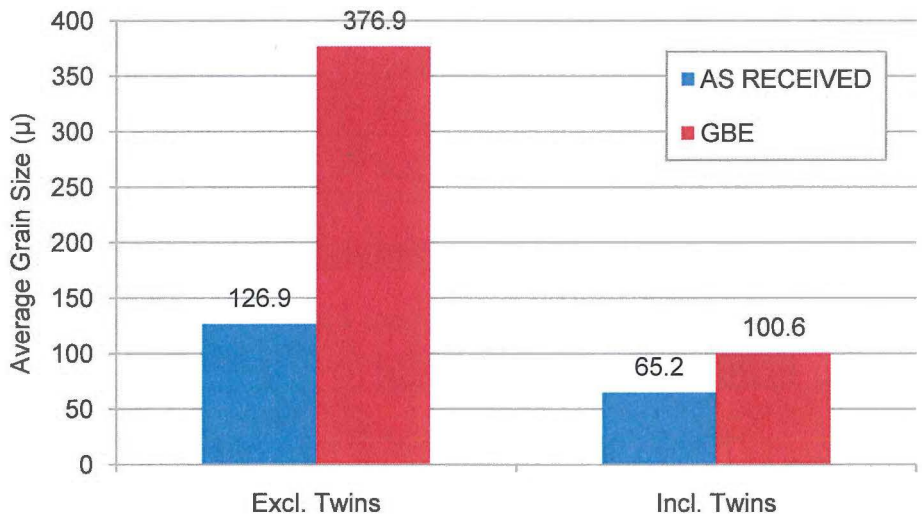

Figure 9.3 Grain size comparison between as-received pipe and GBE pipe

As a consequence of the GBE processing, it is apparent that the twin-excluded grain size has increased by more than 200% compared with the initial condition. This grain growth is much larger than the increase of 30% observed in the corresponding plate sample. There are a couple of factors which may contribute to this discrepancy.

The shape of the pipe in comparison to the plate samples meant the physical distance between the pipe sample and the heating elements was less than the corresponding distance between the plate samples and the heating elements. Therefore, it is possible that the effective

annealing temperature was 10-15°C higher than the nominal 1100°C measured for the plate experiments. However, an increase in annealing temperature of this magnitude is not expected to be completely responsible for the discrepancy in grain size, given that the plate sample annealed at 1150°C exhibited a maximum grain size of 225μm.

The other factor which may be responsible for the discrepancy in grain size between plate and pipe samples is the fact that the pipe swaging operation is fundamentally different to the plate rolling operation. This is evident in the fact that the swaging process did not result in a reduction in wall thickness, but rather caused a 6% reduction in pipe length. It is possible that the deformation profile differs between the plate and pipe samples, which would provide local variation in driving force for grain growth. Changes in the way strain is stored throughout the sample thickness may be identified by transmission electron microscopy (TEM) or may be predicted by finite element analysis (FEA) involving plastic deformation. However, both of these analyses were considered outside the scope of the present project. In future experiments, the large grain growth in the pipe sample may be limited simply by reducing the annealing time to 5-10 minutes.

9.4 Conclusions

The present results showed that the total $\Sigma 3^n$ boundary length fraction was increased by more than 50% by "grain boundary engineering" a sample of Methanex pigtail pipe, proving that it is possible to reproduce the GBE microstructures in pigtail pipe. It is also possible to reduce the number of cycles performed from four to two, without severely affecting the grain boundary character distribution (GBCD). However, due to the significant grain growth which was associated with the processing in this case, it is recommended that the annealing time be reduced to the range 5-10 minutes in future iterations.

CHAPTER 10: SUMMARY AND CONCLUDING REMARKS

10.1 Introduction

This chapter provides a summary of the main achievements of this research, and details of the way in which the present work contributes to the broad field of high-temperature material design and characterisation. Finally, this chapter leaves the reader with some concluding remarks regarding the initial objectives of the research and the way in which they have been achieved.

10.2 Summary of Achievements

Although the process of grain boundary engineering was relatively well-established at the commencement of the present study, few available research articles documented the testing of a wide range of GBE processing parameters. In general [e.g. 1-3], only one set of processing conditions (number of cycles, deformation per cycle, annealing temperature/time) was described and analysed, which obviously varied significantly between different materials. In the present study therefore, over 20 different combinations of processing parameters were used in the manufacturing of GBE 800H, including analysis by EBSD. Results showed that the highest $\Sigma 3^n$ boundary length fractions were achieved by four cycles of 6% deformation and annealing at 1100°C for 10-30 minutes, which resulted in a 55% increase in $\Sigma 3^n$ boundary length fraction compared to the as-received condition.

Importantly however, the effect of varying individual processing parameters was also able to be extracted from the testing matrix. For example, it was shown that varying initial sample thickness had no significant effect in the range 4.5-8mm. Further results supported the trend that low deformation per cycle was generally better for increasing $\Sigma 3^n$ boundary fraction. In terms of temperature, it was also shown that there exists an optimum annealing temperature in the range 1050-1150°C for 800H in terms of both $\Sigma 3^n$ boundary fraction, and controlling grain size, which was explained in terms of boundary migration in line with current thinking.

As some ambiguity remains in the measurement of grain size in GBE materials, the present work documents a method of combining both optical microscopy and EBSD analysis to reduce or eliminate the limitations of each method (for example, the EBSD flood-fill approach may ignore HABs which do not completely encircle a grain). This analysis method was published by the current author in 2009 [4], and it is hoped that such analyses will eventually lead to a standardised method of grain size assessment by EBSD being adopted in the future.

The analysis of the spatial distribution of grain boundaries (grain boundary connectivity) has become increasingly important in the GBE field, and a number of models have been proposed in order to quantify its effect. These existing models were reviewed in the present work and their limitations explained. Consequently, a new model for the analysis of grain boundary connectivity in digitised EBSD images was proposed in this work. The model is centred on evaluating the two-dimensional diffusion resistance of a grain boundary network through conversion to its analogous electric circuit. The model contains the ability to include, or exclude the effects of changes in grain size, which no previous model can do, and therefore is extremely well-suited in the study of grain-size dependent phenomena such as creep. The model has been shown to be theoretically superior to previous models in predicting

diffusional-based properties, and the connectivity parameter has also shown better correlation with minimum creep rate than both the twin-excluded and the twin-included grain size. A journal article [4] describing the diffusion model was accepted for publication in Materials and Metallurgical Transactions A, and is in press at the writing of this thesis.

Analysis of the GBE microstructures in terms of the new connectivity model showed that the highest disruption to the HAB network was exhibited by the samples with the highest $\Sigma 3^n$ fraction. However, it was also noted that the sample annealed at 1150°C exhibited a significant increase in the $\Sigma 3^n$ length fraction, but that the new $\Sigma 3^n$ boundaries did not cause any measurable disruption to the original HAB network. This is an important result for the GBE field in that it proves some measure of boundary connectivity is necessary in the analysis of GBE microstructures, and that the $\Sigma 3^n$ must not be solely relied upon to describe a GBE state.

An analysis of the evolution of microstructure was performed for two separate GBE processing routes as a function of processing cycle, as such studies are currently considered important in the ongoing study into the mechanisms of GBE. Both samples exhibited no change in $\Sigma 3^n$ fraction during the first cycle, which then increased significantly during the second and subsequent cycles. The strain energy was also found to increase during the first cycle, before being reduced significantly in the second. This result adds weight to similar results obtained within the GBE field, and supports the idea that boundary mobility is a key issue in the identification of the GBE mechanisms.

Two separate GBE conditions were also subjected to room-temperature tensile testing and compared with the as-received material. It was found that the ductility of the GBE samples was increased by 8-12% compared to the as-received condition, but that this increase in

ductility did not occur at the expense of yield strength. This result is important in that it illustrates the potential of GBE as a valid processing method to improve room-temperature mechanical properties, which has been the aim of very few studies to date. As a corollary to this, the microstructural analysis provides further evidence for the contribution of twin boundaries to yield strength, which has been a subject of interest recently within the broader materials engineering field [e.g. 5]. For example, a GBE sample with a twin-excluded grain size of 207μ was found to have equal yield strength as the as-received condition with a grain size of 117μ, despite the Hall-Petch prediction to the contrary. This result was considered to be due to the "extra" Σ3 boundaries present in the GBE sample and their hindrance to the motion of dislocations. In fact, both the hardness and the yield strength of GBE materials was found to show a better correlation with grain size when twin boundaries were included in its evaluation, which is contrary to the method described in the ASTM standard for grain size measurement. It is hoped that GBE materials, with their high Σ3 fractions, may be extremely useful in isolating the effect of twin boundaries on strength in the near future.

The major aim of this project was to evaluate the creep properties of GBE material, in comparison to the as-received condition. In the few examples of GBE studies on creep properties reported in the literature, only one GBE condition is tested, and typically the test conditions are heavily accelerated in order to achieve rupture life data. Therefore, in the present project, 8 GBE samples and 4 as-received samples were creep tested in a custom-designed creep rig which allowed strain-rate measurements as low as $4\text{-}5\text{x}10^{-10}$/s. These low strain rates allowed testing to be performed at test conditions only slightly in excess of service conditions, in order to ensure that the test results remained industrially relevant (ie. the creep mechanism was similar).

It was shown that GBE material exhibited a minimum creep rate which was reduced compared to the as-received condition, by up to 30%. This result is the first in the GBE field which shows such a comparison whilst ensuring the results are directly applicable to typical industrial service conditions. The improvement in properties was attributed to a combination of lower grain boundary diffusivity, combined with an increase in grain size. The measured creep rates also showed good correlation with the proposed connectivity model, which serves as validation of the connectivity analysis.

Finally, it was shown that a GBE condition could also be created in pipe through a series of swaging and annealing operations. This procedure has not been documented previously in the literature, and has positive industrial application for the sponsors of this work.

10.3 Concluding Remarks

The main objective of this research was to investigate the method of grain boundary engineering Incoloy 800H, in terms of the optimum procedure, feasibility, the resulting microstructure, and the properties of the material.

Ultimately, it was found that grain boundary engineered 800H was best achieved through a 6% deformation per cycle, 1100°C anneal combination. The resulting microstructures were found to exhibit increased ductility with no loss of yield strength or hardness. The minimum creep rate was also found to be up to 30% lower than as-received material, tested under conditions which approach those of industrial service.

It was also shown that grain boundary engineering could be applied to pipe material, through a series of swaging plus annealing cycles. It should therefore be possible to produce GBE

pipe which exhibits a decreased minimum creep rate compared with non-GBE pipe. This study has therefore met its original aims, and provides a foundation for further research into the industrial application of grain boundary engineering.

10.4 References

[1] Thaveeprungsriporn, V., Was, G.S., *The role of coincidence-site-lattice boundaries in creep of Ni-16Cr-9Fe at 360C*, Metall. and Mat. Trans. A 28A (1997) 2101-2112.

[2] Was, G. S., Thaveeprungsriporn, V., Crawford, D.C., *Grain boundary misorientation effects on creep and cracking in Ni-based alloys*, J. of Mat. 50 (1998) 44-49.

[3] Lehockey, E. M., Palumbo, G., *On the creep behaviour of grain boundary engineered nickel*, Mat. Sci. & Eng. A 237 (1997) 168-172.

[4] Drabble, D. J., Bishop, C. M., Kral, M. V., *A Microstructural Study of Grain Boundary Engineered Alloy 800H*, Metall. & Mater. Trans. DOI: 10.1007/s11661-010-0447-4 (2010).

[5] Pande, C. S., Rath, B. B., Imam, M. A., *Effect of annealing twins on Hall-Petch relation in polycrystalline materials*, Mat. Sci. & Eng. A 367 (2004) 171-175.

CHAPTER 11: FUTURE WORK

11.1 Introduction

The present research has addressed the initially proposed scope, and has shown that GBE processing influences both creep properties and the mechanical properties of alloy 800H. However, it has also opened some further avenues of exploration which may be of scientific or industrial importance. This section details the major areas in which further research may prove useful.

11.2 Identification of Twin Boundaries

The present work has provided further evidence for the influence of twin boundaries on mechanical properties such as hardness and yield stress. In particular, both yield stress and hardness in alloy 800H have been shown to exhibit better correlation according to the Hall-Petch relationship when twin boundaries are included in the grain size measurement, rather than excluded according to ASTM E-112 [1]. There is already evidence in the literature in support of this observation [2-5], however the concept of grain boundary engineering offers a new method of altering the twin density of low-stacking-fault materials in order to achieve twin-densities not attainable by conventional processing. For example, two samples may be produced with similar twin-excluded grain sizes but with twin-included grain sizes that vary by up to 25%. A comparison of such samples allows the effects of each boundary type to be decoupled and provides an excellent test of the theory that twin boundaries have an influence on mechanical properties.

However, the current limitation with this analysis lies in the definition of a twin boundary. In the present study, a twin boundary was defined as any boundary which exhibited a misorientation within 5° of the 60°/<111> relationship. In the case of GBE materials, this definition inevitably includes some Σ3 boundaries that are not coherent annealing twins, such as the incoherent twin boundary on {112} planes, or other configurations that fit the misorientation criterion. It is not currently well known what effect these boundary types have on the motion of dislocations, and therefore their contribution to mechanical properties. In order to fully isolate the effect of the coherent twin boundaries on properties, such boundaries must be able to be distinguished from microstructural analysis. This is not possible by optical methods, and therefore requires the use of EBSD.

In order to fully determine whether a twin boundary is coherent, a three-dimensional analysis such as serial sectioning is required. However, serial sectioning is extremely time consuming, and is susceptible to errors in measurement. A much more feasible method has been proposed [6] based on single section trace analysis. This method involves assigning each linear section of boundary a trace vector, $\boldsymbol{T}$, based on the orientation of the trace relative to the orthogonal crystal axes of each grain (boundaries are often reconstructed as a series of linear segments according to a method described by Wright and Larsen [7]). The trace vector must lie in the boundary plane, and therefore must be orthogonal to the boundary plane normal vector, $\boldsymbol{N}$, according to the condition:

$$\boldsymbol{N}.\boldsymbol{T} = 0 \tag{11.1}$$

For a coherent annealing twin, the boundary plane is <111> in both grains. Therefore, by substituting $\boldsymbol{N}$ for <111>, equation 11.1 must hold for each grain. If the trace vector is not orthogonal to the <111> crystal direction in either grain, the boundary cannot be a coherent twin. Although this method does not fully describe the boundary (only four of the five degrees of freedom are determined), trace analysis can determine which boundaries cannot be

coherent annealing twins according to their crystallography, and therefore provides a much more useful criterion for the classification of Σ3 boundaries.

The reason for trace analysis being excluded from the scope of the current project is that very-high resolution EBSD scans are required in order to yield accurate results. It has been shown [7] that boundaries shorter than 6x the scan resolution cannot be resolved within 2° by trace analysis. For the current material, in order to accurately resolve approximately 90% of the Σ3 boundaries, this would require a scan resolution in the range 0.5μ-1.0μ. Acquiring the same data set as was produced in the current work using this resolution would require a scan time of well over 12,000 hours (500 days) full-time use, which was considered unfeasible. However, in order to validate the relationship between twin boundaries and mechanical properties, a subsequent analysis could be performed, including:

- High-resolution EBSD re-scanning of existing GBE samples
- Boundary reconstruction and subsequent trace analysis to determine which Σ3 boundaries are in fact likely to be coherent annealing twins
- Correlation between yield stress/hardness and grain size both excluding and including likely coherent twin boundaries according to the Hall-Petch relationship
- Possible TEM analysis studying the dislocation transmission/absorption in a twin boundary

It is felt that such an analysis, while not specifically a grain boundary engineering analysis, would benefit the scientific community in providing evidence for or against the claim that coherent twin boundaries influence the motion of dislocations, which is presently not well understood.

11.3 The Effect of Grain Size on Creep Rate

The present results showed that, although decreases in creep rate were observable in GBE samples with similar grain size to the as-received condition, greater decreases in creep rate were measured in GBE samples with an increased grain size. It is desirable to know the precise effect of grain size on creep rate in 800H at the particular test conditions of 950°C, 12MPa, in order to decouple the effect of grain size from the effect of GBE.

The determination of the effect of grain size on creep rate would require a second testing regime, involving testing samples of several different grain sizes, created by re-annealing material in the as-received condition. Material with 4-5 different grain sizes would be required, resulting in a testing period of over 6 months. However, such testing would help to distinguish between the effects of grain size and the effects of GBE, as well as providing information regarding the dominant creep mechanism at the present test conditions.

11.4 Creep Rupture Life Correlation

In order to ensure that creep tests provided reasonable extrapolations to in-service conditions of Methanex pigtails, the test conditions in this work were selected to intentionally produce a very low strain rate (approximately $10x10^{-10}$/s). The limitation of such an analysis is that no data concerning time to failure is produced. As mentioned previously, acquiring rupture life data for all samples in the present work at the test conditions of 950°C and 12MPa would likely require 20,000 or more hours (~850 days) of testing alone, even running two samples simultaneously. Such a testing program was obviously unfeasible for the present project.

Equations describing the relationship between creep rate and creep rupture life exist in the literature. For example, the Monkman-Grant relationship [8] predicts a relationship between minimum strain rate, $\dot{\varepsilon}_s$, and time to rupture, t_f, which is given in equation 11.2:

$$t_f . \dot{\varepsilon}_s^m = C \tag{11.2}$$

where m and C are empirically determined constants. A modified version of the Monkman-Grant relationship includes the strain at failure, ε_f, and is shown in equation 11.3:

$$\dot{\varepsilon}_s . t_f / \varepsilon_f = C' \tag{11.3}$$

These relationships have shown good correlation in creep tests on stainless steels [9-12], and clearly predict an increase in rupture life based on a decrease in minimum creep rate (assuming constant strain at failure). However, in order to be implemented industrially, rupture tests are ultimately required to determine whether or not the GBE material obeys such empirical equations. For example, it has been reported that an increase in grain size can lead to reduced strain at failure (creep ductility) in alloy 800 [13]. It is also noted that the 8-66x reductions in steady-state creep rate achieved by Thaveeprungsriporn [5] resulted in improvements in creep life of between 2.5x and 7.5x, indicating that the relationship was not linear at the test conditions. Therefore, the present creep results should only be treated as a reasonable indicator for an improvement in creep rupture life, and should be supplemented by creep rupture testing of GBE conditions in comparison to the as-received case.

11.5 The Effect of GBE on Other Properties

In the present study, the effects of the GBE processing were analysed in terms of the room-temperature mechanical properties (yield strength, ultimate tensile strength and ductility), as well as the creep properties at high temperature, low stress conditions. However, grain boundary engineering has previously been shown to positively influence many other material

properties, including hydrogen embrittlement [14] and corrosion [15-21], which are also of interest industrially.

It seems a logical next step, therefore, to further characterise GBE 800H in terms of its resistance to environmental attack. It should be noted that the corrosion properties of GBE 800H were studied in 2008 by Tan et al [20], under exposure to supercritical water (SCW) and cyclic oxidation, and shown to be measurably improved compared to the base state. The signs are therefore positive that GBE can simultaneously improve mechanical properties, creep resistance and corrosion resistance, which is very encouraging from an industrial standpoint.

11.6 References

[1] ASTM, *E-112: Standard test methods for determining average grain size*, ASTM International, 1996.

[2] Pande, C. S., Imam, M. A., Rath, B. B., *Study of annealing twins in FCC metals and alloys*, Met. Trans. A 21 (1990) 2891-2896.

[3] Pande, C. S., Rath, B. B., Imam, M. A., *Effect of annealing twins on Hall-Petch relation in polycrystalline materials*, Mat. Sci. & Eng. A 367 (2004) 171-175.

[4] Lei, L., Yongfeng, S., Xianhua, C., Lihua, Q., Lu, K., *Ultrahigh strength and high electrical conductivity in copper*, Science 304 (2004) 422-426.

[5] Thaveeprungsriporn, V., Was, G.S., *The role of coincidence-site-lattice boundaries in creep of Ni-16Cr-9Fe at 360C*, Metall. and Mat. Trans. A 28A (1997) 2101-2112.

[6] Randle, V., *A methodology for grain-boundary plane assessment by single-section trace analysis*, Scripta Mat. 44 (2001) 2789-2794.

[7] Wright, S. I., Larsen, R. J., *Extracting twins from orientation imaging microscopy scan data*, J. of Microscopy 205 (2002) 245-252.

[8] Monkman, F. C., Grant, N. J., *An empirical relationship between rupture life and minimum creep rate in creep-rupture tests*, Proc. ASTM 56 (1956) 593-620.

[9] Castillo, R., Koul, A. K., Toscano, E. H., *Lifetime prediction under constant load creep conditions for a cast Ni-base superalloy*, Trans. AIME: J. of Eng. for Gas Turbines and Power 109 (1987) 99-106.

[10] Toscano, E. H., Bocek, M., *Relationship between strain rate, strain to failure and life time*, J. of Nuclear Mater. 96 (1981) 29-36.

[11] Willis, M., McDonaugh-Smith, A., Hales, R., *Prestrain effects on creep ductility of a 316 stainless steel light forging*, Int. J. of Pressure Vessels and Piping 76 (1999) 355-359.

[12] Phaniraj, C., Nandagopal, M., Mannan, S. L., Rodriguez, P., *The relationship between transient and steady state creep in AISI 304 stainless steel*, Acta Metall. et Mater. 39 (1991) 1651-1656.

[13] Diehl, H., Bodmann, E., *Alloy 800 specifications in compliance with component requirements*, J. of Nuclear Mater. 171 (1990) 63-70.

[14] Bechtle, S., Kumar, M., Somerday, B. P., Launey, M. E., Ritchie, R. O., *Grain-boundary engineering markedly reduces susceptibility to intergranular hydrogen embrittlement in metallic materials*, Acta Mater. 57 (2009) 4148-4157.

[15] Palumbo, G., Lehockey, E.M., Lin, P., *Applications for grain boundary engineered materials*, J. of Mater. 50 (1998) 40-43.

[16] Bi, H. Y., Kokawa, H., Wang, Z. J., Shimada, M., Sato, Y. S., *Suppression of chromium depletion by grain boundary structural change during twin-induced grain boundary engineering of 304 stainless steel*, Scripta Mat. 49 (2003) 219-223.

[17] Kokawa, H., Jin, W. Z., Wang, Z. J., Michiuchi, M., Sato, Y. S., Dong, W., Katada, Y., *Grain boundary engineering of high-nitrogen austenitic stainless steel*, Mater. Sci. Forum 539-543 (2007) 4962-4967.

[18] Michiuchi, M., Kokawa, H., Wang, Z. J., Sato, Y. S., Sakai, K., *Twin-induced grain boundary engineering for 316 austenitic stainless steel*, Acta Mater. 54 (2006) 5179-5184.

[19] Tan, L., Sridharan, K., Allen, T. R., *The effect of grain boundary engineering on the oxidation behavior of INCOLOY alloy 800H in supercritical water*, J. of Nuclear Mater. 348 (2006) 263-271.

[20] Tan, L., Sridharan, K., Allen, T. R., Nanstad, R. K., McClintock, D. A., *Microstructure tailoring for property improvements by grain boundary engineering*, J. of Nuclear Mater. 374 (2008) 270-280.

[21] Fang, X., Wang, W., Guo, H., Zhang, X., Zhou, B., *Corrosion behaviours of random and special grain boundaries in a sensitized 304 stainless steel*, Sino-Swedish Structural Materials Symposium, 2007, pp. 339-343.

APPENDIX A: METHODOLOGY FOR EBSD ANALYSIS

A.1 Introduction

The purpose of this chapter is to document the method of electron backscatter diffraction (EBSD) analysis, including the various microscope and software parameters, in order to ensure such an analysis is repeatable in future studies. The microscope and EBSD setup are detailed first, before the post-processing noise reduction techniques are discussed in the closing paragraphs.

A.2 Microscope Parameters

The interaction of an electron beam with ordered crystals and details of electron backscatter pattern (EBSP) generation are readily available in text books such as [1], and therefore will not be covered in this work. Instead, the following paragraphs detail the use of EBSD in the present study from the end-user's point of view, as a guide to future analysis of this material or stainless steels in general.

A.2.1 Sample Preparation

Material specimens were cut using a high-speed water-cooled abrasive saw, using a feed rate of approximately 0.5-1.0mm/s. Specimens were cut to an approximate size of 15mm x 5mm x 5mm thickness and mounted in 1" moulds using Buehler Probemet conductive moulding compound and a Buehler automated mounting machine.

All samples were ground using silicon carbide paper, beginning with 180-grit and progressing to 240, 320, 400 and 600-grit in sequence. Grinding time was approximately 2-3 minutes per step. Samples were then polished using 9μ diamond suspension for 5 minutes, followed by 1μ diamond suspension for a further 5 minutes. Final polishing was performed using a Buehler Minimet automated polishing machine with a 70/30 mixture of Buehler Mastermet 2 colloidal silica suspension and water. Polishing time for the final step was between 120-180 minutes, and samples were subsequently cleaned with ethanol and dried.

Where samples were etched (e.g. for optical analysis), etching was performed by submersion in glyceregia (10mL HCl, 15mL glycerol, 5mL HNO_3) for a period of 2-4 minutes with light agitation, followed by rinsing with water and then ethanol.

A.2.2 Hardware

The analysis was performed on a JEOL JSM 6100 Scanning Electron Microscope, fitted with an HKL Channel 5 EBSD detector and software package. Electron backscatter diffraction patterns (EBSPs) were processed on an Intel Xeon 2GHz personal desktop computer with Windows 2000 operating system.

A.2.3 Beam Settings

The filament saturation influences both the resolution and signal strength of the electron microscope. Increasing filament current can increase the brightness of the EBSP signal, resulting in shorter exposure times and consequently, faster EBSD map generation. The limitations are the saturation current, at which the increases in resolution and brightness plateau, and the reduction in filament life at high current settings. Due to the low-magnification requirements of the present analysis, it was found that a filament current setting of approximately 80% saturation was entirely adequate to produce well-defined

EBSPs. This current setting resulted in an average filament life of 300-400 hours, far in excess of the typical filament life of approximately 100 hours.

A.2.4 Calibration of Magnification

Because of the geometry of the EBSD setup (i.e. the specimen is tilted 70° relative to the orientation of the incident beam, as was shown in Figure 3.3), certain corrections must be made to the image in order to ensure the original geometry is retained. The microscope settings were calibrated using a standard copper grid. The sequence of corrections is illustrated in Figure A.1.

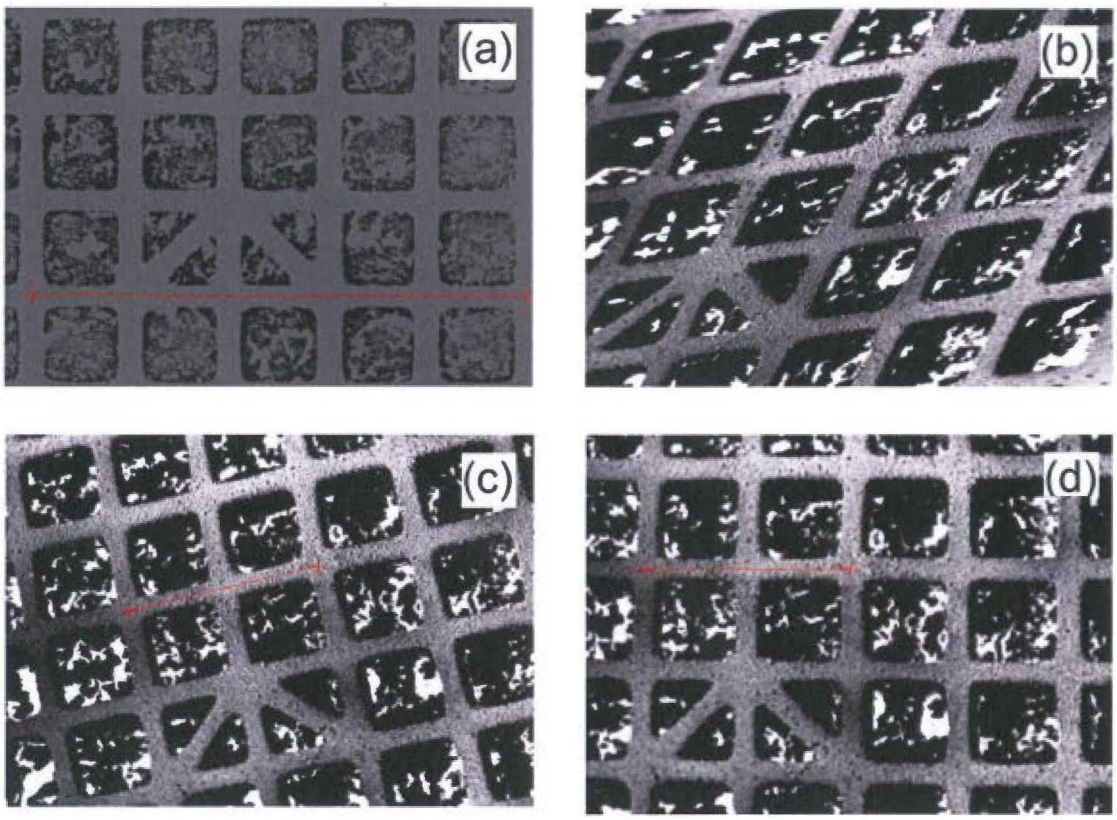

Figure A.1 Sequence of corrections for a standard copper grid starting from (a) no tilt, (b) 70° tilt plus tilt correction, (c) as (b) plus scan rotation, (d) as (c) plus physical rotation of the sample

Figure A.1(a) shows the copper grid at 0° tilt. The sample is then tilted 70° and tilt correction is applied using the HKL Channel 5 software (Figure A.1(b)). In order to correct the image

skew, a 9° scan rotation was applied on the microscope, which results in Figure A.1(c). Finally, the specimen is physically rotated using the microscope stage control by a corresponding angle of 9°, in order to restore the original geometry. These parameters were used for all EBSD maps.

Calibration of distance was also performed by using the HKL software to measure the length of calibration lines (visible in Figure A.1 as red lines in (a), (c) and (d)). The measurement was then compared with the known grid spacing, and found to be within 2% in both the horizontal and vertical directions.

A.3 EBSD Parameters

A.3.1 Pattern Acquisition Time

In order to successfully identify an EBSP, time is required for both the acquisition of the pattern, and the matching of the pattern to a defined crystal orientation by the computer software. The acquisition time is controlled by the exposure time of the camera, which is generally the limiting factor in the speed of generation of EBSD maps. If the camera exposure time is too short, contrast in the EBSP image will be reduced, which may lead to inaccuracies in solving for the correct crystal orientation. If the camera exposure time is too long, saturation may occur in the image, which obscures part of the diffraction pattern and also leads to inaccuracies in solving.

In this study, beam brightness was maximised through the use of low probe current settings, resulting in good contrast at exposure times of approximately 50ms. This resulted in a pattern identification rate of 20 points per second, and map times of 30 minutes for 2mm x 2mm maps at 10μ resolution, or 2 hours at 5μ resolution. It was also determined that

successful EBSP identification was possible at shorter exposure times (i.e. 10-15ms), however this did not result in an increase in the speed of acquisition of the EBSD map. The processing power of the computer was thought to be the limiting factor at these exposure times.

A.3.2 Pattern Calibration

In solving an EBSP for its matching crystallographic orientation, the software requires some information regarding the position of the pattern centre, and the "camera length", or distance between the sample and the screen. This information is required in order to calculate the radius of the "reference sphere", of which the EBSP is a planar section. However, it is possible for the geometrical configuration of the beam and sample to differ depending on the sample, positioning and the alignment of the beam. In order to achieve the most accurate orientation results, it is necessary to calibrate the software parameters against a well-defined pattern of known crystal structure. The difference between a poorly-calibrated match and a well-calibrated match is illustrated in Figure A.2.

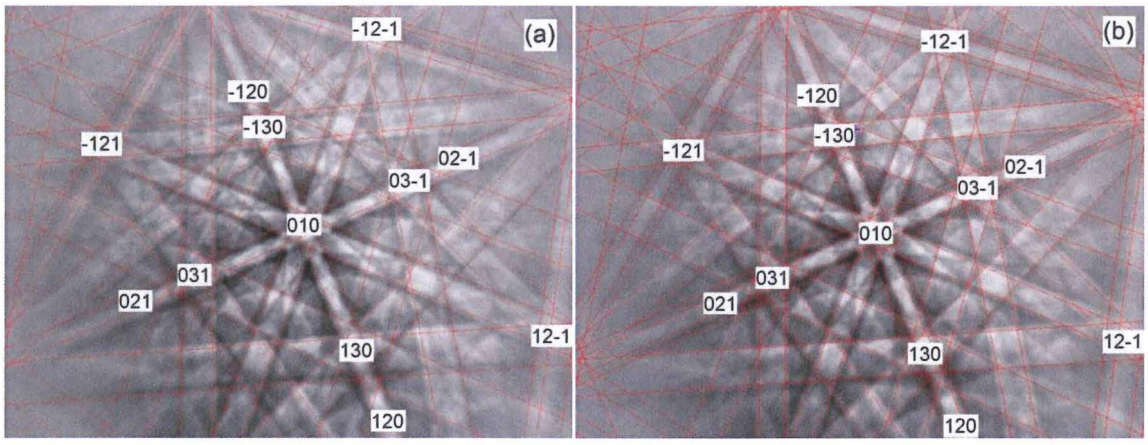

Figure A.2 (a) poorly-calibrated EBSP match and (b) well-calibrated EBSP match

In the present study, calibration was therefore performed before each EBSD map, based on three well-defined patterns obtained from different areas on the field of view.

A.3.3 Map Resolution

Another significant factor in the speed of generation of EBSD maps is the step size, or scan resolution. Decreasing the step size (increasing resolution) results in the resolution of finer grain boundaries, and therefore leads to increased accuracy in grain boundary length fraction calculations. However, decreasing the step size from 10μ to 5μ for example, results in four times as many points to solve, which increases the mapping time by a factor of four. Hence, there is a trade-off between resolution and mapping time.

This relationship was investigated by scanning the same area using a series of different resolutions, and calculating the total $\Sigma 3^n$ boundary length fractions for each map. The results are shown in Figure A.3.

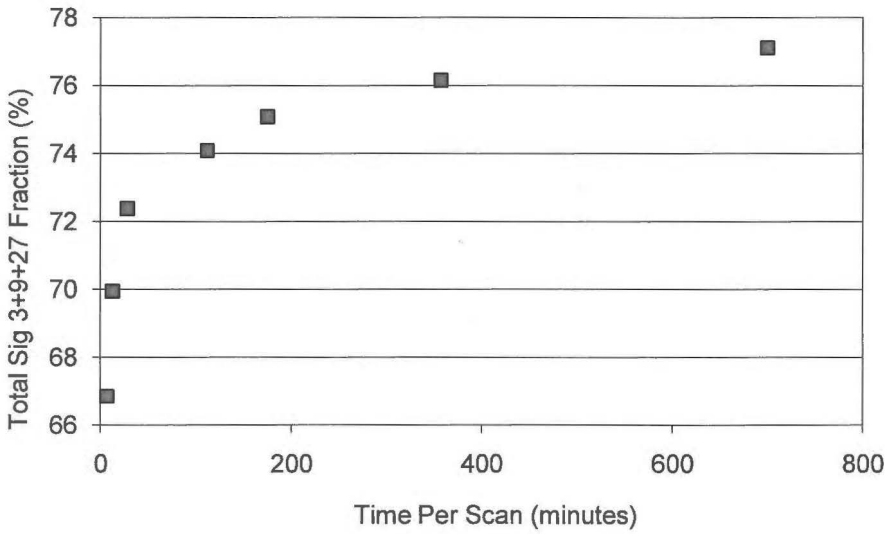

Figure A.3 Relationship between $\Sigma 3^n$ boundary fraction and scan time for a 2mm x 2mm map

The results show that the total $\Sigma 3^n$ fraction is highly dependent on scan time within the first 20-30 minutes, but then begins to level off as the scan time is increased. Therefore, a scan time of 30 minutes (10μ resolution) was selected for the initial GBE microstructure study, which was then increased to 120 minutes (5μ resolution) for the refinement of the GBE

parameters. It is expected that the difference between these two resolutions is approximately 2%, according to Figure A.3.

A.4 Post-Processing

In EBSD analysis, it is normal for a small proportion of data points to remain unindexed due to either the inability to acquire a reasonable EBSP from the specimen surface at a particular point, or the inability to solve the acquired pattern within a reasonable threshold angular deviation. It is also possible for a pattern to be solved incorrectly if the pattern is poorly-defined, or a second "solution" exists which is very close to the preferred solution. The HKL Channel 5 software "Tango" provides two methods to deal with unindexed and misindexed points.

In this study, the first operation performed on the raw data set was a "wild spike" filter. This algorithm compares the crystal orientation at each point to that of each of its eight neighbouring pixels. If the orientation in the centre is significantly different from all of its neighbours, the pixel is assigned Euler angles which correspond to the average of its neighbours. In this way, single-pixel misindexed points are removed.

The second operation performed was the HKL noise reduction algorithm, which artificially fills in points which were not indexed during the acquisition. Again, the algorithm assigns an unindexed point a crystal orientation based on the average orientation of its n neighbouring pixels, where n is a user-defined parameter. For example, if n=4, the algorithm applies averaged data to any unindexed points which have at least four successfully indexed neighbours. In this study, the n parameter was decreased with each iteration until no

unindexed points remained. The effect of the noise reduction algorithm is shown in Figure A.4. Solid green pixels represent unindexed pixels in Figure A.4(a).

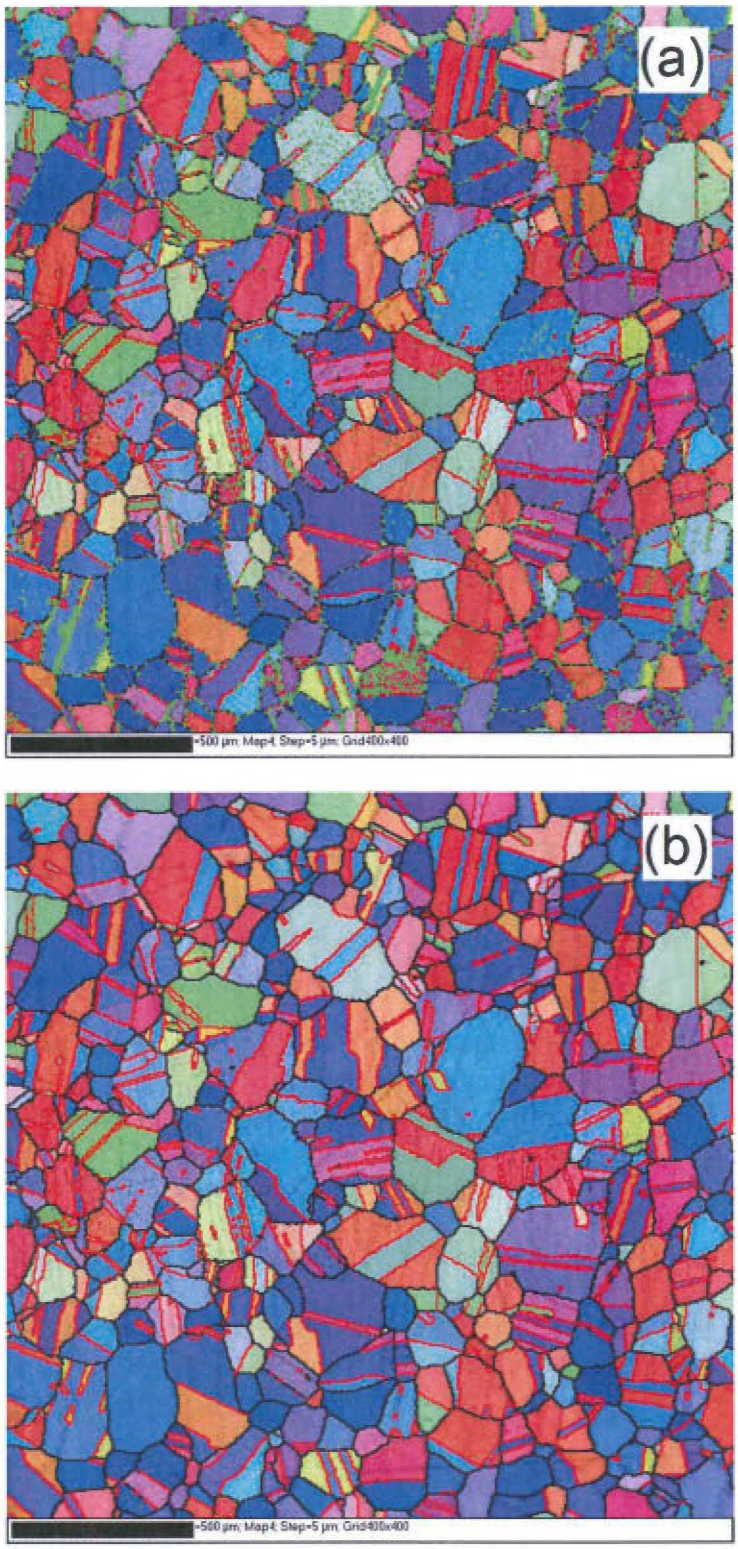

Figure A.4 Effect of HKL noise reduction algorithm. (a) shows original data set, coloured according to the crystal orientation. (b) shows the same area after filtering

It is worth noting that typical successful pattern identification rates in this study were 95-98%, meaning the extrapolated fraction did not measurably alter the microstructure statistics.

A.5 References

[1] Randle, V., *The Measurement of Grain Boundary Geometry*, IOP Publishing Ltd., 1993.

APPENDIX B: DESIGN AND BUILD OF CREEP TEST RIG

B.1 Introduction

One of the requirements of the present study was the testing of 800H specimens at high temperature, low stress creep conditions. Commercially available creep test machines are typically suited to higher load conditions (e.g. 3kN or more [1]) used for creep rupture testing, and typically exhibit poor accuracy at low loads, such as the 200N load used in the present tests. Hence, it was decided that the best solution was to design and build a new creep test machine, capable of accuracy in extension measurement at very low loads. This appendix details the design and evaluation of the creep test rig.

B.2 Design Requirements

The initial requirements for the design of the new creep test rig are listed below.

- Maximum operating temperature must exceed 950°C
- Temperature accuracy must be within 2-3°C
- Maximum operating load must exceed 200N
- Minimum operating load must not be less than 150N
- Minimum resolvable strain rate must be on the order of 5×10^{-10}/s
- Real-time data display
- Operating times of two to four weeks
- Measurement noise of approximately 1μ or lower

It was also considered preferable to design the test rig in such a way that two specimens could be tested simultaneously, allowing the testing time for the entire regime to be halved.

B.3 Final Design

After several design concepts were investigated, a final design was chosen and evaluated. The key aspects of the final creep test rig machine are detailed in this section.

B.3.1 Test Specimen

The creep test specimens were selected to be plate-type specimens, because of the size constraints of the GBE plate (minimum plate thickness was 5.2mm after processing, preventing adequately sized cylindrical samples). Due to the isothermal length within the furnace of >250mm (see Section B.4.1), it was possible to test two samples simultaneously in series.

The geometry of creep samples is determined by ASTM E8 [2], as referenced by the ASTM standard for conducting creep testing, ASTM E139 [3]. A scaled-down version of the pin-holed test specimen specified in E8 was used, with gauge dimensions of 4mm × 3.2mm. Although all proportions were consistent with those specified in E8, the validity of the sample geometry was confirmed by finite element analysis (FEA) at an applied load of 15kg. The results are shown in Figure B.1.

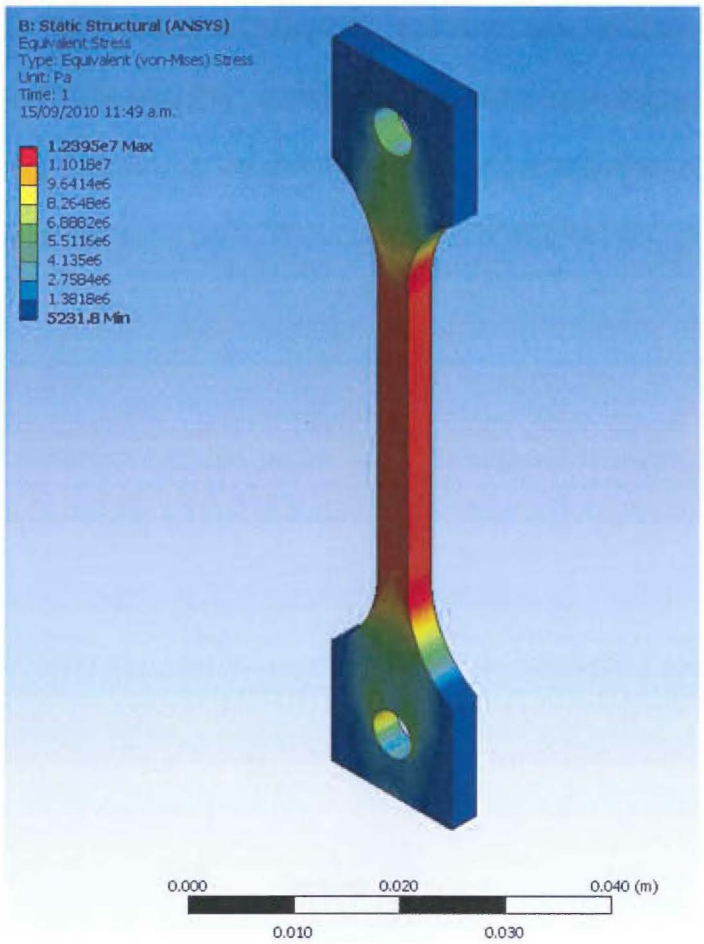

Figure B.1 Von Mises stress distribution in creep specimen at an applied load of 15kg

The results show a maximum stress of approximately 8MPa at the pinhole, and approximately 12MPa within the gauge length of the specimen. It is therefore a reasonable assumption that the vast majority of the strain will be located within the gauge length, as the gauge length contains a stress of 12MPa over a length of 40mm, compared to the pinhole which exhibits 8MPa stress over a length of 1-2mm.

ASTM E139 states that the maximum bending strain within a creep test should not exceed 10% of the axial strain. In order to quantify the bending strain in the selected sample geometry, the "worst case scenario" was modelled using FEA, involving the pin holes being deliberately located out of vertical alignment. The distance between the hole centres and the

centre-line of the sample was modelled at 0.1mm, which is well within the tolerance achievable by computer-numerical-control (CNC) machining. The resulting stress distribution is shown in Figure B.2.

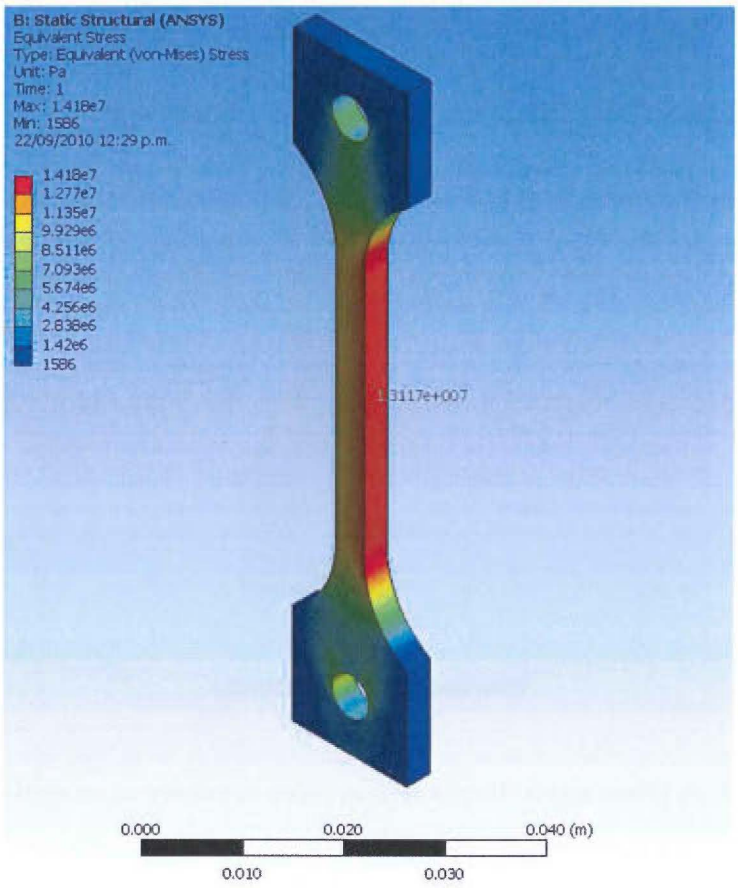

Figure B.2 Von Mises stress distribution in creep samples with pin-holes 0.1mm off-centre

The highest tensile stress within the gauge length of the sample is approximately 13.1MPa (as indicated by the probe), which consists of 12MPa from uniaxial tension and approximately 1.1MPa from bending stress. Therefore, even at the worst case where pin holes are machined 0.1mm from the specified locations, the bending stresses comprises only 9% of the total sample stress.

Creep specimens were also ground to a 1200-grit finish using SiC paper before creep testing to eliminate any effect of surface finish on creep rate.

B.3.2 Sample Grip and Extensometer Design

Due to the high temperatures (950°C), it was not possible to attach extensometers directly to the sample gauge length, meaning the extensometers had to be located outside the furnace. The high temperatures also prevented any attachment directly to the gauge length of the specimens, due to the problems associated with oxide formation in threaded joints and on the specimen surface, and also creep and eventual relaxation of grub screws etc. Instead, it was decided that the extension should be measured between the grips. Grips were designed and machined from Inconel 601, with slots cut by electro-discharge machining (EDM) to accommodate the plate samples. Pin joints were utilised between the grip and each specimen, with alumina pins selected due to their immunity to oxidation and creep resistance. The grips and specimen assembly is shown in Figure B.3.

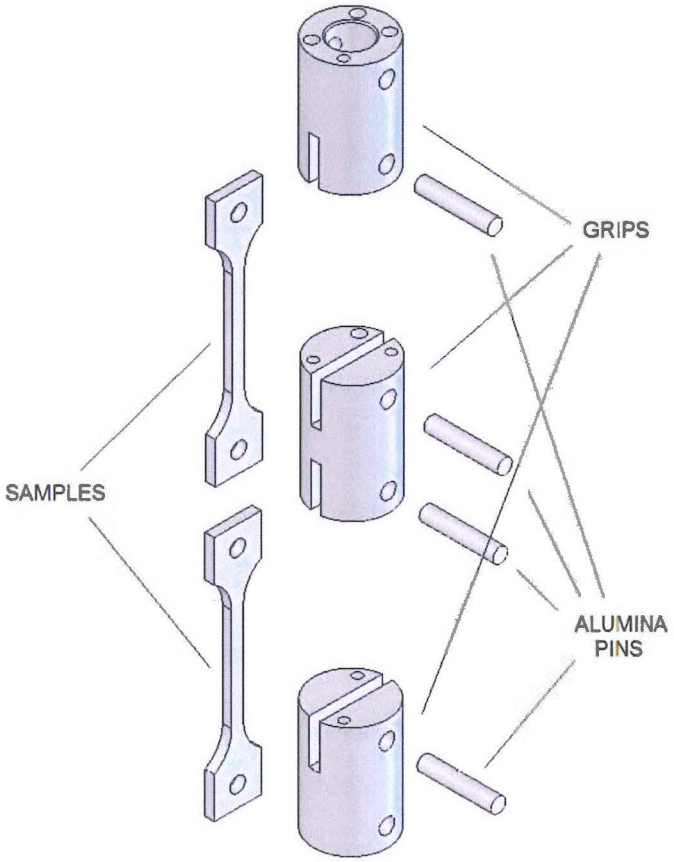

Figure B.3 Grip and specimen assembly

In order to justify the measurement of displacement between the specimen grips, finite element models were constructed using ANSYS [4] to determine the stress distribution within the grips in comparison with that of the creep specimens. In these analyses, the upper pin hole was set as a fixed support and a force loading was applied to the lower pin hole. The results are shown in Figure B.4 for the applied load of 15kg (12MPa sample stress).

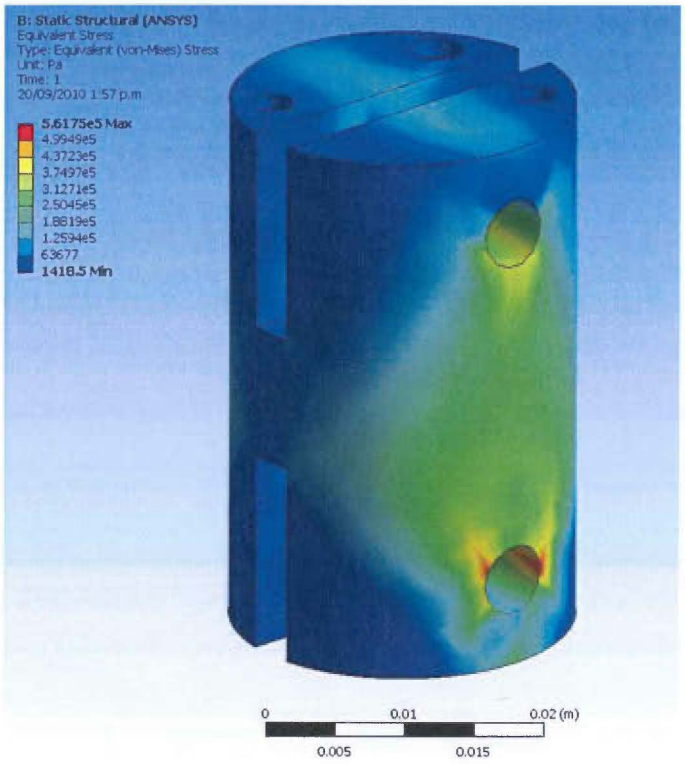

Figure B.4 Von Mises stress distribution for top sample grip at a load of 15kg

The results show a maximum stress of 0.56MPa, located at the lower pin hole. The creep rate of Inconel 601 at 950°C and 0.56MPa is approximately 0.000001%/hr [5], and is considered negligible compared with the creep rate of the specimens (~0.0005%/hr). Therefore measuring the displacement between grips introduces no significant error into the extensometer measurement.

The relative displacement between grips was measured by extending pushrods from each grip (two from the middle grip) and measuring the differential displacement between pushrods by linear variable displacement transducer (LVDT). LVDTs comprise a case and a magnetic core, and measure extension through the change in output voltage resulting from an inductance difference in pairing solenoids. The setup of the pushrod system is shown in Figure B.5.

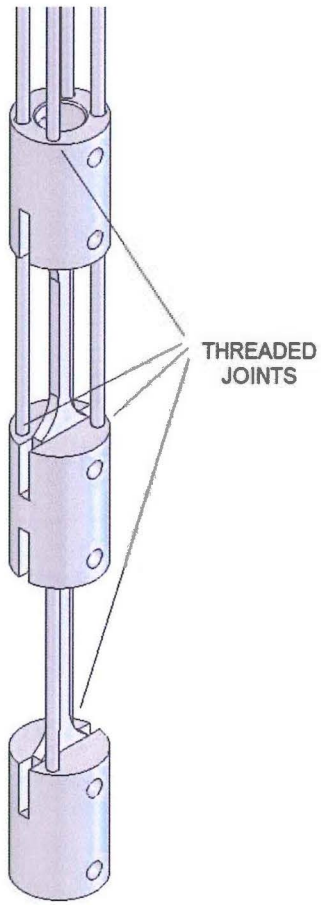

Figure B.5 Extensometer setup

One pushrod is threaded into the bottom grip and extends through the middle and upper grips. Two more pushrods are threaded into the middle grip and extend through the upper grip, and one further pushrod is only threaded into the upper grip. Therefore, extension in the upper sample causes two pushrods to lower, while the pushrod attached to the top grip remains

stationary. Likewise, extension in the lower sample causes the pushrod attached to the lower grip to lower relative to the middle grip. Extension can therefore be measured at the top of the pushrods, which is outside the furnace and therefore not subject to high temperatures. The LVDT setup is shown in Figure B.6.

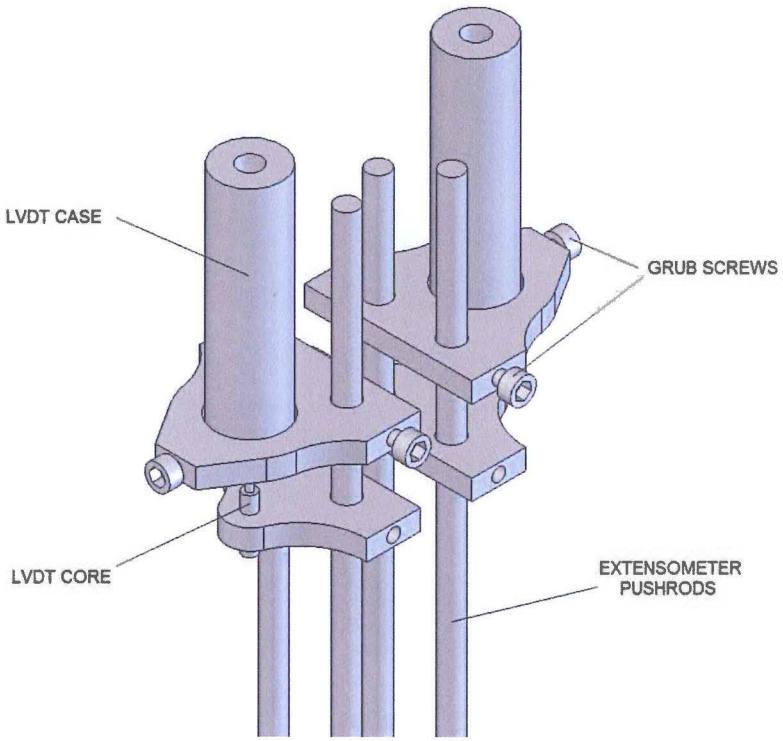

Figure B.6 LVDT setup

The LVDT case and core are attached to separate clamping plates and secured by grub screws. Each clamping plate is then secured to an individual pushrod, which remains free to move through the partner clamping plate. The movement of the pushrods therefore causes the LVDT cores to move relative to the cases, which provides the extension measurement. An advantage of this setup is that thermal expansion effects are nullified, as any thermal expansion within the pushrods (due to changes in ambient temperature) occurs in all four pushrods simultaneously, and hence the relative expansion is zero.

B.3.3 Heating Element and Temperature Control

Due to the series arrangement of creep samples, it was important that the temperature of the two samples was equal to within a tolerance of 1-2°C. The reason for this tolerance is that creep is highly dependent on temperature, and any variation may cause significant uncertainty in creep rate measurement. For example, to the manufacturer's data for 800H [6], a temperature deviation of 55° may result in a change in minimum creep rate of up to 100x. Therefore, the heating element setup was designed with this in mind.

In order to ensure there was no temperature gradient between the two samples, an isothermal furnace liner (IFL) was obtained from Advanced Cooling Technologies [7] in Pennsylvania, USA. The IFL consists of two concentric pipes of high-nickel stainless steel, and a charge of sodium located in between the two pipe walls. At the test temperature of 950°C, sodium exists as a vapour. A local increase in temperature along the length of the pipe causes a local increase in vapour pressure, which drives heat convection away from the hot spot and ensures temperature uniformity. This is illustrated in Figure B.7.

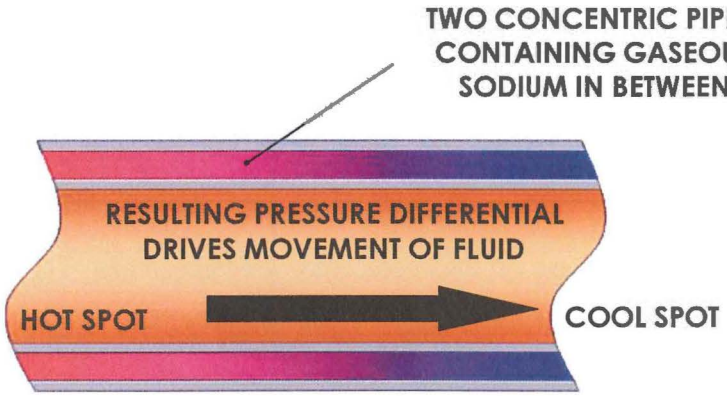

Figure B.7 Isothermal furnace liner operation

The IFL was situated within a 2kW tubular heating element, which measured approximately 200mm long and was located centrally with respect to the furnace liner. Temperature was

measured by two N-type thermocouples situated inside the IFL and controlled by an Omron E5CZ temperature controller. Details of the resulting temperature profile are presented in Section B.4.1.

B.3.4 Sample Loading

Alumina connecting rods were used above and below the grips to suspend a dead-weight load of approximately 150N. Alumina was chosen because of its low thermal conductivity and resistance to creep and environmental attack at the test temperature of 950°C. Pin joints, with alumina pins, were used to connect the connecting rods to the grips, and also to connect the load to the bottom connecting rod. The loading setup is shown in Figure B.8.

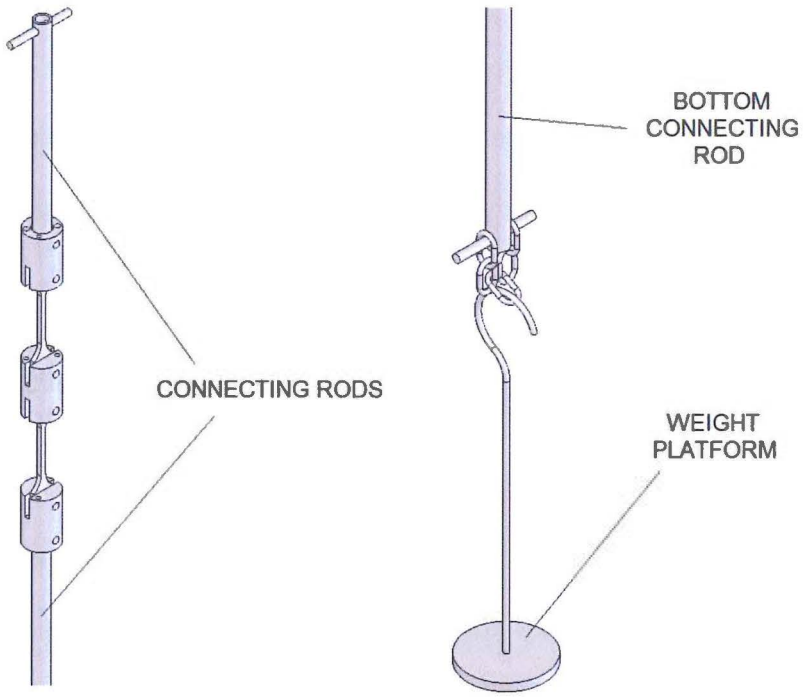

Figure B.8 Connecting rod and pin-joint setup

As the two specimens were arranged in series, the top specimen carried an extra tensile load equivalent to the weight of one sample grip and the bottom tensile specimen. This mass was

measured to be approximately 150g, and therefore contributed an extra stress according to the equation:

$$\sigma = \frac{F}{A} = \frac{mg}{A} = \frac{0.15kg \times 9.81Nkg^{-1}}{12mm^2} = 0.12MPa \quad \text{(B.4)}$$

This extra loading comprises only 1% of the total load on the sample, and therefore was considered negligible in the creep rate analysis.

B.3.5 Data Acquisition System

Temperature and LVDT extension were transmitted to a National Instruments NI-cDAQ-9172 data acquisition system, interfaced with a 2.4GHz Pentium 4 PC. A project was created in National Instruments LabVIEW to display and record the data at a sampling rate of 0.1Hz.

B.3.6 Test Procedure

The test assembly was constructed at room temperature and inserted into the IFL. The furnace was heated at a rate of 3°C/min to the test temperature of 950°C with a load of 1.5kg (10% of the final load) as per ASTM E139 [3]. The aim of this procedure is to eliminate movement in the pin joints. Specimens were allowed to remain at the test temperature for a period of two hours before the application of load, in order to achieve equilibrium temperature. Sample loading was performed by gently loading steel weights in 5kg increments. LVDT extensometers were then set to zero and recording was initiated approximately 2-3 minutes after the load was applied.

B.4 Evaluation and Calibration

B.4.1 Temperature Profile

The temperature profile of the heating element was initially measured by N-type thermocouple at a temperature of approximately 950°C. This process was then repeated with the IFL installed and both ends sealed. Measurements were recorded in the central 250mm, approximately 50mm longer than the distance between the top of the upper sample grip and the bottom of the lower sample grip. The results are shown in Figure B.9.

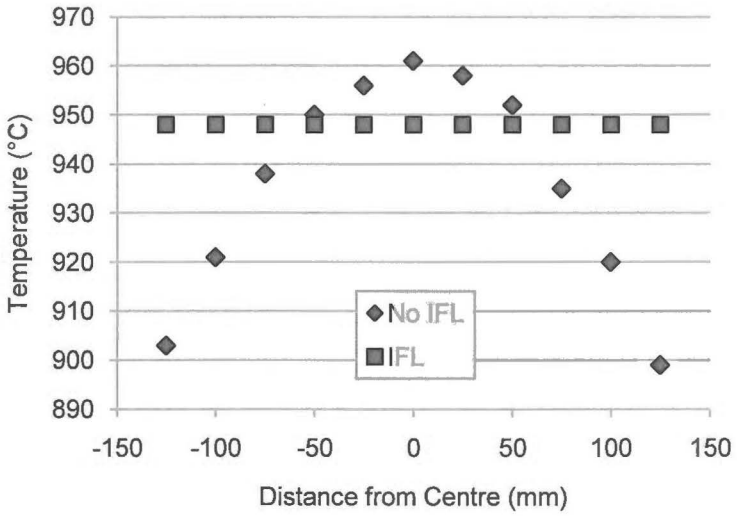

Figure B.9 Temperature profile of the furnace, excluding and including the IFL

The results show that there is no discernable temperature fluctuation in the central 250mm of the furnace with the IFL installed. This result is consistent with the manufacturer's claim of <1° variation.

A typical temperature/time curve for the duration of a creep test is shown in Figure B.10.

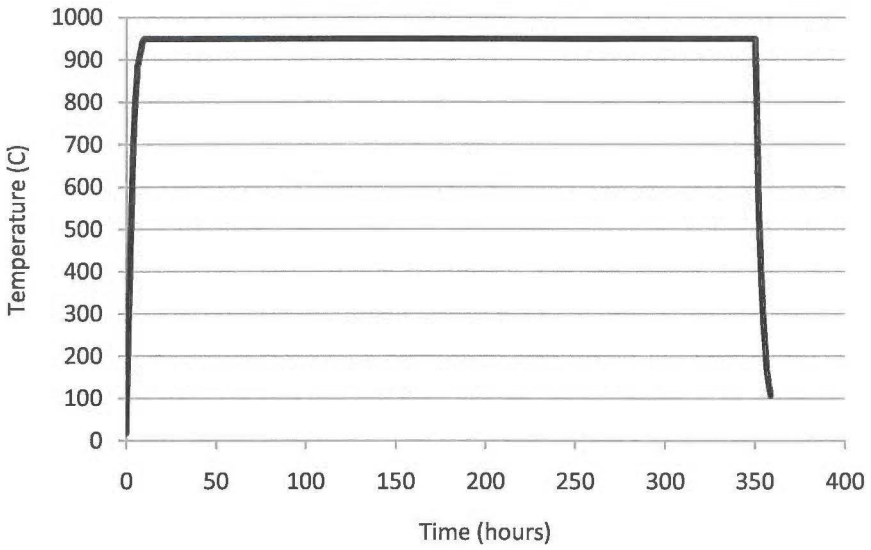

Figure B.10 Temperature/time curve for typical creep test

No temperature "spikes" were noticed in excess of 1°C above the intended test temperature. Figure B.11 shows a selected portion of this temperature profile, in order to evaluate the short-range variation in temperature.

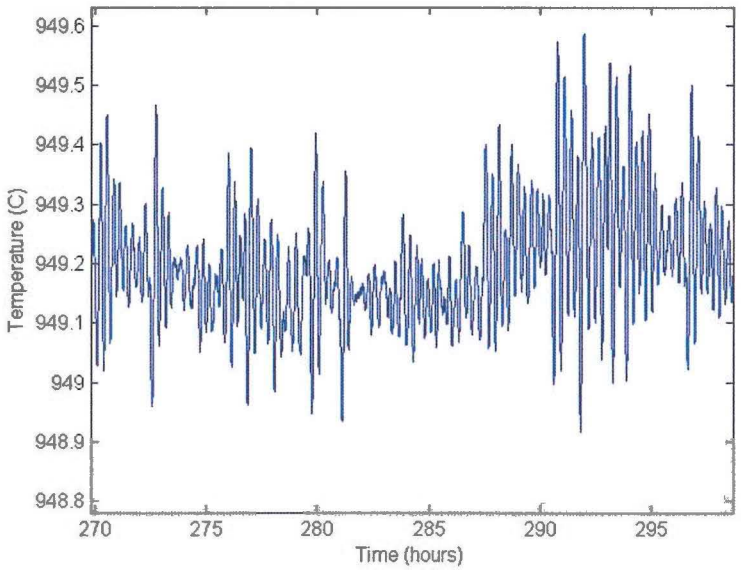

Figure B.11 Short-range temperature variation

The results show that the variation in temperature is approximately ±0.5°C, which is well within the specifications of ASTM E139.

B.4.2 LVDT Calibration

The output voltage of the LVDT must be converted into an extension according to a linear scaling factor. In order to determine this scaling factor, the LVDTs were individually attached to a micrometer as shown in Figure B.12.

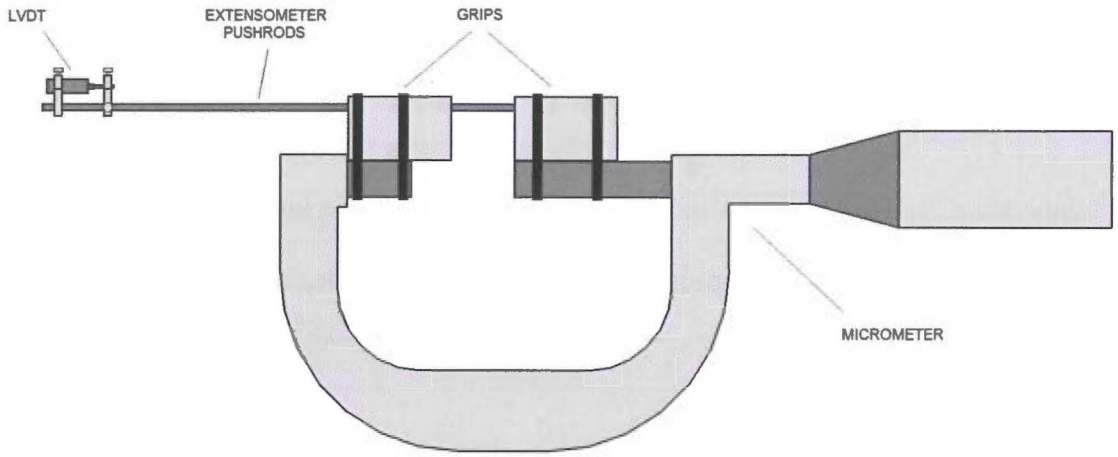

Figure B.12 Calibration setup of the LVDT extensometers

The micrometer was adjusted manually in steps of 100μm, and the resulting LVDT data were recorded at a frequency of 1Hz. The results are shown in Figure B.13.

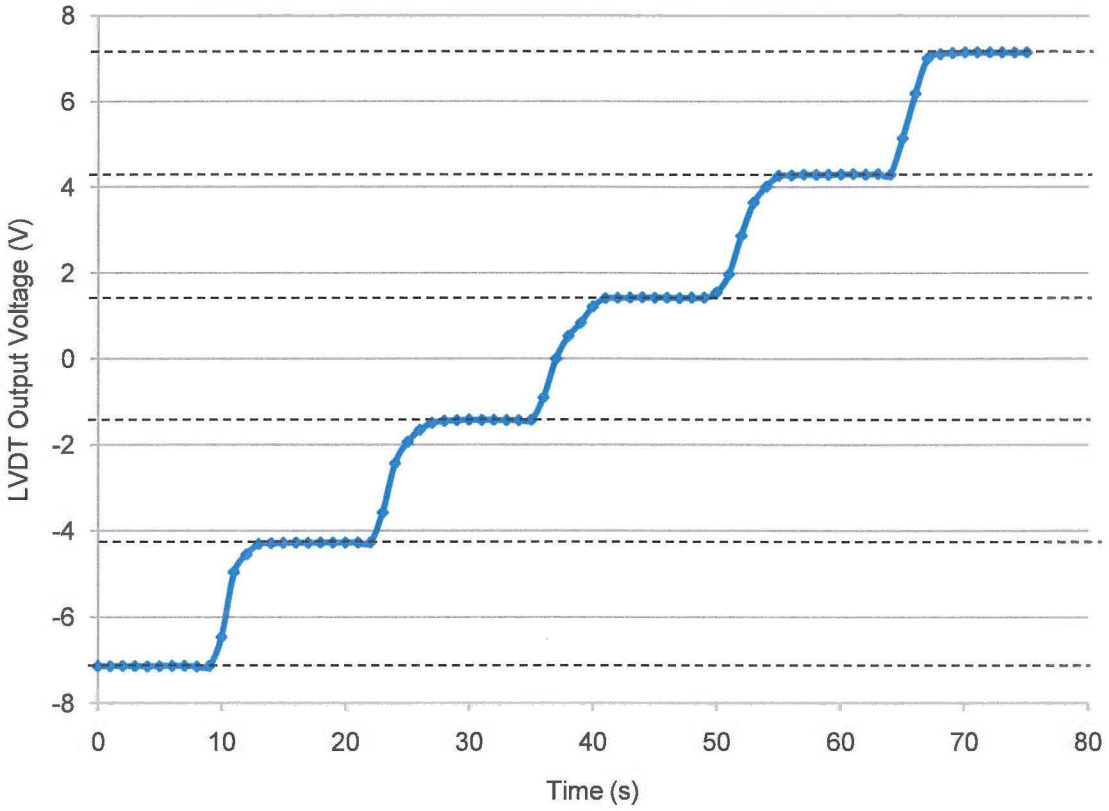

Figure B.13 LVDT response to input steps of 100μm

The voltage difference was measured between each "ledge". From these voltage differences, the scale factor was determined to be 0.028553V/μm with an accuracy of ±1% (1μm).

B.4.3 LVDT Drift

In order to determine whether or not the LVDT extensometer was affected by vibrations or changes in ambient temperature, the extensometer was set up in a static condition and data were recorded for a period of four days (96 hours). The ambient temperature was recorded via thermocouple at a distance of 300mm from the LVDT case. The results are shown in Figure B.14, with a moving average filter of 10 points per point applied to remove the majority of measurement noise.

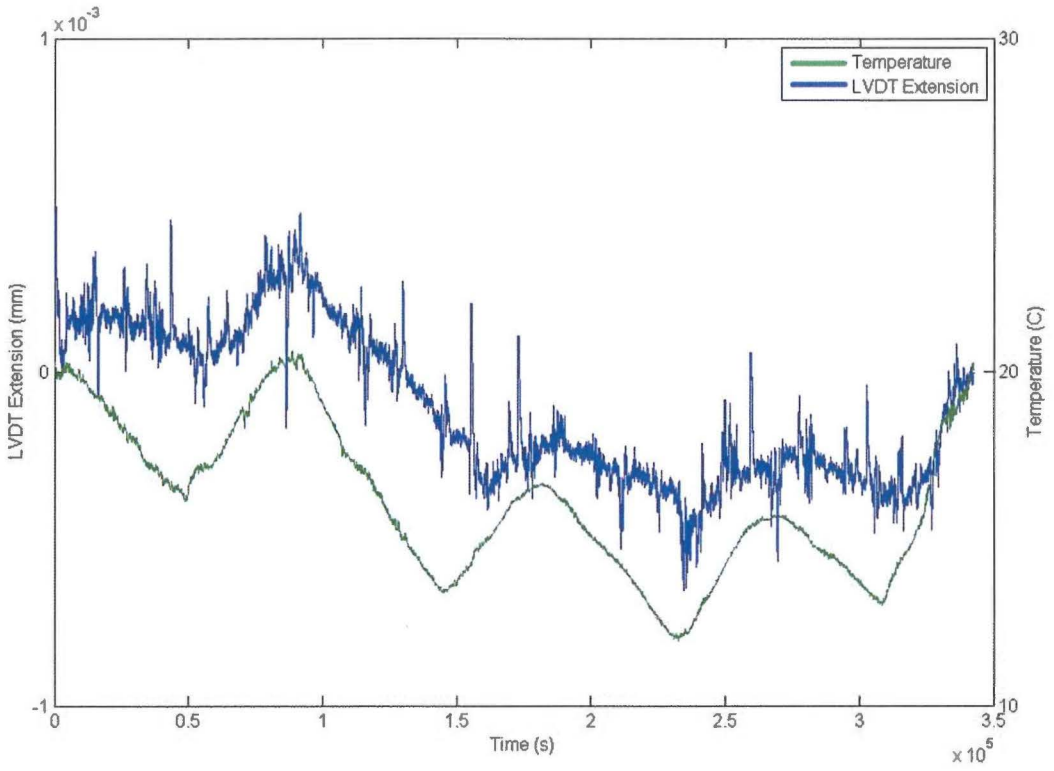

Figure B.14 LVDT drift with ambient temperature for a period of 96 hours

The results show that there is some dependence of LVDT extension on ambient temperature. However, the entire y-scale in Figure B.14 represents a range of ±1μm, which shows that this dependence is on the order of ±0.5μ over the ambient temperature range considered (12-20°C). This variation was considered acceptable for the current testing. The fact that the LVDT data exhibits no discontinuities also shows that there is no effect from floor vibrations, air currents etc. Measurement noise is also considered negligible after data averaging.

B.5 References

[1] Instron, *M3 Creep and Stress Rupture Systems*, available http://www.instron.co.uk-/wa/product/Creep-Stress-Relaxation-Testers.aspx.

[2] ASTM, *E8: Standard Test Methods for Tension Testing of Metallic Materials*, 1996.

[3] ASTM, *E139 - 06: Standard test methods for conducting creep, creep-rupture and stress-rupture tests of metallic materials*, 1996.

[4] ANSYS Inc., *ANSYS Workbench v13.0*.

[5] Special Metals Corporation, *Technical Bulletin - Alloy 601*, 2004.

[6] Special Metals Corporation, *Technical Publication - Alloy 800H & 800HT*, 2004.

[7] Advanced Cooling Technologies Inc. (ACT), *http://www.1-act.com/products-/temperature-calibration-control/isothermal-furnace-liner.php*.

APPENDIX C: DETERMINATION OF BOUNDARY DEVIATION PARAMETER

This appendix provides the source-code used for the determination of the deviation from ideal parameter (v/v_m) for all $\Sigma 3^n$ boundaries. The software requires an input matrix of raw Euler angles, which is extracted from the Channel 5 EBSD software and saved in the .xls format.

```
function [] = gbdeviation2()
tic
%This function reads in a .xls spreadsheet and calculates
%grain boundary disorientations and CSL deviations for all
%sigma 3^n boundaries

%Define initial settings
LAB_thold=2;
HAB_thold=10;
GB_thold=10;
gtob=4;

%Read in the raw Euler angle data
fname=input('Input filename: ');
fnameeuler=strcat(fname,'euler');
fprintf('\nLoading data...\n');
fnamemean=strcat(fname,'mean');
eulerraw=xlsread(fnameeuler,1,'C:G');
res=5;
max_y=(max(eulerraw(:,1))/res)+1;
max_x=(max(eulerraw(:,2))/res)+1;
numpix=max_x*max_y;

%Convert it to a cell based matrix
for c=1:(max_x*max_y)
    x=eulerraw(c,1)/res+1;
    y=eulerraw(c,2)/res+1;
    ang=eulerraw(c,3:5);
    eulercell{y,x}=ang;
end

fprintf('Defining grain boundaries...\n');

%Calculate the disorientations down and right of each pixel

for x=1:max_x
    for y=1:max_y
        %Extract the euler angles of each pixel
        eulerc(1,1:3)=eulercell{x,y};
        phi1=eulerc(1,1)*pi/180;
        phi=eulerc(1,2)*pi/180;
        phi2=eulerc(1,3)*pi/180;

        %Create a quaternion for each pixel
        qone=angle2quat(phi1,phi,phi2,'XZX');

        if y~=max_y
            %Create quaternion for pixel to the right
            eulerc(2,1:3)=eulercell{x,y+1};
            twophi1=eulerc(2,1)*pi/180;
```

```
    twophi=eulerc(2,2)*pi/180;
    twophi2=eulerc(2,3)*pi/180;

    qtwo=angle2quat(twophi1,twophi,twophi2,'XZX');

    %Create rotation difference quaternion
    qdright=quatmultiply(quatinv(qone),qtwo);

    %Order the quaternion such that e4>e3>e2>e1 and all are positive
    qdright=abs(qdright);
    qdright=sort(qdright);
    e1=qdright(1);
    e2=qdright(2);
    e3=qdright(3);
    e4=qdright(4);

    %The disorientation is then given by one of the following three
    %crystallographic equivalent quaternions
    disq(1,:)=qdright;
    disq(2,:)=(1/sqrt(2))*[e1-e2,e2+e1,e3-e4,e4+e3];
    disq(3,:)=(1/2)*[e1-e4-e2+e3,e2-e4-e3+e1,e3-e4-e1+e2,e4+e1+e2+e3];

    %The disorientation is given by the disq quaternion with the largest
    %fourth component
    [m disc]=max(disq(:,4));
    disc=disq(disc,:);

    %Calculate disorientation angle
    disright=2*acosd(disc(4));

    %Calculate disorientation axes (do we need this?)
    disaxesright(1)=disc(1);
    disaxesright(2)=disc(2);
    disaxesright(3)=disc(3);

    %Write this data into a seperate matrix
    finaldisangright(x,y)=disright;
    finaldisaxesright{x,y}=disaxesright;
end

%Create quaternion for pixel below
if x~=max_x
    eulerc(3,1:3)=eulercell{x+1,y};
    threephi1=eulerc(3,1)*pi/180;
    threephi=eulerc(3,2)*pi/180;
    threephi2=eulerc(3,3)*pi/180;

    qthree=angle2quat(threephi1,threephi,threephi2,'XZX');

    %Create rotation difference matrices
    qddown=quatmultiply(quatinv(qone),qthree);

    %Order the quaternion such that e4>e3>e2>e1 and all are positive
    qddown=abs(qddown);
    qddown=sort(qddown);
    e1=qddown(1);
    e2=qddown(2);
    e3=qddown(3);
    e4=qddown(4);

    %The disorientation is then given by one of the following three
    %crystallographic equivalent quaternions
    disq(1,:)=qddown;
    disq(2,:)=(1/sqrt(2))*[e1-e2,e2+e1,e3-e4,e4+e3];
    disq(3,:)=(1/2)*[e1-e4-e2+e3,e2-e4-e3+e1,e3-e4-e1+e2,e4+e1+e2+e3];

    %The disorientation is given by the disq quaternion with the largest
    %fourth component
    [m disc]=max(disq(:,4));
    disc=disq(disc,:);

    %Calculate disorientation angle
    disdown=2*acosd(disc(4));

    %Calculate disorientation axes (do we need this?)
    disaxesdown(1)=disc(1);
    disaxesdown(2)=disc(2);
```

```
            disaxesdown(3)=disc(3);

            %Write this data into a seperate matrix
            finaldisangdown(x,y)=disdown;
            finaldisaxesdown{x,y}=disaxesdown;
        end
    end
end

%Set up a matrix to make sure all pixels are counted
grainnos=zeros(max_x,max_y);
cgrain=0;

%Loop through while there is still any pixel not assigned to a grain
while nnz(grainnos)<numpix

    %Find first pixel that has not been assigned to a grain
    [xc yc]=find(grainnos==0,1);
    tocheck=[xc yc];

    %Assign it the next available grain number
    cgrain=cgrain+1;
    grainnos(xc,yc)=cgrain;

    while size(tocheck,1)>0
        xc=tocheck(1,1);
        yc=tocheck(1,2);

        %Check which neighbours are same grain
        if xc>1 && grainnos(xc-1,yc)==0
            if finaldisangdown(xc-1,yc)<GB_thold
                grainnos(xc-1,yc)=cgrain;
                if ismember([xc-1 yc],tocheck,'rows')==0
                    tocheck=[tocheck;xc-1,yc];
                end
            end
        end

        if xc<max_x && grainnos(xc+1,yc)==0
            if finaldisangdown(xc,yc)<GB_thold
                grainnos(xc+1,yc)=cgrain;
                if ismember([xc+1 yc],tocheck,'rows')==0
                    tocheck=[tocheck;xc+1,yc];
                end
            end
        end

        if yc<max_y && grainnos(xc,yc+1)==0
            if finaldisangright(xc,yc)<GB_thold
                grainnos(xc,yc+1)=cgrain;
                if ismember([xc yc+1],tocheck,'rows')==0
                    tocheck=[tocheck;xc,yc+1];
                end
            end
        end

        if yc>1 && grainnos(xc,yc-1)==0
            if finaldisangright(xc,yc-1)<GB_thold
                grainnos(xc,yc-1)=cgrain;
                if ismember([xc yc-1],tocheck,'rows')==0
                    tocheck=[tocheck;xc,yc-1];
                end
            end
        end

        %Delete the line just checked
        tocheck(1,:)=[];
    end
end

num_grains=cgrain;

fprintf('Reading average orientation data...\n');

%Now we need to read in the average orientation for each grain
meanraw=xlsread(fnamemean,1,'C:M');
found=[];
```

```
cc=1;
grainolist=zeros(num_grains,4);

%Check that they are all valid numbers
valchk=isnan(meanraw(:,1));
[dd ee]=find(valchk);

if isempty(dd)~=1
    fprintf('Invalid number in mean data.');
end

%Loop through and match up detected grains with mean list
for x=1:max_x
    for y=1:max_y
        if ismember(grainnos(x,y),found)==0
            grainolist(grainnos(x,y),1)=meanraw(cc,1);
            grainolist(grainnos(x,y),2:4)=meanraw(cc,9:11);
            cc=cc+1;
            found=[found grainnos(x,y)];
        end
    end
end

%Create a record of grain area
for n=1:num_grains
    gareas(n)=length(find(grainnos==n))*res*res;
end

%Check that the read area matches the calculated area
for o=1:num_grains
    if gareas(o)~=grainolist(o,1)
        if gareas(o)~=(0.5*grainolist(o,1))
            if gareas(o)~=(0.25*grainolist(o,1))
                fprintf('WARNING: Grain area mismatch!\n')
            end
        end
    end
end

fprintf('Defining grain boundary segments...\n');

%Write two matrices indicating a boundary to the right or down
cbs=-1;     %Current boundary segment
bsegs=zeros(num_grains,num_grains);
bright=zeros(max_x,max_y-1);
bdown=zeros(max_x-1,max_y);

for x=1:max_x
    for y=1:max_y
        gc=grainnos(x,y);

        if x~=max_x
            if y~=max_y
                gr=grainnos(x,y+1);
                gd=grainnos(x+1,y);
            else
                gr=gc;
                gd=grainnos(x+1,y);
            end
        else
            if y~=max_y
                gr=grainnos(x,y+1);
                gd=gc;
            else
                gr=gc;
                gd=gc;
            end
        end

        if gr~=gc
            %There is a boundary there
            gbr=sort([gc gr]);

            if bsegs(gbr(1),gbr(2))==0
                %This is a new boundary
                bright(x,y)=cbs;
                bsegs(gbr(1),gbr(2))=cbs;
```

```
                cbs=cbs-1;
            else
                bright(x,y)=bsegs(gbr(1),gbr(2));
            end
        end

        if gc~=gd
            %There is a boundary there
            gbd=sort([gc gd]);

            if bsegs(gbd(1),gbd(2))==0
                %This is a new boundary
                bdown(x,y)=cbs;
                bsegs(gbd(1),gbd(2))=cbs;
                cbs=cbs-1;
            else
                bdown(x,y)=bsegs(gbd(1),gbd(2));
            end
        end
    end
end

num_btypes=abs(cbs)-1;
boundaries=[];
condir=[-1 0;1 0;0 0;0 1;-1 0;-1 1];
condid=[0 -1;0 1;0 -1;1 -1;0 0;1 0];


%Check for continuous segments
for f=1:num_btypes

    [brx bry]=find(bright==-f);
    br=[brx bry];
    [bdx bdy]=find(bdown==-f);
    bd=[bdx bdy];
    btog=[br;bd];
    numr=size(br,1);
    numd=size(bd,1);
    npix=0;

    %Connections matrix
    cons=zeros(size(btog,1),17);
    cons(:,1:2)=btog;
    cons(:,3)=1;
    cons(1:size(br,1),3)=0;
    b2count=cons(:,1:3);

    %Cons looks like:
    %x     y     r/d     #con(u/l)     #con(d/r)     con1(u/l)     type1(u/l)
    %con2(u/l)     type2     con3(u/l)     type3     con1(b/r)     type1(b/r)
    %con2(b/r)     type2(b/r)     con3(b/r)     type3(b/r)

    %Connection types are:
    %(1)top/up (2)bottom/down (3)bottom/left (4)bottom/right
    %(5)top/left (6)top/right (7)left/left (8)right/right
    %(9)left/up (10)left/down (11)right/up (12)right/down

    ep=[];
    ncs=zeros(1,size(btog,1));

    %Find the connections for each pixel segment
    for dr=1:numr
        nc=0;
        cp=br(dr,:);
        conup=[];
        condown=[];

        %Check top up and bottom down connections
        for t=1:2
            chk=cp+condir(t,:);
            [k l] = ismember(chk,br,'rows');
            if k~=0
                %This is a valid connection
                if t==1
                    %This is a top connection
                    conup=[conup l t];
                else
```

```
                %This is a bottom connection
                condown=[condown l t];
            end
            nc=nc+1;
        end
    end

    %Check bottom left/right and top left/right connections
    for t=3:6
        chk=cp+condir(t,:);
        [k l] = ismember(chk,bd,'rows');
        if k~=0
            %This is a valid connection
            if t<5
                %This is a bottom connection
                condown=[condown l+numr t];
            else
                %This is a top connection
                conup=[conup l+numr t];
            end
            nc=nc+1;
        end
    end

    %Write the number of connections as well
    cons(dr,4)=length(conup)/2;
    cons(dr,5)=length(condown)/2;

    %And write to the cons matrix
    cons(dr,6:5+nnz(conup))=conup;
    cons(dr,12:11+nnz(condown))=condown;
end

for dd=1:numd
    nc=0;
    cp=bd(dd,:);
    conleft=[];
    conright=[];

    %Check left/left and right/right connections
    for t=1:2
        chk=cp+condid(t,:);
        [k l] = ismember(chk,bd,'rows');
        if k~=0
            %This is a valid connection
            if t==1
                %This is a left connection
                conleft=[conleft l+numr t+6];
            else
                %This is a right connection
                conright=[conright l+numr t+6];
            end
            nc=nc+1;
        end
    end


    %Check left/up, left/down, right/up, right/down connections
    for t=3:6
        chk=cp+condid(t,:);
        [k l] = ismember(chk,br,'rows');
        if k~=0
            %This is a valid connection
            if t<5
                %This is a left connection
                conleft=[conleft l t+6];
            else
                %This is a right connection
                conright=[conright l t+6];
            end
            nc=nc+1;
        end
    end

    %Write the number of connections as well
    cons(numr+dd,4)=length(conleft)/2;
    cons(numr+dd,5)=length(conright)/2;
```

```
    %And write to the cons matrix
    cons(numr+dd,6:5+nnz(conleft))=conleft;
    cons(numr+dd,12:11+nnz(conright))=conright;
end

%Boundaries matrix looks like
%(1)    Grain 1
%(2)    Grain 2
%(3)    GB Length
%(4)    Misorientation angle
%(5-7)  Misorientation axis
%(8)    Dev from sigma 3
%(9)    Dev from sigma 9
%(10)   Dev from sigma 27a
%(11)   Dev from sigma 27b
%(12)   Sigma type

cp=[];      %Current path
nodes=[];

%Find out where the nodes are
for w=1:size(cons,1)
    if cons(w,4)==0 || cons(w,4)>1
        %The top or left is a node
        nodes=[nodes;w 0];
    end
    if cons(w,5)==0 || cons(w,5)>1
        %The bottom or right is a node
        nodes=[nodes;w 1];
    end
end

%Now follow the boundary paths until all segments are counted
while nnz(b2count(:,1))>0

    %Start two paths (i.e. from each node in first segment)
    ii=find(b2count(:,1),1);
    cp1=[];
    cp2=[];

    %Write top/left path...
    cp1(1,1)=ii;        %Boundary segment
    cp1(2,1)=0;         %Top/left

    %Write bottom/right path...
    cp2(1,1)=ii;
    cp2(2,1)=1;

    %Now follow cp1 until it meets another node
    found1=0;
    found2=0;
    scp1=1;
    scp2=1;

    while found1==0
        if ismember((cp1(:,scp1))',nodes,'rows')~=0
            %This is a node - found end of path
            found1=1;

        elseif ismember(cp1(:,scp1)',cp2','rows')~=0
            %We have completed a loop - found end of path
            found1=1;
            found2=1;
            cp1(:,scp1)=[];

        else
            %We need to extend the path - find available
            %Test if same number, different node is available
            test1=cp1(:,scp1)';
            test2=cp1(:,scp1)';

            if test1(1,2)==0
                test2(1,2)=1;
            else
                test2(1,2)=0;
            end
```

```
        if ismember(test2,cp1','rows')~=0 || ismember(test2,cp2','rows')~=0
            %We can't use same number, different node

            if cp1(2,scp1)==0
                %We are looking at conns from up/left
                nextn=cons(cp1(1,scp1),6);
                if ismember(cp1(1,scp1),cons(nextn,6:2:10))==1
                    cp1=[cp1 [nextn;0]];
                elseif ismember(cp1(1,scp1),cons(nextn,12:2:16))==1
                    cp1=[cp1 [nextn;1]];
                else
                    fprintf('WARNING: Connection error.');
                end
            else
                %We are looking at conns from bot/right
                nextn=cons(cp1(1,scp1),12);
                if ismember(cp1(1,scp1),cons(nextn,6:2:10))==1
                    cp1=[cp1 [nextn;0]];
                elseif ismember(cp1(1,scp1),cons(nextn,12:2:16))==1
                    cp1=[cp1 [nextn;1]];
                else
                    fprintf('WARNING: Connection error.');
                end
            end

            scp1=scp1+1;

        else
            %We can use same number, different node
            cp1=[cp1 test2'];
            scp1=scp1+1;
        end

    end
end

%Now follow cp2 until it meets another node
while found2==0
    if ismember((cp2(:,scp2))',nodes,'rows')~=0
        %This is a node - found end of path
        found2=1;

    elseif ismember(cp2(:,scp2)',cp1','rows')~=0
        %We have completed a loop - found end of path
        found1=1;
        found2=1;
        cp2(:,scp2)=[];

    else
        %We need to extend the path - find available
        %Test if same number, different node is available
        test1=cp2(:,scp2)';
        test2=cp2(:,scp2)';

        if test1(1,2)==0
            test2(1,2)=1;
        else
            test2(1,2)=0;
        end

        if ismember(test2,cp1','rows')~=0 || ismember(test2,cp2','rows')~=0
            %We can't use same number, different node

            %Find available nodes

            if cp2(2,scp2)==0
                %We are looking at conns from up/left
                nextn=cons(cp2(1,scp2),6);
                if ismember(cp2(1,scp2),cons(nextn,6:2:10))==1
                    cp2=[cp2 [nextn;0]];
                elseif ismember(cp2(1,scp2),cons(nextn,12:2:16))==1
                    cp2=[cp2 [nextn;1]];
                else
                    fprintf('Error.');
                end
            else
```

```
                %We are looking at conns from bot/right
                nextn=cons(cp2(1,scp2),12);
                if ismember(cp2(1,scp2),cons(nextn,6:2:10))==1
                    cp2=[cp2 [nextn;0]];
                elseif ismember(cp2(1,scp2),cons(nextn,12:2:16))==1
                    cp2=[cp2 [nextn;1]];
                else
                    fprintf('Error.');
                end
            end

            scp2=scp2+1;

        else
            %We can use same number, different node
            cp2=[cp2 test2'];
            scp2=scp2+1;

        end
    end
end

%Now join the two paths, delete from b2count and write to
%boundaries matrix
nodepath=[];

%Swap the order of cp1
for ff=1:size(cp1,2)
    nodepath=[nodepath cp1(:,size(cp1,2)+1-ff)];
end

%And add on cp2
nodepath=[nodepath cp2];
bpath=[];
btype=[];

%Now extract the path in terms of boundary segments travelled
for gg=2:size(nodepath,2)
    if nodepath(1,gg)==nodepath(1,gg-1)
        %We have travelled along a boundary segment
        bpath=[bpath nodepath(1,gg)];
        btype=[btype cons(nodepath(1,gg),3)];
    end
end

%Delete these paths from the b2count matrix
b2count(bpath,:)=0;

%Calculate the approximate corrected length for the segment
blength=1;
reset=1;

for s=1:(length(btype)-1)
    sca=btype(s);
    scb=btype(s+1);

    if sca~=scb
        %Change of direction
        if reset==1
            blength=blength+sqrt(2)-1;
            reset=0;
        else
            blength=blength+1;
            reset=1;
        end
    else
        blength=blength+1;
        reset=1;
    end
end

%Write to boundaries matrix
[g1 g2]=find(bsegs==-f);
boundaries=[boundaries;g1 g2 blength];

if size(boundaries,1)>10000
    fprintf('WARNING: Eternal loop.\n')
```

```
        end

    end
end

fprintf('Calculating misorientations based on average data...\n');

%Define rotation quaternions for sigma 3, 9, 27a, 27b
q3=[0.28867513 0.28867513 0.28867513 0.86602540];
q9=[0 0.23568806 0.23568806 0.94281614];
q27a=[0 0.19241246 0.19241246 0.96226550];
q27b=[0 0.13604207 0.27208415 0.95260840];

%Set up Brandon's (or other) criteria
v3thold=15/sqrt(3);
v9thold=15/sqrt(9);
v27thold=15/sqrt(27);

%Set up seperate matrices for s3, s9, s27
sig3s=[];
sig9s=[];
sig27s=[];

%Now go through the boundaries matrix and calculate the misorientation
%angle and axis for each boundary segment
for v=1:size(boundaries,1)
    eulerg1=grainolist(boundaries(v,1),2:4);
    eulerg2=grainolist(boundaries(v,2),2:4);

    phi1=eulerg1(1)*pi/180;
    phi=eulerg1(2)*pi/180;
    phi2=eulerg1(3)*pi/180;

    %Create rotation quaternion for grain 1
    qone=angle2quat(phi1,phi,phi2,'XZX');

    twophi1=eulerg2(1)*pi/180;
    twophi=eulerg2(2)*pi/180;
    twophi2=eulerg2(3)*pi/180;

    %Create rotation quaternion for grain 2
    qtwo=angle2quat(twophi1,twophi,twophi2,'XZX');

    %Create rotation difference quaternion
    qd=quatmultiply(quatinv(qone),qtwo);

    %Order the quaternion such that e4>e3>e2>e1 and all are positive
    qd=abs(qd);
    qd=sort(qd);
    e1=qd(1);
    e2=qd(2);
    e3=qd(3);
    e4=qd(4);

    %The disorientation is then given by one of the following three
    %crystallographic equivalent quaternions
    disq(1,:)=qd;
    disq(2,:)=(1/sqrt(2))*[e1-e2,e2+e1,e3-e4,e4+e3];
    disq(3,:)=(1/2)*[e1-e4-e2+e3,e2-e4-e3+e1,e3-e4-e1+e2,e4+e1+e2+e3];

    %The disorientation is given by the disq quaternion with the largest
    %fourth component
    [m disc]=max(disq(:,4));
    disc=disq(disc,:);

    %Calculate disorientation angle
    dis=2*acosd(disc(4));

    %Calculate disorientation axes (do we need this?)
    disaxes(1)=disc(1);
    disaxes(2)=disc(2);
    disaxes(3)=disc(3);

    %Write this data into the boundaries matrix
    boundaries(v,4)=dis;
    boundaries(v,5:7)=disaxes;
```

```
    %Sort the quaternion into positive, ascending order again
    disc=abs(disc);
    disc=sort(disc);

    %Now test for sigma 3, 9 or 27a/b
    v3=2*acosd(dot(q3,disc));
    boundaries(v,8)=v3;
    v9=2*acosd(dot(q9,disc));
    boundaries(v,9)=v9;
    v27a=2*acosd(dot(q27a,disc));
    boundaries(v,10)=v27a;
    v27b=2*acosd(dot(q27b,disc));
    boundaries(v,11)=v27b;

    %Now assign this boundary a sigma value
    if v3<v3thold
        %This is a sigma 3 boundary
        boundaries(v,12)=3;
        sig3s=[sig3s;boundaries(v,:)];

    elseif v9<v9thold
        %This is a sigma 9 boundary
        boundaries(v,12)=9;
        sig9s=[sig9s;boundaries(v,:)];

    elseif v27a<v27thold
        %This is a sigma 27a boundary
        boundaries(v,12)=27;
        sig27s=[sig27s;boundaries(v,:)];

    elseif v27b<v27thold
        %This is a sigma 27b boundary
        boundaries(v,12)=27;
        sig27s=[sig27s;boundaries(v,:)];

    else
        %This is none of the above
        boundaries(v,12)=0;
    end
end

%Now calculate number fractions and length fractions for each type
totalboundnum=size(boundaries,1);
totalboundlen=sum(boundaries(:,3)*res);

sig3num=size(sig3s,1);

if sig3num==0
    sig3len=0;
else
    sig3len=sum(sig3s(:,3)*res);
end

sig9num=size(sig9s,1);

if sig9num==0
    sig9len=0;
else
    sig9len=sum(sig9s(:,3)*res);
end

sig27num=size(sig27s,1);

if sig27num==0
    sig27len=0;
else
    sig27len=sum(sig27s(:,3)*res);
end

sig3numf=100*sig3num/totalboundnum;
sig3lenf=100*sig3len/totalboundlen;
sig9numf=100*sig9num/totalboundnum;
sig9lenf=100*sig9len/totalboundlen;
sig27numf=100*sig27num/totalboundnum;
sig27lenf=100*sig27len/totalboundlen;

%Display this information
```

```
fprintf('\nSigma 3s make up %g%% by number and %g%% by length.\n',sig3numf,sig3lenf);
fprintf('Sigma 9s make up %g%% by number and %g%% by length.\n',sig9numf,sig9lenf);
fprintf('Sigma 27s make up %g%% by number and %g%% by length.\n\n',sig27numf,sig27lenf);

save(fname,'sig3s','sig9s','sig27s','sig3numf','sig9numf',...
    'sig27numf','sig3lenf','sig9lenf','sig27lenf','totalboundnum',...
    'totalboundlen','v3thold','v9thold','v27thold','boundaries',...
    'sig3num','sig3len','sig9num','sig9len','sig27num','sig27len','res')

%Plot this information on Figure 1
figure(1)

%Create a matrix including GBs as pixels along rhs and bottom
%of each conventional pixel in the ratio given as gtobratio
%
%    [      ] ]
%    [  Gr  ] ]
%    [______] ]
%    [__bdry__]

vismap=zeros((gtob)*max_x,(gtob)*max_y);
bgrains=boundaries(:,1:2);

%Add on a row of zeros to bright and bdown
bright(:,size(bright,2)+1)=0;
bdown(size(bdown,1)+1,:)=0;

for x=1:max_x
    for y=1:max_y

        %Fill in the square and then overwrite the boundary pixels
        vismap((x*gtob-(gtob-1)):(x*gtob),(y*gtob-(gtob-1)):(y*gtob))=grainnos(x,y);

        if bright(x,y)~=0
            %We need to draw in a right boundary
            gone=grainnos(x,y);
            gtwo=grainnos(x,y+1);
            ggbb=sort([gone gtwo]);

            [p q]=ismember(ggbb,bgrains,'rows');

            btype=boundaries(q,12);

            if x==1
                vismap((x*gtob-(gtob-1)):x*gtob,y*gtob)=-btype;
            else
                vismap((x*gtob-(gtob)):x*gtob,y*gtob)=-btype;
            end
        end

        if bdown(x,y)~=0
            %We need to draw in a down boundary
            gone=grainnos(x,y);
            gtwo=grainnos(x+1,y);
            ggbb=sort([gone gtwo]);

            [p q]=ismember(ggbb,bgrains,'rows');

            btype=boundaries(q,12);

            vismap(x*gtob,(y*gtob-(gtob-1)):(y*gtob))=-btype;
        end
    end
end

%Make the grains random shades of grey/colour
map=zeros(96,3);
map(:,:)=0.5;
map=map+0.2*(rand(96,3)-0.1);
map(97,:)=[0 0 0];     %HAB
map(98,:)=[1 0 0];     %Sigma 3
map(99,:)=[1 1 0];     %Sigma 9
map(100,:)=[0 0 1];     %Sigma 27

%Set the grains to random colours
for gg=1:num_grains
    vismap(find(vismap==gg))=96*rand;
```

```
end

% %Scale the vismap matrix
% vismap(find(vismap>0))=vismap(find(vismap>0))*96/num_grains;

%Convert the grain boundaries
habpix=find(vismap==0);
vismap(habpix)=97;
s3pix=find(vismap==-3);
vismap(s3pix)=98;
s9pix=find(vismap==-9);
vismap(s9pix)=99;
s27pix=find(vismap==-27);
vismap(s27pix)=100;

%Plot the figure
colormap(map);
image(vismap)
daspect([1 1 1])

%Save the figure
 print('-r300','-dtiff',fname);

 toc
```

APPENDIX D: PUBLICATIONS

The following article was accepted for publication in Metallurgical and Materials Transactions A, and is in press at the time of completion of this document.

- **D.J.F. Drabble, C.M. Bishop, M.V. Kral**, *A Microstructural Study of Grain Boundary Engineered 800H*, Metallurgical and Materials Transactions A (in press)

A Microstructural Study of Grain Boundary Engineered Alloy 800H

Daniel J. Drabble, Catherine M. Bishop and Milo V. Kral

Department of Mechanical Engineering, University of Canterbury
Private Bag 4800, Christchurch, New Zealand

Abstract
A series of grain boundary engineering (GBE) procedures was performed on samples of 800H, a common iron-nickel base alloy. The effects of varying the GBE parameters (deformation percentage, annealing temperature/time) were examined using electron backscatter diffraction orientation mapping. GBE samples exhibited up to a 70% increase in $\Sigma 3^n$ boundary length fraction compared to the as-received condition. The incorporation of these $\Sigma 3^n$ boundaries was also measured using a simplified model of two-dimensional grain boundary transport and its electrical analogy. The results showed that GBE resulted in increased resistance to grain boundary diffusion compared to the as-received condition. The evolution of a GBE microstructure was also studied on a per-cycle basis, and the results are shown to be consistent with previous studies.

Keywords
Coincidence Site Lattice (CSL), Electron Backscattering Diffraction (EBSD), grain boundary engineering (GBE), thermomechanical processing, twin grain boundary

Introduction

Grain boundary engineering (GBE) is a relatively new technique for improving the material properties of metals and alloys with low stacking-fault energy. The aim of GBE processing is to manipulate the grain boundary network in order to create greater resistance to grain boundary-influenced damage mechanisms. First proposed in 1984 [1], many GBE studies have shown success in improving desired properties in face-centred-cubic materials such as nickel alloys, copper and brass through the use of GBE. A summary of such studies is contained in an overview by Randle [2].

GBE has been employed typically to combat the effects of intergranular corrosion [3], cracking [4] and creep [5], although success has also been shown in areas of ductility [6], weldability [7] and microstructural stability [8]. In almost all cases, the GBE process itself involves a series of thermomechanical cycles. These cycles typically consist of a deformation step (such as plate rolling) followed by an annealing step, and are normally repeated between three and seven times. The effect of the processing has generally been an increase the fraction of low-Σ coincidence-site-lattice (CSL) grain boundaries with respect to the fraction of randomly oriented high-angle boundaries (HABs). Early work suggested that these low-Σ grain boundaries (sometimes termed "special boundaries", although this term has become somewhat ambiguous), have superior properties compared to random high-angle boundaries (HABs) due to their potential for structural order in the boundary plane [9].

The term "special boundary" generally refers to a boundary classed according to the CSL nomenclature as having $\Sigma < 29$, where Σ is the reciprocal of the fraction of coincident lattice sites across a grain boundary, should the two grains be theoretically superimposed. Hence, there is some periodicity across the boundary (i.e. it is geometrically "special"), as opposed to a random HAB.

Electron Backscattered Diffraction (EBSD) is typically employed to identify these low-Σ grain boundaries, and provides a measure of the effectiveness of GBE processing by simple statistics such as the fraction of total grain boundary length identified as low-Σ. EBSD orientation maps are built up by calculating the crystal orientation from diffraction patterns in a defined grid of points on a polished surface. These crystal orientation data are then used to determine grain boundary misorientation for each boundary segment. This misorientation is checked against specific misorientations unique to each Σ-value, and thus a Σ-value can be assigned to a grain boundary based on the misorientation between adjoining crystals. However, the CSL model used in EBSD measurements only describes the relative misorientation between two adjacent grains (three parameters) but does not give the orientation of the grain boundary plane itself (two parameters) and so provides an incomplete description of the boundary. In addition, although the link between low-Σ boundaries and improved properties has been suggested on many occasions, recent studies have shown this is almost certainly an indirect relationship [10]. A technique has been documented for measuring the five-parameter grain boundary distribution (FPGBD) [11], based on single section trace analysis. Despite this, the CSL model is still often used, though it is normally in conjunction with other information such as triple point analyses [e.g. 12]). The main reason for using the CSL model is convenience, since identification of specific Σ-value grain boundaries by EBSD is fast, accurate and repeatable.

The Σ3 boundary fraction is thought to be the greatest contributor to improved material properties and is the only CSL boundary type shown to have consistently different characteristics to those of random HABs. The coherent annealing twin boundary has {1 1 1} boundary planes and the lowest free volume of the Σ3 boundaries [13]. Also, a linear correlation exists between the energy of a boundary and its free volume [14]. Other Σ3 boundaries, such as the incoherent twin on {1 1 2} planes and other incoherent boundaries including tilt and twist boundaries on low-index planes, have higher energies than the coherent twin, but still are much lower than the average of random HABs. A study by Randle [10] showed that in pure nickel, those Σ3 boundaries considered to be special (classed as symmetrical tilt, twist or asymmetrical tilt boundaries with one low index plane, as well as those on the 011 zone) comprised over 80% of the total number of Σ3s. In fact, recent research [15] has suggested that the boundaries with special properties are the ones terminated by low-index planes.

Of the other low-Σ boundaries, only the fractions of the $\Sigma 3^n$ family (Σ9 and Σ27) are generally increased by GBE processing. Thus, it is useful to know whether these boundaries also exhibit special properties. Certainly the Σ9 descriptor includes boundary configurations which are of lower energy than the HAB average [13]. However, the boundary must again be fully described to calculate this. In the same study mentioned previously [10], the proportion of Σ9s with assumed special properties was approximately 60%. An investigation using atomic force microscopy combined with EBSD orientation mapping [16] showed that in a "bamboo-structured" sample of Inconel 600 the Σ9 and Σ27 boundaries generally possessed lower energies than the average of the HABs. A recent study [17] concluded that the Σ9 boundaries are more resistant to corrosion than HABs in sensitised 304 stainless steel sheet. The authors came to the common conclusion that the more a boundary plane deviates from the exact CSL position, the more "normal" (in this case, more susceptible to corrosion) the properties become. In contrast to this, another recent study [18] using copper showed that Σ9 and Σ27 boundaries had irrational boundary planes, implying that they had no special properties.

The property improvements which are achieved via GBE are often attributed to the interruption of the HABs as an interconnected network, through the incorporation of grain boundaries with special properties (i.e. lower diffusivity, higher probability of crack arrest etc). Attempts have been made to quantify the level of disruption to the HAB network by such means as triple point analysis (e.g. [12]), or cluster analysis [19,20]. In typical triple point analyses, the number of adjoining random (non-special) boundaries is counted at each triple point. The effects of GBE are measured by the fractions of triple points at the intersection of two or three special boundaries, which are shown to increase relative to the fractions of those at the intersection of zero or one special boundary. However, triple point analysis does not quantify the disruption to the random boundary network, since there is no way to distinguish special boundaries which interrupt the random boundary network from those which do not. In cluster analysis, the individual interconnected "clusters" of each boundary type are analysed and the average "cluster mass" for random boundary clusters is shown to decrease significantly after GBE processing. For example, in as-received René 41, over 95% of the random HABs were in clusters larger than 500 grain diameters [20]. This percentage was then reduced to zero in the grain boundary engineered microstructures, indicating that the percolating network of HABs was disrupted by the GBE process. This method is a much more direct measure of boundary connectivity, and has shown some correlation with material properties [19]. A third method was used by Chen and Schuh [21], who analysed GBE structures as two-dimensional hexagonal diffusion networks. In their analysis, each grain boundary segment was classified according to a binary system as either special or non-special, and assigned a diffusivity based on its boundary classification. The geometric network of grain boundaries was then solved using Fick's first law combined with mass conservation at each junction, and a single "effective grain boundary diffusivity" was extracted. However, the microstructures used in this analysis were simulated, made up of perfect hexagons in a grid pattern where the fraction of "special" boundaries could be adjusted to simulate various degrees of grain boundary engineering.

In the present work, a model of grain boundary connectivity is presented which is similar to the work of Chen and Schuh, but applied to real microstructures, digitised by EBSD analysis. The model also describes a situation of two-dimensional grain boundary diffusion and an analogous electric circuit model is applied. In the analogous electric circuit, the grain boundaries become a network of resistors of varying resistance, depending on boundary length and character. The aim of this model was to quantify the effect of "special" boundaries in a real microstructure, based on the actual boundary topology that GBE microstructures exhibit, and to compare this effect between samples of differing thermomechanical history. By modelling the diffusional properties of the microstructure, it is expected that correlations may also be drawn with grain boundary diffusion-based material properties, such as Coble creep rate.

For each sample analysed in this work, 24 EBSD maps measuring 1mm x 1mm were examined. The digitised images were used to construct a network of resistors

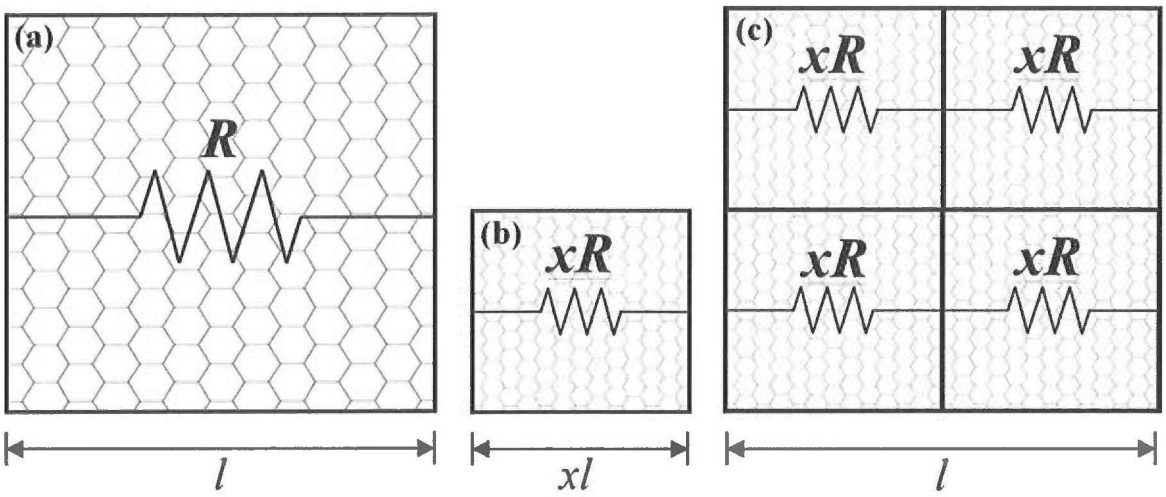

Figure 1. Idealised microstructures (a) initial microstructure, (b) initial microstructure scaled by factor x (0.5 as shown), (c) scaled microstructure repeated to restore initial geometry

and the effective resistance of the network was calculated. Grain boundaries are interpreted as resistors with a resistivity determined by the grain boundary character. For this model, boundary segments were identified as either special ($\Sigma 3^n$) or non-special. A study in 2003 of an austenitic Ni-16Cr-9Fe alloy [22] concluded that, on average, the low-Σ (Σ<29) grain boundary diffusion coefficient was approximately 12x lower than that of the HABs (this low-Σ network consisted primarily of Σ3s, as do the present microstructures). Therefore, in the present analysis, the resistivity ratio of $\rho_{(\Sigma 3n)} / \rho_{(HAB)} = 12$ was also used, although it is recognised that there is potential for further refinement of the model to include information based on boundary type and boundary plane configurations.

The resistance of resistor j is $R_j = l_j\rho_j$ where l_j is the length of the grain boundary segment and ρ_j is the resistivity (either $\rho_{(\Sigma 3n)}$ or $\rho_{(HAB)}$ depending on the grain boundary character). There are a total of n_t nodes in the network where subsets of the m resistors meet. The set of n_l terminating nodes on the left are assigned a voltage V^+ and the set of n_r terminating nodes on the right are assigned voltage zero. The current in each resistor is determined by solving a set of m linearly independent equations generated from $n=n_t - n_l - n_r$ equations corresponding to Kirchoff's Current Law at each internal node and m-n equations corresponding to Kirchoff's Voltage Law for independent paths across the network from left to right.

The first n equations have the form $\Sigma_k a_{jk}i_k = 0$ for node j where $a_{jk} = \pm 1$ for resistors transporting current to/from the node and $a_{jk} = 0$ for all others. The final m-n equations have the form $\Sigma_k c_{jk}R_k i_k = V^+$, where $c_{jk} = 1$ for resistors in the j^{th} path and $c_{jk} = 0$ for all others. In matrix form, $\boldsymbol{Ai=b}$ is solved for $\boldsymbol{i}$, where A is the $m \times m$ matrix of coefficients, $\boldsymbol{i}$ is the $m \times 1$ vector of currents and $\boldsymbol{b}$ is an $m \times 1$ vector.

The effective resistance depends on the grain size in that as grain size increases, the number of paths decreases and R_{eff} increases. The aim of the following analysis is to isolate the topological effects of GBE by removing the grain size effect. An exact solution for the grain size dependence of the effective resistance can be obtained for a self-similar microstructure.

Consider a network of resistors arranged in a regular hexagonal grid, as shown in Figure 1a. Compare such a network comprising resistors of unit length to a network comprising the same number of resistors of length x (shown in Figure 1b). The ratio of the effective resistances of these two networks is $R_{eff,x} / R_{eff,1} = 1/x$. The relationship can be shown by considering the equations from which the net current is determined. For the first case, $\boldsymbol{Ai=b}$ according to the method above. For the second case, $\boldsymbol{A_x i_x = b_x}$. Note that the first n rows of A_x correspond to equations of the form $\Sigma_k a_{jk} i_{k,x} = 0$ for each node j and that they can be scaled by an arbitrary non-zero factor without affecting the solution of the matrix equation. The final m-n rows of A_x derive from equations $\Sigma_k c_{jk} R_{k,x} i_{k,x} = V^+$ that are related to the corresponding rows of A by a factor of $R_k / R_{k,x} = 1/x$. Therefore, $A_x = xA$, and $b_x = b$, from which we obtain $i_x = (1/x)i$ and thus $R_{eff,x} / R_{eff,1} = x$.

In order to calculate the resistance per unit cross sectional length for square images, the effective resistances in the regular hexagonal grid must be repeated $1/x$ times in the vertical and horizontal directions to fill the same space as the original network of unit length resistors (as shown in Figure 1c). This construction corresponds to a circuit with $1/x$ resistors in parallel, where each of those resistors corresponds to

a series arrangement of resistors, each with resistance $R_{eff,x} = xR_{eff,1}$. The effective resistance of such a construction is given by Equation 1:

$$R_{eff,total} = \left[\left(\frac{1}{x}\right)\frac{1}{\left(\frac{1}{x}\right)xR_{eff,1}}\right]^{-1} = xR_{eff,1} \quad (1)$$

This equation shows that for a perfect hexagonal grid, altering the grain size by a factor of x will result in the effective resistance of a unit area also being multiplied by x. Therefore, to decouple the effect of grain size when comparing two samples, the effective resistance of the second sample can be multiplied by $(1/x)$, where x is the ratio of grain size between the two.

In the present analysis, because of the difficulties in selecting an appropriate grain size for a binary system of boundaries, the total HAB length ratio was used in place of the grain size ratio. The justification for considering only HABs in this case is that in a parallel system, it is the low-resistance boundaries which dominate the resistance of the network. For example, for the resistivity ratio $\rho_{(\Sigma 3n)} / \rho_{(HAB)} = 12$, adding a similar $\Sigma 3^n$ boundary in parallel with an HAB will decrease the resistance of the system by ~7.7%. Adding a similar HAB instead will decrease the resistance of the system by 50%. It should be noted that for the analytical solution concerning a hexagonal grid, the HAB length ratio is linearly related to the grain size ratio and hence may be substituted.

The overall aim of the present study is to determine the effect of GBE on the microstructure of alloy 800H, a high temperature single-phase alloy used commonly in the petrochemical industry. This alloy is employed at high temperatures (~0.7 melting point) and relatively low stresses. Future studies will investigate whether GBE has the potential to improve the creep performance of this alloy.

Experimental Procedures

Material was obtained from Thyssenkrupp VDM Australia, in 4.5mm and 8mm sections of plate measuring 300mm x 150mm. The nominal composition of 800H is 30-35wt%Ni, 19-23wt%Cr with a balance of iron and small additions of aluminium and titanium [23]. The plate was cold-machined into strips measuring 150mm x 25mm for rolling.

Each strip was then cold-rolled using one of three different deformation percentages. Subsequent annealing was performed in a box furnace at one of three different temperatures and for one of three different times. This cycle was performed four times for each sample, with the same set of parameters (deformation percentage, annealing temperature, annealing time). In this article, each individual process (deformation or annealing) is referred to as a step, and each combination of these two steps is referred to as a cycle.

Each processing parameter was assigned three relative states (low/medium/high). For reasons of intellectual property ownership, the exact parameters are unable to be reported, and hence the GBE samples are identified using the labels S1-S11. The remaining sample was not processed and hence represents the "as-received" condition, labelled as AR. The relationship between the labels and the processing parameters is shown in Table 1.

Table 1. Relative parameter states for each sample. Specific conditions are unable to be reported.

Sample	Deformation per cycle	Annealing Temp.	Annealing Time
AR	-	-	-
S1	low	low	low
S2	low	low	med
S3	low	med	low
S4	low	med	med
S5	low	med	high
S6	low	high	low
S7	low	high	high
S8	med	med	med
S9	med	med	high
S10	high	med	low
S11	high	med	high

Sections were cut from each of the samples with the surface of interest being a cross-section perpendicular to the rolling direction. These sections were mounted using Buehler Probemet conductive moulding compound and ground to a 600-grit finish using SiC pads. They were then polished to a three micron finish using diamond paste and finally electropolished using a 10% oxalic acid solution at 1.5V for 12 seconds.

Orientation maps were obtained using EBSD for each sample using an HKL Channel 5 EBSD package coupled with a JEOL JSM 6100 Scanning Electron Microscope. A total of 24mm^2 was mapped for each sample at a step size of 10μm. Typical successful pattern identification rates were between 95% and 98%. These maps were then processed using the HKL noise reduction algorithm to extrapolate the remaining unindexed data points, which were almost all in the grain boundaries. $\Sigma 3^n$ ($n \leq 3$) boundaries were identified using the Brandon criterion [24]. For each map, the total boundary length fractions for $\Sigma 3$, $\Sigma 9$ and $\Sigma 27$ were calculated automatically by the HKL software.

Grain size measurement was semi-automated, using the HKL software. Since each data point reflects a specific crystal orientation, grain boundaries are automatically determined as lines dividing groups of points of similar crystal orientation. Therefore, it is possible to detect

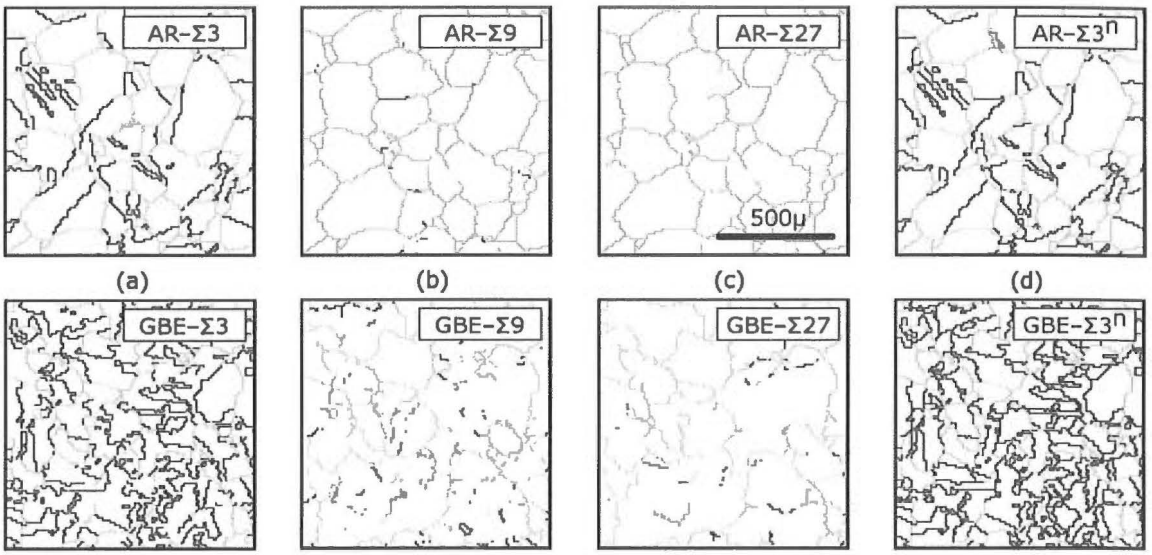

Figure 2. Representative comparison between as-received (top) and GBE (bottom) conditions showing (a) Σ3 boundaries, (b) Σ9 boundaries, (c) Σ27 boundaries and (d) Σ3, Σ9 and Σ27 boundaries highlighted in black. Grey lines indicate HABs.

every grain automatically and calculate statistics such as mean grain diameter. However, without user input, this method is prone to including some small "false" grains, often misindexed due to changes in pattern quality either near grain boundaries or occasionally within grains. In order to remove these false grains from the count, the initial average grain diameter was calculated, and then a filter was applied. A threshold value of 4% initial average area was employed and found to exclude most visually-identified false grains, whilst including most small, true grains. The main advantages in using this semi-automated method over the optical methods described in ASTM E112 (Standard Methods For Determining Average Grain Size) are the increased accuracy and repeatability, and also the ability to automatically identify grain boundaries with specific misorientations (i.e. twin boundaries), which is a significant part of this work.

There is evidence to support the inclusion of twin boundaries in grain size calculations [e.g. 25], on the basis that twins have an effect on the motion of dislocations. Therefore, both "twin-excluded" and "twin-included" grain sizes have been calculated for comparison in this study. The numbers given in the results section indicate the mean grain diameter based on equivalent circular grains.

The grain boundary connectivity was analysed by considering a simplified model of two-dimensional grain boundary diffusion, as explained in the introduction. The effective resistance to diffusion (of a specific unit area) was extracted from the analogous electric circuit, where grain boundary segments were each assigned a resistance based on their length and type. The effective resistance of each sample was normalised by its total HAB length to decouple the effect of changes in grain size and isolate the changes in boundary topology.

In order to investigate the microstructural evolution through GBE processing, two further samples were processed using the same parameters as S3 and S5. These samples were analysed after each of five cycles to determine the changes in proportion of $\Sigma 3^n$ boundaries, grain size, and mean Σ3 angular deviation. This mean Σ3 angular deviation was calculated based on the raw orientation data from the HKL EBSD system. Each grain boundary segment (defined as a single section of boundary between two triple points) was assigned a single misorientation based on the difference between the mean grain orientation of each neighbouring grain. The deviation from ideal, v, was calculated by then comparing the boundary misorientation with the ideal Σ3 misorientation using standard matrix multiplication methods [26]. The low-angle boundary (LAB) fraction was also calculated within the HKL software, representing the length fraction of all grain boundaries with misorientations $2°<\theta<15°$.

Results and Discussion

This discussion is divided into four sections detailing the appearance of a typical GBE microstructure, the contribution to the GBE mechanism that the present work provides, the effects of variations in individual processing parameters, and the microstructural evaluation of GBE samples through connectivity analysis.

I. GBE Microstructure

Figure 2 shows a comparison between the as-received microstructure (AR) and a representative GBE microstructure (S3). Four images, highlighting Σ3, Σ9, Σ27 and all $\Sigma 3^n$ ($n \leq 3$) boundaries respectively in black with general HABs in grey are presented.

These images are typical of GBE microstructures reported in the literature. After processing, there is a clear increase in the number fraction (and correspondingly the length fraction) of Σ3 boundaries, accompanied also by increases in the relative length of Σ9 and Σ27 boundaries. These Σ9 and Σ27 boundaries are a result of the interactions between dissimilar Σ3 boundaries and are geometrically constrained where three $\Sigma 3^n$ boundaries meet at a triple junction.

II. Microstructural Evolution

In order to track the evolution of the microstructure throughout the GBE processing, two samples (with the same processing parameters as S3 and S5) were analysed after each of five GBE processing cycles. These samples were subjected to identical deformation percentages and annealing temperatures, and therefore their only difference is in annealing time. For convenience, these two samples are referred to in this section as "short-annealed" and "long-annealed". The length fractions of $\Sigma 3^n$ boundaries were calculated after each GBE cycle, and the results are shown in Figure 3.

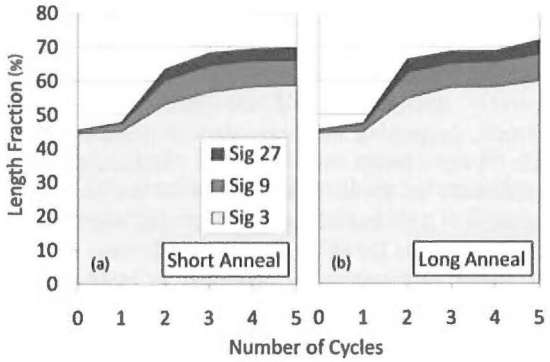

Figure 3. Length fractions of $\Sigma 3^n$ boundaries for (a) short-annealed and (b) long-annealed samples after each of five GBE cycles.

A "diminishing return" trend in terms of total $\Sigma 3^n$ length fraction is observed for both samples. However, it is important to note that this trend actually begins at cycle two. During the first cycle, the $\Sigma 3^n$ length fraction undergoes very little change, which indicates that under these specific conditions more than one step is necessary to achieve a GBE state. This statement is in general agreement with the majority of work in this field [12, 20, 27-28], although there are occasional instances of GBE states being reported after a single cycle. For example, Kokawa et al. [29] report very high length fractions of Σ<29 boundaries in an austenitic 304 stainless steel after one cycle of 5% rolling and annealing at 1200-1240K. Colman and Randle [18] also showed that in copper a single GBE cycle increased the fraction of Σ3s, although these new Σ3s were mainly not incorporated into the GB network until subsequent processing cycles.

When $\Sigma 3^n$ fractions are reported as a function of processing cycle in the literature [30-32], the results generally show a somewhat erratic first or first few steps (the Σ3 fraction may actually decrease slightly), followed by a general increase in the fraction of $\Sigma 3^n$ boundaries. In this present work, little effect was obtained from performing the first step, but subsequent processing steps resulted in increasing fractions of Σ3, Σ9 and Σ27 boundaries.

The reasons for this trend are not well understood, although the issue has been addressed by Randle and Davies [31] in a study of alpha-brass. They suggest that in the initial stages the immobile twin boundaries provide strain retention. This is thought to be due mainly to the back stress generated from dislocation pile-up at these boundaries. The retained strain is increased with the early deformation steps until it reaches a threshold level, at which point there is sufficient driving force for the mobile GB network to move through the structure, absorbing dislocations and hence removing the retained strain. During the next cycle, there is little retained strain. There is evidence of new twinning during these subsequent cycles, and the $\Sigma 3^n$ fraction increases. Owen and Randle go further in a study of 316 stainless steel [32]. They suggest that the boundary migration is slower when the material has little retained strain (in the later cycles) and that this slower migration velocity is more suitable for the nucleation of annealing twins.

In the present work, it was desirable to determine whether or not the results supported the theories given in previous studies. The angular deviation from ideal misorientation provides important information about the energy of boundaries classified as Σ3 in the network [33], and the amount of retained strain in the grains either side of these boundaries. The data is plotted as a weighted mean deviation parameter, $\bar{v}$, which is defined as follows:

$$\bar{v} = \frac{\sum_{i}^{numof\,\Sigma 3s} v_i L_i}{v_{\max} \sum_{i}^{numof\,\Sigma 3s} L_i} \qquad (2)$$

where v_i is the angular deviation from ideal of Σ3 boundary segment i,

L_i is the length of Σ3 boundary segment i,

v_{max} is the maximum allowable deviation from the Brandon criterion (~8.7°).

The weighted mean deviation parameter for both samples is shown in Figure 4. The LAB fraction is a separate indicator of retained strain in the lattice, and is

also included in Figure 4. In this figure, points are joined as a guide only.

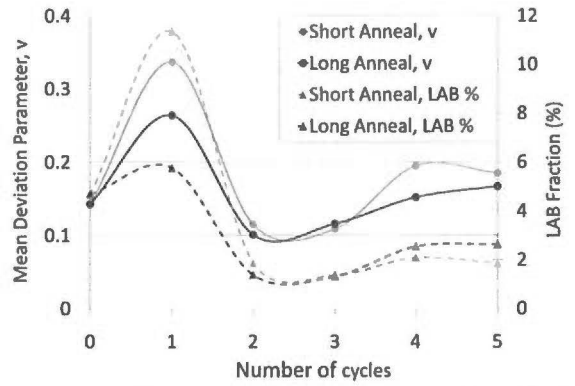

Figure 4. Mean Σ3 deviation parameter ($\bar{\nu}$) and LAB fraction for short-annealed and long-annealed samples after each of five GBE cycles.

Figure 4 shows that the mean Σ3 angular deviation increases significantly after the first processing cycle. This trend is present for both samples, although the increase is greater for the short-annealed sample. The same result was obtained in a previous study of this material [34], where the Σ3 deviation was then found to decrease with increasing annealing time up to 90 minutes after one deformation step. In both cases, the increase in Σ3 deviation is likely due to the effect of dislocation pile-up in the neighbouring lattices. Correspondingly, the LAB fraction increases from 4.7% to 11.4% for the short annealed sample and to 5.8% for the long annealed sample. These results show that the first processing cycle served to increase the overall amount of retained strain in the material. It follows that the annealing conditions were not sufficient in either case to remove the deformation introduced during the rolling step, although the long-anneal step should lead to lower retained strain levels. After the second cycle however, the mean Σ3 deviation parameter decreased to a level below that of the as-received material in both samples. Similarly, the LAB fractions decreased to levels approximately one-third of the as-received condition. These results indicate that a significant proportion of the retained strain that was present in the material after one cycle has been removed by the second cycle. Certainly, migration of mobile boundaries and dislocation absorption could explain this result. The simplest evidence for boundary migration is the change in grain size for both samples, plotted in Figure 5.

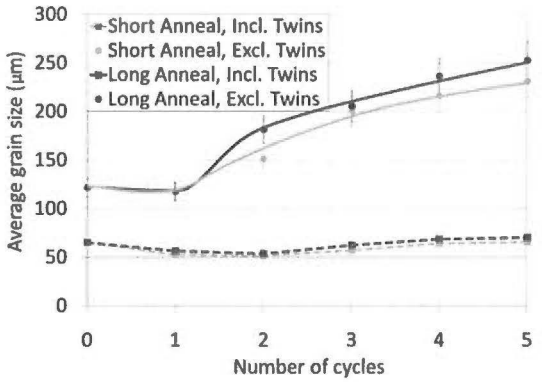

Figure 5. Grain sizes (including and excluding twin-boundaries) of short-annealed and long-annealed samples after each of five GBE cycles. Error bars show standard deviation from each set of 24 images.

The trend in grain size reflects that of the $\Sigma 3^n$ fraction, in that it remains constant for the first cycle before increasing significantly during the second. Less significant increases are also observed in the subsequent cycles. This analysis therefore provides evidence of boundary migration through cycles 2-5, which is probably most significant during cycle two. Smaller increases in $\Sigma 3^n$ fraction and retained strain levels are also noticed during these later cycles.

In summary of this information, both the short-annealed sample and the long-annealed sample exhibited similar trends during GBE processing. During cycle one, levels of retained strain increased, the $\Sigma 3^n$ fraction remained relatively unchanged, and the grain size remained constant, suggesting little boundary migration. During cycle two, levels of retained strain decreased significantly to levels below those of the as-received condition. $\Sigma 3^n$ fraction and grain size showed their largest increases for all cycles after cycle two. In cycles 3-5, small increases were observed in retained strain levels, grain size and $\Sigma 3^n$ fraction.

These results are consistent with the mechanisms discussed previously in the literature. The largest increases in Σ3 fraction were observed in both (a) the same cycle as the largest decrease in Σ3 deviation parameter (as in the present study, and also [31]) and (b) the cycle immediately following the largest decrease in Σ3 deviation parameter [32]. With regard to the theory that low retained strain levels (and hence relatively slow boundary migration) are more suitable for the generation of annealing twins as suggested for case (b), it is still possible that the absorption of retained strain (relatively high boundary velocity) and the Σ3 generation occur consecutively within the same annealing step, which would be consistent with case (a). The fact that the as-received condition contained few Σ9 and Σ27 boundaries after its manufacturing process of heavy deformation and high-temperature annealing would suggest that extremely high boundary velocities are not suitable for creating a GBE state.

III. Effects of Processing Parameters

The length fractions of $\Sigma 3^n$ boundaries were calculated for all eleven GBE samples representing different combinations of the three GBE parameters. These results are shown in Figure 6.

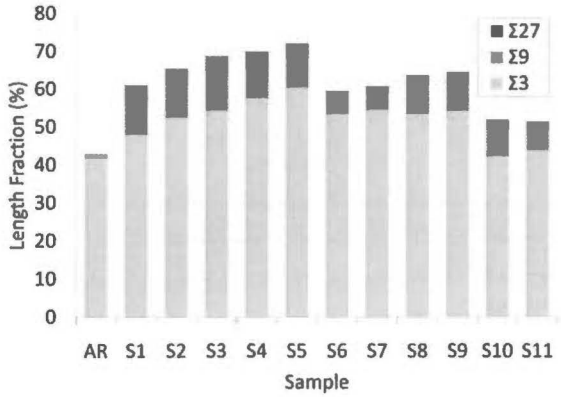

Figure 6. Length fractions of $\Sigma 3^n$ boundaries for all GBE samples.

The as-received sample (AR) contains boundary length fractions of approximately 42% for Σ3, ~1% for Σ9 and ~0% for Σ27. The lack of the Σ3 geometric counterparts (Σ9 and Σ27) shows that the material is not in a GBE state. The results show that all combinations of GBE parameters resulted in increases in the length fraction of $\Sigma 3^n$ boundaries, as compared to the as-received sample. Specifically, the increases in Σ9 and Σ27 fractions show that some amount of GBE has taken place in all eleven processed samples.

The average grain size was also calculated for each sample (both excluding twins and including twins as grain boundaries) and the results are shown in Figure 7.

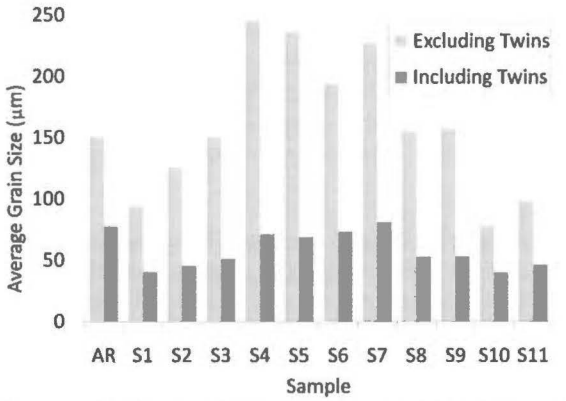

Figure 7. Grain sizes, including and excluding twins for all GBE samples

In the majority of cases, the GBE process has caused the ratio between the twin-excluded grain size and the twin-included grain size to change. For example, this ratio is ~2 in the AR sample and shows increases up to ~3.5 in the GBE samples. This is obviously consistent with the introduction of new twins.

As one of the aims of this work was to optimise the GBE conditions with respect to $\Sigma 3^n$ fraction as well as grain size, the local effect of variation in each GBE parameter is briefly discussed in turn.

i. Deformation Percentage

The effect of deformation percentage can be seen when comparing samples S5, S9 and S11. These samples have all been annealed under the same conditions, and represent the three states of deformation (low, medium, high). Figure 3 shows that increasing the deformation percentage within this range causes the length fraction of $\Sigma 3^n$ boundaries to decrease relative to S5. This general trend is also noticeable when considering the entire range of the samples, in that the low-deformation samples (S1-S7) generally show higher $\Sigma 3^n$ fractions than the medium (S8-S9) or high-deformation (S10-S11) samples. In terms of grain size, Figure 4 shows that for the same samples (S5, S9 and S11), the grain size decreases with increasing deformation.

ii. Annealing Temperature

The effect of annealing temperature can be isolated by considering samples S1, S3 and S6, representing low deformation, low annealing time and low, medium and high annealing temperatures respectively. Figure 6 shows that there is a local maximum in the $\Sigma 3^n$ fraction in between T_{low} and T_{high}, indicating that there is a local intermediate temperature which will yield the greatest return in terms of $\Sigma 3^n$ fraction. Figure 7 shows the expected trend of increasing grain size with increasing annealing temperature over these three samples.

iii. Annealing Time

The effect of annealing time is isolated by considering samples S3, S4 and S5, representing low deformation, intermediate annealing temperature and low, medium and high annealing times respectively. In these three samples, $\Sigma 3^n$ fraction is seen to increase slightly with increasing annealing time. This result is also noticeable in the other conditions (e.g. S1-S2). Figure 7 again shows the expected trend of increasing grain size with increasing annealing time for most conditions, although S4 is slightly anomalous compared to S3 and S5.

iv. Summary of GBE Parameters

Although the actual parameters used in these experiments cannot be reported, it is important to note that alloy 800H appears to have a certain combination of GBE parameters within the range tested which results in a local maximum in boundary length fraction of Σ3, Σ9 and Σ27 boundaries. Small deviations from these parameters have been shown to still result in GBE, but with reduced $\Sigma 3^n$ fractions compared to this maximum. Hence it is likely that for many examples of GBE presented in the literature, small alterations in the relevant parameters may increase the $\Sigma 3^n$ boundary

fraction, possibly leading to a more optimised microstructure. The reasons for this are obviously linked to the GBE mechanism, which is still under research, although the amount of retained strain in the material and the migration speed of mobile boundaries have been suggested as important [32]. Retained strain is built up during the deformation steps and provides the driving force for boundary migration. If the retained strain is insufficient for boundary migration, GBE likely cannot occur. If the retained strain is too high, "special" boundaries may be destroyed by the introduction of dislocations and may not necessarily revert to their original geometry. It has also been proposed previously that boundary velocity may be too high to support new twin generation. In the present work, it was found that of the three deformation percentages, the "low" state was most successful in increasing $\Sigma 3^n$ length fraction and therefore it follows that boundary migration occurred in all samples. The annealing temperature obviously also influences boundary migration speed and it follows that annealing conditions could also be insufficient for migration or too high for new twin generation. In fact, at least one study [35] has been published in the literature where the $\Sigma 3^n$ boundary fraction was slightly decreased by attempted GBE processing. Therefore, if the specific aim of a GBE procedure is to optimise the fraction of $\Sigma 3^n$ CSL boundaries, it is recommended that a range of conditions is first tested and then refined surrounding those that seem to be optimal.

IV. Microstructural Evaluation

While the length fraction of low-Σ CSL boundaries is used in this case as a measure of how "engineered" the material is, it should not be used as a predictor of material properties. Instead, this information should be combined with other information such as an indication of the boundary planes (where possible) and a knowledge of the likely damage mechanisms. Some damage mechanisms such as stress corrosion or Coble creep (grain boundary diffusion-based creep) rely on the grain boundary network as a transport network. One major way in which GBE is thought to resist such mechanisms is by breaking up the interconnected HAB network and therefore reducing its transport properties. In fact, there has been some work published regarding the influence of boundaries with special properties and their effect on theoretical GB transport networks [e.g. 36-37]. However, the measurement of such disruption has not been standardised. A common method of measuring the connectivity of the HAB network is to analyse all of the triple points and classify each based on the number of special (usually $\Sigma<29$) boundaries it joins. However, a situation where multiple twins and twin variants meet inside a single grain will certainly increase this fraction, but will likely offer no disruption to the transport network provided the original HABs remain. Therefore, a more direct measurement of grain boundary connectivity is needed.

In the present work, this disruption of the HAB network can be shown in two ways. Figure 8 shows sample HAB networks from two of the twelve samples (AR and S5). These images have been processed by removing the $\Sigma 3^n$ family.

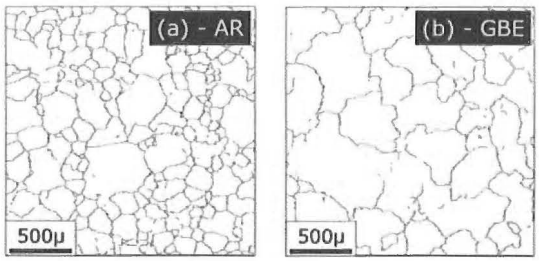

Figure 8. HAB networks of (a) AR and (b) S5 (highest $\Sigma 3^n$ fraction)

Visual comparison with the as-received sample shows qualitatively that the connectivity of the HAB network has been interrupted through the inclusion of these extra $\Sigma 3^n$ boundaries in the GBE sample.

Figure 9 shows the results of the grain boundary network connectivity analysis, explained in the introduction. This analysis was performed by converting each EBSD map to a network of resistors where each grain boundary segment was assigned a resistance value based on its length and boundary type. The two-dimensional effective resistance, R_{eff}, of the network was then found by solving the analogous electric circuit problem. Plotted are the ratios between the R_{eff}-value for each sample and the R_{eff}-value for the as-received sample. This ratio is denoted $\bar{R}$.

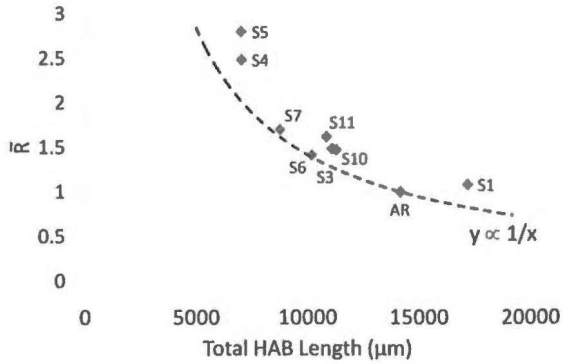

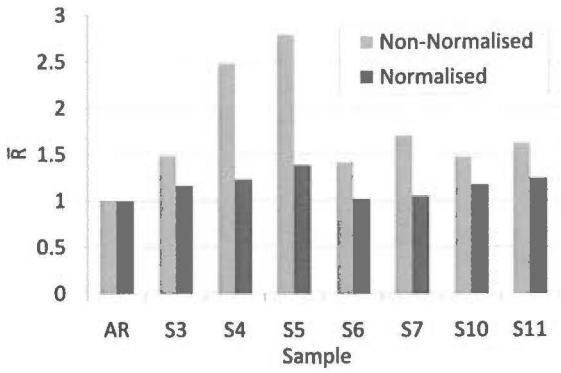

Figure 9. (a) Correlation between $\bar{R}$ and total HAB length for selected samples, showing the analytical solution for microstructural scaling effects (b) $\bar{R}$ for selected GBE conditions, normalised against total HAB length.

Figure 9a shows $\bar{R}$ for each sample, as a function of total HAB length. The dotted line in this figure indicates the $\bar{R}$ values that would result solely from changes in grain size according to the derived relationship $\bar{R} \propto (1/x)$. It is apparent that the majority of the GBE data lie well above this line, signifying that there is a definite change in boundary topology which acts in addition to the change in boundary length. This is confirmed in Figure 9b, showing both the raw and normalised $\bar{R}$ for each sample. These figures show all of the GBE samples exhibited some increase in effective resistance, with the greatest disruption to the HAB network occurring in samples S4 and S5. These are also the samples with the highest $\Sigma 3^n$ fractions (Figure 6). It should also be noted that this difference would be compounded in the real, three-dimensional case. These results show that the high temperature annealed samples (S6, S7) exhibit increases in $\Sigma 3^n$ boundary fraction of ~40%, but only a very small increase in normalised effective resistance. This is consistent with twin and twin variants being introduced internally within the existing HAB structure, which will not effectively disrupt the existing HAB network, and may not reduce grain boundary transport properties compared to an as-received sample with a similar grain size.

As the present analysis has not been previously published in the literature, a triple junction analysis is also presented in order to provide some continuity with existing studies. Figure 10 shows the relative fraction of triple junctions joining 0, 1, 2 and 3 special ($\Sigma 3^n$) boundaries for each sample (0-3SP).

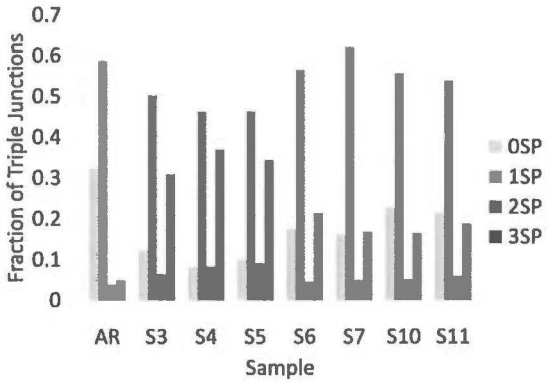

Figure 10. Fraction of triple junctions joining zero, one, two and three $\Sigma 3^n$ boundaries (0-3SP) for as-received and selected GBE samples.

Similar trends are seen when the triple junction analysis results are considered. Figure 10 shows that 32% of the triple junctions in the as-received sample join only HABs, and approximately 5% join three $\Sigma 3^n$ boundaries. In the highest $\Sigma 3^n$ fraction samples (S4 & S5), the number of HAB-only triple junctions drops to 10-12% and the number of $\Sigma 3^n$-only triple junctions is increased to 34-37%. For these samples, the $\Sigma 3^n$-only fraction is predominantly made up of the $\Sigma 3$-$\Sigma 3$-$\Sigma 9$ (~66%) and $\Sigma 3$-$\Sigma 9$-$\Sigma 27$ (~33%) junctions. When the high-temperature annealed samples are considered (S6, S7), similar trends are observed, but to a lesser extent than samples S4 and S5. In this case, the $\Sigma 3^n$-only fraction is made up of the same two junctions ($\Sigma 3$-$\Sigma 3$-$\Sigma 9$ and $\Sigma 3$-$\Sigma 9$-$\Sigma 27$) but in the ratio ~73% to ~27%. This shows that fewer multiple twinning operations have taken place compared to S4 and S5, which is consistent with the lower $\Sigma 9$ and $\Sigma 27$ fractions from Figure 6. Importantly however, these results could be misinterpreted as a significant disruption to the HAB network when compared to the as-received triple junction fractions. The present analysis has shown that this is likely not the case for these samples. Despite this disagreement, in general there is reasonable correlation between the triple junction analysis and the connectivity model used in this work. Both analyses suggest that the greatest disruption to the HAB network occurs in samples S4 & S5, which also exhibit the highest $\Sigma 3^n$ fractions.

Summary and Conclusions

A microstructural study of eleven grain boundary engineered samples of alloy 800H was performed using EBSD. Each sample received a different GBE treatment as defined by a matrix of GBE parameters (rolling deformation percentage, annealing temperature, annealing time). The relative length fraction of $\Sigma 3^n$ CSL boundaries was increased in all cases, and thus it can be concluded that there a variety of parameter combinations that will create a GBE material. The maximum $\Sigma 3^n$ length fraction of 72.1% was attained using a relatively low deformation level, and an intermediate annealing temperature (the specific

conditions are unable to be reported due to confidentiality). Annealing time had only a small effect under these conditions. The maximum attained $\Sigma 3^n$ fraction represents a 70% increase over the as-received sample.

Two samples were subjected to a further study, involving characterisation after each of five total GBE cycles. For both samples, the $\Sigma 3^n$ fraction was shown to remain unchanged during the first cycle, before increasing through the next four. Retained strain levels (as measured by $\Sigma 3$ deviation and LAB fraction) were shown to increase during this first cycle, before decreasing sharply during the second. These results are consistent with other such analyses published in the literature and add support to these studies.

A boundary connectivity analysis method was developed to measure the extent of $\Sigma 3^n$ incorporation into the GB network by means of a simplified two-dimensional diffusion model. All GBE samples exhibited some extent of $\Sigma 3^n$ incorporation, shown by increases in two-dimensional diffusion resistance, however the highest levels of incorporation were consistent with the highest $\Sigma 3^n$ length fractions. These results were also consistent with an analysis of the triple junctions for each sample, which is a common method of analysing boundary connectivity found in the literature. A study of secondary creep rate in these GBE conditions is in progress and is expected to show some correlation with the effective resistance results. The results of this study will be reported at a later date.

Acknowledgements
The authors wish to acknowledge the continued generous support of Methanex New Zealand, Schmidt and Clemens (S.A.) and Tubacex (S.A.), as well as the financial support of the New Zealand Tertiary Education Commission (TEC).

References

[1] T. Watanabe, Res. Mech. 11 (1984) 47-84
[2] V. Randle, Mat. Sci. & Tech. 26 (2010) 253-261
[3] P. Lin, G. Palumbo, U. Erb, K.T. Aust, Scripta Metal. Mater. 33 (1995) 1387-1392
[4] E.M. Lehockey, A.M. Brennenstuhl, I. Thompson, Corros. Sci. 46 (2004) 2383-2404
[5] V. Thaveeprungsriporn, G.S. Was, Met. Mater. Trans. 28A (1997) 2101-2112
[6] T. Watanabe, S. Tsurekawa, Acta Mater. 47 (1999) 4171-4185
[7] E.M. Lehockey, G. Palumbo, P. Lin, Metall. Mater. Trans. A 29A (1998) 3069-3079
[8] S.M. Schlegel, S. Hopkins, M. Frary, Scripta Mater. 61 (2009) 88-91
[9] L.S. Shvindlerman, B.B. Straumal, Acta Metall. 33 (1985) 1735-1749
[10] V. Randle, Mat. Sci. & Tech. 15 (1999) 246-252
[11] V. Randle, Scripta Mater. 44 (2001) 2789-2794
[12] M. Kumar, W.E. King, A.J. Schwartz, Acta Mater. 48 (2000) 2081-2091
[13] V. Randle, Acta Mater. 46 (1997) 1459-1480
[14] K.L. Merkle, D. Wolf, Philos. Mag. A 65 (1992) 513-530
[15] G.S. Rohrer, D.M. Saylor, B.S. El-Dasher, B.L. Adams, A.D. Rollett, P. Wynblatt, Z. Metallkd. 95 (2004) 197-214
[16] T. Skidmore, R.G. Bucheit, M.C. Juhas, Scripta Mater. 50 (2004) 873-877
[17] X. Fang, W. Wang, H. Guo, X. Zhang, B. Zhou, Proceedings of Sino-Swedish Structural Materials Symposium (2007) 339-343
[18] M. Coleman, V. Randle, Metall. & Mater. Trans. A 39 (2008) 2175-2183
[19] C.A. Schuh, M. Kumar, W.E. King, Acta Mater. 51 (2003) 687-700
[20] Y. Gao, J.S. Stölken, M. Kumar, R.O. Ritchie, Acta Mater. 55 (2007) 3155-3167
[21] Y. Chen, C.A. Schuh, Acta Mater. 54 (2006) 4709-4720
[22] B. Alexandreanu, B.H. Sencer, V. Thaveeprungsriporn, G.S. Was, Acta Mater. 51 (2003) 3831-3848
[23] Special Metals Technical Bulletin SMC-047 – "Incoloy 800H and 800HT", available www.specialmetals.com
[24] D.G. Brandon, Acta Metall. 14 (1966) 1479-1484
[25] L. Lu, Y. Shen, X. Chen, L. Qian, K. Lu, Sci. 304 (2004) 422-426
[26] V. Randle, The Measurement of Grain Boundary Geometry, IOP Publishing Ltd, 1993
[27] V. Thaveeprunsriporn, P. Sinsrok, D. Thong-Aram, Scripta Mater. 44 (2001) 67-71
[28] U. Krupp, W.M. Kane, X. Liu, O. Dueber, C. Laird, C.J. McMahon, Mater. Sci. Eng. A 349 (2003) 213-217
[29] H. Kokawa, M. Shimada, M. Michiuchi, Z.J. Wang, Y.S. Sato, Acta Mater. 55 (2007) 5401-5407
[30] W.E. King, A.J. Schwartz, Scripta Mater. 38 (1998) 449-455
[31] V. Randle, H. Davies, Met. Mater. Trans. A 33 (2002) 1853-1857
[32] G. Owen, V. Randle, Scripta Mater. 55 (2006) 959-962
[33] J. Furley, V. Randle, J. Mat. Sci. Tech. 7 (1991) 12-19
[34] L. Tan, T.R. Allen, Met. Mat. Trans. 36A (2005) 1921-1925
[35] C.J. Boehlert, Mat. Sci. Eng. A 473 (2008) 233-237
[36] W.S. Tong, J.M. Rickman, H.M. Chan, M.P. Harmer, J. Mater. Res. 17 (2002) 348-352
[37] Y. Chen, C.A. Schuh, Phys. Rev. B. 76 (2007) 064111:1-12